Universidad de Concepción

Facultad de Ingeniería

Departamento de Ingeniería Química

MULTIPHYSICS MODELING OF CO_2 METHANATION IN A MONOLITHIC REACTOR: DYNAMIC RESPONSES TO TEMPORARY H_2 DISTURBANCES

Tesis presentada al Departamento de Ingeniería Química de la Facultad de Ingeniería de la Universidad de Concepción para optar al grado de Doctor en Ciencias de la Ingeniería con mención en Ingeniería Química

POR: Douglas Enrique Pérez Vilela

Profesora Guía: Ximena Andrea García Carmona

Abril, 2025

Concepción, Chile

En primer lugar, dedico este trabajo a mi madre. Gracias por ser un pilar fundamental, así como ejemplo de fortaleza y buenos valores para seguir un camino correcto de vida.

También dedico este logro a mi esposa Einis. Sin ti esto no hubiera sido posible. Gracias por estar siempre conmigo y apoyarme en todo momento. Este logro también es tuyo.

Adicionalmente, quiero dedicar este trabajo a mi hijo Adrián, por brindarnos más felicidad a nuestras vidas, siendo una gran motivación para cumplir este objetivo.

Por otra parte, agradezco a mi padre y demás familiares por su apoyo. Esto se extiende también a mis hermanos y hermanas de vida.

También quiero dar un especial agradecimiento a mi cuñada Aneriz, quien llegó a apoyarnos en las últimas semanas de la culminación de este proyecto. Gracias por todo.

Aprovecho para agradecer a la Prof. Ximena García por proponerme este tema de tesis. Gracias por su confianza y paciencia. Sin usted, esto tampoco hubiera sido posible.

Agradezco por otra parte a los Profesores Romel Jiménez y Katherina Fernández por su gran apoyo como directores del programa durante mis estudios doctorales.

También agradezco a los profesores con los que trabajé en las ayudantías, así como al personal académico y administrativo del Departamento de Ing. Química por su apoyo.

Muchas gracias a mis compañeros de oficina y de posgrado por los buenos momentos que compartí con ustedes, así como el gran apoyo que me brindaron durante mis estudios.

De igual forma, doy gracias a CarboCat por permitirme ser parte de sus integrantes. Muchas gracias a Verónica, a los profesores y demás integrantes del grupo por su apoyo.

Por supuesto, doy agradecimientos al Prof. Siegfried Bajohr y a Mr. Martin Kansy por darme la oportunidad de realizar una estadía internacional en el EBI-CEB, KIT, Alemania. Gracias por el apoyo y contribuciones brindadas para el desarrollo de este trabajo. Aprecio el trato ameno que me dieron junto con Simon, Mathias, Crispin, Brahim y demás integrantes del instituto durante mi estadía.

También agradezco a los Profesores Alejandro Karelovic, Luis Arteaga y Francisco Gracia por sus correcciones y sugerencias para presentar un trabajo de mejor calidad.

Finalmente, quiero dar gracias al Prof. Claudio Olivera y a Freddy Figueira por haberme apoyado a realizar mis estudios doctorales a través de sus recomendaciones.

Acknowledgments

Douglas E. Pérez-Vilela acknowledges the Chilean National Agency for Research and Development (ANID) for the Doctoral Scholarship, 2020-21200674, and its associated Complementary Funds Project. We thank Dr. Siegfried Bajohr and Mr. Martin Kansy to made it possible to carry out the experimental research in the monolithic honeycomb reactor installed at the Engler-Bunte-Institute, Karlsruhe Institute of Technology, Germany. Their valuable support during the experimental tests, fruitful discussions and recommendations, which resulted in the enrichment of this research are sincerely appreciated. We also extend these thanks to their research group, and colleagues at the Engler Bunte Institute.

Content

List of Tables

List of Figures

Nomenclature

$A_{\mu i}, B_{\mu i}, C_{\mu i}, D_{\mu i}$ constants to calculate gas viscocity of *i-th* compound with DIPPR equation
$A_{C_p i}, B_{C_p i}, C_{C_p i}, D_{C_p i}, E_{C_p i}$ constants to calculate specific heat of *i-th* compound with DIPPR equation
$A_{\lambda i}, B_{\lambda i}, C_{\lambda i}, D_{\lambda i}$ constants to calculate thermal conductivity of *i-th* compound with DIPPR equation
a_v gas-solid specific surface area [m^{-1}]
C_p mass specific heat [kJ/(kg°C)]
d_h hydraulic diameter of monolith channel [m]
d_p pore diameter of catalytic washcoat [m]
D_i diffusivity of *i-th* compound within bulk phase [m^2/s]
D_{i_axial} axial dispersion of *i-th* compound [m^2/s]
$D_{i\_eff,cat}$ effective diffusivity of *i-th* compound within catalyst [m^2/s]
$D_{i,j}$ binary diffusivity of *i-th* compound respect to *j-th* compound [m^2/s]
$D_{i,K}$ Knudsen diffusivity of *i-th* compound [m^2/s]
E_a activation energy [kJ/mol]
f friction factor [-]
g gravity acceleration [m/s^2]
Gr_m mass Grashof number [-]
Gr_T thermal Grashof number [-]
$GHSV$ Gas Hour Space Velocity [h^{-1}]
h_{gs} gas-solid heat transfer coefficient [$kW/(m^2°C)$]
j_i mass diffusive flux of *i-th* compound [$kg/(m^2s)$]
k reaction rate constant [units depend on kinetic expression used]
k_0 pre-exponential factor [units depend on kinetic expression used]
$k_{i,gs}$ gas-solid mass transfer coefficient of *i-th* compound [m/s]
K_i adsorption constant of *i-th* compound (Koschany's kinetic expression) [$bar^{-1/2}$]
K_{eq} chemical equilibrium constant [bar^{-2}]
L reactor length [m]
$\dot{m_{i,gs}}$ gas-solid mass flux of *i-th* compound [$kg/(m^2s)$]
MW molecular weight [kg/kmol]
MW_i molecular weight of *i-th* compound [kg/kmol]
n reaction order (Falbo's kinetic expression) [-]
N_C number of compounds
N_R number of reactions
Nu_{gs} gas-solid Nusselt number [-]
p_i partial pressure *i-th* compound [kPa]
P pressure [kPa]
Pr Prandtl number [-]
q axial heat flux [kW/m^2]
$\dot{q_{gs}}$ gas-solid transferred heat flux [kW/m^2]
r radial coordinate [m]
r_j *j-th* reaction rate [$kmol/(kg_{cat}·s)$]
$\overline{r_j}$ *j-th* average reaction rate [$kmol/(kg_{cat}·s)$]
R monolithic reactor radius [m]
R_{gases} gases universal constant [kJ/(kmol·K)]
Re Reynolds number [-]
Sc_i Schmidt number of *i-th* compound [-]
$Sh_{i,gs}$ gas-solid Sherwood number of *i-th* compound [-]
t time [s]

$t_{residence,inlet}$ residence time at the reactor's entrance [s]
$t_{rxn,CO_2,inlet}$ characteristic reaction time of CO_2 at the reactor's entrance [s]
T temperature [°C]
$T_{reactor}$ reactor temperature [°C]
u superficial velocity [m/s]
U_{sc} solid-cooling system heat transfer coefficient [kW/(m²°C)]
w_i mass fraction of *i-th* compound [-]
X_{CO_2} CO_2 conversion [%]
z axial coordinate [m]
z_{f,Re_g} nondimensional axial coordinate respect to Re_g and d_h [-]

Greek letters
α parameter of Falbo's kinetic expression [atm^{-1}]
δ characteristic length of washcoat thickness [m]
$\Delta H_{ads,i}$ adsorption heat of *i-th* compound [kJ/mol]
ΔH°_{rxn} standard reaction heat [kJ/mol]
$\Delta H_{rxn,j}$ *j-th* reaction heat [kJ/mol]
ε volumetric fraction respect to monolith reactor volume [-]
$\varepsilon_{g,cat}$ gas volumetric fraction within catalytic washcoat [-]
η_j effectiveness factor of *j-th* reaction [-]
λ bulk phase thermal conductivity [kW/(m°C)]
λ_{axial}, λ_{radial} axial and radial thermal conductivity [kW/(m°C)]
μ viscosity [Pa·s]
ξ catalyst main coordinate (transversal direction to bulk gas axial flow) [m]
ρ density [m^3/kg]
ρ_i mass concentration of *i-th* compound [m^3/kg]
τ shear stress [kPa]
τ_{cat} catalyst tortuosity [-]
$\dot{\tau_{gs}}$ gas-solid transferred moment flux [kPa/m]
$\vartheta_{i,j}$ stoichiometric coefficient of *i-th* compound in *j-th* reaction [-]
φ_{eq} Equilibrium aproach [-]

Subscripts
0 initial
c cooling system
cat catalyst phase
g gas phase
g_cat gas within catalyst
$hotspot, ss$ hotspot location in steady state
i *i-th* compound
in inlet
j *j-th* reaction; *j-th* compound in physical properties correlations
max maximum
$pert$ perturbation
$ramp, start$ start of ramp fluctuation
$ramp, end$ end of ramp fluctuation
rec recovery
ref reference
s solid phase
ss steady state

$ss, 2$ steady state after perturbation
sup monolithic support
$surf$ gas-solid surface
$Wall$ monolithic reactor wall

Resumen

El tren de reactores de lecho fijo en serie, con enfriamiento intermedio entre etapas, es la tecnología utilizada actualmente para la metanación de CO_2, aunque su implementación es compleja y costosa. Esta realidad ha incentivado la búsqueda de alternativas más eficientes y costo-efectivas. Entre estas los reactores de tipo monolito panal de abeja han generado gran interés y su estudio se ha incrementado de manera relevante en los últimos años. Por otro lado, si se utiliza H_2 verde en esta reacción, su flujo experimentará fluctuaciones debido a la intermitencia de las energías renovables que lo generan. Con base en lo anterior, se propone en esta tesis evaluar la respuesta dinámica de un reactor monolítico de metanación de CO_2, frente a perturbaciones en el flujo de H_2. Para lograr el objetivo, se realizó en primer lugar una revisión bibliográfica de los estudios sobre el modelado de reactores de metanación de CO_2. A continuación, se desarrolló un modelo matemático del reactor monolítico y se sugirieron estudios esenciales para su análisis. El modelo se empleó para analizar el comportamiento transitorio del reactor monolítico ante fluctuaciones en la carga de H_2 según las condiciones de operación propuestas. A través de un estudio paramétrico se evaluaron los efectos de la actividad catalítica, el tipo de perturbación y el tamaño del equipo sobre la respuesta dinámica del reactor. Posteriormente, se llevó a cabo una evaluación dinámica-experimental del reactor monolítico ante un cambio repentino en la carga de H_2. Estos resultados fueron esenciales para validar el modelo y comparar teóricamente la respuesta dinámica del monolito panal de abeja con la de un reactor de lecho fijo bajo distintas condiciones fluctuantes de carga de H_2. La revisión de la literatura indicó que el modelo de escala completa, axialsimétrico, bidimensional, heterogéneo y transiente es adecuado para modelar el reactor monolítico de panal de abeja. El modelo formulado reveló que, al usar un catalizador de alta actividad como el Ru, el reactor muestra un comportamiento dinámico similar al observado cuando se utiliza un catalizador más convencional en base a Ni. Por otra parte, aunque se obtiene una mejor respuesta dinámica ante una fluctuación gradual (rampa) del flujo de H_2, el monolito también responde adecuadamente a una perturbación repentina (escalón). Además, el tamaño del equipo influye significativamente en la tendencia no estacionaria del monolito ante cambios en el flujo de H_2. La evaluación dinámico-experimental, permitió validar el modelo matemático del reactor. La comparación con un reactor de lecho fijo, bajo las mismas condiciones de operación, tamaño de reactor y temperatura máxima, evidenció diferencias dinámicas entre el monolito y el lecho fijo en los casos de estudio seleccionados. Estas diferencias están relacionadas con las distintas cargas de catalizador y las estructuras internas de ambos equipos, evidenciándose en la mayoría de los casos que el monolito tiene mayor estabilidad dinámica ante fluctuaciones de la carga de H_2 verde. Con base en los resultados obtenidos de las evaluaciones del monolito panal de abeja bajo régimen transiente, se concluye que este tipo de reactor muestra una respuesta dinámica favorable ante la fluctuación de la carga de H_2 verde para diferentes condiciones de operación, demostrando ser incluso una alternativa tecnológica atractiva en contraste con el reactor de lecho fijo para la metanación de CO_2.

Abstract

The fixed-bed reactor train in series with intermediate cooling between stages is the current technology used for CO_2 methanation. However, its implementation is complex and costly. This reality has prompted a pursuit of more efficient and cost-effective solutions. Among these, honeycomb monolith reactors have attracted considerable attention, leading to a significant rise in their study in recent years. On the other hand, if green H_2 is used in this reaction, its flow will fluctuate due to the intermittent nature of the renewable energies that produce it. Based on the above, this thesis proposes evaluating the dynamic response of a monolithic reactor against perturbations in the H_2 flow. In order to achieve this objective, a bibliographic review on CO_2 methanation reactor modeling was carried out. Then, a mathematical model of the monolithic reactor was developed and essential studies were suggested for its analysis. The model was used to analyze the transient behavior of the monolithic reactor under fluctuations in the H_2 load according to the proposed operating conditions. A parametric study was conducted to evaluate how catalytic activity, type of perturbation, and equipment size affect the dynamic response of the reactor. Subsequently, a dynamic-experimental evaluation of the monolithic reactor was conducted to assess its performance under a sudden change in the H_2 load. These results were crucial for validating the model and theoretically comparing the dynamic response of the honeycomb monolith to that of a fixed-bed reactor under various fluctuating H_2 load conditions. The literature review indicated that the full-scale, axialsymmetric, two-dimensional, heterogeneous, transient model is suitable for modeling the monolithic honeycomb reactor. The model demonstrated that with a high-activity catalyst like Ru, the reactor shows dynamic behavior similar to that seen with a conventional Ni-based catalyst. On the other hand, the monolith not only shows a better dynamic response to gradual fluctuations (ramp) in H_2 flow, but it also responds adequately to sudden perturbations (step). Furthermore, the equipment's size greatly affects the monolith's nonstationary tendency in response to changes in H_2 load. The dynamic-experimental evaluation allowed validating the mathematical model of the reactor. The comparison between a monolith and a fixed bed reactor, under identical operating conditions, reactor size, and maximum temperature, revealed dynamic differences in the selected study cases. The differences between the reactors are due to varying catalyst loads and internal structures, with the monolith exhibiting greater dynamic stability in response to fluctuations in the green H_2 load. Based on the results obtained from the evaluations of the honeycomb monolith under transient conditions, it is concluded that this type of reactor has a favorable dynamic response to fluctuations in green H_2 load across various operating conditions. This makes it an attractive technological alternative compared to the fixed bed reactor for CO_2 methanation.

General introduction

Carbon dioxide (CO_2) is the main greenhouse gas affecting climate change [1], prompting many nations to aim for zero emissions by 2050 [2,3]. Technologies like carbon capture, utilization, and storage (CCUS) are being utilized to aid the transition from fossil fuels to clean energy [3]. One such option is the Power to Gas process, which produces methane (CH_4) through the thermocatalytic hydrogenation of CO_2 [2–9], known as CO_2 methanation or the Sabatier reaction [3,4]. Renewable energies such as wind and solar power are also employed for water electrolysis, producing the hydrogen (H_2) used in CO_2 methanation [2–9].

To carry out this reaction, Nickel (Ni) is preferred as a catalyst for the CO_2 methanation reaction due to its high conversion rate, satisfactory CH_4 selectivity, easy availability, and low cost compared to other metals [3,5,10–14]. Despite its benefits, the highly exothermic nature of the reaction can increase the reactor temperature beyond recommended limits, leading to catalyst deactivation through sintering or coking and reduced CH_4 selectivity due to side reactions [3,5,10–14]. An adiabatic fixed-bed reactor train with intermediate cooling is used to address this issue. However, this technology is complex in design and operation [2,4,6,10].

On the other hand, H_2 flow experiences fluctuations because of the intermittent nature of the renewable energies that produce it, impacting reactor operation [3,4,10,15]. To address this, storing H_2 in a backup supply can help to maintain steady operations, though this is expensive and limited due to the gas's low density [3,4,10,15]. Consequently, non-stationary operation is advised for the CO_2 methanation reactor, emphasizing the need for flexible operation and quick adaptation to changes in H_2 load [3,4,10,15].

The monolithic honeycomb reactor offers a technological alternative to the fixed-bed reactor, having a low pressure drop, reduced mass/heat transfer limitations, and excellent thermal control

[3,15–19]. These advantages lower the maximum reactor temperature and overcome thermodynamic constraints, minimizing catalyst deactivation with less cost and effort [3,15–19]. Consequently, many experimental studies have shown that this reactor type demonstrates excellent activity and stability for this industrial application [20,21].

Five modeling studies of the steady-state honeycomb monolithic reactor have also been conducted. These have demonstrated the effectiveness of this technology in achieving targeted conditions for CO_2 methanation [22–26]. Comparative analyses of various scales of mathematical models for this structured reactor have been conducted [22]. Also, these efforts lay the groundwork for scaling the equipment from a laboratory to a demonstration scale [23] and suggest designs for monolithic reactor configurations using different materials [23] or catalytic activities [24]. In addition, a study contrasts a monolithic reactor with a fixed bed under stationary conditions, highlighting previously noted advantages [26]. Moreover, it examines the reactor's performance using a chessboard arrangement of channels [26]. Finally, another study investigates how the number of cells and the catalyst's distribution within the monolith channels affect the reactor's steady-state performance under isothermal conditions [25].

Based on the above, the literature indicates that there are relatively few studies on modeling monolithic honeycomb reactors for CO_2 methanation, especially when compared to fixed-bed reactors, which are more frequently cited in this area.

On the other hand, research has been carried out on the impact of H_2 load fluctuation on the performance and dynamic response of CO_2 methanation reactors, such as fixed bed reactors, slurry bubble column, and plate heat exchanger, especially for the first one. **However, there are no studies on the honeycomb monolith's dynamic response to changes in H_2 flow, which represents a gap in the field of knowledge of the CO_2 methanation reactor.**

In addition, **comparative studies** on the impact of perturbation functionality on H_2 feed, the effect of the catalyst, and equipment dimensions on dynamic performance of honeycomb monolithic reactors **have not been conducted, highlighting another gap in this industrial application**.

Conversely, **the absence of experimental evidence on the dynamic response of the honeycomb monolith to fluctuations in H_2 load in the Sabatier reaction is remarkable**. Such tests are crucial for validating the dynamic response analysis of the reactor, which is predicted to be used with a mathematical model.

It is also important to note that a comparison between the dynamic responses of the honeycomb monolith reactor and the fixed bed reactor has not been conducted. The fixed bed reactor serves as the primary reference in catalytic and numerical evaluations of the CO2 methanation reactor, which highlights the importance of such a comparison.

Addressing these knowledge gaps in CO_2 methanation will boost the number of studies on the monolithic honeycomb reactor in this industrial application, encouraging experimental and numerical investigations of this and other technological alternatives to the fixed-bed reactor during its transient operation.

Background

Power to Gas

The August 9th, 2021, IPCC (Intergovernmental Panel on Climate Change) report emphasizes that climate change effects due to global warming may last hundreds or even thousands of years. Carbon dioxide (CO_2) is identified as the main driver of climate change, necessitating rapid and substantial reduction in its emissions. This action is crucial to limit warming to around 1.5°C or 2°C in the coming decades; otherwise, this target will become unreachable [1]. Moreover, during the climate action summit on September 23, 2019, 77 nations committed to achieve net-zero carbon emissions by 2050, focusing on promoting clean energy technologies [2,3].

Technologies for carbon capture, utilization, and storage (CCUS) are essential for addressing fossil fuel consumption as the world moves towards cleaner energy. They can be used in building materials, chemical intermediates, fuels, and polymers. Without CCUS, cutting carbon emissions is difficult, especially for high CO_2-emitting industries. However, these technologies need more development and are costly, slowing their rapid adoption [3].

Simultaneously, there's been significant progress in alternative energy sources, focusing on cleaner technologies such as wind and solar energy. However, their intermittent nature requires the development of large-scale, long-term energy storage solutions [2]. On the other hand, the alternative energy market highlights the hydrogen (H_2) economy's potential to reduce carbon emissions. However, a major challenge is the high energy demand for storing and transporting H_2 due to its low molecular density [3]. Surplus renewable hydrogen can convert CO_2 into fuels and products such as methane, methanol, ethanol, formic acid, and dimethyl carbonate through methods like Power to Fuel. CO_2 is also used in industries for manufacturing, carbonation, food preservation, fire extinguishing, and water treatment facilities [2].

Among this wide variety of alternatives, the conversion of CO_2 to methane (CH_4) is of great interest [2–4]. To this end, Power-to-Gas (PtG) technologies are evaluated in future energy systems to convert renewable electric energy into storable methane. This involves electrolysis and the thermal-catalytic hydrogenation of CO_2 into CH_4, known as CO_2 methanation or the Sabatier reaction [3,4]. Figure 1 shows that PtG process consists of three key phases: generating renewable electricity, producing renewable hydrogen through water electrolysis using excess renewable energy, and utilizing this hydrogen for CO_2 methanation. The resulting methane can be integrated into the natural gas infrastructure for storage, heating, industrial use, and Gas to Power plants. Therefore, the CO_2 methanation reactor is crucial to the PtG process [2–4,10]. However, the main challenge of this process is its high production costs compared to methane produced through conventional techniques, highlighting the need to improve efficiency and reduce process costs [2].

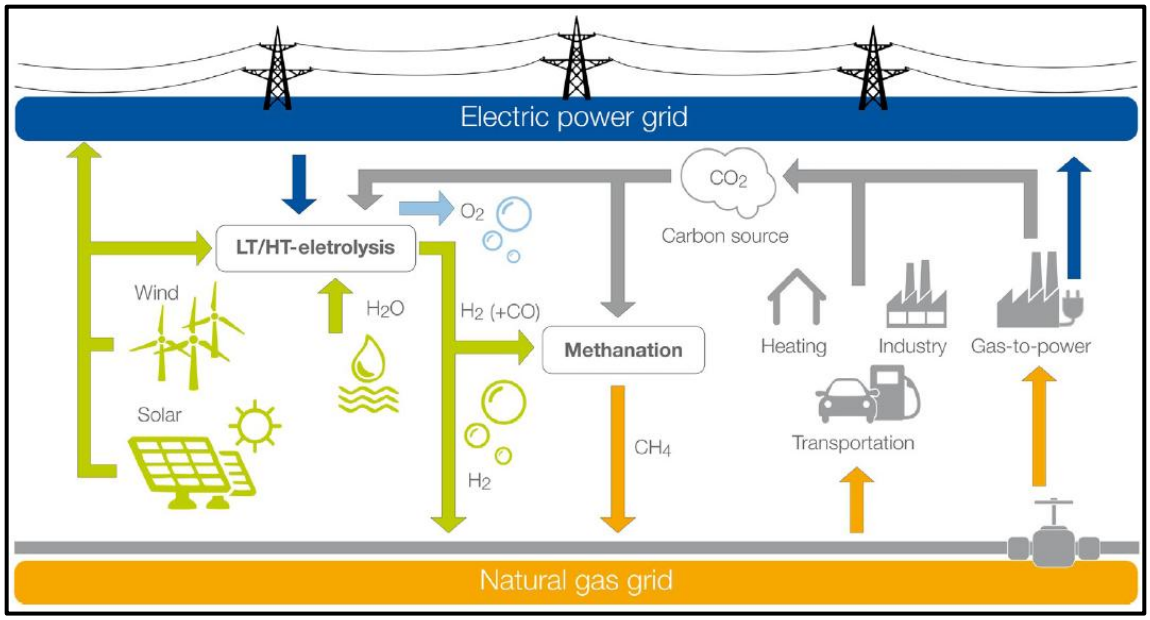

Figure 1. Connections of electric power grid, natural gas grid, carbon cycle and CO_2 as feedstock through PtG concept [2].

Thermodynamical considerations

Understanding the principal reactions in the Sabatier process is essential for hydrogenating carbon oxides (Table 1). The methanation of CO_2 (R1) and the Reverse Water Gas Shift (RWGS) reaction (R4) occur with hydrogen (H_2), producing carbon monoxide (CO) and water (H_2O). The formation of CO allows for CO methanation (R2) and CO_2-CH_4 reverse reforming (R3). Thermodynamically, reactions generating methane from carbon oxides are exothermic, while the RWGS reaction is endothermic. Depending on pressure and temperature conditions, exothermic reactions like the Boudouard reaction (R5) and carbon oxide reduction (R7 and R8) can occur, along with the endothermic CH_4 cracking reaction (R6). Additionally, CO hydrogenation under specific conditions may lead to hydrocarbons, mainly alkanes (Fischer-Tropsch) (R9) and alkenes (R10).

Table 1. Reactions related to the hydrogenation of carbon oxides [2].

Reaction		Reaction Type	$\Delta H_{298\ K}$ (kJ/mol)[a]
Methane forming			
R1	$CO_{2(g)} + 4H_{2(g)} \rightleftarrows CH_{4(g)} + 2H_2O_{(g)}$	CO_2 methanation (Sabatier reaction)	−164.7
R2	$CO_{(g)} + 3H_{2(g)} \rightleftarrows CH_{4(g)} + H_2O_{(g)}$	CO methanation	−205.9
R3	$2CO_{(g)} + 2H_{2(g)} \rightleftarrows CH_{4(g)} + CO_{2(g)}$	Inverse methane CO_2 reforming	−247.0
Shift reaction			
R4	$CO_{2(g)} + H_{2(g)} \rightleftarrows CO_{(g)} + H_2O_{(g)}$	Reverse water-gas-shift (rWGS)	41.1
Carbon forming			
R5	$2CO_{(g)} \rightleftarrows C_{graphite(s)} + CO_{2(g)}$	Boudouard reaction	−172.4
R6	$CH_{4(g)} \rightleftarrows 2\ H_{2(g)} + C_{graphite(s)}$	Methane cracking	74.6
R7	$CO_{(g)} + H_{2(g)} \rightleftarrows C_{graphite(s)} + H_2O_{(g)}$	CO reduction	−131.3
R8	$CO_{2(g)} + 2H_{2(g)} \rightleftarrows C_{graphite(s)} + 2H_2O_{(g)}$	CO_2 reduction	−90.1
Hydrocarbon forming			
R9	$nCO_{(g)} + (2n+1)H_{2(g)} \rightleftarrows C_nH_{2n+2(g)} + nH_2O_{(g)}$	Alkane formation (Fischer-Tropsch, FT)	–
R10	$nCO_{(g)} + 2nH_{2(g)} \rightleftarrows C_nH_{2n(g)} + nH_2O_{(g)}$	Alkene formation	–

Significant thermodynamic research has been conducted on the hydrogenation reactions involving carbon oxides, with Gao *et al.*, [27] 's work being notable. They extensively studied the effects of pressure, temperature, H_2/CO_2 ratio, and the presence of H_2O on the methanation of CO_2 and CO. Across the operational parameters analyzed, no formation of hydrocarbons or reverse reforming of CO_2 to CH_4 was observed. Figure 2 shows the relationship between CO_2 conversion and selectivity towards CH_4, highlighting the effects of different temperature, pressure and H_2/CO_2 ratio conditions.

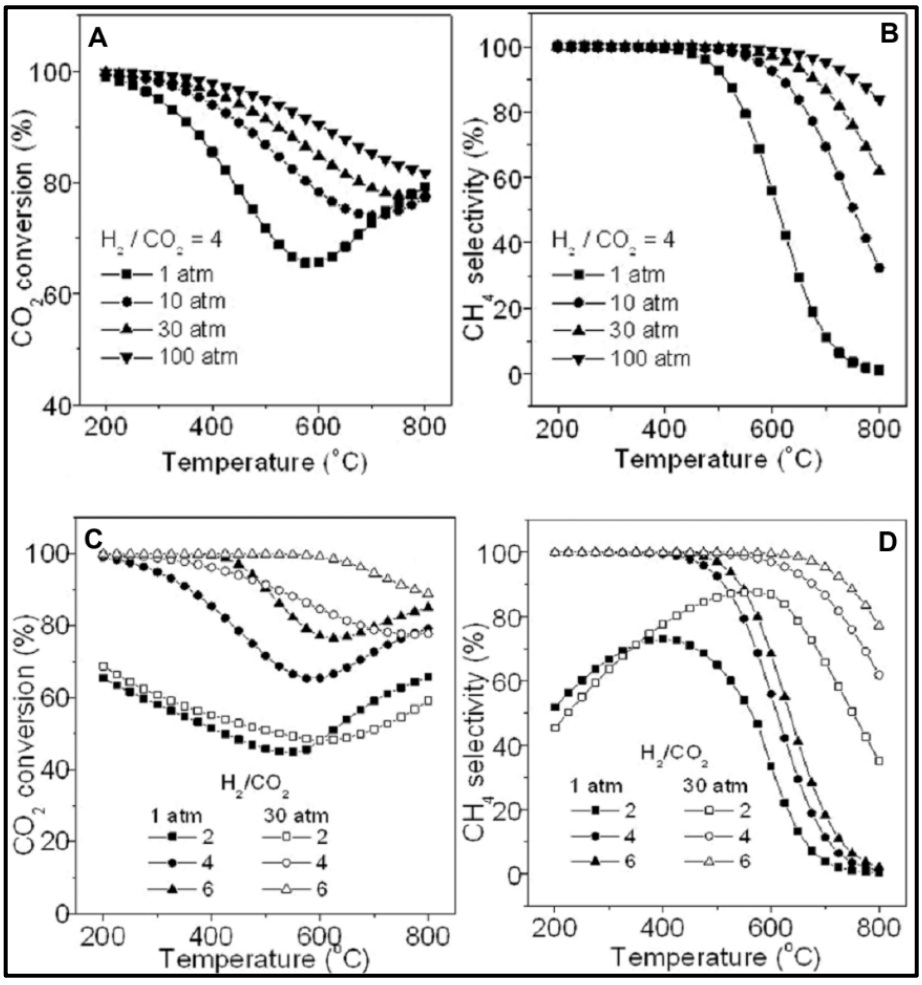

Figure 2. CO_2 conversion (A, C) and CH_4 selectivity (B, D) in chemical equilibrium conditions [27]. Effect of pressure at $H_2/CO_2 = 4$ (A, B). Effect of H_2/CO_2 at 1 and 30 atm (C, D).

Based on their results, these authors indicated that to achieve optimal CO_2 methanation performance, pressure should be increased, temperature lowered, and a H_2/CO_2 ratio greater than 4 should be used. Maximum methane selectivity occurs at temperatures between 300-350 °C, pressures up to 30 atm, and a H_2/CO_2 ratio of 4 [2,5,14]. However, CO_2 hydrogenation to methane faces significant kinetic barriers, requiring a catalyst for adequate CO_2 conversion and CH_4 selectivity within these temperature limits [14].

Catalyst

Numerous studies have examined the use of various metals as catalysts for CO_2 methanation, highlighting nickel (Ni) for its effective performance, availability, and affordability. However, Ni catalysts operate optimally at temperatures that are not ideal for CO_2 conversion, and poor temperature control can increase CO production. Additionally, these catalysts can deactivate due to sintering and the formation of Ni-carbonyl species in the presence of CO, which blocks the active sites necessary for CO_2 adsorption [3].

Noble metals like Ruthenium (Ru) and Rhodium (Rh) are highly effective and selective catalysts for producing methane (CH_4) from CO_2, outperforming nickel and other non-noble metals. Ruthenium is the most effective, followed by Rhodium, Platinum (Pt), and Palladium (Pd). Ru and Rh also show greater selectivity for methane production than Pt and Pd. Noble metals offer enhanced stability against deactivation over a wide temperature range due to lower rates of sintering and carbon accumulation. However, their use is restricted by their limited availability and high costs [3].

Additionally, selecting the appropriate catalyst support is crucial, with alumina (Al_2O_3) being the most used material for methanation catalysts due to its industrial efficiency. However, Al_2O_3 tends

to sinter when exposed to high temperatures and water, necessitating the use of promoters to enhance its performance and durability [3].

Considering the aforementioned information, extensive studies have focused on developing catalysts that perform effectively under favorable thermodynamic conditions while remaining stable. The effectiveness of these catalysts is affected by the characteristics of the support and its interaction with the promoter. For more details on the roles of promoters, active phases, and supports in the Sabatier reaction catalyst, it is suggested to refer to the research by Lee *et al.*, [3], Ashok *et al.*, [14], Jangam *et al.*, [10] and Saeidi *et al.*, [5].

Reactor configuration and technology

The main challenges in studying reactor configurations for CO_2 methanation involve thermodynamic limitations related to temperature and catalyst deactivation. The exothermic nature of the Sabatier reaction requires effective cooling systems in the reactor to avoid hot spots [5,28]. Figure 3 shows that various reactor configurations for CO_2 methanation are categorized based on the temperature of their hot spots [5].

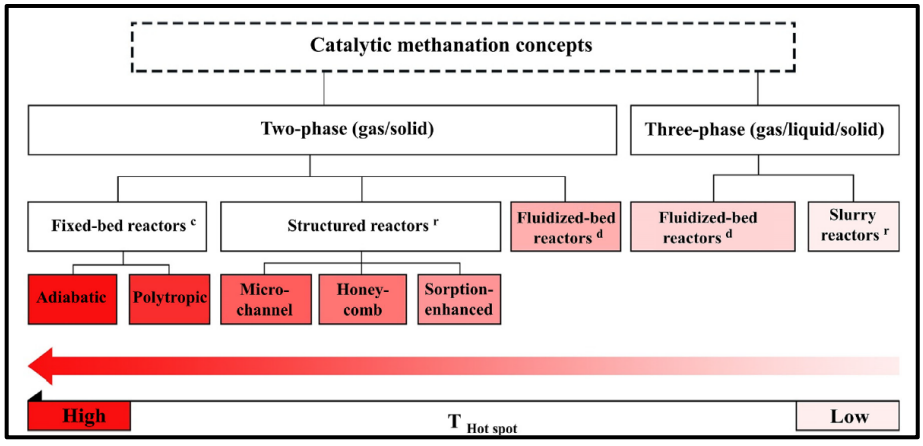

Figure 3. Summary of various reactor configurations for CO_2 methanation; d-demonstration scale, c-commercial, r-research [5].

Three-phase reactors generally are easier to control than two-phase reactors. Three-phase reactors include bubbling sludge columns and three-phase fluidized beds. Two-phase reactors are classified into fixed-bed reactors, structured reactors, and two-phase fluidized beds. Fixed-bed reactors can operate adiabatically or polytrophically, whereas structured reactors feature microchannels, honeycomb monoliths, and enhanced sorption techniques.

The adiabatic fixed bed reactor is the most advanced approach for the Sabatier reaction, featuring reactors in series with inter-stage cooling (Figure 4). Developed by companies such as Air Liquide, Haldor Topsøe, BCG, and Johnson Matthey, this approach manages heat generated during the reaction by recycling the product into the feed. However, a major challenge is the complex process for product recirculation and the need for multiple heat exchangers, resulting in high design costs and limited load adaptability [3,4,15,16,28,29].

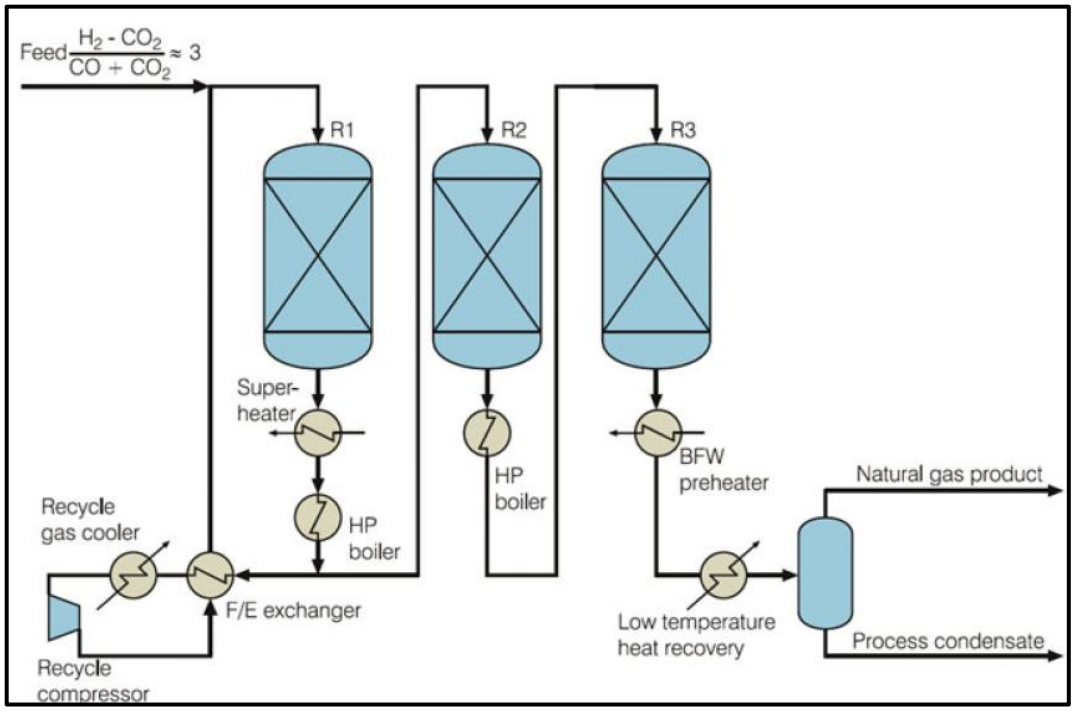

Figure 4. The TREMP process. Example of current technology for CO_2 methanation reactor [29].

A proposal suggests using a single fixed-bed reactor with a cooling medium to manage heat during CO_2 methanation. This reactor has been extensively studied through modeling and simulations. Fixed-bed reactors with cooling can be multi-tubular systems, with the catalyst in tubes and coolant in the shell (Figure 5.A), or coolant in tubes with the packed bed in the shell (Figure 5.B). These reactors offer simpler processes than adiabatic reactors, with lower temperature gradients that extend catalyst life and enhance operational flexibility. However, they face challenges in controlling temperature and pressure drops. Several companies, like Etogas, have developed technologies using these reactors, but currently, only Linde is actively commercializing this technology [3,4,15,16,28,29].

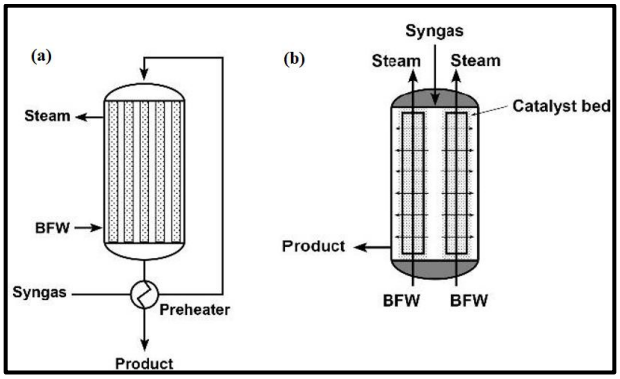

Figure 5. Fixed bed with cooling. a) Catalyst in the tubes and cooling in the shell; b) Catalyst in the shell and cooling in the tubes [5].

Dynamic operation

Conversely, in Power-to-Gas (PtG) systems, the hydrogen used in the Sabatier reaction is produced by a water electrolysis unit. Due to the fluctuating power supply from renewable energy sources, this water electrolysis unit operates non-steadily, causing variations in the feed to the CO_2 methanation reactor over time [3,4,10,15].For instance, the Figure 6 shows how the intermittent changes in wind power influence the percentage of total load in scenarios with both high and low wind energy availability [30].

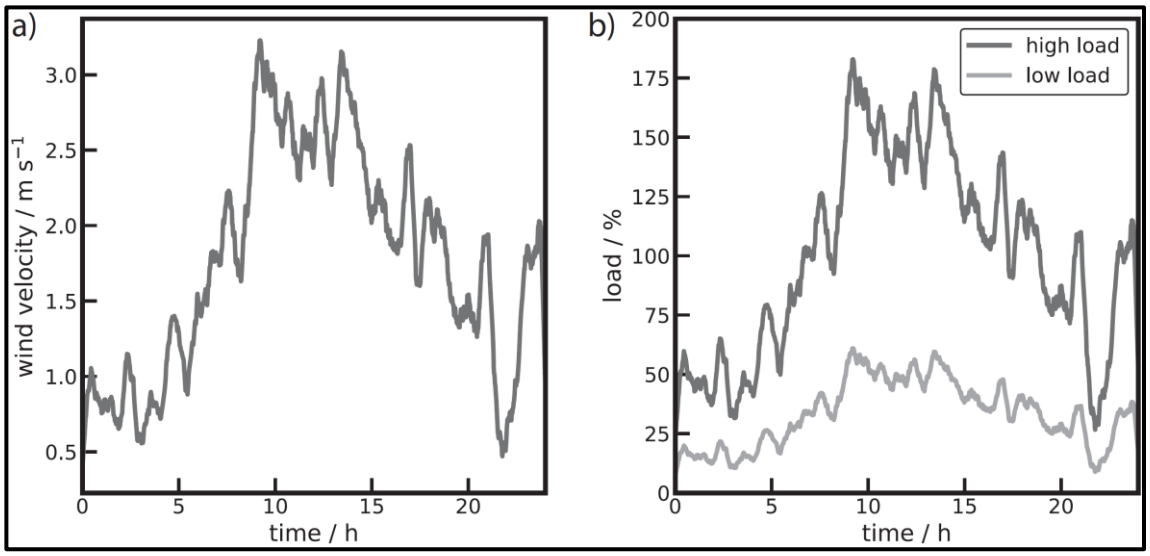

Figure 6. a) Variation of wind velocity with time throughout the day. b) Changes in gas load percentage due to wind velocity variation, in high and low energy availability scenarios [30].

A steady-state operation approach proposes requires the use of large-scale hydrogen storage to ensure a consistent supply to the methanation reactor, particularly when surplus energy is unavailable, requiring a pause in water electrolysis. However, hydrogen's low-density results in increased storage and transportation costs at Power-to-Gas (PtG) facilities, along with specific operational limitations [3,4,10,15].

Given these considerations, it is recommended that the CO_2 methanation reactor within PtG be designed for dynamic operation. The equipment should be capable of adaptable functioning to promptly respond to temporary changes in process variables [3,4,10,15]. Therefore, when analyzing a reactor's response to changes in operational variables, it's crucial to consider both the load flexibility and the time needed to return to a new steady-state. These factors are especially significant for methanation units in Power-to-Gas (PtG) applications [4].

Furthermore, catalysts need to be designed to endure feed streams that deviate from the ideal H_2 composition, inlet flow rate, and operating temperature [3,4,10,15]. Catalysts featuring a noble metal as the active phase present a promising alternative [14]. Moreover, these catalysts must be capable of tolerating intermittent reactor operation [4].

Honeycomb monolith

Figure 7 illustrates honeycomb monoliths of various materials with parallel channels employed in methanation systems. This reactor is ideal for PtG plants due to its flexible capacity and high methane production [17].

The honeycomb monolith offers several advantages over other reactor designs, including enhanced thermal and mechanical resistance for the catalyst, improved heat management, and a lower pressure drop compared to fixed beds. It also allows for more flexible loading than fluidized beds, has fewer mass transfer limitations than slurry bubble columns, is less complex than enhanced sorption reactors, and has a longer lifespan than microchannels [3,15].

Moreover, the literature indicates that this type of structured reactor is adequate in managing temporary fluctuations in process variables [14]. These benefits make it an ideal choice for the Sabatier reaction. Nonetheless, large-scale deployment is challenging. Constructed from ceramic or metal (Figure 7), these monoliths vary in mechanical strength and heat transfer properties, impacting production and design costs [16].

Catalytic evaluation of honeycomb monolith

Catalytic evaluation assesses the reactor's performance in real-world conditions, which are often limited by operational constraints and resource availability.

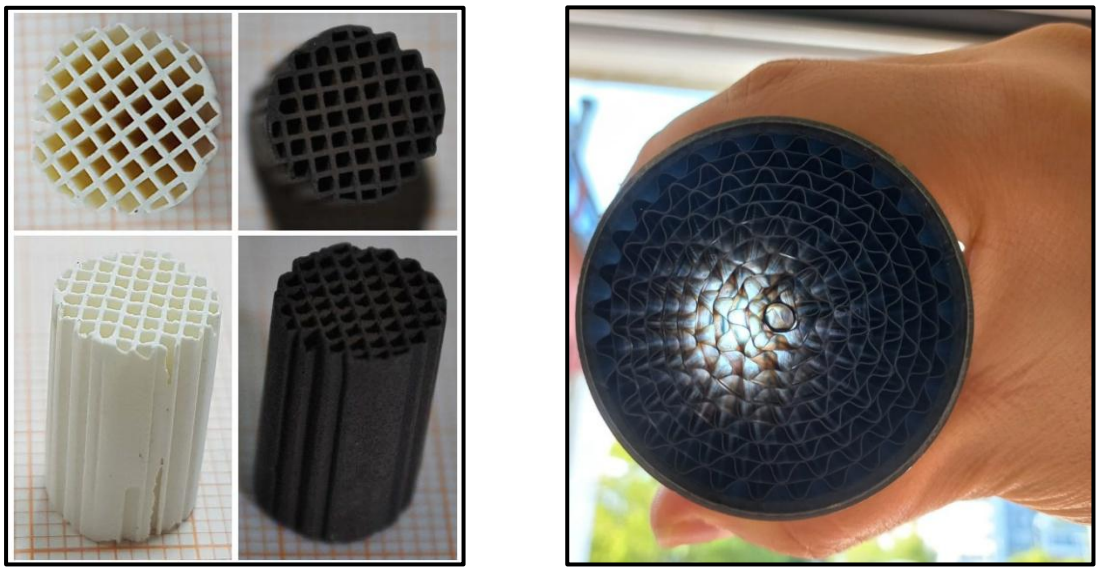

Figure 7. Honeycomb monoliths. Ceramic substrate (left, [18]) and metallic corrugated plates (right).

In this type of studies, Nickel (Ni) and ruthenium (Ru) are used as active components in catalysts, with nickel being favored for its affordability and activity. Moreover, aluminum oxide (Al_2O_3) is the most common support due to its practicality and cost, followed by cerium oxide (CeO_2). Additionally, ceramic honeycomb substrates are preferred for their lower cost. Catalytic assessments yield excellent results in CO_2 conversion, methane (CH_4) selectivity, and stability within a temperature range of 200-350 °C, making this reactor a promising option for heat management and preventing catalyst deactivation. However, outcomes depend on the monolith channels' design, influenced by manufacturing techniques [31–33]. Held *et al*., [17] and Biegger *et al*., [34] have proposed technological concepts for monolithic reactors that enable high-quality syngas production with significant loading flexibility; however, their effectiveness depends on the dynamic operation efficiency. Increasing evidence supports monolithic reactors as a great option in Power-to-Gas (PtG) processes, especially for dynamic operations.

Modeling and simulation of honeycomb monolith

In contrast, simulation utilizes mathematical models to predict the reactor's performance under various conditions. Five modeling studies of the steady-state honeycomb monolithic reactor have been conducted. With these studies, this technology has proven to be effective in achieving targeted conditions for CO_2 methanation [22–26]. Comparative analyses of various scales of the mathematical model for this structured reactor have been conducted [22,35]. Additionally, these efforts lay the groundwork for scaling the equipment from a laboratory to a demonstration scale [23] and suggest designs for monolithic reactor configurations utilizing different materials [23] or varying catalytic activities [24]. Moreover, two studies compare a monolithic reactor with a fixed bed under stationary conditions, highlighting previously noted advantages [22,26]. There is also a study that examines the reactor's performance using a chessboard arrangement of channels [26]. Finally, another work investigates how the number of cells and the catalyst's distribution within the monolith channels affect the reactor's steady-state performance under isothermal conditions [25].

Conversely, the number of modeling and simulation studies is less than the number of catalytic evaluations. Furthermore, the number of dynamic modeling studies of the monolith is even less frequent than those of the fixed-bed reactors with cooling systems. **There is a gap in analyzing the monolith's response to changes in feed flow and how different operational parameters impact reactor flexibility and performance during the dynamic operation of the Sabatier reaction**.

Full-scale model of honeycomb monolith

When all channels in the monolith experience identical conditions, a model focusing on a single channel might suffice to represent the monolith's overall performance. However, variations in flow distribution and inevitable heat loss can cause temperature differences across the reactor's radius. Therefore, the single-channel model may not accurately depict reality in some cases, making it

better to use a full-scale model that more precisely captures the complexities of mass and heat transfer processes [36].

To achieve realistic outcomes with the full-scale model, it must be continuous and heterogeneous. Key factors include the momentum balance equation, effective thermal conductivity, and a technique that integrates diffusion and reaction within the catalytic coating. These elements will improve the model's computational efficiency and reliability [36].

It is crucial to recognize that the full-scale model views the monolith as a diverse porous medium with uniform porosity, volumetrically averaging conservation equations for each phase Figure 8 .This leads to the formation of exchange terms between phases and includes a loss term for fluid movement through the monolith in the gas's momentum balance under laminar flow conditions [36].

On the other hand, Hayes *et al*., [36] note that in the full-scale model applied to the monolith, the radial mass and heat dispersion of the gas is minimal compared to other physical factors. This enables a one-dimensional resolution of mass and energy balances for the fluid through volumetric averaging, which can lead to differences when compared to a single-channel model. Additionally, Zergani *et al*., [37] note that these terms can be ignored if the ratio between the length and hydraulic diameter of the channels is sufficiently high.

However, energy transfer within the monolith requires accounting for both radial and axial conduction in its solid matrix. Although mass and energy balances in the gas are one-dimensional, the fluid's composition and temperature show radial variations, influenced by the solid's temperature and the compositions on the catalyst's Surface [36,37].

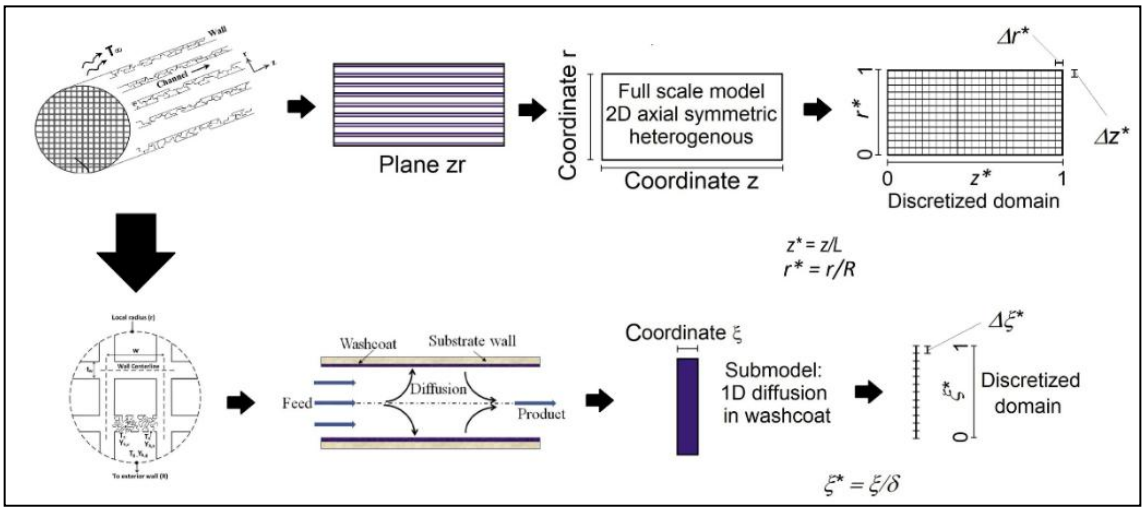

Figure 8. Full-scale model representation for a honeycomb monolith.

Additionally, Hayes *et al*., [36] recommend addressing momentum conservation equations for the entire monolith model in a two-dimensional axially symmetric scenario, due to the gas flow behavior along channels within the solid framework.

Alternatively, it is suggested to solve the conservation equations of the full-scale model in conjunction with a one-dimensional sub-model for the catalytic washcoating (Figure 8). This approach is important because resistance to mass transfer within the particles can affect the monolith's performance [36]. Additionally, since the coating is smaller than the particles in a fixed bed, temperature gradients are typically absent, and therefore, the energy balance within the catalyst is usually not considered in this type of reactor [3,15–20,22,36–42].

Hypothesis and objectives

Based on the information provided, the corresponding hypotheses, general objective, and specific objectives of this work are established.

Hypothesis

The honeycomb monolith is an attractive technological alternative for operating the CO_2 methanation reactor under transient conditions, as it responds well to sudden fluctuations in H_2 load and to different levels of catalytic activity. It adapts well to variations in H_2 flow and exhibits favorable dynamic behavior at different reactor sizes. In addition, it offers better dynamic stability compared to a fixed bed reactor, showing shorter recovery time to the new steady state and lower transient variation of the maximum temperature.

General objective

To evaluate the transient response of a honeycomb monolith reactor for CO_2 methanation under fluctuating green H_2 loads, focusing on its dynamic stability and response rate in comparison to traditional fixed-bed systems.

Specific objectives

- To formulate the mathematical model of the monolithic reactor for the Sabatier reaction, considering the analysis of the state of the art of CO_2 methanation reactor modeling.
- To perform both a theoretical and an experimental validation of the mathematical model and to study the dynamic behavior of the monolithic reactor to H_2 fluctuations under variable operating conditions.
- To determine the effect of catalytic activity, H_2 flow disturbance functionality, and reactor size on the dynamic response of the monolithic reactor.
- To compare the response to H_2 load fluctuation of the monolithic reactor with that of the fixed bed reactor, at equivalent operating conditions and dimensions.

Thesis outline

This thesis evaluates the dynamic response of a honeycomb monolith, utilized as a CO_2 methanation reactor, under varying H_2 load conditions. The outcomes are documented as articles that have either been published or submitted to scientific journals. This research analyzed the transient behavior of a monolithic reactor when faced with sudden changes in H_2 flow, examining the effect of various operational variables. The behavior of the structured reactor was compared to that of a fixed-bed reactor.

Chapter 1 review the advancements in CO_2 methanation reactor modeling over the past decade. It covered topics like validation techniques, phases, dimensions, time resolution, H_2 loading fluctuations, effectiveness factor calculation methods, catalysts, and kinetic expressions. The chapter also review the initial and boundary conditions of the models. This publication offers an overview of the various modeling approaches for CO_2 methanation reactors and provides recommendations for future research.

Chapter 2 formulates and validates a mathematical model of the monolithic honeycomb reactor, building on **Chapter 1**'s analysis. The model examines the reactor's dynamic response to sudden changes in H_2 load under specific operating conditions. It evaluates how this response varies with catalytic activity levels, H_2 flow perturbation functionality, and equipment size, offering insights into the reactor's flexibility against fluctuating H_2 loading conditions.

In **Chapter 3**, an experimental test of the monolithic honeycomb reactor was conducted to validate the mathematical model developed earlier. The model was tailored to fit the experimental monolith's conditions and characteristics, assessing both its steady state and transient outcomes. These outcomes were compared with previous data and were used to establish the model's boundary conditions. Once validated, the model facilitated comparisons between the dynamic trends of the monolithic reactor and a fixed bed under identical conditions of H_2 load fluctuations and dimensions. This comparison offered insights into the monolith's response to H_2 load fluctuations, enabling an evaluation of its potential advantages over the fixed bed for dynamic CO_2 methanation technology.

Chapter 1.

CO_2 Methanation Reactors Modeling. Reviewing the last decade.

The information provided in this chapter is redrafted after submitting in*: CO_2 Methanation Reactors Modeling. Reviewing the last decade. Pérez-Vilela, D.E & Garcia, X. (2025). Chemical Engineering Journal. Manuscript Number CEJ-D-25-18764.*

ABSTRACT

This review provides useful insights into modeling CO_2 methanation reactors. There has been a significant rise in modeling studies for different reactor types in the last decade, reflecting a worldwide effort to move away from the existing technology. Furthermore, this review highlights the contributions made by these works and the techniques employed for their validation. However, there is a notable lack of studies concerning reactor dynamic response to changes in the green H_2 load and other operational variables. In addition, due to its low cost, Ni is the catalyst most frequently utilized in these works. Meanwhile, Ru serves as a benchmark for designing and evaluating reactors that use Ni. Finally, this review emphasizes the essential elements involved in choosing the reaction rate expression, dimension, phase, method for calculating the effectiveness factor, boundary conditions, and assumptions for reactor modeling. These aspects ensure that the reactor model precisely represents the real reactor's performance.

Keywords: CO_2 methanation; Reactors modeling; Historical evolution; Methodologies; Comparative studies; Contributions.

1.1.Introduction

Carbon dioxide (CO_2), the main greenhouse gas contributing to climate change, can be converted into a helpful resource. One effective method for reducing CO_2 emissions is transforming CO_2 into methane (CH_4) [2–7]. This approach becomes even more relevant with the development of Power to Gas (PtG) technologies in future energy frameworks. These technologies include the electrolysis of water (H_2O) to generate hydrogen (H_2), which is then utilized in the thermal-catalytic hydrogenation of CO_2 to produce CH_4, known as CO_2 methanation or the Sabatier reaction [2–9].

$$CO_{2(g)} + 4H_{2(g)} \leftrightarrow CH_{4(g)} + 2H_2O_{(g)};\ \Delta H^{\circ}_{rxn} = -165\frac{kJ}{mol}$$

Nickel (Ni) is commonly used as the active component in catalysts for this reaction due to its satisfactory CO_2 conversion and CH_4 selectivity under recommended conditions. Nickel is also more accessible and less expensive compared to other metals used for this purpose [3,5,10–14]. Nonetheless, since the reaction is exothermic, the reactor's temperature might exceed the desired range. This could trigger secondary reactions that reduce methane production and exceed sintering and coking temperatures, accelerating catalyst deactivation [3,5,10–14]. Ruthenium (Ru) is a promising alternative to Ni for the catalyst's active phase due to its superior dynamic stability [14] and enhanced resistance to thermal sintering [3,5,10–14] compared to nickel and other non-noble metals. However, Ru is significantly more expensive than Ni [3,5,10–14].

To overcome these limitations, a method using multiple adiabatic fixed bed reactors in series, with cooling between each unit, has been adopted as the main technology. This approach, however, is complex in both design and operation, requiring higher capital investment [2,4,6,10]. As a result, various alternatives have been developed to potentially replace this technology. Among these are honeycomb monolith reactors, microchannels, enhanced sorption, membranes, fluidized beds, slurry bubble columns, and plate heat exchangers [3,15–19].

In addition, when using green hydrogen, it's important to consider the temporal variations in hydrogen load due to the intermittent nature of renewable energy sources like solar and wind. These variations can affect the effectiveness of the Sabatier reaction within the Power to Gas (PtG) process [3,4,14,15]. A steady-state operation proposes storing enough hydrogen to ensure a constant supply. However, this results in higher costs and operational limitations because of hydrogen's low density [3,4,14,15]. Therefore, Transient operation of the CO_2 methanation reactor is still recommended to ensure flexible operation and rapid adaptation to inevitable fluctuations in hydrogen load [3,4,14,15].

According to the previously mentioned context, there is extensive research available on the industrial application of CO_2 methanation. This includes detailed information on catalysts, kinetic expressions, and reaction mechanisms. Numerous studies also provide updates on technologies using this reaction to produce synthetic natural gas, like Power to Gas, Power to X, or Power to Methane. These publications play a critical role in advancing CO_2 methanation reactor modeling, indicating that this field is well-covered in scientific literature.

New updates for review publications in various areas of expertise have been released for this application. However, the most recent comprehensive review on CO_2 methanation reactor modeling was authored by Ronsch *et al*. [19] in 2016. This review, titled “Review on methanation—From fundamentals to current projects,” details methodologies, suggestions, and new challenges.

For these reasons, this review article aims to compile and highlight significant information from the past decade on CO_2 methanation reactor modeling. It focuses on research volume and updates on validation methodologies, reactor dimensions, time conditions, phases, effectiveness factor calculation, catalysts, kinetics expressions, boundary conditions, and assumptions for reactor modeling. The article explicitly addresses CO_2 thermocatalytic methanation, excluding methane

or natural gas production via biological means, electrolysis, photocatalysis, and plasma processes. It concentrates solely on reactors, not covering process engineering aspects like plant simulation or control systems.

1.2.Studies number: 2014-2024

Between 2014 and 2024, 115 studies focused on modeling CO_2 thermocatalytic methanation reactors. Of these, 64 studies examined fixed bed (FXB) reactors, while 51 explored newer technologies. Figure 1.1 illustrates that since 2014, FXB reactors have been the most commonly modeled, with the highest number of related studies published in 2020.

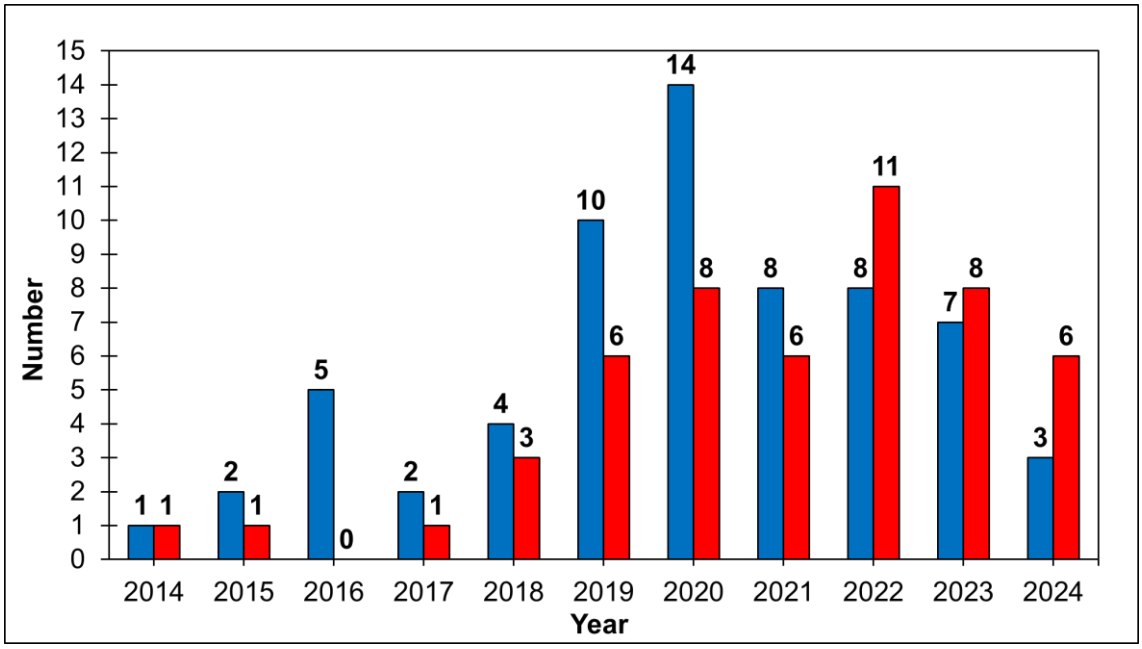

Figure 1.1. Historical evolution of reactor modeling publications number in thermocatalytic CO_2 methanation. Fixed bed, Technological alternatives.

Conversely, the number of modeling studies for technological alternatives increased over time, reaching a peak in 2022. From 2022 to 2024, annual publications on fixed bed technologies

declined in comparison to other technological alternatives. This pattern reflects what was highlighted in the introduction of this study, a trend towards developing more cost-effective and efficient technologies to replace the current CO_2 methanation method, particularly the adiabatic fixed bed reactor train with intermediate cooling.

1.2.1.Technological alternatives

The honeycomb monolith (HM), microchannel (MC), enhanced sorption (ES), membrane (M), fluidized bed (FB), slurry bubble column (SBC), and plate heat exchanger (PHE) are prominent technological alternatives to the fixed bed, mainly due to their growing industrial significance in areas beyond CO_2 methanation.

Table 1.1 indicates that the reactor with the most publications is MC, as cited in the sources [43–50]. It is followed by M with references [51–57], then HM as per [20,22–26], ES in [58–63], PHE with citations [64–67], FB found in [68–71], and finally, SBC as detailed in [72,73].

Additionally, options such as foams, fibers, milichannels, flat surfaces, plates, parallel channels, U-channels, spirals, catalytic tubes, and taps are acknowledged as alternatives to the fixed bed. Publications on these options are classified under other alternatives (OA). It's important to note that the number of OA articles represents the total count of papers from each reactor in this category. Notably, foams (from 2019, [74,75]), parallel channels (years 2019 and 2022; [76,77]), U-channel (also from 2019 and 2022; [77,78]), fibers (2020 and 2022; [79,80]), catalytic tube (years 2020 and 2021; [81,82]), and plate (2022 and 2023; [83,84]) each have 2 publications. In contrast, the millichannel (2019, [85]), flat surface (2020, [86]), and tap (2023, [87]) each have a single published paper.

Table 1.1. Number of publications of technological alternatives to fixed bed reactors.

Year	HM	MC	ES	M	FB	SBC	PHE	OA
2014	-	-	-	1	-	-	-	-
2015	1	-	-	-	-	-	-	-
2017	-	1	-	-	-	-	-	-
2018	1	-	-	-	-	-	2	-
2019	-	-	1	1	-	-	-	4
2020	-	-	1	1	2	1	-	3
2021	-	1	1	1	2	-	-	1
2022	1	3	-	2	-	-	1	4
2023	-	2	1	1	-	1	1	2
2024	3	1	2	-	-	-	-	-
Total Number of Studies	**6**	**8**	**6**	**7**	**4**	**2**	**4**	**14**

HM: Honeycomb monolith; MC: Microchannel; ES: Enhanced Sorption; M: Membrane; FB: Fluidized bed; SBC: Slurry bubble column (SBC); PHE: Plate heat exchanger; OA: Other alternatives.

The PHE and foam reactors saw the highest number of publications in 2018 and 2019, respectively. In 2020 and 2021, the FB reactor garnered the most attention in studies. Between 2022 and 2023, the MC reactor led in the number of papers. Finally, in 2024, the honeycomb monolith reactor had the highest count of modeling publications.

This section highlights the increasing diversity of research on technological alternatives to the FXB over time. MC, M, and ES reactors have consistently been the focus of modeling studies from 2014 to 2024. There is also a significant increase in studies concentrating on HM and ES reactors.

1.3.Countries where these studies have been carried out

According to Figure 1.2.A, Europe dominates the field of chemical reactor modeling studies for CO_2 methanation, conducting 64 out of 115 studies from 2014 to 2024. Figure 1.2.B further illustrates that Europe leads in various reactor studies compared to other regions: FXB (43 out of 64), HM (4 out of 6), ES (4 out of 6), M (4 out of 7), SBC (2 out of 2), PHE (3 out of 4), and OA (9 out of 14).

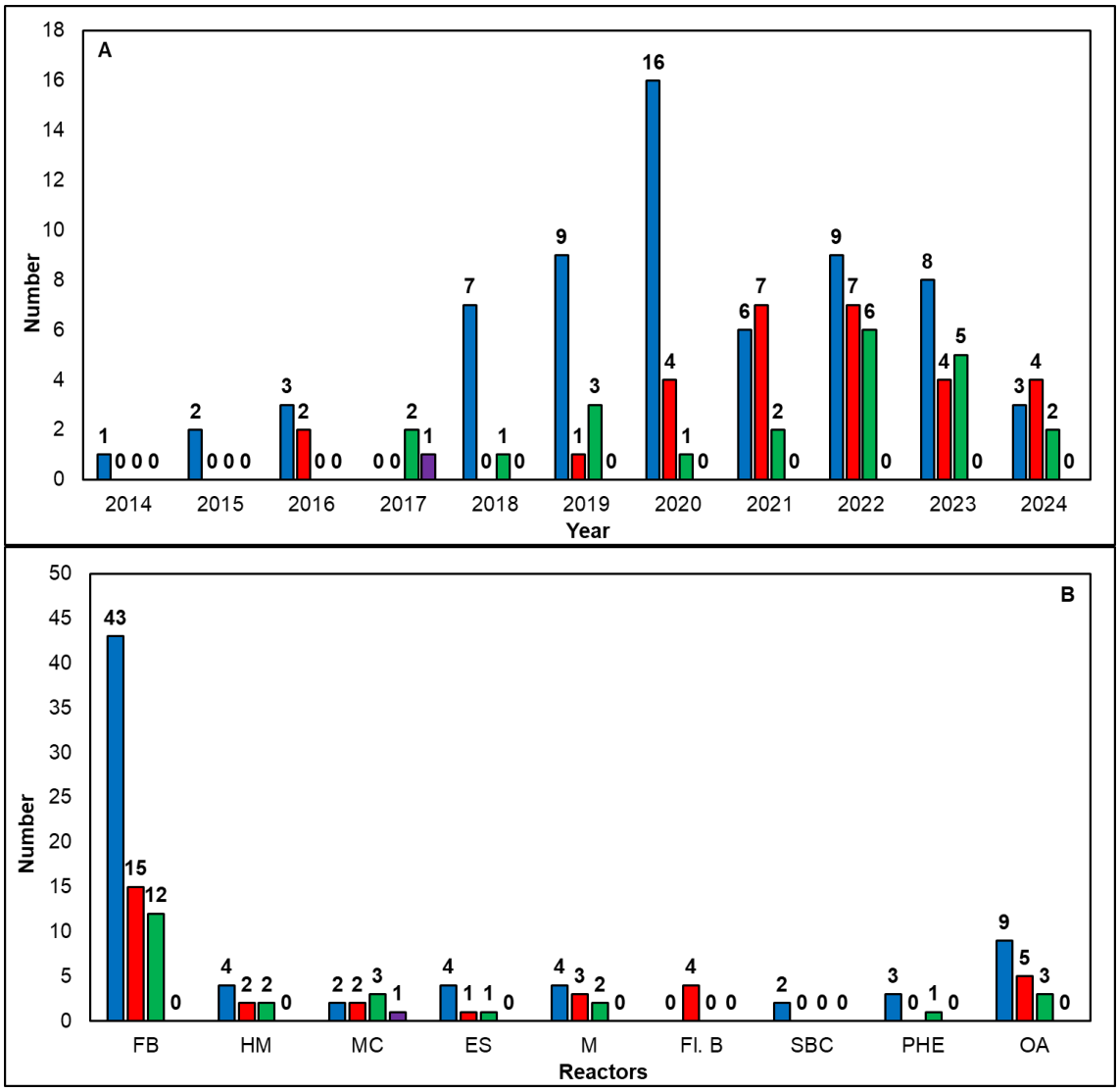

Figure 1.2. Number of publications in every continent per year (A) and reactor type (B).

Germany leads in the number of modeling publications both in Europe and worldwide, contributing 33 out of 115. Notably, Germany has also conducted modeling studies on many reactors featured in this research. This includes FXB models cited in references [22,30,53,73–75,88–105], HM in [22,23], MC in [45,46], M in [53], SBC in [72,73], PHE in [64], foams in [74,75], fibers in [79,80], flat surface in [86], and tap in [87]. Germany is the global leader in FXB publications, contributing

24 out of 64 publications. It is also the only contributor to SBC, foam, flat surface, and tap models to date.

The remaining publications from Europe include contributions from Spain [25,59,62,85,106–110], Italy [60,61,65,83,111–113], France [114–119], Switzerland [67,120–122], Portugal [51,56], the UK [54], Greece [54], Cyprus [54], Norway [24], Sweden [84], and Finland [65]. Spain [59,62] and Italy [60,61] lead in the number of ES reactor modeling studies worldwide. Spain is unique in having conducted the only study on millichannel reactors to date [85], and Portugal [51,56] stands out with a higher volume of publications on M reactor modeling compared to the other countries discussed in this paper. Figure 1.2.A illustrates that from 2014 to 2024, Asia ranks as the second continent in terms of the number of reactor modeling articles focused on the Sabatier reaction, accounting for 30 out of 115 articles. Figure 1.2.B indicates that Asia is unique in featuring studies on FB reactor models [68–71], emphasizing that CO_2 methanation is the primary reaction in all instances. China leads in Asia and ranks second globally, with 12 articles, predominantly focusing on FXB [26,123–129], HM [24,26], and, M [55], and FB [69] types of reactors.

Countries across the Asian continent, including Japan [26,58,81,82,124,126,127,129–131], South Korea [68,70,71,132,133], India [43,76–78], Iran [48,57], Kuwait [54], Singapore [69], and Taiwan [134], have also contributed to the research on CO_2 methanation reactor modeling. To date, on a global scale, Japan stands out as the only nation with studies on catalytic tube reactors [81,82], while South Korea boasts the highest number of publications on FB reactors [68,70,71]. As for India, it is notable for having the sole investigations into the parallel channel [76,77], U-channel [77,78], and spiral [78] reactors to date.

In the Americas, 22 out of 115 studies on reactor modeling for the Sabatier reaction have been published between 2014 and 2024 (see Figure 1.2.A). Across this continent, the most frequently

researched reactor on a global scale is the MC reactor [44,47,50] (refer to Figure 1.2.B). Canada stands out in the Americas with 10 out of 115 articles, making it the third leading nation, alongside Japan, in publications on CO_2 methanation reactor modeling. Research in Canada has focused on FXB reactors [52,135–139], MC [47,50], ES [63], M [52], and plate reactors [83].

Across the American continent, countries like Chile [20,44,47,50,140,141], the USA [54,89], Argentina [79,80], Ecuador [107,108], Mexico [25], and Colombia [66] have conducted research on modeling reactors for the Sabatier reaction. Among these nations, Chile is notable for having the highest number of publications (6 out of 115). This country has produced studies on FXB [140,141], HM [20], and MC [44,47,50] reactors, offering a wider range of research topics compared to other American countries, excluding Canada.

Africa, as the final continent, is represented by South Africa. In this instance, South Africa is notable for a modeling study conducted in 2017, which was published by Engelbrecht *et al.*, [49]. This research focuses on the MC reactor and has served as a foundation for subsequent studies published in the following years [43–48,50] concerning this reactor.

Hence, between 2014 and 2024, Asia and the Americas have ramped up their modeling studies on different CO_2 methanation reactor types, indicating their intention to develop technologies for synthetic natural gas production like Europe. These technologies strive to be more efficient and cost-effective than the traditional adiabatic fixed bed reactor train with intermediate cooling.

1.4.Models validation

Table 1.2 highlights the distribution of publications on experimentally validated CO_2 methanation reactor models. It shows that FXB, MC, M, and OA research is mainly validated theoretically, unlike ES and SBC reactors. Meanwhile, HM, FB, and PHE have an equal balance of theoretical and

experimental validation. Ideally, modeling research with experimental validation should be more common because it is essential for defining the right conditions to ensure the model accurately represents real reactor behavior, enhancing the scientific value and contribution of the findings.

Table 1.2. Modeling studies number for CO_2 methanation reactors with experimental validation.

Reactor	Experimental Validation with Own Data	Studies Number
FXB	[51,73,75,89,92,95,98,99,103,105,107,110–112,119,120,123,124,127,130,133,137]	22/64
HM	[23–25]	3/6
MC	[49,50]	2/8
ES	[58–60,62]	4/6
M	[51,55,57]	3/7
FB	[68,69]	2/4
SBC	[72,73]	2/2
PHE	[64,67]	2/4
OA	[75,79–83,85,87]	8/14

1.4.1.Theoretical validation. Methodologies.

Securing full funding for experimental validation of a reactor's mathematical model is not always feasible, making theoretical validation essential. This approach confirms the accuracy of the outcomes derived from the reactor modeling. To achieve this, the following theoretical validation techniques have been employed:

- Evaluation against experimental data provided by various researchers [43,45,46,48,54,56,61,71,84,86,88,99,113,124–126,128,129,131,134,140,141].
- Comparison with simulation outcomes from different researchers [54,71,101,115,138,139].
- Obtain results in the kinetic regime condition as referenced by others [20,53,63,74,76–78,88,94,113,115,116,128].
- Achieve outcomes under the state of chemical equilibrium [20,115,116,136].
- Acquire outcomes for a first order reaction under conditions of isothermal plug flow [22].

- Investigating the idle state where there is a halt in gas flow and no external heat input or removal [116].
- Contrasting non-reactive fluid dynamic behavior with experimental findings [70].
- Evaluating thermal resistance models for cases involving non-reactive stationary fluid [22].
- Examining the calculated heat transfer coefficient for the reactor shell [140].

The most frequently employed technique for validating reactor simulations is in comparison with experimental data from other researchers. This approach is essential for simulating reactors with the same dimensions and conditions as those in the reference study. While the model isn't tailored to the specific reactor data of interest, it demonstrates the model's ability to represent actual reactor behavior under various conditions. Comparing with other authors' simulations requires adjusting the model to match the reference study's conditions and information. This validation is valuable as it serves as an alternative when experimental data isn't available and confirms the model's effectiveness by achieving similar results to cited modeling work.

The kinetic regime is a second essential approach. This requires that the model matches the same space velocity/catalyst loading and operating conditions as the experimental reactor from which the kinetic expression was derived. Key reactor parameters, such as catalyst size, velocity, thermal conductivity, length, and diameter, must be adjusted to eliminate mass and heat transfer resistances, ensuring isothermal conditions and constant pressure. Consequently, the model must replicate trends observed during catalytic evaluation for accuracy. Additionally, studies have validated the model by achieving chemical equilibrium, requiring similar parameter adjustments except for a sufficiently low flux value. Results are compared with literature data, particularly for CO_2 methanation, considering temperature, pressure, H_2/CO_2 ratio, and mole fractions. This dual-condition analysis is crucial for verifying the model's functionality by comparing results with experimental data.

The rest of theoretical validation methods are useful for verifying the reactor model's effectiveness. This involves checking if results match analytical solutions from literature, like a first-order reaction in an isothermal plug flow reactor or align with experimental data on fluid dynamics and thermal properties in non-reactive situations. Therefore, modeling studies with theoretical validation are crucial for expanding knowledge as they help predict reactor behavior. This is beneficial for advancing future experimental and modeling efforts concerning CO_2 methanation reactors.

1.5.Dimensions

Figure 1.3 shows that the one-dimensional (1D) model is the most used in CO_2 methanation reactor modeling, featured in 55 studies from 2014 to 2024. In contrast, two-dimensional (2D) and three-dimensional (3D) models were used in 33 and 35 studies, respectively. Since 2015, the 1D model has predominantly been used for the FXB reactor, peaking in 2020 (as shown in Figure 1.3.A). After this, the 3D model became the most studied annually, except in 2022. The 2D model consistently ranked second each year, with exceptions in 2016 and 2022. Technological alternatives to the FXB reactor (depicted in Figure 1.3.B), have shown growth across different model dimensions, with the 1D model peaking in 2020 and the 2D and 3D models peaking in 2022. In 2022, the number of publications for all three model dimensions was nearly equal.

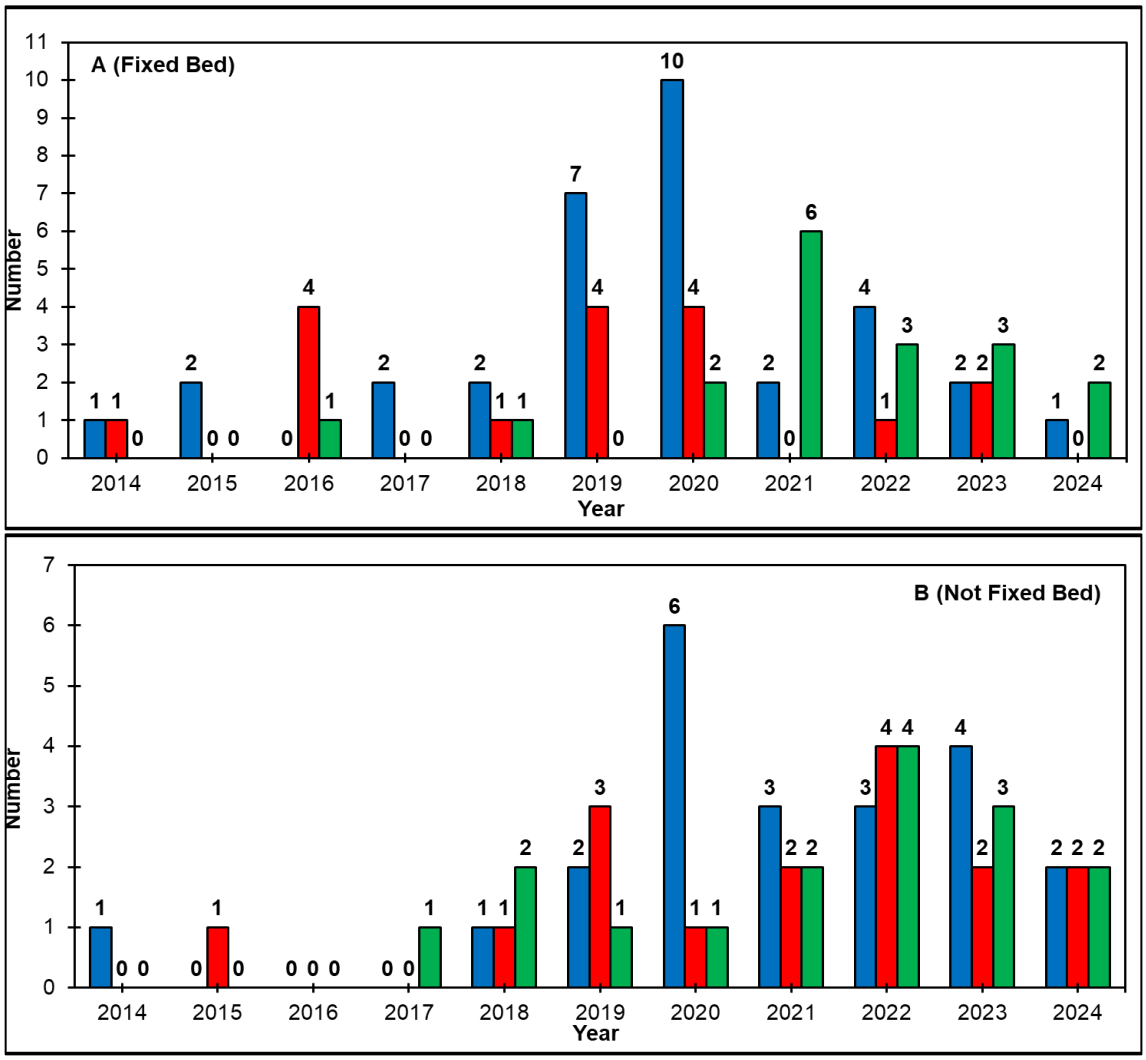

Figure 1.3. Dimensions used in reactor modeling of thermocatalytic CO_2 methanation. Historical evolution. One-dimensional (1D), Two-dimensional (2D), Three-dimensional (3D).

Table 1.3 shows the distribution of dimensions used in modeling methanation reactors. The FXB reactor has conducted 33 studies with the 1D model, 17 with the 2D model, and 18 with the 3D model. In contrast, other reactors have conducted 23 studies using the 1D model, and 16 studies each for the 2D and 3D models.

Table 1.3. Dimensions used in modeling studies for CO_2 methanation reactors.

Reactor	1D	Studies Number	2D	Studies Number	3D	Studies Number
FXB	[22,30,52,53,71,73,88–94,96,97,99,100,102,105,109–112,115,116,120–122,131,132,135–137]	33	[53,54,74,75,95,98,99,101–104,114,117–119,124,134]	17	[26,99,106–108,113,123,125–130,133,138–141]	18
HM	-	0	[20,22,23]	3	[24–26]	3
MC	[44,46]	2	[45,48]	2	[43,46,47,49,50]	5
ES	[58–60,62,63]	5	[61]	1	-	0
M	[51–53,56,57]	5	[54,55]	2	-	0
FB	[69,71]	2	[70]	1	[68]	1
SBC	[72,73]	2	-	0	-	0
PHE	[64,67]	2	-	0	[64–66]	3
OA	[79,80,84,87]	4	[74–78,81,82]	7	[83–86]	4

The ES (5), M (5), FB (2), and SBC (2) reactors have mainly been studied in a one-dimensional context. Regarding OA, seven studies focus on the 2D case, examining foam, catalytic tube, parallel channel, U-channel, and spiral reactors. For MC and PHE reactors, most research involves 3D modeling, with five and three studies, respectively. The HM reactor has an equal number of studies for both 2D and 3D models.

From the trends shown in the previous paragraphs, the text highlights that most studies have used one-dimensional (1D) models, particularly for FXB reactors, due to their simplicity and lower computational costs compared to 2D and 3D models. These models provide an initial approximation of catalytic and thermal performance and can be very accurate for reactors with excellent radial mixing, such as FB and SBC reactors. However, in cases where reactors have significant radial concentration and temperature gradients, especially due to size or operating conditions, 1D models may not suffice. In these instances, more comprehensive 2D or 3D models are necessary to ensure accurate results, particularly if experimental verification is unavailable.

1.5.1.Comparative studies for different model dimensions

Literature includes modeling studies that have compared results across various dimensional scales. Schlereth *et al*., [53] highlighted that while 1D pseudohomogeneous models offer a basic understanding of qualitative trends in the FXB reactor, 2D pseudohomogeneous models are preferred for more accurate quantitative results. These models should be validated using available experimental data specific to this reactor type. Conversely, Gruber *et al*., [64] found that in a PHE reactor, temperature profiles from 1D and 3D pseudohomogeneous models exhibit minimal differences with small catalyst sizes (128-160 μm). However, with larger catalytic particles (750 μm), a notable temperature difference of 5 K appears between the models. For CO_2 conversion, there is a consistent 5% difference in model results, regardless of catalyst size. Furthermore, the research by Fischer *et al*., [102] demonstrated that there are no significant differences in maximum

CO_2 conversion predictions between 1D and 2D models for an FXB reactor in either pseudohomogeneous or heterogeneous phases. However, differences appear in the reactor's dynamic behavior. The 1D model satisfactorily predicts the axial behavior but fails to accurately predict the time trend, as the 2D model shows a faster temperature increase under conditions of substantial thermal resistance. Similarly, Gruber *et al*., [99] performed a comparative analysis of various dimensional scales in FXB reactor modeling. They concluded that their model accurately reflects the experimental results regarding the reactor's temperature profile, with no significant differences between the predictions of 1D and 2D models, both of which are considered pseudohomogeneous. Meanwhile, Blauth *et al*., [46] conducted kinetics parameters fitting using a pseudohomogeneous model for a MC reactor on both 1D and 3D scales. To assess the results from both models, they averaged the 3D model's calculated properties over the reactor's cross-sectional area to create a one-dimensional profile. The discrepancy between the two models was found to be less than 1%, indicating that the 1D model is sufficient for determining the kinetic parameters of a MC reactor, while also reducing computational costs. In a related study, Omojola *et al*., [84] conducted a comparative analysis of a 1D and a 2D pseudohomogeneous model in a plate reactor context. Using existing literature data for model validation, they concluded that the 2D model was more suitable for their research objectives.

The examination of these comparative studies highlights the significance of evaluating the performance of the reactor's mathematical model in 1D, 2D, and 3D scales under specific operational conditions. This assessment is crucial to determine if simplifying the model's complexity is feasible, which could potentially reduce computational costs.

1.6.Dynamic studies

Figure 1.4 highlights the historical progression of research on dynamic modeling of CO_2 methanation reactors.

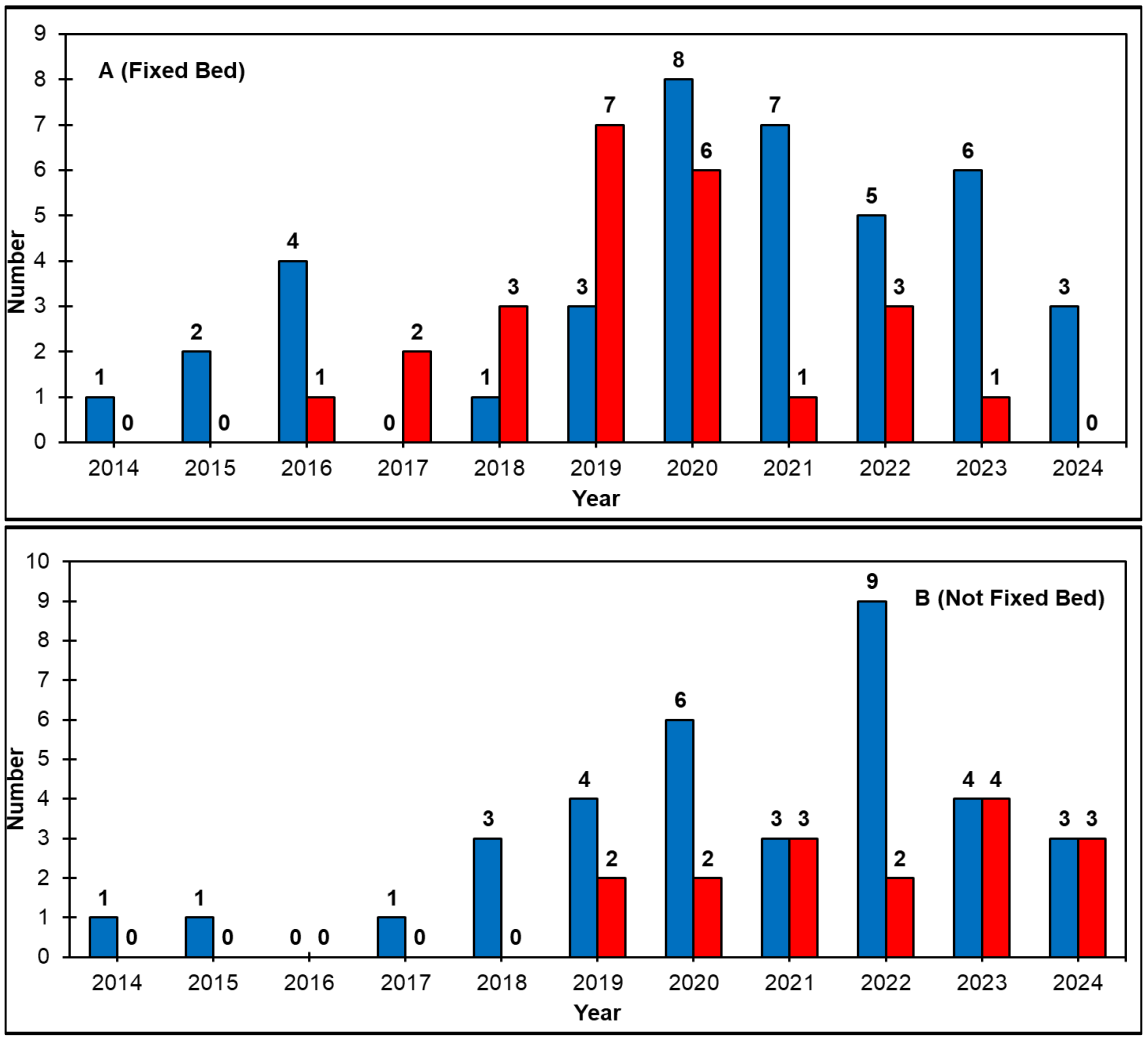

Figure 1.4. Historical evolution of dynamic reactor modeling of thermocatalytic CO_2 methanation. Steady-state (SS), Non-Steady-state (NSS).

As shown in Figure 1.4.A, there is a increase in non-steady-state investigations of FXB reactors starting in 2016, peaking by 2019 and 2022. Figure 1.4.B, shows a rise in dynamic modeling studies for other technological alternatives to FXB, beginning in 2020 and continuing to grow and develop to the present. Table 1.4 reveals that most reactor modeling has focused on steady-state conditions. Among dynamic studies, FXB reactors have more publications (24 out of 64) than other technologies (16 out of 51).

The ES reactor is an exception, operating under dynamic conditions due to changes in active catalyst sites influenced by the adsorbent used [58–63]. In the field of dynamic studies, research has concentrated on reactor start-up behavior [47,94,137], the effects of catalyst deactivation [45,52,57,135], and the dynamics of interfacial displacement [126]. Ngo *et al*., [68,70] specifically investigated the temporal displacement of the interphase in FB.

Table 1.4. Dynamics studies for CO_2 methanation reactors.

Reactor	Non-Steady-State	Studies Number
FXB	[30,52,73,90–94,96,97,100–102,104,105,115–118,126,135–137,141]	24/64
HM	[20]	1/6
MC	[45,47]	2/8
ES	[58–63]	6/6
M	[52,57]	2/7
FB	[69,71]	2/4
SBC	[72,73]	2/2
PHE	[67]	1/3

1.6.1.Studies of reactor response to fluctuations

Section 1.5 highlights that most contributions focus on steady-state modeling (76) rather than dynamic conditions (40) for reactors used in the Sabatier reaction. These steady-state studies are crucial for understanding continuous processes. However, as noted in section 1.1, the intermittent nature of renewable energy sources, which produce green H_2 for industrial purposes, leads to variations in the feed flow.

Table 1.5 outlines studies on the dynamic behavior of CO_2 methanation reactors as operational parameters change over time. Researchers have investigated the effects of sudden changes in several factors: i) green H_2 load (5 studies), ii) total feed flow (16 studies), iii) inlet temperature (3

studies), iv) cooling temperature (5 studies), and v) outlet pressure (1 study) on reactor performance.

The FXB (17) reactor has been the focus of research on how fluctuations affect the dynamic response and performance of the Sabatier reaction. In comparison, there have been two dynamic studies on the SBC reactor, but only one study each for the PHE and HM reactors. The step change in fluctuation functionality has been the most extensively researched, with studies showing occurrences of 9 for FXB, and 1 for SBC, PHE, and HM.

This scenario poses significant challenges in achieving a new steady-state [20,67,73,91,92,100,102,105,118,118,136,141]. In contrast, ramp functionality was observed 5 times for FXB, and once for both SBC and HM. There's also interest in analyzing the dynamic response and recovery time of the FXB reactor to fluctuations involving multiple steps, noted 4 times, or other functionalities, noted once [116]. Additionally, research has explored scenarios where the FXB feed flow fluctuation shows an oscillatory pattern, whether regular (1, [93]) or irregular (1, [30]).

Comparative analyses on the impact of fluctuation functionality on reactors' dynamic behavior have been documented. Initially, Try *et al*., [118] found that in an FXB reactor, a gradual change (ramp perturbation) in cooling temperature causes a less pronounced temperature increase than a sudden change (step fluctuation). Conversely, Theurich *et al*., [92] noted that in an adiabatic FXB reactor, a sudden feed flow change (step perturbation) leads to more significant dynamic variation than a slow, prolonged fluctuation (ramp type). Lastly, Perez-Vilela & Garcia [20] showed that in an HM reactor, a new stable condition is achieved more quickly with a gradual feed flow fluctuation (ramp) than with a sudden change (step).

Table 1.5. Analysis of the CO_2 methanation reactor's dynamic response to perturbations in operational variables.

Operational Variable Perturbated	Reactor	Perturbation Functionality					
		Step	Ramp	Multiples Step	Sinusoidal	Irregular Oscillations	Others
Inlet Flow	FXB	[73,92,100,102,105,118,141]	[92,96,116,117]	[90,97,100]	-	[30]	-
	SBC	[73]	[72]	-	-	-	-
	PHE	[67]	-	-	-	-	-
	HM	[20]	[20]	-	-	-	-
H_2 Load	FXB	[105,141]	[116]	-	[93]	[30]	-
Inlet Temperature	FXB	[91,118,136]	-	-	-	-	-
Coolant Temperature	FXB	[91,100,118]	[118]	[100,104]	-	-	[116]
Outlet Pressure	FXB	[118]	-	-	-	-	-

Despite investigations into the effects of sudden changes in feed flow on the performance of SBC, PHE, and HM reactors, and comparative analyses on how load perturbation affects the dynamic response of the HM reactor [20], there remains a notable lack in dynamic studies exploring how different feed flow fluctuations and other operational parameters impact CO_2 methanation performance across all technological alternatives to FXB.

1.7.Phase

Figure 1.5 shows the trends from 2014 to 2024 in using pseudohomogeneous (PH) and heterogeneous (HET) phases to model CO_2 methanation reactors. In studies of the FXB reactor, the PH phase has been the focus of most research (35 studies) compared to the HET phase (33 studies). For different reactor types, HET phase research (26 studies) slightly exceeds PH phase research by one study. Historically, PH phase studies for the FXB reactor were more common in 2016, 2017, and 2021, whereas HET phase modeling was more prevalent in 2019, 2020, 2022, and 2023 (Figure 1.5.A).

In contrast, the growth of PH studies in alternative technologies to the FXB reactor peaked in 2022 (Figure 1.5.B). Simultaneously, studies using the HET phase for modeling reactors other than the FXB have been increasing since 2019, reaching their highest point in 2023, indicating annual growth in the use of this phase.

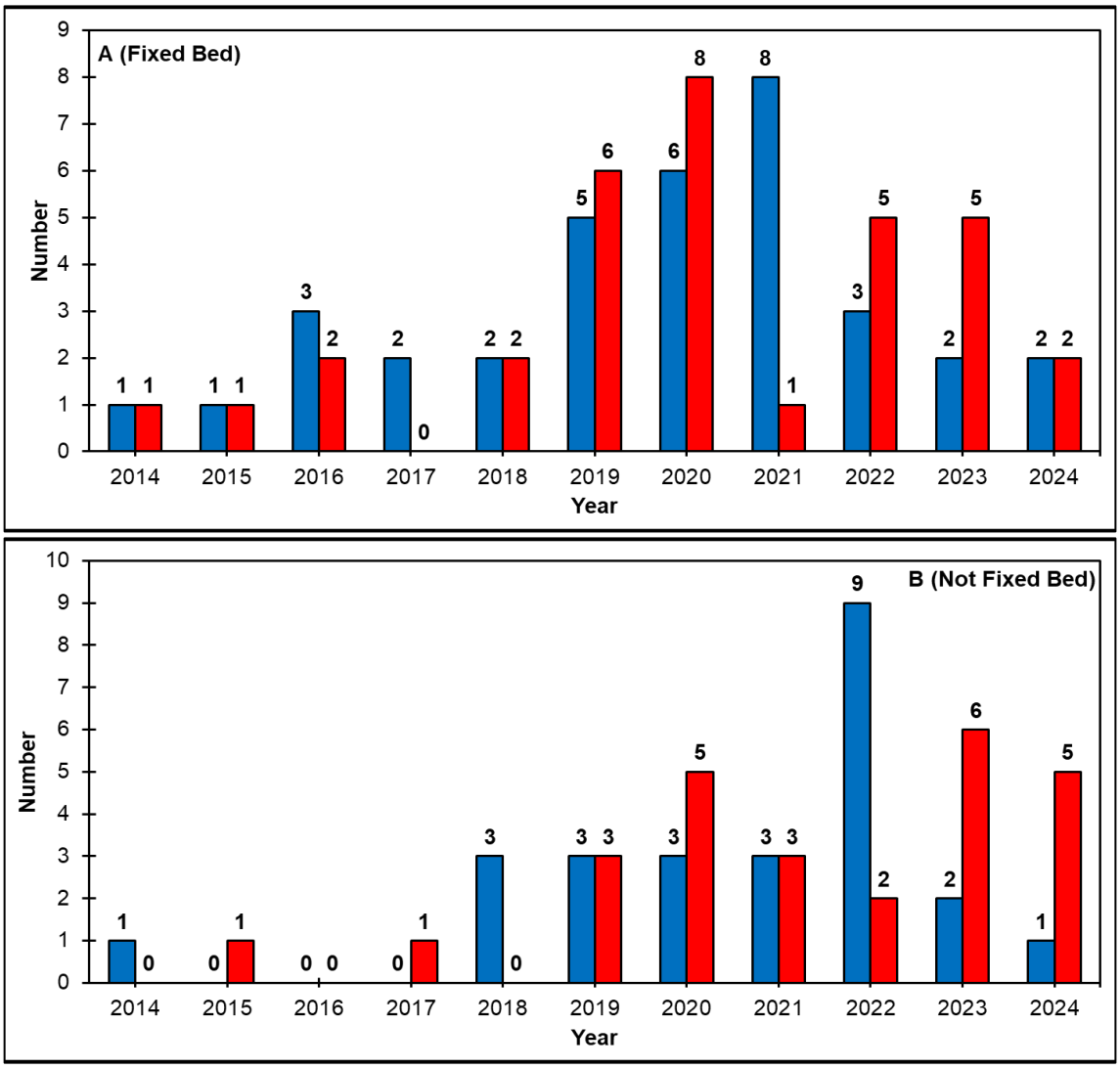

Figure 1.5. Historical evolution of utilization of different phases in reactor modeling of thermocatalytic CO_2 methanation. Pseudohomogeneous, Heterogeneous.

Table 1.6 outlines the distribution of studies using various phase types for CO_2 methanation reactors. Studies with ES, FB, and SBC reactors are typically HET. In contrast, HM, MC, and PHE reactors have an equal number of studies in both phases. M and OA reactors are mainly modeled in the PH phase.

Table 1.6. Phases used in modeling studies for CO_2 methanation reactors.

Reactor	PH	Studies Number	HET	Studies Number
FXB	[51–53,73,88,95–105,107–113,116,124,125,128,129,131–134,136,142,143]	35	[22,26,30,53,54,71,74,75,89–94,99,102,106,110,114,117–123,126,127,130,138–141]	33
HM	[23–25]	3	[20,22,26]	3
MC	[43,45,46]	4	[47–50]	4
ES	-	0	[58–62]	6
M	[51–53,55–57]	6	[54]	1
FB	-	0	[68–71]	4
SBC	-	0	[73]	2
PHE	[66,67]	2	[64,66]	2
OA	[76–78,81–87]	10	[74,75,79,80]	4

There are nearly equal studies for PH phase (25) and HET phase (26) in reactors, excluding FXB. For FXB reactors, there is a slight difference between the number of studies in the PH phase (35) and the HET phase (33), leading to a similar conclusion.

In certain scenarios, resistance to mass and energy transfer can be overlooked for some technological alternatives to the FXB reactor, but not for the FXB reactor itself. Literature indicates that catalyst particles in the FXB reactor are larger than in other reactor types mentioned in the article. Other reactor types, where catalysts are coated on walls of channels or structures such as HM, MC, PHE, foams, and fibers, benefit from increased mass and heat transfer due to smaller catalyst size and larger specific surface area.

Consequently, using the PH phase simplifies the reactor's mathematical model and reduces computational costs, but it's essential to ensure that mass and energy transport resistances between phases are negligible. This can be done by following criteria or approximations from existing literature. If these criteria aren't met, the results from a PH model may be unreliable, requiring a HET model for more accurate predictions.

1.7.1.Comparative studies for different reactor model dimensions

In the literature on CO_2 methanation reactor modeling, comparisons between PH and HET models have mainly focused on FXB reactors. Initially, Schlereth *et al*., [53] found minimal divergence between PH and HET models when catalyst particle size is small and when both pore radius and Reynolds number are high. Conversely, Fischer *et al*., [102] highlighted the significance of inter/intraparticle mass and heat transfer limitations for accurate dynamic predictions. Although the PH model effectively captures concentration and temperature trends and estimates maximum CO_2 conversion accurately, it differs significantly in the time of reaching a new steady-state after feed changes compared to the HET model. This is because the PH model does not account for mass and energy transport limitations, especially within the catalyst. Furthermore, Gomez-Bravo *et al*., [110] indicated that their model required consideration of mass and heat transfer resistances to better match experimental results, suggesting the PH model is unsuitable in this context.

The analysis of this section confirms that comparative studies between models at different phases are beneficial. They help confirm the applicability of using a PH model and identify suitable operational conditions for its use in both steady-state and dynamic studies.

1.8.Effectiveness factor

Figure 1.6 shows the historical development of methods used to determine the effectiveness factor. Most studies use the formal definition, where concentration and temperature profiles within the catalyst are established, indicating significant transport limitations. The effectiveness factor is calculated by taking the ratio of average catalyst reaction rate to the reaction rate at the solid surface. Table 1.7 and Table 1.8 provide data on methods for determining the effectiveness factor in reactor modeling.

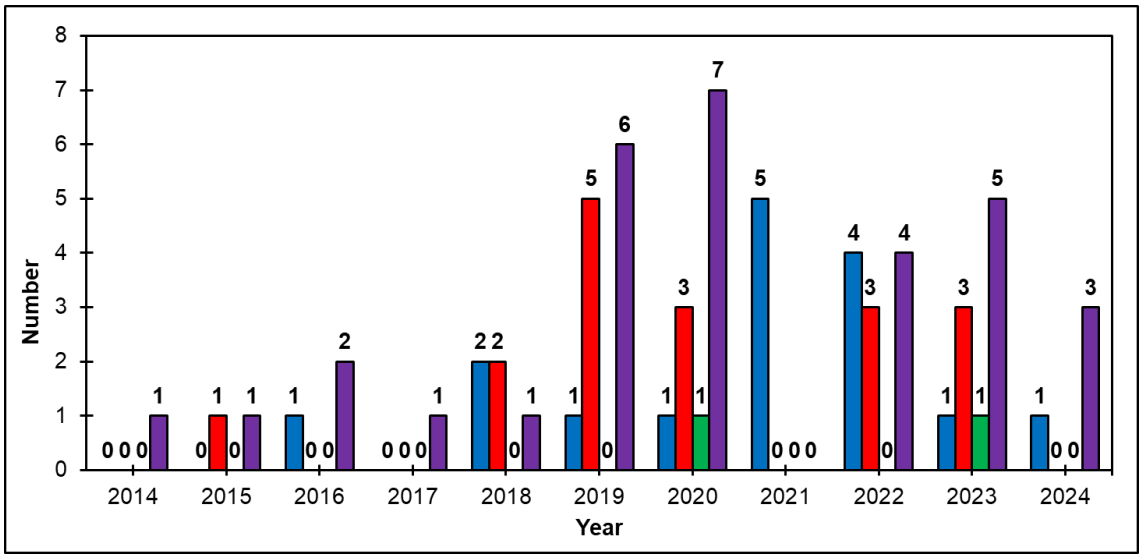

Figure 1.6. Effectiveness factor in reactors modeling of CO_2 methanation. Historical Evolution. Constant Value, First order reaction, spherical catalyst, First order reaction, flat catalyst, Formal Definition.

Table 1.7. Effectiveness factors used in modeling studies for CO_2 methanation reactors. Formal definition and constant value.

Parameters	Formal Definition	Studies Number	Constant Value	Studies Number
FXB	[22,26,30,53,54,71,74,75,90–93,99,102,110,114,117–119,123,138,139]	22	[92,94,96,104,109,113,115,116,124,126,128,129,132,140,141]	15
HM	[20,26]	2	-	0
MC	[45,47,49,50]	4	-	0
ES	[61,63]	2	-	0
M	[54]	1	-	0
FB	[71]	1	[68]	1
OA	[74,75,79,80]	4	-	0

Table 1.8. Effectiveness factors used in modeling studies for CO_2 methanation reactors. First order reaction expression for different catalyst shapes.

Parameters	Sphere	Studies Number	Flat	Studies Number
FXB	[52,73,88–90,92,94,98,101,120–122,131,137]	14	[95,99]	2
M	[52,57]	2	-	0
PHE	[64]	1	-	0
SBC	[72,73]	2	-	0

In FXB reactor studies, formal definition is the most common method used to calculate the effectiveness factor, applied in 22 out of 64 cases. Less frequently, a constant value is assigned (15 cases) or theoretical expressions for first-order reactions on spherical (14 cases) and flat (2 cases) catalysts are used. For non-FXB reactors, the formal methodology is used in MC (4/8), OA (4/14), HM (2/6), ES (2/6), M (1/7), and FB (1/4) reactors. The first-order reaction expression for spherical catalysts is employed in M (2/7), SBC (2/2) and PHE (1/4) reactors. The assumption of a constant effectiveness factor is applied in the FB (1/4) reactor.

Many modeling studies focus on estimating the effectiveness factor (66), with 31 conducting this rigorously to enhance credibility by considering catalyst intraparticle restrictions. However, 49 studies assume an effectiveness factor of one, indicating no transport resistance, either due to suitable operating conditions or for model simplification. Specifically, 49 out of 64 studies on the FXB reactor calculate the effectiveness factor, compared to 17 that assume no intraparticle resistance. For other reactor types, the opposite trend is observed, attributed to factors like operating conditions, model simplification, or exclusion of mass and heat transfer limitations due to catalyst size in specific scenarios such as HM, MC, PHE, foams, fibers, tap, flat surface, plate, parallel channels, U-channel, and spiral.

1.8.1.Effectiveness factor in PH models and comparative studies

Some studies using PH phase have addressed catalysts diffusional limitations by either using a fixed value or a theoretical formula to determine the effectiveness factor [52,57,64,72,73,88,95,96,98,99,101,104,109,113,115,116,124,128,129,131,132,137]. Employing a constant value simplifies the mathematical model and reduces computational costs [101,104,115,116]. For instance, Matthischke *et al*., [94] found that in an FXB reactor with cooling, the effectiveness factor (calculated with the expression for first reaction order in a spherical catalyst) stayed constant along the axial direction under certain conditions, supporting the use of a fixed value. However, in an adiabatic FXB reactor, this factor increased significantly at chemical equilibrium. Di Nardo *et al*., [113] adjusted the factor to align model predictions with experimental data, consistent with results from Kiewidt *et al.,* [88] under similar conditions. Ngo *et al*., [132] used a similar method but noted that this approach limits transient simulations [98,99], and requires adjustment if catalyst structure or size changes [124]. In another approach, Li *et al*., [128] developed an empirical formula linking the effectiveness factor to temperature. Furthermore, Scharl *et al*., [98] used a theoretical equation for a first reaction order in a spherical catalyst, suitable for high temperatures but cautioned against its use at low temperatures.

The use of effectiveness factor expressions for PH models is feasible once validated by experiments, and these expressions depend on catalyst characteristics, temperature, and operating conditions. New approaches have been developed to simplify effectiveness factor calculations, yielding results comparable to experimental data or complex models [99,128]. These efforts involve creating concentration profiles within the catalyst at different temperatures and surface mole fractions [99,128]. Insights from these studies help reduce reactor model complexity and minimize computational costs related to mass and heat transport limitations within the catalyst.

1.9.Catalyst

As stated in section 1.1, Nickel (Ni) is the catalyst most used in CO_2 methanation. Nonetheless, as pointed out in the introduction section, the Ruthenium (Ru) catalyst is the second most frequently used choice. Figure 1.7 shows the historical development of using these catalysts in CO_2 methanation reactor modeling research.

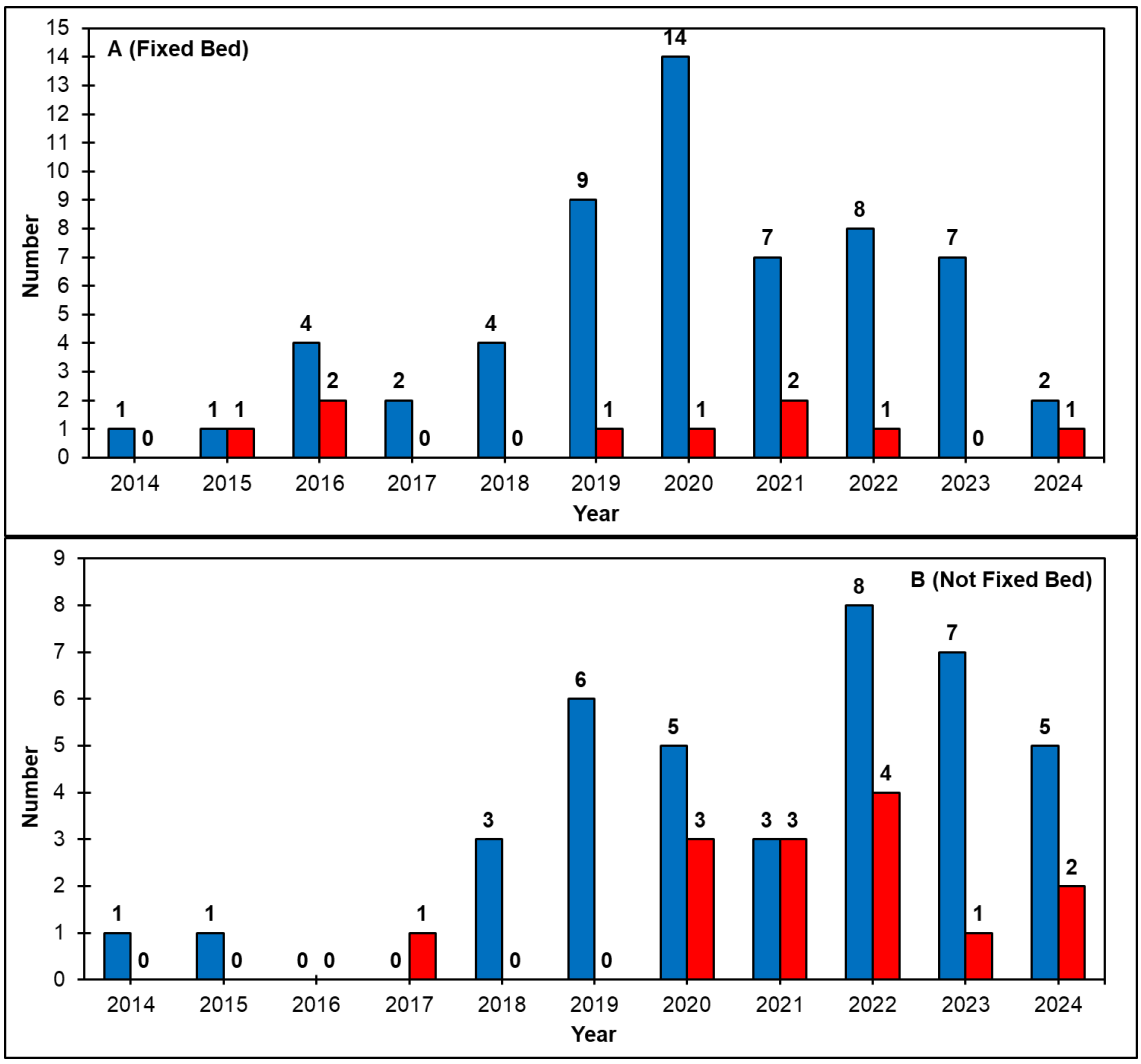

Figure 1.7. Catalysts used in reactor modeling of CO_2 methanation. Historical evolution. Ni, Ru.

From 2014 to 2024, Ni has been predominantly used in FXB reactor modeling, appearing in 59 instances (Figure 1.7.A), whereas Ru was used in only 9 cases. In other reactor types, Ni was used in 39 studies, and Ru appeared in 14 studies (Figure 1.7.B).Table 1.9 highlights studies using Ru as a catalyst. Ru is predominantly used in MC reactor modeling, with only one study not using it. However, in other reactor types like FXB (9 out of 64), HM (1 out of 6), ES (2 out of 6), and M (3 out of 7), fewer studies have used Ru compared to Ni.

Table 1.9. Studies that have employed Ru as a catalyst in the modeling of CO_2 methanation reactors.

Reactor	Ru	Studies Number
FXB	[22,51,113,120–123,128,134]	9
HM	[20]	1
MC	[43–49]	7
ES	[59,62]	2
M	[51,55,56]	3
OA	[86]	1

1.9.1.Comparative studies regarding catalysts in reactor modeling studies

Four research papers have evaluated catalysts in modeling studies, focusing on Ru and Ni. Chein *et al*., [134] demonstrated that Ru yields higher catalytic activity for CO_2 methanation than Ni in a FXB reactor results. Conversely, Moioli *et al*., [121] highlighted the importance of catalytic activity for the Sabatier reaction in an FXB reactor. Despite the thermodynamic and diffusional limitations linked to Ru's higher catalytic activity compared to Ni, both catalysts achieve the same maximum conversions. Ru is preferred due to its ability to handle thermodynamic limitations without needing a cooling system for significant CO_2 conversions. In contrast, using Ni requires altering its properties and using more of it to match Ru's performance. Ru is especially advantageous for small-scale systems despite its higher cost. Additionally, Moioli *et al*., [120] studied a FXB reactor's performance with Ni, Co, and Ru catalysts. While Ru showed lower activation temperatures and

higher CO_2 conversion, its high cost is a drawback compared to Ni and Co. Therefore, the authors recommended using a single reactor divided into three sections with the more affordable Ni catalyst, supported by a mechanistic study to optimize the design. Lastly, Pérez-Vilela & García [20] examined the dynamic response of a HM reactor with reduced H_2 load using Ni or Ru catalysts. They confirmed previous findings on the steady-state benefits and noted Ru's higher catalytic activity affecting diffusional limitations (Moioli *et al.*, [121]). Their study showed that although Ru causes a more significant temperature shift after H_2 flow reduction, the recovery time to a new steady-state is unchanged, and there is no hot spot displacement. They also found that the reactor's outlet temperature remained stable, ensuring CO_2 conversion at the outlet was unaffected by changes in H_2 flow, regardless of the catalyst used.

Hence, the Ru catalyst is preferred over the Ni catalyst due to its lower activation temperature, better CO_2 conversion, and improved resistance to deactivation through sintering. Additionally, the Ru catalyst demonstrates dynamic stability at high catalytic activity levels. However, in cases of budget constraints, the Ni catalyst is a suitable alternative. Reactor models using the Ru catalyst can serve as benchmarks for designing Ni catalyst systems to achieve similar benefits.

1.10.Kinetics

Figure 1.8 illustrates the progression over time in the application of CO_2 methanation reaction rate expressions within reactor modeling research.

The Xu-Froment expression is the most frequently used kinetic model, with 40 instances of usage, peaking in studies from 2022. Originally derived from a nickel catalyst, it accounts for CO_2 methanation, steam reforming, and the Water Gas Shift [144]. It was initially developed for the steam reforming process, suitable for temperatures of 300-575 °C and pressures of 3-15 atm, conditions not ideal for CO_2 methanation [19,144,145].

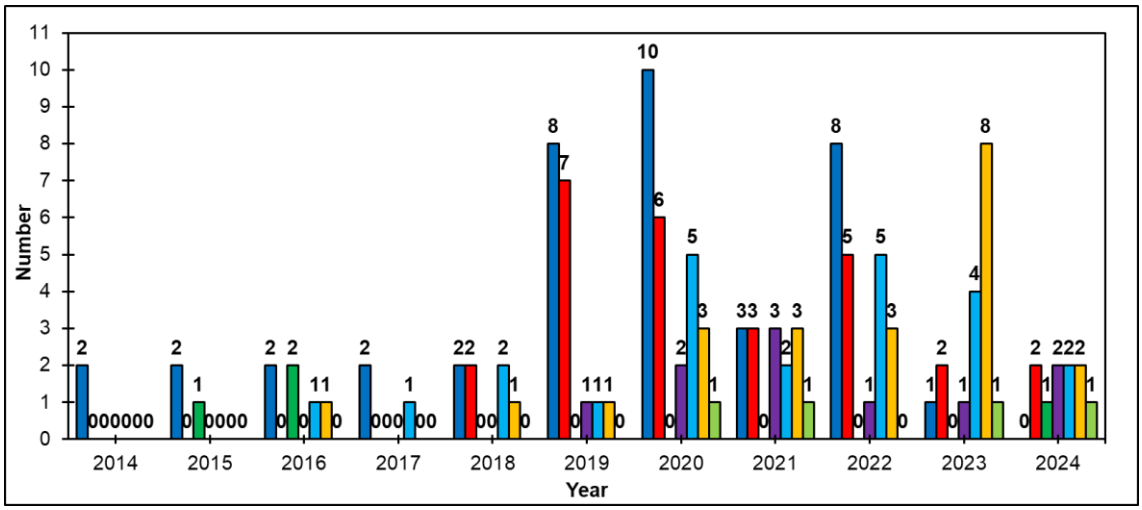

Figure 1.8. Reaction rate expressions used in reactors modeling of CO_2 methanation. Historical Evolution. Xu-Froment, Koschany, Lunde-Kester, Falbo, Power Law (Others), LHHW (Others), Dynamic/Microkinetics (Others).

However, researchers have adjusted the Xu-Froment kinetic parameters to match experimental results for the Sabatier reaction [52,65,75,79,80,119,137]. This modification has enhanced the expression's applicability in modeling methanation reactors with a nickel catalyst.

As an alternative to the Xu-Froment expression, the Koschany reaction rate expression has been adopted, with this second option being frequently used in modeling articles (27). It gained traction in reactor modeling articles starting in 2018, with a peak in 2019, and has been more widely used than the Xu-Froment expression since 2023. Koschany's expression shows higher activity and selectivity for CH_4 without forming CO, indicating the absence of CO methanation and Reverse Water Gas Shift reactions [146]. Additionally, this kinetic expression is effective within temperature and pressure ranges of 180-340 °C and 1-15 atm, suitable for CO_2 methanation.

As a third alternative, power law type equations are commonly used in modeling CO_2 methanation reactors, specifically for Ni and Ru. Out of 24 contributions, 12 studies developed their own

equations [23,46,49,50,69,73,85,86,103,106–108], while the rest utilized existing ones from the literature [26,55,99,120,130,139]. The adoption of power law equations from other authors has increased since 2016, reaching its highest in 2020 and 2022. By 2024, the number of studies using power law equations exceeded those using Koschany's equation.

Other authors' Langmuir-Hinshelwood-Hougen-Watson (LHHW) expressions are the fourth most frequently used, with 22 instances, mainly applied to Ni catalysts. Since 2016, there has been a rising trend in papers using these expressions, peaking in 2023. Afterward, the number of modeling papers using LHHW expressions equaled those using Koschany's expression.

Given that there are fewer studies employing Ru as a catalyst, this is also evident in the limited number of research papers utilizing the Lunde-Kester (4) and Falbo (10) reaction rate expressions. The Lunde-Kester expression works effectively for methane (CH_4) production at temperatures between 200-350 °C and a pressure of 1 atm [147]. Falbo modified this expression, expanding its applicability to pressures from 1 to 7 atm for temperatures of 250-410 °C [148].

Since 2020, research has developed more complex kinetic expressions than those previously used, such as LHHW and power law. Three studies have applied non-stationary kinetics specifically for the ES reactor [58,59,62], based on their experimental findings, while another study used a reaction rate expression from microkinetic theory [89].

Table 1.10 highlights that the Xu-Froment and Koschany reaction rate expressions are mainly used in FXB reactor modeling. Xu-Froment accounts for side reactions in the Sabatier reaction, while Koschany is tailored for a selective Ni catalyst for CH_4 production. In contrast, alternative technologies like MC and SBC primarily use power-law-type rate expressions, as shown in Table 1.11 .On the other hand, the PHE reactor primarily uses LHHW-type reaction rate expressions for

its modeling. Similarly, the ES reactor employs LHHW-type expressions but distinguishes itself by focusing on reaction rate expressions for non-stationary conditions, as active catalyst sites change over time. The FB and OA reactors extensively use the Xu-Froment reaction rate expression in their modeling. Both HM and M reactors incorporate LHHW and power-law type reaction rate expressions in their studies.

As discussed in this section, if determining a reaction rate expression for a CO_2 methanation reactor is not feasible due to budget constraints, selecting an appropriate kinetic expression that aligns with the study's goals is crucial. For studies using Ni as a catalyst with a focus on high CH_4 selectivity and no side reactions, the Koschany expression is recommended for its versatility in temperature and pressure. If the study also considers CO methanation and Reverse Water Gas Shift reactions, the Xu-Froment expression is preferable, utilizing kinetic parameters from literature concerning Sabatier conditions. For studies using Ru, the Falbo expression is suggested, because this is an improvement upon the Lunde-Kester expression. Alternatively, power-law or Langmuir-Hinshelwood-Hougen-Watson (LHHW) type expressions from the literature can be chosen to match the specific operating conditions, catalyst features, and reactor dimensions.

1.10.1.Comparative studies with different reaction rate expressions

In addition to the comparative studies from section 1.9.1, four more research works in the literature have explored different reaction rate expressions. Firstly, Bremer *et al.*, [101] examined the effects of two Ni catalysts with different catalytic activities on a steady-state FXB reactor. They used specifically reaction rate expressions of Xu-Froment and Koschany, to represent each catalyst's activity. The Koschany expression showed greater catalytic activity than the Xu-Froment expression. The study produced ignition-extinction curves and found that higher catalyst activity leads to sharper, more localized hot spots in different reactor locations.

Table 1.10. Kinetic expressions used in modeling studies for CO_2 methanation reactors. Langmuir Hinshelwood-Hougen Watson expressions.

Reaction Rate Expression	Xu-Froment	Studies Number	Koschany	Studies Number	LHHW (Others)	Studies Number
FXB	[22,52,53,71,75,99,101,104,109,111,112,114–117,119–121,125,135,136,143]	22	[30,74,90–94,96–102,105,121,132,140,141]	19	[98,99,118,130,134]	13
HM	[22]	1	[20,24]	2	[25,26]	2
MC	-	0	-	0	[45]	1
ES	[63]	1	[60,61]	2	[63]	1
M	[52,53,57]	3	-	0	[54]	1
FB	[68,70,71]	3	-	0	-	0
PHE	[65,67]	2	[64,66,67]	3	-	0
OA	[74–80]	7	[74]	1	[81–84,87]	5

Table 1.11. Reaction rate expressions used in modeling studies for CO_2 methanation reactors. Power law expressions.

Reaction Rate Expression	Lunde-Kester	Studies Number	Falbo	Studies Number	Power Law (Others)	Studies Number
FXB	[88,110,123,134]	4	[51,113,120–122,128]	6	[73,99,103,106–108,120,127,130,139]	10
HM	-	0	[20]	1	[23]	1
MC	-	0	-	0	[43,44,46–50]	7
M	-	0	[51,56]	2	[55]	1
FB	-	0	-	0	[69]	1
SBC	-	0	-	0	[72,73]	2
OA	-	0	-	0	[85,86]	2

Conversely, Gruber *et al*., [99] studied a FXB reactor operating outside the typical temperature and pressure ranges for reaction rate expressions. To select a suitable kinetic expression, they analyzed conversion rates while varying temperature and pressure. They discarded expressions reaching chemical equilibrium at low temperatures and those with non-monotonic trends. They also reviewed ignition curves, excluding kinetics with low ignition temperatures. Ultimately, they chose Koschany kinetics for their study. Furthermore, Scharl *et al*., [98] proposed a kinetic model using reaction rate expressions from existing literature to evaluate a carbon oxide methanation FXB reactor's performance. They chose expressions that showed an increasing normalized reaction rate with temperature and avoided negative reaction orders within the study's operational range. For the Sabatier reaction, they selected the Koschany expression. Ultimately, Zhang *et al*., [130] developed a mathematical model for the FXB reactor and tested its effectiveness by simulating the reactor with three different reaction rate expressions. They compared the model's predictions with existing experimental data, finding that the model's predicted temperature and CO_2 conversion trends closely matched the experimental results qualitatively.

Concerning this, comparing the catalytic activities of the same catalyst is beneficial for selecting a reaction rate expression and evaluating a chemical reactor.

1.11.Boundary and initial conditions

Section A.1 focuses on initial and boundary conditions in CO_2 methanation reactor modeling. Most research sets initial composition, temperature, density, and pressure to match inlet flow values, with initial velocity either being zero or matching the inlet. Unlike some studies using the Danckwerts condition [30,51,52,56,57,60,61,63,67,71,90,93,110,135–137], 82 studies align these variables with inlet flow values at the inlet reactor. In the case of reactor outlet, it is typically assumed that temperature and composition gradients are absent, with constant pressure. Adiabatic conditions are maintained for the solid phase at both the inlet and outlet, specifically for

the monolithic HM reactor substrate (3/6) and the FXB reactor wall (2/64). In 2D and 3D analyses, symmetry is assumed at the reactor's center, except for annular reactors. Reactor walls are treated as impermeable, with no gas velocity at these surfaces, and the thermal condition affects the energy balance boundary condition at the wall. For catalyst particles, symmetry is presumed at their center, while catalytic washcoatings (e.g. HM, MC, PHE, foams, fiber, millichannels, plates, taps, U-channels and spirals reactors) are assumed to have no mass and energy gradients with the walls that cover. Furthermore, most research applies to the Robin condition at the gas and catalyst interface. This analysis suggests that selecting boundary conditions for a reactor's mathematical model depends on the study's goals and operational conditions. For experimental validation, it's crucial to choose appropriate boundary conditions; otherwise, the results may significantly differ from the actual reactor's observed behavior.

1.12.Assumptions

Section A.2.1 notes that most of studies (85) have determined the gas's physical properties using correlations based on pressure, temperature, and composition. For the tube containing the reactor (31), catalyst (100), and cooling medium (59), it is assumed that their properties remain constant, except for those influenced by temperature, like the reactor's radial thermal conductivity of HM reactor or the gaseous cooling medium's physical properties. Moreover, while catalyst porosity can be considered constant in scenarios without deactivation reactions, this is often not the case for reactors with catalyst particle beds (FB, SBC and some studies of FXB). The choice to assume constant properties can significantly impact mathematical model outcomes, as these properties are influenced by composition, temperature, and pressure.

In section A.2.2 is observed that most reactor modeling studies for the Sabatier reaction do not assume isothermal conditions due to the highly exothermic nature of CO_2 methanation. There are few studies on adiabatic conditions, despite the aim to replace adiabatic FXB reactor technology.

Most studies assume constant reactor wall and cooling medium temperatures, valid if there's a high flow rate of the cooling medium and minimal heat transfer resistance. For assessing cooling medium impact, determining optimal flow rates, or proposing suitable reactor designs, existing literature provides valuable insights for future research.

From the information provided section A.2.3, a significant part of CO_2 methanation reactor modeling research has focused on including the effects of both axial and radial mass and heat dispersion, as well as axial and radial conduction impacts on the monolithic HM reactor substrate and the FXB reactor wall. Additionally, many studies have mainly addressed the limitations of mass and heat transfer in surface and within the solid catalyst. These findings are particularly useful in scenarios where these phenomena are crucial, providing more accurate predictions of reactor performance.

Section A.2.4 shows that the ideal gas equation is primarily used for modeling CO_2 methanation reactors because the gas mixture involved (CO_2, H_2, CH_4, H_2O, etc.) behaves as an ideal gas under the usual industrial conditions of temperature, pressure, and composition [57,65,73].

To simplify reactor modeling for the Sabatier reaction, researchers use a pseudo-stationary momentum conservation equation when solving transient state mass and energy conservation equations, focusing on the pressure drop as the key factor in the momentum equation (detailed explanation in section A.2.4). This simplification is based on no mass accumulation [30,93], weak compressibility, or a plug flow velocity profile. These assumptions are made because the momentum balance introduces minor time constant effects compared to component mass and energy balances, which significantly increase the stiffness of the system's partial differential equations during non-steady-state conditions, thereby elevating computational costs [74,75,101,104]. The momentum balance resolution for deriving velocity and pressure profiles is

challenging without proper computational tools. Simplifications may be recommended if the study's primary focus is not on gas fluid dynamics and if velocity and density have lower time constants compared to composition and temperature.

1.13.Contributions

This review examines several contributions to comparative studies on anticipated reactor behavior concerning different model dimensions and phases. It analyzes the reactors' dynamic response to various H_2 load fluctuations and other operational parameters. The review also includes a study on how different methodologies for calculating the effectiveness factor impact model predictions. Additionally, it investigates how catalytic activities linked to different reaction rate expressions influence the performance of the CO_2 methanation reactor.

In addition to the previously mentioned points, the primary contributions from most modeling studies of reactors used in the Sabatier reaction focus on evaluating the reactor's behavior under specific operating conditions. These studies conduct parametric analysis to explore the dependence of performance variables like CO_2 conversion, temperature, and pressure on operational factors such as inlet flow, feed temperature, and cooling temperature. Some have also contributed to advancements in reactor design and optimization of operating conditions. Beyond these contributions, other significant advancements in modeling work include comparative studies of various reactor types and the creation of innovative operational methodologies (Section A.3).

Section A.3.1 notes that comparing different reactor types, using the FXB reactor as a benchmark, is essential for selecting the appropriate technology for CO_2 methanation. This choice depends on factors like budget, process scale, operational conditions, and the reactor's dynamic properties. Although these studies may not be as numerous as those on evaluation work, parametric studies, reactor design, and optimization, they can lay the groundwork for tackling future challenges in CO_2

methanation reactor modeling and enhance the quality of results in related areas. Section A.3.2 also illustrates other types of comparative studies that can lay the groundwork for addressing future challenges in CO_2 methanation reactor modeling and improve the quality of results in related areas. Additionally, section A.3.3 describes that new methods have been developed to improve the catalytic efficiency and thermal management of CO_2 methanation reactors. These proposals contribute to improving reactor performance, but securing adequate funding is essential to conducting tests and confirming their future applicability. Additionally, it is suggested that these studies extend to encompass other reactors beyond FXB and HM.

Conclusions

Reactor modeling is crucial in CO_2 methanation for predicting equipment performance under specific conditions. It evaluates the impact of operational variables on the Sabatier reaction, aids in reactor design by determining dimensions, and identifies optimal operating conditions. It also facilitates comparative studies of different reactor types and methodologies. This review article focuses on these key aspects and aims to provide essential information for modeling a CO_2 methanation reactor.

Initially, since 2014, there has been a rise in reactor modeling studies aimed at replacing the existing Sabatier reaction technology, specifically the adiabatic fixed bed reactor with intermediate cooling. Regions such as Asia and the Americas, like Europe, are striving to produce synthetic natural gas more efficiently and at lower costs, as shown by the increase in modeling research over the past decade. The dynamic modeling studies focus on the reactor's dynamic response to variations in H_2 loading and other operational conditions. However, there is a significant lack of dynamic studies for reactors used in the Sabatier reaction that differ from the fixed bed reactor.

Secondly, in the field of CO_2 methanation, the number of modeling studies with experimental validation is fewer than usual compared to those validated theoretically. One-dimensional models are predominantly used for mathematical modeling of CO_2 methanation reactors, regardless of whether they consider the phase as pseudo-homogeneous or heterogeneous. Most heterogeneous model studies aim to determine concentration and temperature profiles within the catalyst, which helps calculate an effectiveness factor with high precision. These studies have shown that using a constant effectiveness factor is impractical due to its dependency on temperature and catalyst structure.

As a third point to discuss, in the context of CO_2 methanation reactors, nickel is commonly used as a catalyst in most studies. However, research using ruthenium as a catalyst serves as a benchmark for developing alternative reactors and Ni catalyst designs to achieve similar advantages. The Koschany and Xu-Froment expressions (with kinetic parameters customized to specific operating conditions) are typically used for modeling studies with nickel catalysts. In contrast, the Falbo kinetic expression is favored in studies using the Ru catalyst. Notably, there is a growing trend of developing unique kinetics, whether of the power-law or Langmuir-Hinshelwood-Hougen-Watson type.

Fourthly, Modeling studies of literature have calculated gas's physical properties with correlations, often assuming constant properties for reactor tube walls, monolithic substrates, and cooling mediums, which can vary by case. The energy balance for walls and cooling mediums depends on operational conditions and study goals. For the gas phase, models often consider mass dispersion and heat conduction both axially and radially, extending to solid axial and radial heat conduction in monolithic substrates and fixed bed reactor walls. Most works also account for inter- and intra-particle transport limitations. In modeling CO_2 methanation reactors, the ideal gas equation is commonly used to determine gas density. Many studies apply a pseudo-stationary

momentum balance equation, focusing on pressure drop, assuming weak compressibility flow and no material accumulation.

Finally, the focus of the modeling efforts has been on assessing, conducting parametric studies, designing and optimizing the reactor's operating conditions. There has been a notable increase in comparative studies involving different reactors alongside the fixed bed reactor, along with innovative proposals for its operation.

Recommendations

This article proposes future research suggestions for modeling CO_2 methanation reactors based on the analyses and conclusions presented:

- For emerging technologies, it is recommended to broaden the scope of dynamic studies because the hydrogen used in CO_2 methanation is mainly derived from renewable energy sources, which leads to an inconsistent supply and variation in gas load. It is also advisable to explore how fluctuations in H_2 load and disturbances in other operating variables affect the dynamic response of reactors beyond those with a fixed bed.
- Calculating the concentration and temperature profiles within the catalyst requires substantial computational resources for accuracy. Future research should aim to develop methods that simplify the calculation of the effectiveness factor while maintaining accuracy comparable to the most precise models.
- Comparing outcomes from the one-dimensional pseudohomogeneous model with those from more complex models helps in choosing the right features while ensuring theoretical and experimental validation. Hence, conducting comparative studies is advised to assess the influence of the reactor's phase and size, along with typical simplifications.
- Finally, it is suggested to enhance the contributions from modeling studies, as they offer a foundation to address both new and existing challenges in solving CO_2 methanation issues.

Chapter 2.

Modeling the dynamic operation of a monolithic CO_2 methanation reactor. Evaluation of the response to H_2 load fluctuation

The information provided in this chapter is redrafted after publishing in*: Pérez-Vilela, D.E & Garcia, X. (2024). Modeling the dynamic operation of a monolithic CO_2 methanation reactor. Evaluation of the response to H_2 load fluctuation. International Journal of Hidrogen Energy, 77, 769-783.* https://doi.org/10.1016/j.ijhydene.2024.06.148.

ABSTRACT

A full-scale, 2-D, axially symmetric, heterogeneous, and transient mathematical model is utilized to evaluate the dynamic operation of a honeycomb monolithic reactor during CO_2 methanation. A base case is defined, which considers a step-type functionality for H_2 load reduction (-20%) and a Ni catalyst. The impacts of the catalyst type (Ni vs Ru), the functionality of the H_2 load disturbance, and the monolith's diameter on reactor performance are studied and compared to the base case. Results show that the use of Ru as catalyst, a ramp-type disturbance and a smaller reactor diameter generate a superior dynamic response to the H_2 feed disturbance as well as favorable effects on thermal behavior. This is despite the higher temperature gradient generated when using Ru. These findings suggest that the monolithic reactor is a viable technological option for CO_2 methanation under flow variations, such as those encountered when employing green hydrogen.

Keywords: CO_2 methanation; H_2 load fluctuation; Honeycomb monolithic reactor; Dynamic response; Thermal stability; Catalytic performance.

2.1.Introduction

Carbon dioxide (CO_2), the main greenhouse gas, has amplified the effects of climate change in recent years. Among the numerous solutions proposed to reduce its emissions and convert them into useful products, the transformation of CO_2 into methane (CH_4) has gained significant interest [2–7]. To achieve this, the Power to Gas (PtG) technologies are being viewed as potential future energy systems. This process involves water electrolysis (H_2O) to produce hydrogen (H_2), followed by the thermal-catalytic hydrogenation of CO_2 to CH_4, also known as CO_2 methanation or Sabatier reaction [2–9].

$$CO_{2_{(g)}} + 4H_{2_{(g)}} \leftrightarrow CH_{4_{(g)}} + 2H_2O_{(g)};\ \Delta H^{\circ}_{rxn} = -165\frac{kJ}{mol} \quad 2.1$$

Nickel (Ni) is typically employed as the active phase of the catalyst in this reaction due to its satisfactory CO_2 conversion values and selectivity towards CH_4. Moreover, it offers increased accessibility and is more cost-effective compared to other metals utilized in this reaction [3,5,10–14]. However, given that this reaction is exothermic, the temperature may exceed the specified range, possibly leading to secondary reactions that could diminish methane production. It may also surpass the sintering and coking temperature, hastening the catalyst's deactivation [3,5,10–14].

The main technology used to overcome these limitations involves a series of fixed-bed adiabatic reactors with an intermediate cooling system at the end of each unit. However, this solution is complex in design and operation, and necessitates a significant investment [2,4,6,10]. Alternatively, the monolithic reactor is a desirable choice that meets the operational needs of this industrial application. When compared to a fixed-bed reactor, it generates a lower pressure drop due to the parallel distribution of its channels, a larger contact surface area (which notably decreases the mass/heat transfer limitations), and superior thermal properties [3,15–18].

Consequently, the peak temperature of the reactor (hot spot) is significantly lowered, making it an excellent technological solution to surpass thermodynamic constraints and prevent the deactivation of the Sabatier reaction catalyst, at a lower cost and effort [3,15–18].

On the other hand, when green H_2 is used as reactant, the temporary variations in its load, due to the intermittent nature of renewable energy sources (solar and wind power), must be considered. These will inevitably impact the performance of the Sabatier reaction in the PtG process [3,4,14,15]. A steady state operation, with enough stored H_2 to ensure a constant gas flow, has been suggested. However, this operation model increases costs and operational constraints due to the low density of H_2 [3,4,14,15]. Therefore, the transient operation of CO_2 methanation reactor is still favored, but it requires flexibility and quick responses to H_2 load fluctuations [3,4,14,15].

For these reasons, a growing number of studies are proposing the use of honeycomb-type monolith reactors for CO_2 methanation. The literature shows (see Table 2.1) that Ni, Al_2O_3, and ceramics are mainly used as the active phase, support, and substrate material (monolith), respectively. It's worth noting that these catalytic evaluations have yielded impressive results in terms of CO_2 conversion, CH_4 selectivity, and catalytic stability. Therefore, this type of reactor is an excellent choice for managing the heat produced by the reaction and preventing catalyst deactivation due to sintering during CO_2 methanation.

Research focusing on the modeling and simulation of this kind of structured reactor in the methanation of CO_2 has also been carried out, utilizing mainly Nickel as the catalyst's active phase.

Table 2.1. Summary of the studies on catalytic CO_2 methanation using honeycomb monolithic reactors.

Catalyst	Substrate material	Reference
$Ru/\gamma Al_2O_3$	Cordierite	[149]
Ni/CeO_2	Alumina	[31,32]
$Ni/\gamma Al_2O_3$	Cordierite	[34]
Ni/GDC (ceria-doped gadolinium)	Cordierite	[18,150]
Ni/CeO_2, Ni/TiO_2, Ni/Al_2O_3, Ni/Y_2O_3	Commercial ceramics	[151]
Ni/Al_2O_3, $Ni\text{-}Ru/Al_2O_3$, Ru/Al_2O_3	Cordierite	[152]
Ni/Al_2O_3	Ni/Al_2O_3	[153]
$Ni/CeO_2\text{-}ZrO_2$	Silicium carbide	[154]
Commercial *BASF ES*	Stainless steel	[17]
$NiFe/Al_2O_3$, $NiFe/SiO_2$	Cordierite	[155,156]
$Ru\text{-}Ni/MgAl_2O_4$	Stainless steel	[157]
$Ni/MgAl_2O_4$	Stainless steel	[33]
Ni/CeO_2	Stainless steel	[158]
$Ru/\gamma Al_2O_3$	Cordierite	[159]
Ni/CeO_2	Integral carbon	[160]

Sudiro *et al*., [38], carried out a dynamic simulation of a monolithic reactor using a one-dimensional, heterogeneous, and dynamic model, starting from certain initial conditions up to the steady state. However, the main reaction in this study was the methanation of CO, with the Sabatier reaction being a secondary process. Schlereth *et al*., [161] employed stationary and heterogeneous models and performed a comparison between the full two-dimensional scale and the three-dimensional scale. These researchers noted that, under certain operational conditions, the axial symmetric two-dimensional scale could sufficiently represent the predicted trend in the three-dimensional situation. Schollenberger *et al*., [162] implemented the scale-up of a laboratory-scale monolithic reactor to a demonstration scale using an axial symmetric, two-dimensional, pseudo-homogeneous, and stationary model. Consequently, they proposed the use of two reaction stages, the first with an aluminum monolith and the second with a stainless-steel monolith. A substantial production of CH_4 and a higher conversion of CO_2 were achieved. Huyhn *et al*., [156] employed a three-dimensional, pseudo-homogeneous, and stationary model to validate the

experimental results of a series of three monolithic reactors with equal and/or varying catalytic activities. By locating the hotspot and examining the temperature profile trend, these researchers concluded that a combination of monoliths with high and low catalytic activities is more appropriate for achieving outstanding CO_2 methanation performance at low and controlled temperatures. Lastly, Méndez *et al*., [163] compared the performance of Baena Moreno *et al*.,'s gyroid-type monolithic reactor [33] with the honeycomb type reactor of Schlereth *et al*., [161]. A pseudo-homogeneous, dynamic, and zero-dimensional model was utilized. Despite these authors' inability to satisfactorily replicate the experimental data of both monolith types, their findings showed that the gyroid's performance surpasses that of the honeycomb, solely due to differences in catalyst porosity and surface area.

As can be seen, for CO_2 methanation, there are more experimental studies of the honeycomb monolithic reactor compared to the modeling publications. Furthermore, the number of studies on the honeycomb monolithic reactor using dynamic modeling is significantly less than those considering the fixed-bed reactor with cooling as the most appropriate alternative for this industrial application. It should be noted that no research has been conducted on the dynamic response of a honeycomb-style monolithic reactor to green H_2 load fluctuations. In the literature of CO_2 methanation reactor modeling, this aspect has been mainly examined in the context of fixed bed and slurry bubble column reactors. Various load functionality types for the total feed of H_2 have been studied, including step [164–170]; ramp [168,171–174]; sinusoidal [175] and a sequence of steps [169,176,177]. A similar situation arises with the study of other operational parameters' impact on both the flexibility and performance of the reactor during the dynamic operation of the Sabatier reaction.

In this article a mathematical model for a monolithic CO_2 methanation reactor is formulated, with the purpose of determining how complex and sensitive its dynamic response is to the perturbation

of the H_2 load. Additionally, the dependence of the reactor's dynamic response on catalyst, type of load fluctuation, and monolith size was described and analyzed. This helped to determine how important each of these variables is for the transient behavior of this type of reactor in the Sabatier reaction. Thus, this study contributes to reducing the existing information gap and offers valuable insights regarding the transient operation of this structured reactor.

2.2.Material and methods

2.2.1.Modeling

A full-scale, transient, two-dimensional, axial symmetric, and heterogeneous mathematical model was formulated. The restrictions of internal and external mass transfer within the catalytic layer of the channels were considered, given their potential impact on the reactor's performance. The effectiveness factor was computed using its formal definition (see more details in the appendix). Furthermore, the impacts of thermal transfer resistance in the interface gas-washcoating, as well as the axial heat/mass dispersion of the gas within the channels, were integrated into the model.

2.2.1.1.Assumptions

No mass transfer between the gas and the monolithic substrate was considered in the full-scale model, as the latter is impermeable. Variations from the ideal gas conditions are very small within the pressure, temperature, and composition range typically seen in this reaction [164]. Thus, in the current study, gas behaves as an ideal gas. Regarding the cooling system, its temperature remains constant and is equal to that of the gas fed to the reactor. The catalyst and the monolith's physical properties were assumed to be constant (with the monolith's thermal conductivity being the only exception), and the feed's lack of substances that could deactivate the catalyst due to poisoning was postulated.

2.2.1.2.Conservation equations

Published full-scale models [36,39], along with several other contributions [37,38,40–42,161,162], have considered the monolithic substrate and the catalyst as a unified solid phase, emphasizing the isothermal nature of the catalyst. In line with Hayes *et al.*,'s recommendations [36], the effectiveness factor of the reaction was determined. The composition profiles of each substance within the catalyst were established using the methodology outlined in earlier papers [37,40,178–181]. To depict the gas's velocity profile in the monolith, the same physical assumptions as those documented in previous research [37,38,40,182] were applied. Consequently, the conservation equations were averaged volumetrically for the full-scale model [36]. These are presented in Table 2.2.

Table 2.2. Conservation equations.

Mass balance of each compound in the gas	
$\varepsilon_g \rho_g \frac{\partial w_{i,g}}{\partial t} = -\rho_g u_{z,g} \frac{\partial w_{i,g}}{\partial z} - \varepsilon_g \frac{\partial}{\partial z}\left(\underbrace{-\rho_g D_{i\_axial,g} \frac{\partial w_{i,g}}{\partial z}}_{j_{iz,g}}\right) - a_v \underbrace{k_{i,gs}\left(\rho_{i,g} - \rho_{i,surf}\right)}_{\dot{m}_{i,gs}}$	2.2
Energy balance in the gas	
$\varepsilon_g \rho_g C_{p,g} \frac{\partial T_g}{\partial t} = -\rho_g u_{z,g} C_{p,g} \frac{\partial T_g}{\partial z} - \varepsilon_g \frac{\partial}{\partial z}\left(\underbrace{-\lambda_{axial,g} \frac{\partial T_g}{\partial z}}_{q_{z,g}}\right) - a_v \underbrace{h_{gs}\left(T_g - T_s\right)}_{\dot{q}_{gs}}$	2.3
Energy balance in the solid	
$\left(\varepsilon_{cat}\rho_{cat}C_{p,cat} + \varepsilon_{sup}\rho_{sup}C_{p,sup}\right)\frac{\partial T_s}{\partial t} = -\frac{\partial}{\partial z}\left(\underbrace{-\lambda_{axial,s}\frac{\partial T_s}{\partial z}}_{q_{z,s}}\right) - \frac{1}{r}\frac{\partial}{\partial r}\left(r\left(\underbrace{-\lambda_{radial,s}\frac{\partial T_s}{\partial r}}_{q_{r,s}}\right)\right) + a_v \underbrace{h_{gs}\left(T_g - T_s\right)}_{\dot{q}_{gs}} + \varepsilon_{cat}\rho_{cat}\sum_{j=1}^{N_R}\underbrace{\eta_j r_j\big\vert_{\rho_{i,surf},T_s}}_{\tilde{r}_j}\left(-\Delta H_{rxn,j}\right)$	2.4
Mass balance of each compound within the catalyst	
$\varepsilon_{g,cat}\rho_{g,cat}\frac{\partial w_{i,cat}}{\partial t} = -\frac{\partial}{\partial \xi}\left(\underbrace{-\rho_{g,cat}D_{i\_eff,cat}\frac{\partial w_{i,cat}}{\partial \xi}}_{j_{i\xi,cat}}\right) + MW_i\rho_{cat}\sum_{j=1}^{N_R}\vartheta_{i,j}r_j$	2.5
Continuity equation	2.6

$$\varepsilon_g \frac{\partial \rho_g}{\partial t} = -\frac{\partial(\rho_g u_{z,g})}{\partial z}$$

Momentum balance in gas

$$\rho_g \frac{\partial u_{z,g}}{\partial t} = -\frac{\rho_g u_{z,g}}{\varepsilon_g}\frac{\partial u_{z,g}}{\partial z} - \varepsilon_g \frac{\partial}{\partial z}\left(\underbrace{\left(-2\mu_g + \frac{2}{3}\mu_g\right)\frac{\partial u_{z,g}}{\partial z}}_{\tau_{zz,g}}\right) - \varepsilon_g \frac{\partial P}{\partial z} + \varepsilon_g \rho_g g_z - a_v \underbrace{\left(\frac{f \rho_g {u_{z,g}}^2}{2{\varepsilon_g}^2}\right)}_{\tau_{gs}} \quad 2.7$$

2.2.1.3.Initial and boundary conditions

The initial conditions were taken from the literature and are detailed in Table 2.3. It is observed that the composition and temperature in both solid and gas phases are identical. Values that are congruent with those of the gaseous stream entering the reactor (Equations 2.8-2.9) were considered. Moreover, the initial values of gas velocity and pressure remain constant, matching those of the inlet gas stream (Equations 2.10-2.11). Ultimately, from these values, the initial density of the gas was determined (Equation 2.12) by applying the equation for ideal gas.

Table 2.3. Initial conditions.

$w_{i,g} = w_{i,cat} = w_{i,g\_0} = w_{i,cat\_0} = w_{i,g\_in}$	2.8
$T_g = T_s = T_{g\_0} = T_{s\_0} = T_{g\_in}$	2.9
$P = P_0 = P_{in}$	2.10
$u_{z,g} = u_{z,g\_0} = u_{z,g\_in}$	2.11
$\rho_g = \rho_{g,cat} = \rho_{g_0} = \rho_{g,cat_0} = \rho_{g_{in}}$	2.12

Table 2.4 shows the chosen boundary conditions. At the reactor's inlet (z = 0), the composition, temperature, pressure, and velocity values (Equations 2.13-2.14, 2.16-2.17) are equal to those of the gas stream that enters the reactor. It's noteworthy that the solid's temperature gradient at the reactor's inlet doesn't exist (Equation 2.15). Conversely, at the reactor's outlet (z = L), it was stated that there are no axial gradients for composition, temperature, and velocity (Equations 2.18-2.22).

When it comes to the radial direction, the solid's temperature profile was formulated to be symmetrical (Equation 2.23), with the heat transferred by radial conduction through the monolithic substrate's wall, matching the heat transferred between the monolith's outer surface and the reactor's cooling system (Equation 2.24).

Table 2.4. Boundary conditions.

$z = 0$	$w_{i,g} = w_{i,g\_in}$	2.13
	$T_g = T_{g\_in}$	2.14
	$\left.\frac{\partial T_s}{\partial z}\right\|_{z=0,r} = 0$	2.15
	$P = P_{in} \rightarrow \rho_g = \rho_{g\_in}$	2.16
	$u_{z,g} = u_{z,g\_in}$	2.17
$z = L$	$\left.\frac{\partial w_{i,g}}{\partial z}\right\|_{z=L,r} = 0$	2.18
	$\left.\frac{\partial T_g}{\partial z}\right\|_{z=L,r} = 0$	2.19
	$\left.\frac{\partial T_c}{\partial z}\right\|_{z=L} = 0$	2.20
	$\left.\frac{\partial T_s}{\partial z}\right\|_{z=L,r} = 0$	2.21
	$\left.\frac{\partial u_{z,g}}{\partial z}\right\|_{z=L,r} = 0$	2.22
$r = 0$	$\left.\frac{\partial T_s}{\partial z}\right\|_{z,r=0} = 0$	2.23
$r = R$	$\lambda_{radial,s} \left.\frac{\partial T_s}{\partial r}\right\|_{r=R} = U_{sc}(T_{Wall} - T_c) = U_{sc}(T_s\|_{r=R} - T_c);\ T_c = T_{g\_in}\ (constant)$	2.24
$\xi = \delta$	$\left.\frac{\partial w_{i,cat}}{\partial \xi}\right\|_{\xi = \delta} = 0$	2.25
$\xi = 0$	$\rho_{g,cat} D_{i\_eff,cat} \left.\frac{\partial w_{i,cat}}{\partial z}\right\|_{\xi = 0} = k_{i,gs}(\rho_{i,g} - \rho_{i,surf}) = k_{i,gs}\left(\rho_{i,g} - \rho_{i,cat}\|_{\xi = 0}\right)$	2.26

With regards to the catalytic coating, it was determined that no mass transfer occurs between the catalyst and the monolith substrate (as indicated in Equation 2.25). Hence, it was stated that the

diffusive transport within the catalytic coating's surface equates to the interphase mass transfer between the gas and solid (Equation 2.26).

The correlations used to calculate the mass/heat transfer coefficients, friction factor, axial dispersion and axial/radial thermal conductivity of the solid are those given in Table B.1 of the appendix. The correlations in Table B.2 were used to obtain the values of the physical properties of the gas.

2.2.1.4.Kinetic expression, reaction heat and effectiveness factor

As previously stated, Ni is the most utilized catalyst in the honeycomb monolithic reactor applications, which is why it was selected as the main catalyst in this study. Regarding the kinetics of this reaction, Xu & Froment's kinetics [144] are still in use, but there is a growing interest in the model developed by Koschany *et al*., [146]. This was designed for a $NiAl(O)_X$ catalyst, with surface area, dispersion and average crystallite size of 235 m^2/g, 6 % and 17 nm, respectively. Consequently, the Koschany's equation was employed as the fundamental kinetic expression for the Ni-catalyst. The kinetic parameters of this expression are given in Equation 2.27.

Koschany's kinetic expression

($180 \leq T[°C] \leq 340$; $1 \leq P[bar] \leq 15$; $\frac{H_2}{CO_2}$ *with values of* $0.25, 4$ *or* 8)

$$r_1 = \frac{kp_{CO_2}{}^{0.5} p_{H_2}{}^{0.5} \left(1 - \underbrace{\frac{p_{CH_4} p_{H_2O}{}^2}{p_{CO_2} p_{H_2}{}^4 K_{eq}}}_{\varphi_{eq}}\right)}{DEN^2}; \; DEN = 1 + K_{OH}\frac{p_{H_2O}}{p_{H_2}{}^{0.5}} + K_{H_2} p_{H_2}{}^{0.5} + K_{mix} p_{CO_2}{}^{0.5};$$

$$k\left[\frac{kmol}{kg_{cat} \cdot s \cdot bar}\right] = k_{ref} exp\left(-\frac{E_a}{R_{gases}}\left(\frac{1}{T[K]} - \frac{1}{T_{ref}}\right)\right); \; K_i\left[bar^{-\frac{1}{2}}\right] = K_{i,ref} exp\left(-\frac{\Delta H_{ads,i}}{R_{gases}}\left(\frac{1}{T[K]} - \frac{1}{T_{ref}}\right)\right);$$

$$K_{eq}[bar^{-2}] = 137 \cdot T^{-3.998} exp\left(\frac{158700}{R_{gases} T}\right);$$

$$E_a = 77.5 \; \frac{kJ}{mol} \; ; \; \Delta H_{ads,OH} = 22.4 \; \frac{kJ}{mol}; \; \Delta H_{ads,H_2} = -6.2 \; \frac{kJ}{mol}; \; \Delta H_{ads,mix} = -10 \; \frac{kJ}{mol}; \; T_{ref} = 555 \; K$$

$$k_{ref} = 3.46 \cdot 10^{-4} \; \frac{kmol}{kg_{cat} \cdot s \cdot bar} \; ; \; K_{OH,ref} = 0.50 \; bar^{-\frac{1}{2}}; \; K_{H_2,ref} = 0.44 \; bar^{-\frac{1}{2}}; \; K_{mix,ref} = 0.88 \; bar^{-\frac{1}{2}}$$

2.27

With respect to the reaction effectiveness factor, this was computed using its formal definition (Equation 2.28). The characteristic length definition of the catalytic coating of the channels (δ) ([40,183–185]) was considered in this calculation. Lastly, if the reactor's temperature underwent a significant change, the reaction's heat was calculated using its formal definition (Equation 2.29).

$$\eta_j = \frac{\frac{\int_0^{\delta} r_j d\xi}{\delta}}{r_j\big|_{\rho_{i,surf},T_s}} = \frac{Average\ reaction\ rate\ within\ the\ catalyst}{Reaction\ rate\ at\ the\ catalyst\ surface}; \qquad 2.28$$

$$\delta = \frac{Volume\ of\ catalyst\ occupied\ in\ the\ monolith\ cell}{Internal\ Surface\ Area\ of\ the\ Channel\ in\ the\ Monolith\ Cell}$$

$$\Delta H_{rxn,j} = \Delta H_{rxn,j}{}^{º} + \sum_{i=1}^{NC} \vartheta_{i,j} \int_{T^º}^{T} C_{pi,g}\, dT;\ T^º = 298.15\ K \qquad 2.29$$

2.2.2.Operational conditions and restrictions

2.2.2.1.H_2 load fluctuation functionality

The step-type fluctuation represents the most drastic scenario that can instigate significant alterations in reactor performance and operation [164–170]. This reasoning underlies the choice of this basic functionality type for the H_2 load disturbance in the current study (Figure 2.1). Surveying the literature led to the decision that the fluctuation should result in a percentage decrease in the H_2 load, as this would have a more substantial negative operational impact. Concerning the percentage reduction of hydrogen, values of 25 [175], 50 [175], 75 [175], 83 [167] and 100 % [170], [172] have been implemented.

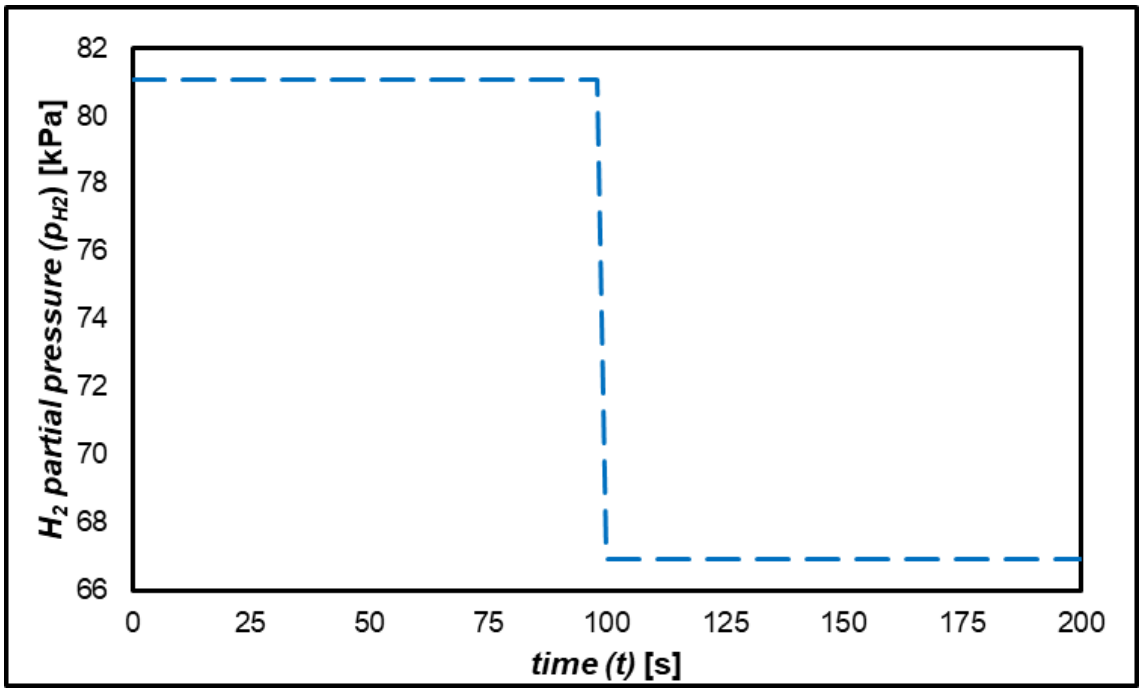

Figure 2.1. Step fluctuation of the H_2 load, with a reduction of 20 %.

Given that transport limitations can significantly influence the dynamic response of the reactor to H_2 load fluctuations, a reduction of 20 % in the H_2 flow was established (Figure 2.1). This value is proximate to the lowest value documented in existing literature [167,170,172,175]. It's also crucial to keep a constant H_2/CO_2 ratio throughout the reactor's dynamic operation for this industrial application. If this is not done and $H_2/CO_2 < 4$, the effect of secondary reactions must be considered. These affect selectivity towards CH_4. For this reason, it was decided to keep the H_2/CO_2 ratio constant for all the case studies in this work, and for this purpose, the CO_2 flow was reduced in the same proportion as the H_2 load at the time the fluctuation was generated.

Lastly, under the initial and operational conditions outlined in this study, a steady state was attained within a time of 100 seconds or less. Hence, it was considered that the H_2 load disturbance would originate from this value.

2.2.2.2.Operating conditions

To select the values outlined in Table 2.5, the operational conditions, and the dimensions of the monolith, experimental (Table 2.1) as well as modeling studies were analyzed.

Table 2.5. Operating conditions, reactor dimensions and physical properties of the catalyst.

Operating conditions	
Input H_2/CO_2 molar ratio	4/1
Inlet gas pressure [kPa]	101.325
Inlet gas temperature [ºC]	280
Inlet GHSV [1/h]	2130
Type of cooling system	Double-tube with external cooling
Cooling system temperature [ºC] (constant)	Inlet gas temperature
Gas Flow direction	Horizontal
Dimensions of the honeycomb monolith	
Channel shape	Square
Diameter [cm]	2.54
Length [m]	2
CPSI (cells per square inch)	26
Substrate thickness between channels [μm]	612
Catalytic coating thickness	200
Substrate material and physical properties of the catalytic coating	
Substrate material	Cordierite
Catalytic coating density [$kg_{washcoat}/m^3_{washcoat}$]	900
Porosity of the catalytic coating [$m^3_{gas\ in\ washcoat}/m^3_{washcoat}$]	0.70
Catalytic coating pore diameter [nm]	50
Catalytic coating tortuosity [-]	4

The values of the H_2/CO_2 (4/1) ratio, operational pressure (1 atm), and temperature (280 °C) are within the range of typical values used for CO_2 methanation, which were also selected based on their compatibility with the range of validity of the kinetic expressions chosen for this research.

In terms of GHSV, the value from Table 2.5 was employed to achieve a CO_2 conversion of 95 % or more. A double-tube cooling system with external cooling was chosen for thermal control. The thicknesses of the catalytic coating in the monolith cell and the substrate between the channels were determined based on the values provided by Schlereth *et al*., [161]. This choice was influenced by the significant heat and mass transfer limitations between phases and within the catalyst. For the remaining dimensions of the monolith, the data from these authors were also adopted, coinciding with the measurements of the monolithic square channel reactor developed by Groppi *et al*., [186]. In the literature of catalytic monolithic reactors (Table 2.1), the use of an average value of 2 cm diameter has been observed and a length range between 2 to 15 cm has been applied. For the case of a pilot-scale monolithic reactor such as Schollenberger *et al*., [162], the diameter was between 3.5 and 10.5 cm, while the range of equipment length was between 10 and 50 cm. Therefore, the values selected for size of the monolithic reactor are within the range of the values mentioned previously. Cordierite was chosen as the support material to create a stronger resistance to heat transfer compared to the metal monolithic support. The density and porosity values of the catalytic coating were taken from Sudiro *et al*., [38], to avoid a higher impact of intraparticle mass transfer limitations. Lastly, the tortuosity and pore diameter values were in line with the approximate values suggested in various literary sources.

2.2.2.3.Operational restrictions

Gao *et al*., [27] recommend a reaction temperature below 300 °C, a pressure greater than 30 atm, and a H_2/CO_2 ratio above 4. However, it is crucial to adhere to the limitations associated with the range of application of the kinetic expressions selected in this research. Moreover, it's important to recognize that the deactivation (sintering) temperature for the Nickel catalyst, which is 590 °C, should not be surpassed [28,187]. In terms of deactivation by nickel carbonyl, [3,19], this could occur if the reactor's temperature falls below 230 °C and there is a significant concentration of CO.

2.2.3.Numerical resolution

Figure 2.2 shows a schematic of the problem-solving domain, which contains equispaced elements in the *zr*-plane of the entire monolithic reactor.

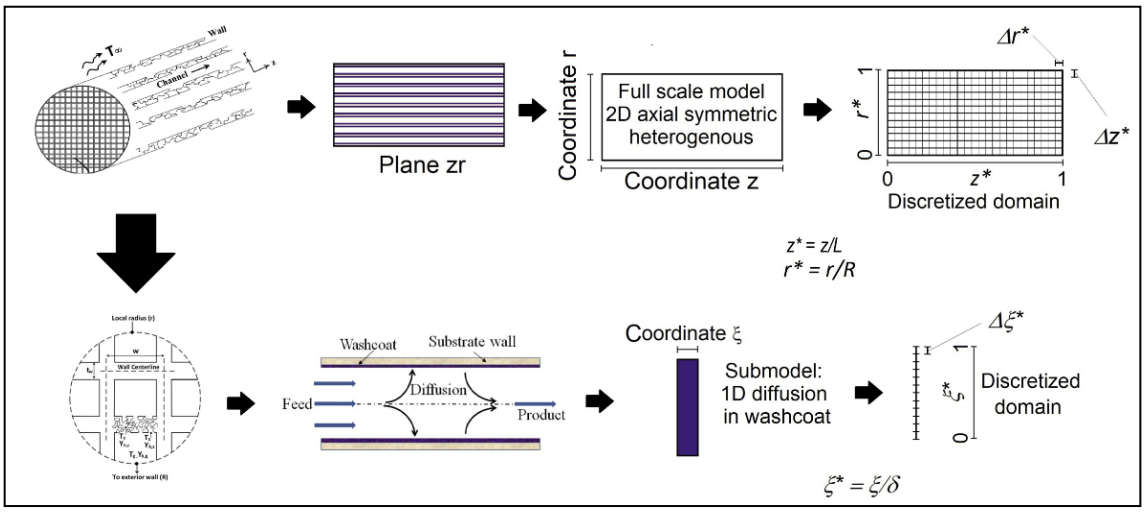

Figure 2.2. Mathematical model resolution domain.

This domain is governed by the gas conservation equations and the solid energy balance of the selected mathematical model. It is also seen that each element contains a one-dimensional equispaced subdomain, which is governed by the mass conservation equation of the catalytic coating.

The numerical methods employed in the referenced modeling studies, along with specifics found in the literature [188], were used to solve the system of partial differential equations of the full-scale, two-dimensional, axially symmetrical, heterogeneous, and dynamic model in the resolution domain of Figure 2.2.

First, the spatial derivatives of the transport terms and the boundary conditions for each conservation equation were discretized, resulting in a system of differential equations with an initial value problem. For diffusive terms and boundary conditions of the Neumann type, a spatial discretization, utilizing a second order centered finite differences scheme was adopted. For convective terms and pressure gradients, spatial discretization with a first order backward finite difference scheme was utilized.

The conservation equations, along with their discretized boundary conditions, were solved using Matlab software. This was done in combination with their initial and operational conditions, correlations to determine mass/heat transfer coefficients between phases, and the physical properties of the gas. Additionally, kinetic expressions, H_2 feed disturbances, and the dimensions of the monolithic reactor were included. The ode15s subroutine was employed to solve the system of differential equations with initial value problem. This subroutine can solve stiff differential equation problems via numerical differentiation formulas of first through fifth order and is a step adaptive subroutine.

The number of points, and consequently, the size of the integration step, is variable for the time interval used. It's crucial to note that the default accuracy of the ode15s subroutine must be achieved. It was suggested that 50 evenly spaced intervals be used based on the discretization of the axial coordinate, as well as 5 equispaced intervals for the radial and spatial coordinates designated for the catalytic coating of the monolith channels.

2.2.4.Study cases. Dynamic response to different operational characteristics

To compare the results of the selected study cases with those of the base case, same operating and reaction conditions were used, emphasizing that in all cases the same values of catalyst density and GHSV from Table 2.5 were used, as well as the same mass percentage and dispersion

of the active phase of the selected catalyst. In this way, all results are comparable to each other. It is also important to note that, as described in section 2.2.1, the H_2/CO_2 ratio was kept constant for all study cases throughout the dynamic operation of the monolithic reactor.

2.2.4.1.Base case

After confirming the accuracy of the mathematical model, the trends in temperature and pressure profiles of the monolithic reactor were examined, along with the performance of the CO_2 conversion profile, from the start-up to the point of steady state condition. The impact of mass transfer limitation during the entire dynamic operation of the monolithic reactor was also analyzed. The operational conditions outlined in Table 2.5, as well as the kinetic expression by Koschany *et al.*, [146], for a $NiAl(O)_X$ catalyst, were used as the base case. Following this, the dynamic response of the monolithic reactor when decreasing the hydrogen load by 20 % for a step fluctuation was analyzed. The results derived from the reactor's response to this variation were compared against the start-up condition. Key points of analysis included the recovery time required to reach the new steady state, the shift in the hot spot, the rise in the reactor's maximum temperature, and the impact this had on CO_2 conversion.

2.2.4.2.Study Case 1: Effect of the catalyst

Ruthenium emerges as a viable substitution for nickel as the active phase of the catalyst. This metal shows excellent dynamic stability [14] and superior resistance to thermal sintering in comparison to nickel and other non-precious metals [3,5,10–14]. Consequently, an evaluation of the performance of the monolithic reactor was conducted, using either Ni or Ru as the active phase of the catalyst. Concerning the kinetic expression, the proposition made by Falbo *et al.*, [148] (Equation 2.30) for a 0.5 wt % Ru/Al_2O_3 catalyst (103 m^2/g, 35 % and 4 nm), which is an amplified version of the expression first derived by Lunde & Kester [147], was employed, because this is the most widely used expression in the literature related to CO_2 methanation reactors modeling.

Falbo's kinetic expression ($250 \leq T[°C] \leq 410$; $1 \leq P[atm] \leq 7$; $1 \leq \frac{H_2}{CO_2} \leq 5$)

$$r_1 = \frac{k{p_{CO_2}}^n {p_{H_2}}^{4n}}{1+\alpha p_{H_2O}} \left(1 - \left(\frac{p_{CH_4} {p_{H_2O}}^2}{\underbrace{p_{CO_2} {p_{H_2}}^4 K_{eq}}_{\varphi_{eq}}}\right)^n\right) \quad 2.30$$

$$k\left[\frac{kmol}{kg_{cat} \cdot s \cdot atm^{5n}}\right] = k_0 exp\left(-\frac{E_a}{R_{gases} T[K]}\right); \; K_{eq}[bar^{-2}] = 137 \cdot T^{-3.998} exp\left(\frac{158700}{R_{gases} T}\right)$$

$$E_a = 75.3 \; \frac{kJ}{mol}; \; k_0 = 95.43 \; \frac{kmol}{kg_{cat} \cdot s \cdot atm^{5n}}; \; \alpha = 0.91 \; atm^{-1}; \; n = 0.152$$

Since the values of loading (0.5 %) and dispersion (35 %) of Ru of Falbo are different from those of the Koschany's Ni catalyst (58 % loading and 6 %), a multiplication factor was applied to Equation 2.30 so that the values of the reaction rates of both kinetic expressions were a function of the same loading and dispersion of the active metal. Based on the above, Equation 2.31 was obtained and used. Its derivation can be consulted in section B.3 of the appendix. In this way, a comparison of the effect of the type of catalyst on the dynamic response of the reactor under the same reaction conditions was carried out.

$$r_{Falbo,corrected}\left[\frac{kmol}{kg_{catalyst} \cdot s}\right] = 342.45 \; \frac{kmol_{Ni \; in \; catalyst \; surface}}{kmol_{Ru \; in \; catalyst \; surface}} \; r_{Falbo}\left[\frac{kmol}{kg_{catalyst} \cdot s}\right] \quad 2.31$$

2.2.4.3.Study Case 2: Effect of the functionality of the H_2 load fluctuation

The ramp-type functionality in the H_2 load offers a more gradual adjustment in the response of the reactor, as opposed to the abrupt changes seen in the step variation. This results in improved control and stability in both the operation and performance of the process variables during the recovery of the new steady state [168,171–174].

Therefore, in line with the comparative research conducted by Try *et al*., [165] and Theurich *et al*., [168], this study also explored the impact of the functionality in the H_2 load disturbance on the performance and dynamic operation of the honeycomb monolithic reactor during CO_2 methanation (Figure 2.3).

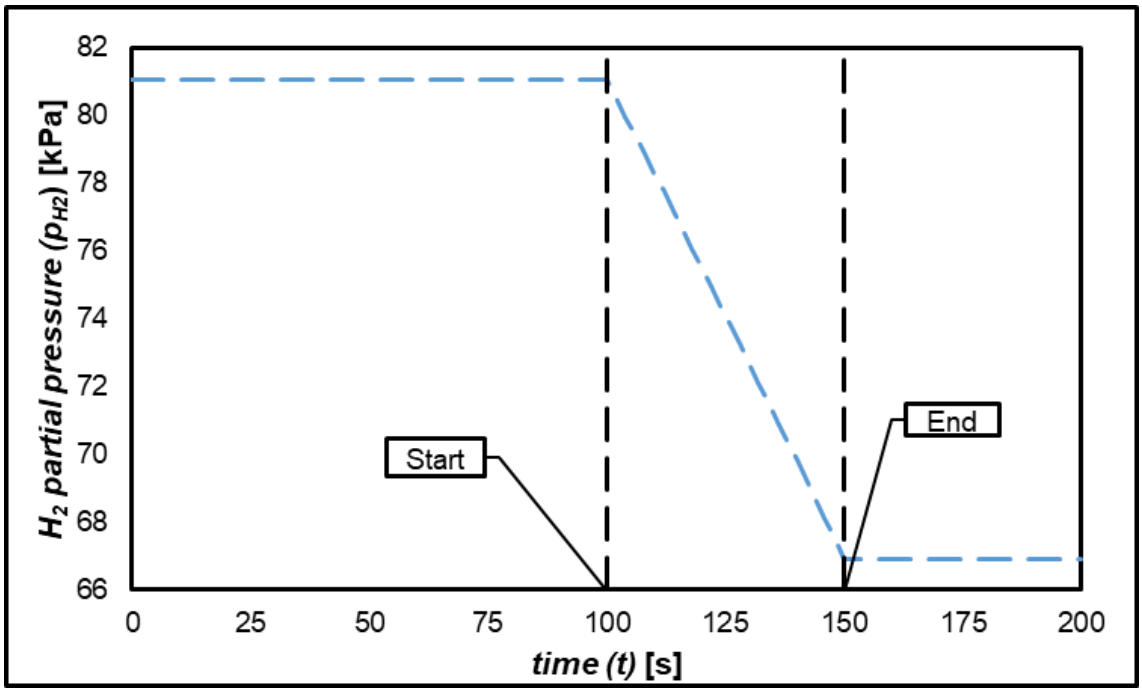

Figure 2.3. Ramp fluctuation of the H_2 load, with a duration of 50 s and a final reduction of 20 %.

A duration time of 50 seconds was chosen (Figure 2.3), which falls within the range of values employed by Fache *et al*., [171–173] and Prabhakaran *et al*., [174]. Lastly, like the step-type variation of the base case, it was also postulated for the ramp disturbance, that the H_2 load was decreased by 20 % (Figure 2.3).

2.2.4.4.Study Case 3: Effect of the monolithic reactor diameter

As a final analysis, the impact of the monolith diameter on the reactor's dynamic response to H_2 load fluctuation was examined. A diameter larger than the base case was chosen, specifically a 3.5 cm diameter, like the monolithic reactor designed by Schollenberger *et al*., [162].

2.3.Results and discussion

It is important to mention that the mathematical model was previously validated. To this end, the independence of the results concerning the number of intervals used for each spatial coordinate was first confirmed. Subsequently, the model was validated using the methodology recommended by Fache *et al*., [171,172]. The methodology applied and the results obtained from the validation of the mathematical model can be found in section B.4 of the appendix.

2.3.1.Base case

In Figure 2.4.A, the temperature at the reactor's central axis (r/R = 0) over time is depicted for varying values of the dimensionless axial coordinate (z/L). Upon initiating the reaction (t > 0), an increase in the reactor's temperature ($T_{reactor}$) is noticeable, a consequence of the reaction's exothermic nature.

This temperature starts to decrease when z/L > 0.02, attributable to the cooling system aimed to control the heat produced by the reaction. Furthermore, all temperature profiles in Figure 2.4.A reach a steady state (ss) at 74 s. The temperature profile along the reactor's central axis was also examined in Figure 2.4.B, as a function of z/L, for various values of t.

The presence of a hot spot was confirmed for different times. Moreover, the hot spot appears at z/L = 0.02 regardless of the time. This location, near the reactor's inlet, is a result of the significant amount of heat generated by the reaction ($\Delta H^{o}_{Rxn} = -165\ kJ/mol$). As can be seen in Figure 2.4.B, there is a noticeable rise in reactor temperature over time until it stabilizes. This is a result of the heat accumulation caused by the reaction. The highest temperature is 300 °C. Following this, the temperature consistently drops due to the cooling system's impact.

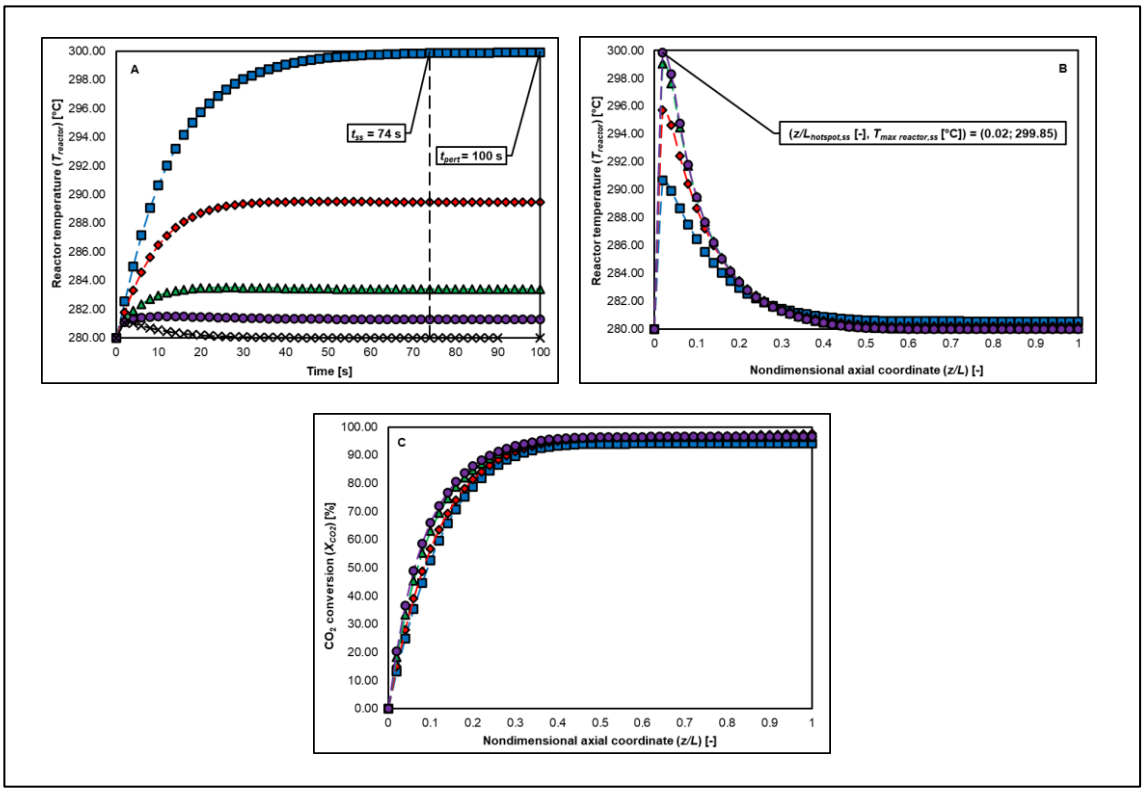

Figure 2.4. Temperature profile at centerline reactor (*r/R* = 0) with respect to time (**A**) and *z/L* (**B**). (**C**) CO_2 conversion, with respect to *z/L* at *r/R* = 0. Base case. Startup (**A**: *z/L* = 0.02, **B**: *t* = 10 s, **C**: *t* = 2 s; **A**: *z/L* = 0.10, **B**: *t* = 20 s, **C**: *t* = 6 s; **A**: *z/L* = 0.20, **B**: *t* = 40 s, **C**: *t* = 18 s; **A**: *z/L* = 0.30, **B, C**: *t* = 74 s; **A**: *z/L* = 1.00).

The steady-state temperature profile based on the z/L function is similar to that of Schlereth *et al*., [161], Schollenberger *et al*., [162], and Huynh *et al*., [156]. The hot spot's closeness to the reactor inlet is consistent with the results obtained by Schollenberger and the values calculated by Huynh when using their most active catalyst and an operating temperature of 300 °C. However, both studies considered the gas's preheating before it enters the reactor, which is a result of the solid's axial heat conduction. The differences in the maximum steady-state reactor temperature between these authors (425 – 500°C and 390 °C) and this study (300 ºC) can be attributed to the varying operating conditions, reactor sizes, and catalysts used in each case. As regards the outlet

temperature, the value achieved in this research matches the cooling temperature, which is also the case with the stainless-steel monolith presented by Schollenberger *et al*., [162].

Regarding the hot spot's location, although Schlereth *et al*.,'s study utilized identical reaction conditions, the hot spot's location is z/L = 0.13. The difference is attributed to the elevated GHSV value (5000 h^{-1} vs. 2130 h^{-1}) and the kinetic expression (Xu & Froment vs. Koschany) employed by these researchers. Concerning the hot spot temperature, (375 vs 300 °C), the difference is also a result of the increased spatial velocity, coupled with the higher pressure (3 bar) and inlet temperature (342 °C). According to Gao *et al*., [27] such parameters favor CO_2 methanation, leading to a rise in the reaction temperature (Huynh *et al*., [156]).

Figure 2.4.C shows the CO_2 conversion (X_{CO2}) profile. This increases with both time and distance along the reactor, culminating in a steady state condition after 74 seconds, with a value equivalent to 96.53 %. The X_{CO2} value at the reactor exit was compared to the one reported by Gao [27], confirming that it is the same for 1 atm, H_2/CO_2 = 4, and 280 °C. This suggests that the condition of chemical equilibrium in a steady state was attained under these conditions. This was also corroborated by achieving an equilibrium approach (φ_{eq}) value of one for z/L > 0.6 (Figure 2.4.C).

2.3.1.1.Response to the H_2 load variation

Figure 2.5.A and Figure 2.5.B demonstrate the impact of altering the H_2 feed flow (at t = 100 s, while keeping the H_2/CO_2 ratio constant) on the temperature profile computed along the reactor's central axis. When the H_2 load undergoes a 20 % reduction in a step functionality, a very slight decrease in the reactor temperature occurs, by 1 °C, until a new steady state is achieved at 144 s. No displacement of the hot spot was detected. This decrease in temperature is attributed to a lower release of heat of reaction, which in turn is explained by the decrease in the average reaction rate, $\overline{(r_1)}$, as shown in Figure B.3 and Figure B.4 of the appendix.

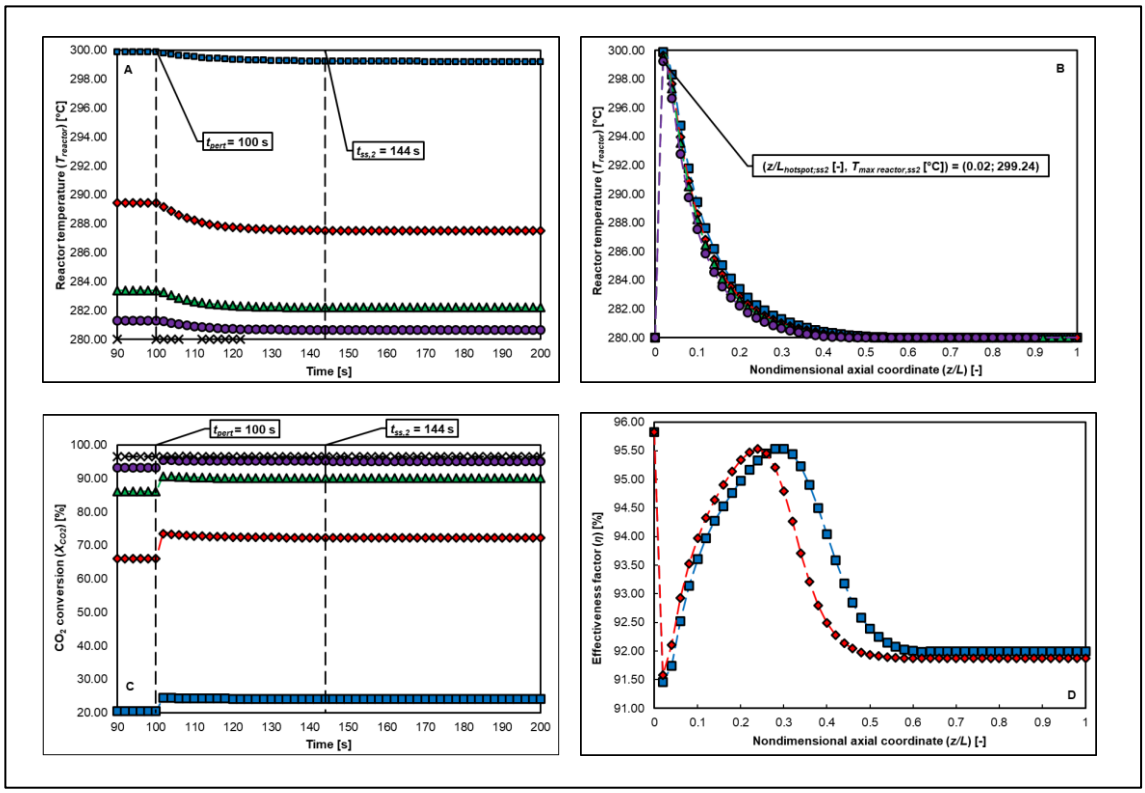

Figure 2.5. Comparison between the base case and the responses to a 20 % H_2 load fluctuation. **(A)** Temperature and **(C)** CO_2 conversion profile at *r/R* = 0 with respect to time. **(B)** Temperature profile as a function of *z/L* at *r/R* = 0. **(D)** Effectiveness factor profile at *r/R* = 0, with respect to *z/L* (**A, C**: *z/L* = 0.02, **B**: *t* = 100 s, **D**: first steady state; **A, C**: *z/L* = 0.10, **B**: *t* = 106 s, **D**: second steady state; **A, C**: *z/L* = 0.20, **B**: *t* = 110 s **A, C**: *z/L* = 0.30, **B**: *t* = 144 s; **A, C**: *z/L* = 1.00).

Same findings are reported by Lefebvre *et al*., [164]. It's worth noting that with the decrease of H_2 flow, a temporary minimum (Lefebvre *et al*., [164] and Try *et al*., [165]) or an increase in maximum reactor temperature (Fischer *et al*., [166,169]) were not detected under the conditions of this study.

This is attributed to the cooling system effectively countering the heat dispersed radially from the solid (a maximum difference of 12 °C between the center and the monolith wall) and the reduction in the gas's convective heat transport.

By reducing the H_2 flow, the total flow decreases (since the H_2/CO_2 ratio must be maintained). This results in an increment of the residence time of the fluid in the reactor, which in turn implies a higher conversion of the reactants. This is predominantly seen in the conversion curves of Figure 2.5.C, generated for the smaller values of $z/L < 0.3$, until a new steady state is achieved ($t_{ss,2}$ = 144 s).

Another key point to consider is that the steady-state values of X_{CO2} at the reactor exit ($z/L = 1$) remain unaffected by the disturbance in the H_2 flow. This is because the reaction re-establishes the chemical equilibrium condition when the new steady state is attained. (see Figure 2.4.B,Figure B.5 and Figure B.6). It is also noted that X_{CO2} have a similar trend (step) to that of the fluctuation in H_2 load over 100 s, aligning well with previously published results [166,167,169].

In this way, it was possible to observe the degree of complexity and sensitivity of the monolithic reactor to the fluctuation of the H_2 load, where although a nonlinear decreasing trend of the temperature concerning time was evidenced, the change of its maximum value at the location of the hot spot (1 °C) was not significant when the second steady state was recovered. A shift of the hot spot was also not witnessed for this study. All this may support the good thermal control of this reactor under fluctuating feed flow conditions. About the conversion, its change was also not considerable in the presence of H_2 flow perturbation, because of the good temperature control during the dynamic operation of the honeycomb monolith.

2.3.1.2.Mass transfer limitations

Firstly, it is important to note that no mass transfer limitations were evident on the catalyst surface. The maximum absolute percentage deviation of the mass compositions of both phases corresponds to CO_2 near the reactor inlet ($z/L = 0.02$), having a value around 2 %. When the H_2 load perturbation was generated, the value of this deviation practically did not change. The latter

was due to the surface area of the catalytic coating used, leading to the fact that the mass transfer limitation on the catalyst surface was not relevant for the case studies of this work.

Instead, as evidenced in Figure 2.5.D, the effectiveness factor falls a 4 to 8 % below 100 %, evidencing the presence of diffusional limitations within the catalyst, both in the first and second steady state.

It was observed that this parameter decreases immediately at the reactor inlet, as a consequence of the sudden increase of the hot spot temperature, which further favors diffusional limitations. Its subsequent growth is related to the decrease of the system temperature after the hot spot location, which caused the reaction rate to decrease as well (Figure B.3-Figure B.6). Then, a maximum value was reached, and the effectiveness factor subsequently decreased, due to the higher consumption of the reagents and the proximity to the chemical equilibrium condition of the Sabatier reaction. About the shift of the effectiveness factor profile concerning time towards a location closer to the reactor inlet, this was caused by the decrease of the system temperature due to the fluctuation of the H_2 load, where there is a higher effectiveness factor due to the reduction of diffusional limitations at locations close to the reactor inlet.

Therefore, it can be confirmed that although diffusional limitations are not negligible, they do not affect the dynamic performance of the monolithic reactor upon H_2 load fluctuation.

2.3.2.Study Case 1: Effect of Catalyst (Ni vs Ru)

Figure 2.6.A and Figure 2.6.B demonstrate that when the Ru catalyst developed by Falbo *et al*., [148] is applied in place of the Ni catalyst from Koschany *et al*., [146], the first steady state was attained quicker (68 s instead 74 s), and a greater maximum temperature was observed (362 °C rather than 300 °C).

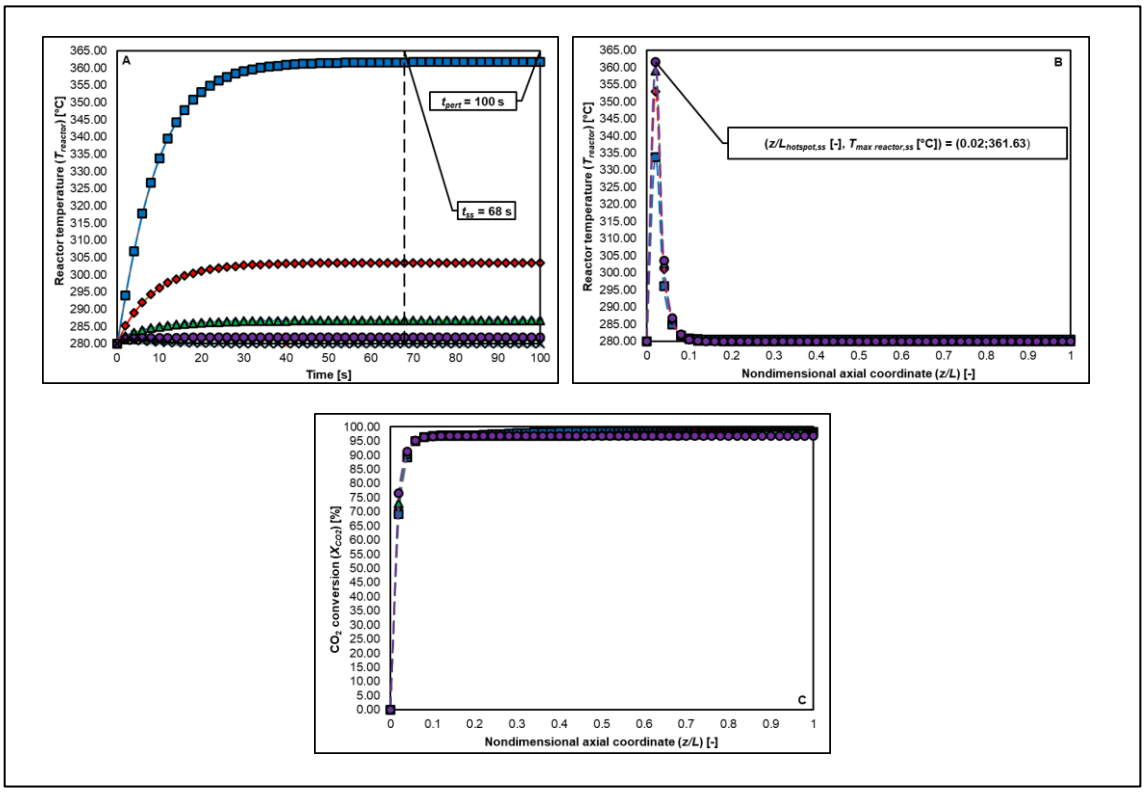

Figure 2.6. Temperature profile as a function of **(A)** time and (**B)** *z/L* at *r/R* = 0. **(C)** CO_2 conversion with respect to *z/L* at *r/R* = 0. Ru as the active phase of the catalyst (**A**: *z/L* = 0.02, **B**: *t* = 10 s, **C**: *t* = 2 s; **A**: *z/L* = 0.04, **B**: *t* = 20 s, **C**: *t* = 4 s; **A**: *z/L* = 0.06, **B**: *t* = 30 s, **C**: *t* = 6 s; **A**: *z/L* = 0.08, **B, C**: *t* = 68 s; **A**: *z/L* = 1.00).

These variations are due to the incremented average reaction rates associated with the Ru catalyst (Figure B.3-Figure B.6), as opposed to the rates calculated when Ni is used as the catalyst [146]. Consequently, this results in an increment of the heat released by the reaction.

Additionally, φ_{eq} = 1 (the system reaches the chemical equilibrium), and there are important effects of mass and heat transfer limitations. The CO_2 equilibrium conversion when using the noble metal catalyst is equal to when Ni is used (Figure 2.6.C). However, in the case of Ru, the equilibrium conversion was reached at a distance closer to the reactor inlet (*z/L* > 0.1), in contrast to that observed for Ni (*z/L* > 0.6).

As described in the existing literature [3,5,10–14], Ruthenium catalyst has a higher catalytic activity in contrast to Nickel catalyst. This was evidenced by the higher reaction rate of the Falbo's Ru catalyst (see Figure B.3-Figure B.6 of the appendix), which resulted in faster consumption of the reactants in contrast to what was observed in the base case, which is why the equilibrium conversion was reached at a distance closer to the reactor inlet. This resulted in a greater release of the heat of the reaction, causing a significant increase in the hot spot temperature at the reactor inlet. Additionally, as the reaction was terminated closer to the reactor inlet, the cooling medium was able to cool the rest of the monolith faster.

2.3.2.1.Response to the H_2 load variation

Utilizing Ru as a catalytic agent, the system attained a new steady state in 150 s, after the perturbation of H_2 load. The maximum temperature was reduced to 348 °C and there was no shift in the hot spot's position (Figure 2.7.A). X_{CO2} did not show a significant increase after the perturbation (Figure 2.7.B). Concerning the trend of temperature and X_{CO2} in function of time, behaviors like those of the base case were obtained, which are shown in Figure B.7 and Figure B.8 (section B.6 of the appendix).

With Ru serving as the catalyst's active phase, the time taken to regain the new steady state ($t_{rec,ss}$) post-disturbance (50 s vs 44 s) and the alteration in the reactor's peak temperature (14 °C vs 1 °C, post-disturbance) were greater compared to those of the Ni catalyst.

Although it can be concluded that the dynamic performance was lower for the Falbo catalyst because of the higher catalytic activity compared to the Koschany's catalyst, the recovery time of the new steady state was not much lower for these severe reaction conditions. This observation is consistent with previous reports suggesting superior stability [3,5,10–14] in response to H_2 load variations for the Ru catalyst.

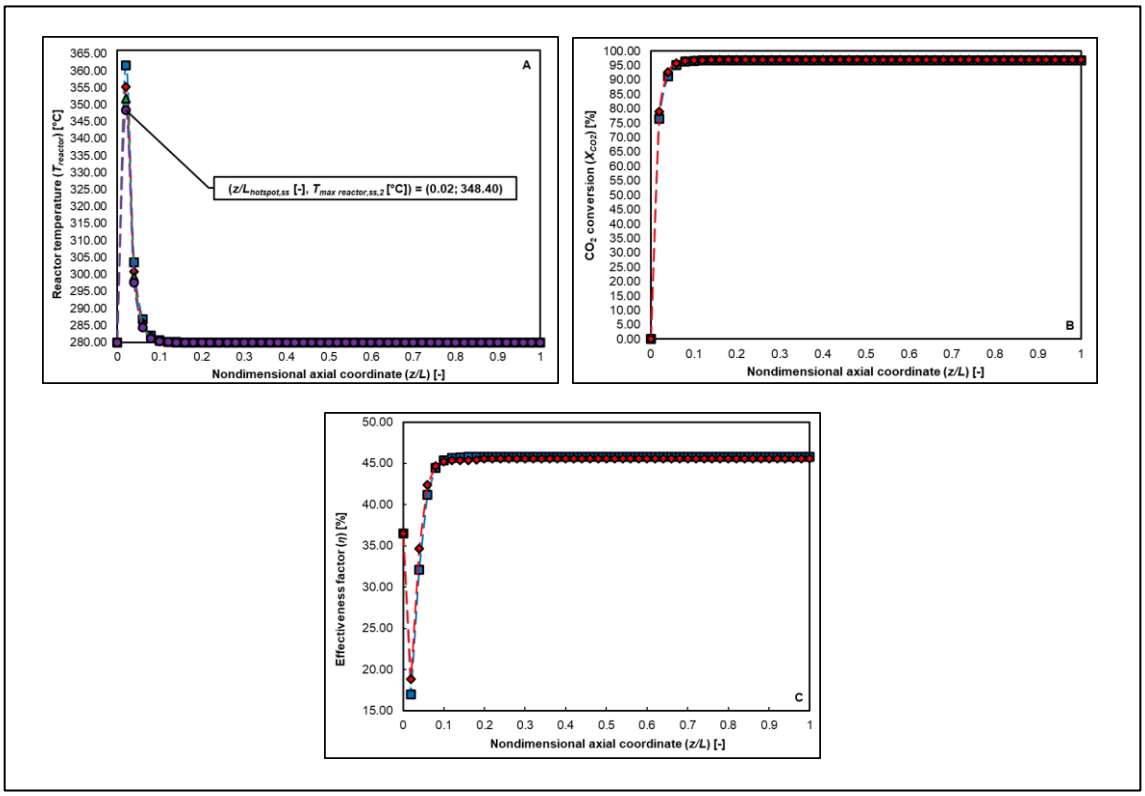

Figure 2.7. (**A)** Temperature and (**B)** CO_2 conversion profiles at *r/R* = 0 as a function of *z/L*. **(C)** Effectiveness factor profile at *r/R* = 0 in function to *z/L*. Ru as the active phase of the catalyst, after the H_2 load disturbance (**A, B**: *t* = 100 s, **C**: first steady state; **A**: *t* = 106 s, **B**: *t* = 150 s, **C**: second steady state; **A**: *t* = 112 s; **A**: *t* = 150 s).

Concerning the temperature change upon perturbation of the H_2 load, an important dependence on the level of reactivity of the catalyst is observed. Whereas the reaction rate increases, there will be a greater release of the heat of the reaction, causing the system to have a greater energy change upon the fluctuation of the H_2 flow. This generates a greater temperature gradient during the recovery of the new steady state.

About the X_{CO2} trend upon perturbation of the H_2 feed, this is again due to the chemical equilibrium condition, only that for this case study, the change is reflected closer to the reactor inlet compared to the base case, due to the higher reactivity of the Ru catalyst.

Therefore, the response of the monolithic CO_2 methanation reactor to the fluctuation of H_2 load shows a significant sensitivity to catalytic activity. However, for the applied conditions, the reactor showed a high dynamic stability, despite the temperature gradients caused by the high catalytic reactivity of Ru.

2.3.2.2.Mass transfer Limitations

In this case, interparticle mass transfer limitations become more important in contrast to the base case. The maximum absolute percentage deviation of the mass compositions of both phases corresponds to CO_2 near the reactor inlet (z/L = 0.02), having a value of 9 %. This is attributed to the effect of the higher temperature on the kinetic parameters. After H_2 fluctuation, the deviation is reduced to 7 %.

In Figure 2.7.C it is observed that the effectiveness factor is between 17 and 46 %, being much lower than the base case (83 - 96 %). This reflects significant diffusional limitations during reactor operation, due to the higher reactivity of the Ru catalyst.

As the H_2 load fluctuation was generated, this factor also increased due to the reduction of the reaction rate. In contrast to the base case, this effect was seen only at distances closer to the reactor inlet, because of the higher reagent consumption and the chemical equilibrium condition, which is rapidly reached. However, as in the base case, there was also no significant difference between the results obtained for the first and second steady state.

Because the equilibrium condition is reached at distances closer to the reactor inlet (z/L > 0.1) in contrast to the Koschany ‘s Ni catalyst (z/L > 0.6), a maximum does not occur as in the base case. Therefore, it was evidenced that, although the system is significantly limited by the diffusional

resistance in the catalytic washcoat, no significant change in the response of the reactor to the fluctuation of H_2 load was observed.

2.3.3.Study Case 2: Effect of H_2 Load Functionality (ramp vs Step)

Figure 2.8.A and Figure 2.8.B illustrate the variations in $T_{reactor}$ and X_{CO2} with the time (at r/R = 0) when a ramp fluctuation is applied to the H_2 load. A linear decrease of gas flow for 50 seconds, leading to a 20 % reduction was considered. As depicted in Figure 2.8.A, there is a gradual shift in the reactor's temperature paralleling the CO_2 conversion (Figure 2.8.B), which adheres to a linear trend. Upon concluding the ramp-like disruption (150 s), it can be seen that $t_{rec,ss}$ is reached 16 s ahead of that of the base case ($t_{rec,ss}$ = 44 s).

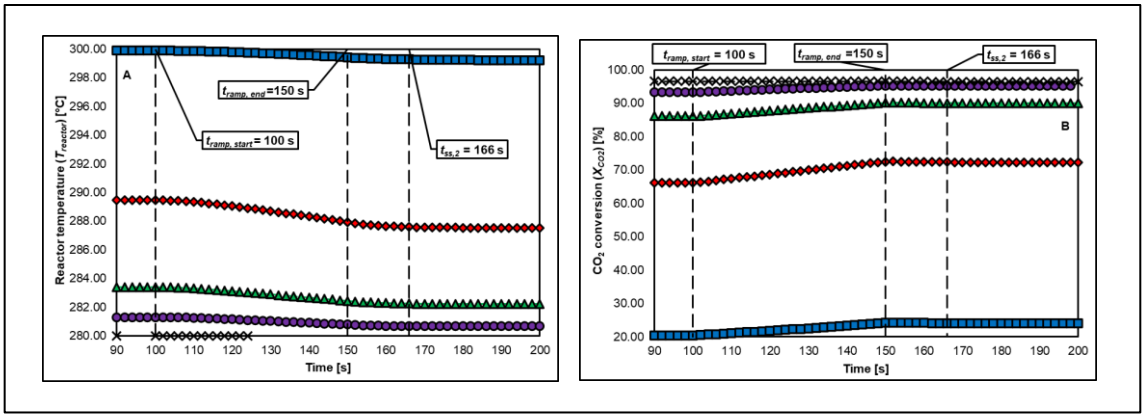

Figure 2.8. Temperature and (**B**) CO_2 conversion profile at r/R = 0, with respect to time. Ramp as a functionality of H_2 load (z/L = 0.02, z/L = 0.10, z/L = 0.20, z/L = 0.30, z/L = 1.00).

This corroborates the existing literature [168,171–174], which reports a quicker system recovery time, improved control over operational variables, and an appropriate response to this type of disturbance. Although, it's more plausible that sudden alterations (step) in the H_2 load might occur, given the intermittent nature of the renewable resources utilized in water hydrolysis H_2 [164–170].

Thus, it was proved with this study that the monolithic reactor can respond adequately to different fluctuations of the H_2 load, even to fluctuations that generate sudden changes, such as those evidenced in the case of a step-type perturbation.

2.3.3.1.Mass transfer Limitations

As in the base case, no mass transport limitations were evident on the catalyst surface either, as mentioned in section 3.1.2. The same effectiveness factor profile of the base case is obtained in function of *z/L*, since the second steady state is the same for both cases. The difference can be seen concerning the dependence of this factor in function of time, where for this case study, a linear trend is obtained between 100 and 150 s, for the functionality of H_2 load fluctuation.

2.3.4.Study Case 3: Effect of the Reactor Diameter

As shown in Figure 2.9.A, by using a larger diameter, 3.5 cm (Schollenberger *et al*., [162]), a more significant temperature increase was obtained, varying from 280 °C to 326 °C. It's also noteworthy that the hot spot was consistently located at *z/L* = 0.02, equal to the base case. The time to reach a steady state in this case was either equal to or more than 100 s, which is greater than the time necessitated by the 2.54 cm diameter monolithic reactor by Groppi *et al*., [186] and Schlereth *et al*., [161], of 74 s. As known, the resistance to heat transfer in the radial direction increases with the diameter, making it more demanding for the cooling system to manage the reaction heat's impact. This results in the reactor temperature rising more significantly compared to the base case, and the system requires more time to achieve a steady state due to higher energy accumulation. Regarding the X_{CO2}, the outlet of the reactor showed the same value as the base case, indicating that a chemical equilibrium state was achieved (Figure 2.9. B). It is also observed that for the case in which a diameter of 3.5 cm is used, a higher conversion is achieved at distances closer to the reactor inlet, in contrast to the base case. This trend is due to the thermal effects outlined in the previous paragraph also impact the rate of reaction, increasing with the reactor's diameter.

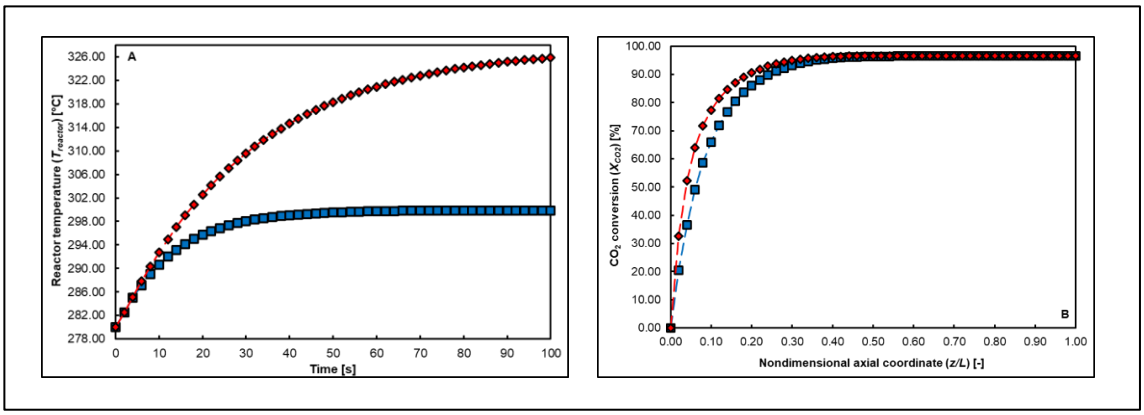

Figure 2.9. **(A)**Temperature as a function of time and **(B)** CO_2 conversion with respect to *z/L*. Profiles at *r/R* = 0. Effect of diameter in first steady state (**A:** Base case $z/L_{hotspot}$ = 0.02, **B**: Base case; **A**: *D* = 3.5 cm, $z/L_{hotspot}$ = 0.02, ***B***: *D* = 3.5 cm).

2.3.4.1.Response to the H_2 load variation

When a 3.5 cm diameter is used, the reactor's maximum temperature drops by 2.52 °C (Figure 2.10.A), and the time it takes for the new steady state to recover increases ($t_{rec,ss}$ > 200 s) due to the heightened limitation of energy transfer in the radial direction. For *z/L* values close to the reactor's exit (Figure 2.10.B), no changes in X_{CO2} were noticeable when the diameter value was altered as the chemical equilibrium condition had been met. In contrast, for *z/L* near the reactor inlet, a reduction of X_{CO2} is evidenced, due to the reduction of the temperature by the fluctuation of the H_2 load. However, this reduction was not significant, because the equilibrium condition is reached faster and there is a higher reagent consumption in contrast to the base case.

Therefore, the diameter not only has an important effect on the thermal and catalytic performance of the monolithic reactor but also has an important influence on the response of this equipment to the fluctuation of the H_2 load, whereby increasing this parameter, a longer recovery time of the system to reach a new steady state is evidenced. Additionally, it was observed that despite the use of a larger diameter than the base case, the system has a greater stability in its dynamic response compared to the case where a more reactive catalyst is used.

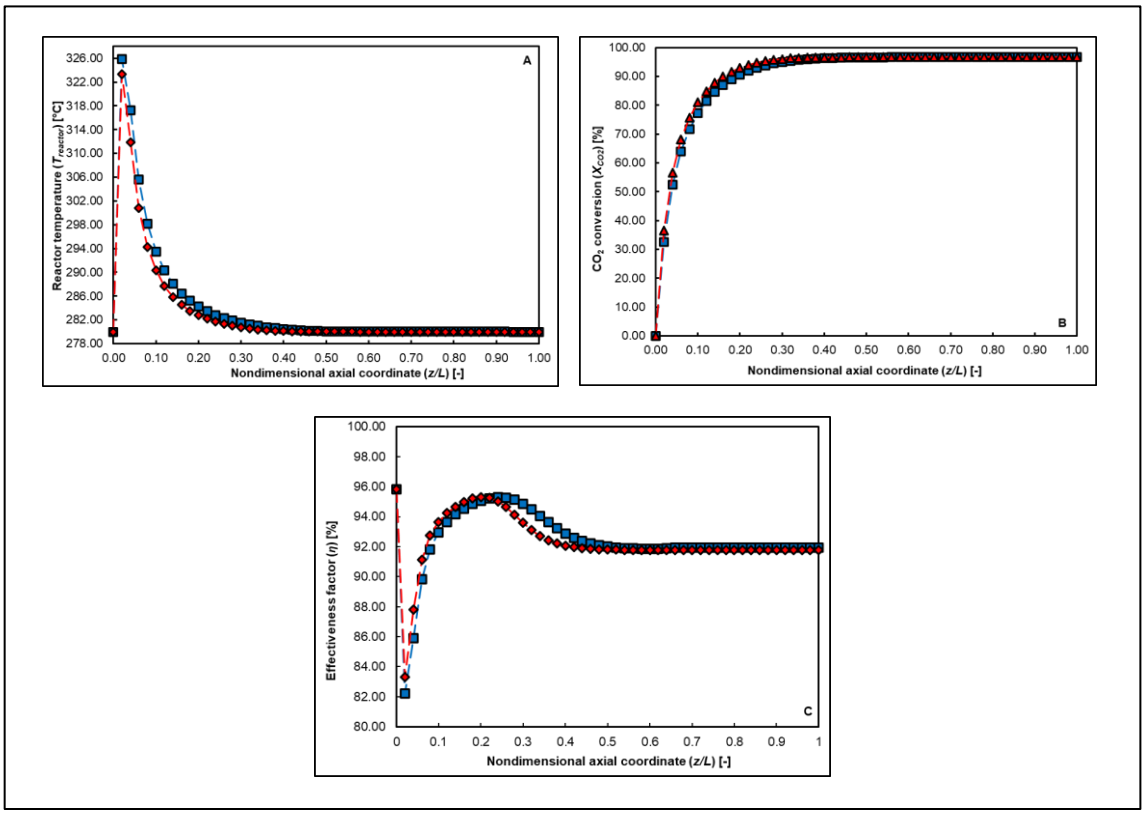

Figure 2.10. (**A**) Temperature, (**B**) CO_2 conversion and (**C**) effectiveness factor profile at r/R = 0 as a function of z/L. Effect of diameter after H_2 load fluctuation (First steady Second steady state).

2.3.4.2.Mass transfer Limitations

The maximum absolute percentage deviation of the mass compositions of both phases corresponds to CO_2, near the reactor inlet (z/L = 0.02), having a value of 3 %. This is attributed to the effect of the higher temperature on the kinetic parameters by increasing the diameter of the monolith. After H_2 fluctuation, the deviation is reduced to 2 %. While there is a greater effect of mass transfer limitation on the catalyst surface in contrast to the base case, it is not considered to be as significant as that observed in the case where a more reactive catalyst was used.

In comparison to the case where a diameter of 2.54 cm was used, in the case of the Figure 2.10.C a lower value of the effectiveness factor (82 %) is shown for *z/L* values closer to the reactor inlet, when using a diameter of 3.5 cm. This is caused by the higher temperature increase when using a larger diameter value, causing an increase in the reaction rate, and therefore generating greater diffusional limitations inside the catalyst. However, the same tendency of the base case is reflected when increasing *z/L*, caused by the same arguments mentioned in section 2.3.1.2. A final value of 92 % is obtained when the chemical equilibrium condition is reached.

About the dynamic response to the fluctuation of the H_2 load, the same tendency of the base case was also obtained, an increase of the effectiveness factor for *z/L* values close to 0, due to the reduction of the reactor temperature during the recovery of the second steady state. However, no significant change in this parameter was observed because of the H_2 flow perturbation, obtaining the same value of the effectiveness factor of the first steady state when the chemical equilibrium condition was reached. Thus, it was again confirmed that the diffusional limitations also had no significant effect on the dynamic response of the reactor to H_2 load fluctuation as the diameter of the monolith increased.

Conclusions

The honeycomb monolithic reactor offers a promising solution for the satisfactory performance of CO_2 methanation, demonstrating an appropriate response to the green H_2 load disturbance under varying operational conditions. The response of the monolithic CO_2 methanation reactor to the fluctuation of H_2 load shows a significant sensitivity to catalytic activity. However, for the applied conditions, the reactor showed a high dynamic stability, despite the temperature gradients caused by the high catalytic reactivity of Ru. In terms of the H_2 feed fluctuation functionality, the monolithic reactor exhibits adequate control and response to a step-type disturbance. However, improved results can be achieved in terms of thermal and dynamic stability, with a more moderate fluctuation of the H_2 load (e.g. ramp). Regarding reactor dimensions, increasing its diameter results in higher

thermal limitations, which negatively affects its dynamic response to H_2 flow fluctuation. Longer recovery time to the new steady state is required. On the other hand, no relevant effect of the effectiveness factor on the dynamic behavior of the reactor was observed since the variations of this parameter were not significant. In summary, this research contributes valuable data concerning the response and dynamic stability of the honeycomb monolithic reactor to the H_2 load disturbance. The findings can be viewed as useful information for subsequent studies related to the dynamic modelling of such reactors, which will provide a foundation for improved design, scaling, and application of this technology for the Sabatier reaction.

Chapter 3.

Dynamic behavior of a monolithic CO_2 methanation reactor to H_2 load disturbance. Experimental validation and theoretical comparison with fixed bed.

The information provided in this chapter will be submitted for publication.

ABSTRACT

The dynamic performance of a monolithic CO_2 methanation reactor was experimentally analyzed by changing the H_2 flow rate while maintaining a constant H_2/CO_2 ratio. The feed flow was suddenly increased by 50% after achieving the first steady state. This adjustment resulted in a rise in the peak gas temperature (hot spot) and CO_2 conversion until a new steady state was achieved. No significant temporal maximum or minimum in the hot spot were observed throughout the process, and its axial displacement was minimal. The experimental findings enabled the establishment of boundary conditions and thermal characteristics for a mathematical model, which qualitatively validated its capability to represent the experimental trends observed in both steady and non-steady state. The model, however, exhibited discrepancies in the temperature profile, particularly beyond the hot spot, and predicted CO_2 conversion rates higher than those observed experimentally. These differences arise from extrapolating the reaction rate to temperatures that fall outside the suitable range for the chosen kinetic expression. Furthermore, a parametric study confirmed that the predicted outcomes for temperature, CO_2 conversion, and the recovery time to a new steady state depend significantly on the radial thermal conductivity of the monolith and the heat transfer coefficient between the monolith and cooling medium. Once the model was experimentally validated, it was applied to forecast the dynamic behavior of the monolithic reactor

under conditions like those in selected fixed-bed reactor studies, demonstrating better dynamic stability during H_2 load disturbances.

Keywords: CO_2 methanation; H_2 load fluctuation; Honeycomb monolith; Reactor modeling; Experimental validation; Dynamic-thermal stability; Fixed-bed comparison.

3.1.Introduction

Power to Gas (PtG) technologies effectively reduce carbon dioxide (CO_2) emissions by converting it into methane (CH_4). The process starts with the electrolysis of water to produce hydrogen (H_2), which is then used in a thermal-catalytic process to hydrogenate CO_2, producing CH_4. This method is known as CO_2 methanation or the Sabatier reaction [2–9].

$$CO_{2_{(g)}} + 4H_{2_{(g)}} \leftrightarrow CH_{4_{(g)}} + 2H_2O_{(g)};\ \Delta H^{\circ}_{rxn} = -165\frac{kJ}{mol}$$

Nickel (Ni) is a common choice as catalyst in this reaction due to its ability to achieve high CO_2 conversion and acceptable CH_4 selectivity under optimal conditions, while also being more accessible and affordable than other metals [3,5,10–14]. However, the reaction's exothermic nature can cause reactor temperatures to rise excessively, potentially initiating secondary reactions that decrease CH_4 production and lead to sintering and coking, thus accelerating catalyst deactivation [3,5,10–14].

The primary technology to overcome these limitations uses fixed-bed adiabatic reactors with an intermediate cooling system. This approach is complex in design and operation, requiring substantial financial investment [2,4,6,10]. Catalytic evaluation studies indicate that monolithic reactors for CO_2 methanation have demonstrated excellent activity and stability [20,21]. This type of reactor is an appealing option for industrial applications due to its advantages over a fixed-bed

reactor. It offers a reduced pressure drop because of its parallel channel arrangement, provides a greater surface area for better mass and heat transfer, and has enhanced thermal characteristics [3,15–19]. Consequently, the reduction in maximum temperature within the reactor significantly addresses thermodynamic limitations and prevents the deactivation of the Sabatier reaction catalyst, offering a cost-effective and efficient technological solution [3,15–19].

In addition, when using green hydrogen, it's important to consider the temporal variations in hydrogen load due to the intermittent nature of renewable energy sources like solar and wind. These variations can affect the effectiveness of the Sabatier reaction within the Power to Gas (PtG) process [3,4,14,15]. A steady-state operation proposes storing enough hydrogen to ensure a constant supply. However, this results in higher costs and operational limitations because of hydrogen's low density [3,4,14,15]. Therefore, transient operation of the CO_2 methanation reactor is still recommended to ensure flexible operation and rapid adaptation to inevitable fluctuations in hydrogen load [3,4,14,15].

In line with the previous information, research has been conducted to examine the impact of varying H_2 load on the reactor's dynamic behavior. It is crucial to highlight that most studies maintained a constant H_2/CO_2 ratio (fluctuation of total feed flow) while establishing a new steady state. This approach was taken to prevent the side reactions' influence on the catalytic performance of the reactor. Research has been carried out to examine how reactors respond to variations in total feed due to multiple temporal changes [30,90,97,100], or ramp perturbations [20,72,92,117]. However, the dynamic response of the reactor to a sudden (step) change in gas inlet has been further examined. Conversely, while dynamic studies have been conducted on reactors such as the honeycomb monolith (HM) [20], plate heat exchanger (PHE) [67], and slurry bubble column (SBC) [72,73], the fixed bed (FXB) reactor is the most extensively researched in

terms of its dynamic behavior in response to changes in H_2 flow, with the H_2/CO_2 ratio remaining constant.

These investigations have examined the time-related aspects of reactor behavior during sudden changes in feed flow (Table 3.1). Try *et al*., [118] and Lefebvre *et al*., [73] identified a wrong-way behavior, marked by a temporary minimum or maximum in the reactor's highest temperature (hot spot) as the feed flow increases or decreases. This phenomenon is important because it can lead to thermal runaway, trigger the formation of side reactions, or result in the deactivation of catalysts [118].

Tauer *et al*., [105] also observed wrong-way behavior, noting that unlike previous research, the hot spot temperature increased when the feed flow suddenly rose. They also identified a temporary minimum during the transition to a new steady state. However, Fischer *et al*., [100,102] did not show wrong-way behavior when the feed flow unexpectedly increased, neither was this noted in either an adiabatic FXB [92], an isothermal SBC [73] or a PHE [67].

Regarding CO_2 conversion, this decreases with increased feed flow unless chemical equilibrium is reached. On the other hand, in the studied reactors, except for the isothermal SBC, the sudden increase in feed flow shifts the hot spot to locations farther away from the reactor inlet. Furthermore, the time needed for reactors to achieve a new steady state is influenced by factors like operating conditions (Table C.1), catalyst properties (Table C.2), and reactor dimensions (Table C.3), especially under adiabatic operation. Lastly, it's important to note that each type of reactor (FXB, SBC, PHE, and HM) displays different dynamic behaviors for their specific phenomenology.

Table 3.1. Transient characteristics of reactor dynamic response to sudden (step) changes in feed flow rate.

Reactor	Percentage of change [%]	Recovery time [s]	Maximum temperature		Location shift from inlet?	Type of CO_2 conversion change	Reference
			Greater or less than the first steady state after recovery?	Temporal maximum or minimum?			
FXB	+ 40.0	70	Less	Maximum	Yes, further away	Reduction	[118]
	- 40.0	70	Less	Minimum	Yes, closer.	Increment	[118]
	+ 700.0	120 (model) and 300 (experiment)	Greater	N/A (model) and minimum (experiment)	Yes, further away	Reduction	[105]
	- 87.5	120 (model) and 330 (experiment)	Less	N/A (model) and maximum (experiment)	Yes, closer.	Increment	[105]
	+ 10.0	218	Less	N/A	Yes, further away	Reduction	[102]
	- 10.0	78	Greater	N/A	Yes, closer.	Increment	[102]
	+ 100.0	540	N/A (Adiabatic)	Maximum	Yes, further away	N/A (Adiabatic)	[92]
	- 50.0	1440	N/A (Adiabatic)	Oscilating	Yes, closer.	N/A (Adiabatic)	[92]
	+100.0	112	Less	N/A	Yes, further away	Reduction	[100]
	-50.0	600	Greater	N/A	Yes, closer.	Increment	[100]
SBC	+ 33.3	18	Less	Maximum	Yes, further away	Reduction	[73]
	- 25.0	15	Greater	Minimum	Yes, closer	Increment	[73]
	+ 33.3	600	Greater	N/A	Isothermal	Reduction	[73]
	- 25.0	600	Less	N/A	Isothermal	Increment	[73]
PHE	+ 40.0	300	Greater	None	Yes, further away	N/A	[67]

Concerning the studies on dynamic modeling of HM, Perez-Vilela & García [20] research has been the only one known to date. It explored the impact of reducing 20 % of H_2 load while keeping a constant H_2/CO_2 ratio [20]. It revealed that using a catalyst with higher activity than Ni doesn't show hot spot movement or change in the recovery time to a new steady state (44 s). The reactor proved resilient to both gradual H_2 loading changes, like ramps, and sudden changes, such as step increases. In addition, the study showed that the time for the reactor to stabilize to a new steady state has an important dependence on the monolith's diameter. Moreover, although the hot spot temperature dropped due to a sudden decrease in total feed flow, no wrong-away behavior and hot spot location shift were observed. Finally, the CO_2 conversion did not change with total flow perturbation, because the reaction reached chemical equilibrium condition.

Pérez-Vilela & García demonstrated that HM shows significant promise for the dynamic operation of CO_2 methanation, mainly due to its excellent adaptability to changes in H_2 load. However, these conclusions have only been validated theoretically. To fill this gap, dynamic experiments with HM were conducted, to analyze and compare experimental trends with those predicted by the dynamic model of reactors used in the Sabatier reaction. This will provide experimentally confirmed insights into the dynamic behavior of the monolithic reactor under H_2 fluctuating conditions.

As mentioned, the FXB is the most studied in the literature on CO_2 methanation reactors. Thus, after validation, a mathematical model is used to compare the dynamic behavior of the monolithic HM and FXB reactor under H_2 loading changes. The parameters mentioned in Table 3.1 are used to compare both reactors. The same operating conditions, catalyst properties, reactor dimensions and hydrogen feed fluctuations used in selected FXB studies were applied for the comparative analysis.

3.2.Methodology

3.2.1.Experimental setup and dynamic test of Honeycomb Monolith Reactor (HMR)

3.2.1.1.Experimental setup

The experimental setup, depicted in Figure C.1, includes a reactor, a gas supply system for water vapor production, and a separation process. A stainless steel double-tube reactor was used for dynamic testing, featuring an inner tube with a 54.50 mm internal diameter and a 2.90 mm thickness. Inside, a honeycomb monolith made of corrugated and flat stainless steel plates was placed. The monolith's channels were coated with a commercial Ni/Al_2O_3 catalyst.

Feed gas passed through these channels, while a commercial thermal oil, acting as a cooling medium, flowed externally in the opposite direction. Two fiber optic probes were positioned within the monolith to monitor axial temperature (Figure 3.1), with one at the center and another near the honeycomb wall, taking measurements every 1.3 mm.

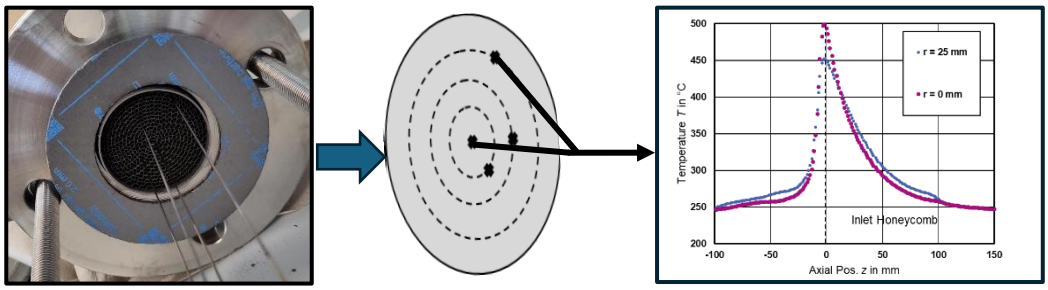

Figure 3.1. Measurement of axial temperature profile in center and wall of HMR

CO_2, H_2, and N_2 gases from pressurized cylinders were measured with a Bronkhorst mass flow controller to form the stream entering the reactor. A system was established to add water vapor to the reactor as needed. A valve could reroute the gas to bypass the reactor for composition analysis. The reactor's piping featured electric heating to raise the temperature of the pre-mixed

gases to match the reactor wall's temperature, adjustable via a regulator. A Julabo high-temperature thermostat regulated the temperature of the cooling medium. The reactor gases were cooled to 3 °C using a water-cooled heat exchanger, causing condensation. The water was then removed with a centrifugal separator. The pipes connecting the reactor to the heat exchanger were electrically heated to prevent early condensation. Following water removal, the test apparatus's pressure was regulated using a Bronkhorst valve, which established the reactor's operating pressure. A portion of the gas was analyzed for its components using an Agilent micro-GC by reducing the product gas pressure to atmospheric levels. The micro-GC was calibrated to identify elements including CO_2, H_2, N_2, CH_4, CO, C_2H_4, C_2H_6, and C_3H_8.

3.2.1.2.Dynamic test

Table 3.2 details the sizes and characteristics of the equipment used. During the dynamic experiment, each species' initial concentrations and the reactor's gas temperature matched those of the inlet flow. After reaching the first steady state (t = 0 s), a sudden increase of 50 % was introduced to the inlet flow as a step (ramp over 0.001 s).

Table 3.2. Dimensions and properties of HMR

Parameter	Value
Channel geometry	Sinusoidal (Figure 7 and Figure C.3)
Internal diameter [mm]	50
External diameter [mm]	53
Length [mm]	90
CPSI [cells / in^2]	200
Gas gap [µm]	750
Substrate thickness in cell [µm]	110
Washcoat thickness [µm]	10-50
Specific surface area of catalyst [$m^2_{catalyst\ surface}$ /$m^3_{reactor}$]	1465
Gas volumetric fraction [m^3_{gas}/$m^3_{reactor}$]	0.82
Catalyst volumetric fraction [$m^3_{washcoat}$/$m^3_{reactor}$]	0.04
Substrate material	Stainless steel
Catalyst load [$kg_{catalyst}$/$m^3_{reactor}$]	110.6

Table 3.3 presents experimental values for the H_2/CO_2 ratio, gas pressure (P_{gas}), inlet space velocity ($GHSV_{inlet}$), and the cooling medium temperature (T_{cool}). A copper coating was applied to the monolithic reactor, to remove the thermal resistance effect of the gas in the monolith-inner tube gap. Gas was routed through a fabric packing before entering the reactor to enhance flow distribution and preheat the gas.

3.2.2.HMR Modeling

A detailed mathematical model from Pérez-Vilela & García was used [20]. The model is full-scale, transient, two-dimensional, axially symmetric, and heterogeneous.

Table 3.3. Operation conditions.

Parameter	Value
H_2/CO_2	4/1 (5 % molar N_2)
P_{gas} [bar] (constant)	8 bar
$GHSV_{inlet}$ [1/h]	1800 and 2700
T_{cool} [ºC]	240

This model considered the restrictions of internal and external mass transfer within the catalytic layer of the channels due to their potential impact on reactor performance [36]. Additionally, the model integrated the effects of interparticle thermal transfer resistance in the coating and the gas' axial heat/mass dispersion within the channels. Unlike the catalyst particles in the FXB reactor, the HMR catalyst washcoating generally does not exhibit an intraparticle temperature gradient due to its smaller size [3,15–20,22,36–42]. However, despite the isothermal nature of the catalyst in the HMR, significant temperature gradients exist within the monolith substrate, both axially and radially [18–20,22,36–42]. Lastly, the assumptions, averaged governing equations, initial/boundary conditions, constitutive equations, and physical properties correlations can be consulted in Pérez-Vilela & García [20].

3.2.2.1.Numerical resolution

Figure 3.2 shows the resolution domain of HMR with evenly spaced elements in the *z-r* plane. This domain is governed by equations for gas conservation and solid energy balance within the selected mathematical model. In this type of reactor, the catalytic washcoating is primarily isothermal, meaning that the model treats the solid as a combination of both the washcoating and the monolith substrate [3,15–20,22,36–42]. It is also seen that each element consists of a one-dimensional equispaced subdomain, governed by the mass conservation equation of the catalytic washcoating.

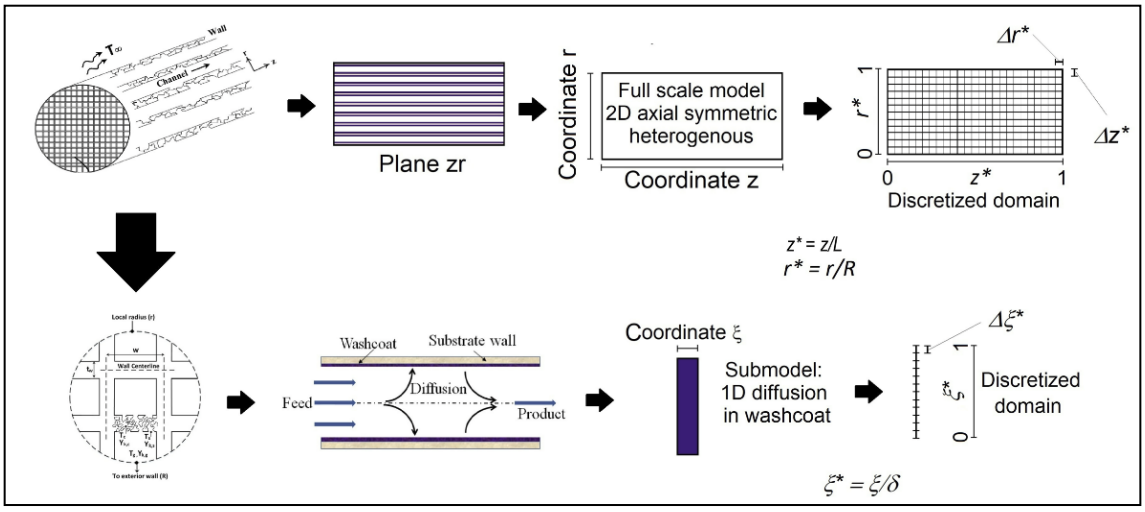

Figure 3.2. Mathematical model resolution domain.

The numerical approach from Pérez-Vilela & García [20] was applied to discretize the conservation equations and boundary conditions to solve the partial differential equations system in the resolution domain. The Matlab ode15s subroutine to solve the differential equations system with initial value problem was used, incorporating initial and operational conditions, reactor dimensions, the reaction rate expression, feed flow fluctuations, constitutive equations, and the gas' physical

properties correlations. The integration step can change depending on the time interval utilized. It's important to emphasize that the default precision of the ode15s subroutine must be maintained.

3.2.3.Experimental validation of the HMR mathematical model

To validate the mathematical model of the HMR, a numerical simulation was conducted using the previously established model. This simulation used the same operating conditions and reactor sizes as detailed in the experimental test from section 3.2.1.2. In this case, the priority was to consider the application range of the selected kinetics in contrast to the thermodynamic restrictions [27]. Moreover, the sintering temperature for Nickel should not exceed 590 °C [28,187].

The fluctuation was directly applied to the total feed flow. After reaching the initial steady state, the total feed was abruptly increased by 50%. Finally, the system was deemed to have achieved a new steady state when the temperature difference between two consecutive times at each reactor location fell below 0.1 °C. This value is lower than the maximum (1-2 °C) and average (0.20-0.30 °C) temperature difference observed in the experiment.

3.2.3.1.Adaptation of boundary conditions to experimental trends.

The radial position affects the HMR inlet temperature profile due to preheating upstream. The reactor entrance temperature also varies over time because of the experimental setup's load change and temperature fluctuations. Thus, developing a function linking the inlet temperature with the radial coordinate and time within the HMR is crucial. It is also necessary to apply the same methodology for the temperature derivative at the outlet of the HMR, due to the temperature fluctuations in the experimental setup and the cooling of the gas in the section downstream of the HMR outlet. The axial derivative of the solid's outlet temperature will match the expression derived from the axial derivative of the gas temperature at that location. At the same time, the adiabatic condition at the inlet will remain applicable for the solid phase. Choosing between Dirichlet and

Danckwerts boundary conditions for the reactor inlet composition depends on the Peclet number. It is assumed that there are no composition gradients at the reactor outlet. A pressure value is implemented at the reactor exit. Lastly, with the reactor inlet pressure established, the velocity at this location can be determined using the equation of state.

3.2.3.2.Reaction rate

The research employed a commercially available Ni catalyst. Also, Schollenberger *et al.,* [23,189] utilized this catalyst and developed a corresponding rate law (r_1), which adheres to the power law model (Equation 3.1). For this reason, this expression was used in this work.

Schollenberger's kinetic expression ($200 \leq T[°C] \leq 300;\ 2 \leq P[bar] \leq 17$)

$$r_1 = kp_{CO_2}{}^{0.47} p_{H_2}{}^{0.54} \left(1 - \frac{p_{CH_4} p_{H_2O}{}^2}{\underbrace{p_{CO_2} p_{H_2}{}^4 K_{eq}}_{\varphi_{eq}}}\right); \qquad k\left[\frac{kmol}{kg_{cat} \cdot s \cdot bar^{1.01}}\right] = 9.98 \cdot 10^2 exp\left(-\frac{84\ kJmol^{-1}}{R_{gases} T[K]}\right); \qquad (3.1)$$

The reaction effectiveness factor was calculated using its formal definition from Equation 2.28 considering the characteristic length of the catalytic washcoating within the channels [40,183–185]. Additionally, when there were significant temperature changes in the reactor, the heat of the reaction was determined using its formal definition from Equation 2.29.

3.2.3.3.Radial thermal conductivity of solid

To validate the model, Schollenberger's formula [189] (Equation 3.2) was used instead of Equation B.6 to determine the radial thermal conductivity of the solid ($\lambda_{radial,s}$). This decision was made because the Schollenberger equation was specifically designed for the same reactor type used in the study, which features sinusoidal channels rather than square ones.

$$\lambda_{radial,s} = \lambda_{radial,eff} \cdot \frac{sin(\gamma + 60°) + sin(\gamma + 120°)}{sin(60°) + sin(120°)} + \lambda_{sup} \frac{d}{b} sin(\gamma);$$

$$\lambda_{radial,eff} = \frac{1}{2R_1 + R_2 + \frac{R_3}{2}} = \frac{1}{2\left(\frac{d}{2b\lambda_{sup}}\right) + \left(\frac{2\delta_{\lambda_{radial,s}}}{d\lambda_g}\right) + \frac{1}{2}\frac{b}{d\lambda_{sup}}} \quad 3.2$$

This formula, based on an analysis of thermal resistance [189], is influenced by the design parameters *d*, *b*, *γ*, and $\delta_{\lambda_{radial,s}}$. Detailed information regarding these parameters is available in section C.3. The experimental data establishes fixed values for d and b at 110 µm and 1.85 mm, respectively. There is no available information regarding the value of *γ*. In this study, the assumption is made that *γ* is 0°, meaning that $\lambda_{radial,s} = \lambda_{radial,eff}$. The parameter $\delta_{\lambda_{radial,s}}$ has a value that lies between 0 and 50 µm, where the maximum value corresponds to the maximum thickness of the catalytic washcoating.

3.2.3.4.Heat transfer coefficient of solid – cooling medium

Glockner [190] also used the same type of reactor as this study. These authors used a rigorous equation (Equation 3.3) to calculate the heat transfer coefficient of the monolith-cooling medium (U_{sc}), considering the thermal resistances of the monolith wall, monolith gap, inner tube wall, and cooling medium.

$$U_{sc} = \frac{1}{R_{monolith\ wall} + R_{gap} + R_{inner\ tube} + R_{coolant}};$$

$$R_{monolith\ wall} = \frac{Monolith\ internal\ radius}{\lambda_{monolith\ wall}} \cdot ln\left(\frac{Monolith\ external\ radius}{Monolith\ internal\ radius}\right);\ R_{gap} = \frac{monolith\ gap}{\lambda_{substance\ inside\ gap}}; \quad 3.3$$

$$R_{inner\ tube} = \frac{Monolith\ internal\ radius}{\lambda_{inner\ tube}} \cdot ln\left(\frac{Inner\ tube\ external\ radius}{Inner\ tube\ internal\ radius}\right);\ R_{coolant} = \frac{1}{U_{coolant}} \cdot \frac{Monolith\ internal\ radius}{Inner\ tube\ external\ radius}$$

The monolith's gap is covered by copper instead of gas ($\lambda_{substance\ inside\ gap} = \lambda_{cupper}$). The dimensions of the monolith and inner tube are known. To calculate the thermal conductivities of the monolith wall and inner tube, the Glockner correlations [190] were used. Regarding the heat transfer coefficient of the cooling medium, its value is around 200 W/(m^2°C).

3.2.3.5.Influence of $\lambda_{radial,s}$ and U_{sc} on results predicted by the HMR mathematical model.

To reduce the discrepancy between the model's forecasted temperature profile and experimental data, the value of $\delta_{\lambda_{radial,s}}$ was adjusted to range between 0 and 50 µm. Moreover, the temperature profile at the monolith wall may significantly differ between model predictions and experimental data due to the computed U_{sc} value during simulations. To address this, altering the $U_{coolant}$ value, which contributes the most variation compared to other thermal resistances, is recommended.

3.2.4.HMR vs. FXB: Analysis of dynamic behavior for both reactors during CO_2 methanation.

After validation, the mathematical model was used to compare the dynamic behavior of the HMR reactor with that of FXB reactor under fluctuating green H_2 loads. With this purpose, three modeling studies of FXB reactors, proposed by Tauer et al., [105], Fischer et al., [102], and Lefebvre et al [73] were selected as case studies for this comparison.

To effectively compare the HMR and FXB reactors, identical operating conditions (Table C.1), catalyst properties, reaction rate expression (Table C.2), and reactor dimensions (Table C.3) were applied in both scenarios. Furthermore, the same pattern of temporal variation in feed flow (Table 3.1) was implemented.

Tauer *et al*., [105]'s study was picked as the first choice, because their findings show "wrong-way" behavior. As a second study case, Fischer *et al*., [102]'s work was selected as the initial comparison point because their model did not exhibit "wrong-way" behavior when the feed flow

was altered. Lastly, Lefebvre *et al.*, [73]'s research was chosen as a third option, as it displayed wrong-way behavior, manifesting a temporal minimum and maximum with decreasing and increasing flow rates.

It is also crucial to mention that, unlike experimental validation, the boundary conditions from Pérez-Vilela & García model [20] were applied, as they align with the conditions of the above mentioned studies selected for comparison. To compute $\lambda_{radial,s}$, equation B.6 is used because of the square geometry of the HMR channels. Moreover, a constant U_{sc} value is set, matching the one required to achieve the same peak temperature of the FXB reactor.

From literature concerning catalytic evaluations of HMR for the Sabatier reaction, the catalyst volume fraction in experimental studies ranges from 0.013 [158] to 0.031 [24,155]. In contrast, simulations show a range from 0.04 [189,190] to 0.134 [20,22]. These values are lower compared to those used in FXB, which range from 0.518 to 0.612 (as shown in Table C.2). This discrepancy arises because, in FXB, the catalyst particles occupy more space within the reactor, unlike the catalytic coatings in HMR. Consequently, the catalyst loading in HMR is much lower, ranging from 11 [24,155] to 500 [18] kg/m^3, compared to 630-1475 kg/m^3 in FXB (refer to Table C.2). Therefore, this parameter cannot be matched for both reactors in the comparative studies. Values for CPSI (from 26 [20,22] to 2063 [157]), catalytic washcoating size (from 2 [157,158] to 200 [20,22]) and substrate thickness between channels (from 50 [158] to 612 [20,22]) are selected to obtain the highest possible catalyst loading of the HMR in the comparative studies.This approach allows for a comparison of the recovery time to a new steady state, the final maximum reactor temperature, the new location of the HMR hot spot, and final CO_2 conversion after a change in feed flow. These results can then be compared with values from selected studies of the FXB reactor under specific operating conditions.

3.3.Results and Discussion

3.3.1.Dynamic test of HMR

As mentioned in sections 3.2.3.3 and 3.2.3.4, this study utilized the same reactor as in Schollenberger [189] and Glockner [190], making their experimental results a key point of comparison for analyzing the experimental results of this work.

The experiment revealed that the reactor reached a new steady state in 281 seconds after feed flow fluctuation (Figure 3.3). The maximum temperature at the monolith center (T_{max}) was around 446 °C in the first steady state, like Glockner [190]'s findings (450 ºC with 1800 h^{-1})

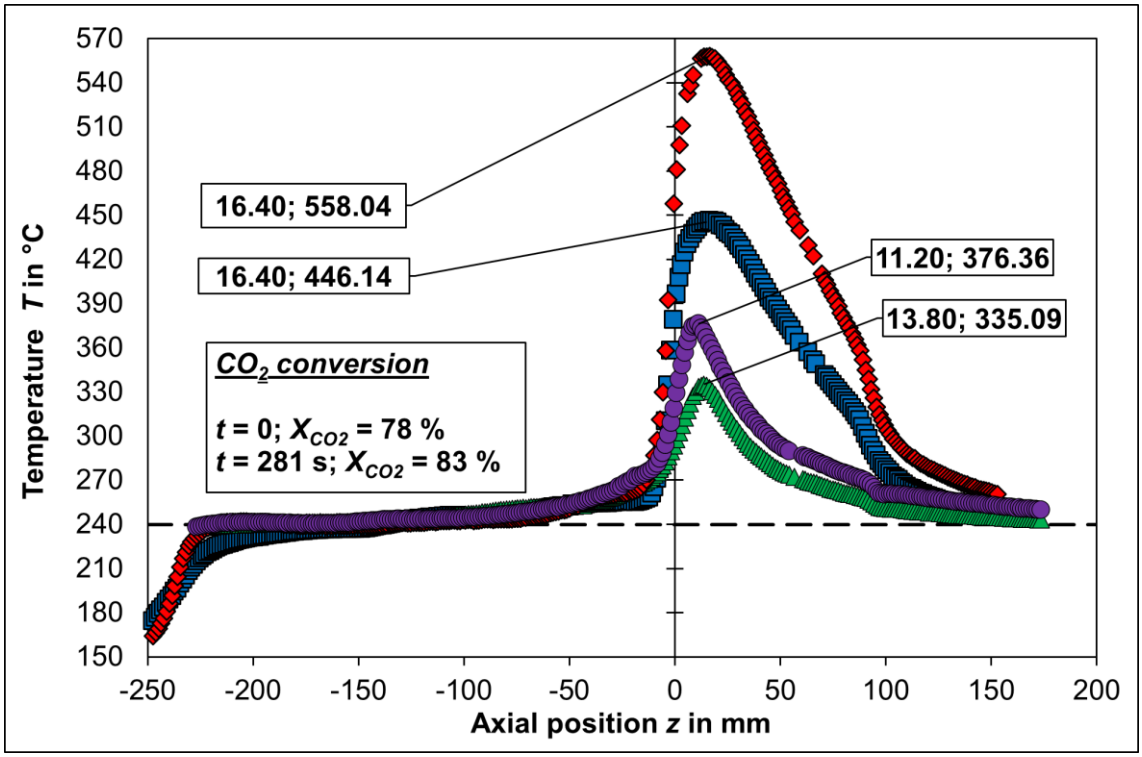

Figure 3.3. Axial temperature profile at 0 and 281 s. Experimental data at the center and the reactor wall. ■ Center, first steady state (t = 0 s). ◆ Center, second steady state (t = 281 s). ▲ Wall, first steady state (t = 0 s). ● Wall, second steady state (t = 281 s). ▬ Cooling medium temperature.

However, the location of the hot spot (z_{Tmax}), positioned 16 mm ahead compared to the entrance location noted by Schollenberger [189] and Glockner [190]. The cooling post-hot spot was more gradual than in previous observations. Additionally, CO_2 conversion (X_{CO2}) was lower, at 78%, compared to Schollenberger's 80% and Glockner's 82%, both measured at a GHSV of 1800 h^{-1}. Regarding the reactor's dynamic behavior, a sudden increase in feed flow led to a rise in T_{max} from 446 to 558 °C, enhancing X_{CO2} from 78 to 83%.

3.3.1.1.Analysis of experimental results at steady state

The behavior of axial profile of gas temperature (T_g) at the center and wall of the monolith matches with that observed by Schollenberger [189] and Glockner [190] (results of these authors are presented in section C.4). Regarding the values of T_{max} and z_{Tmax}, there are deviations between the values obtained in this work and those reported by Schollenberger [189] and Glockner [190]. These differences may arise from measurement deviations due to axial conduction through the protective capillary, significant non-uniformity of the catalyst within the monolith channels between $0 < z < z_{Tmax}$, and variations in the phenomenological aspects of heat transfer within the monolith in both axial and radial directions [189].

For the first steady state, the reduction in T_g after z_{Tmax} at $r = 0$ mm was less than what Glockner observed for a 100 mm monolith with a GHSV of 1800 h^{-1}. This is due to T_g at the reactor's exit being about 302 °C, higher than Glockner's 263 °C. The reduced cooling effect is linked to both the reactor length of 90 mm compared to 100 mm, and the unique heat transfer characteristics of the monolith. This, combined with thermal behavior and possible uneven catalyst distribution in the monolith channels, led to a lower X_{CO2} of 78%, compared to the 80-82% reported by other authors for the same GHSV of 1800 h^{-1}, with a different z_{Tmax} value.

3.3.1.2.Analysis of the dynamic response of HMR to feed flow fluctuation

Increasing the GHSV from 1800 to 2700 h^{-1}, while keeping a constant H_2/CO_2 ratio, resulted in a rise in T_g throughout the reactor over time (Figure 3.4).

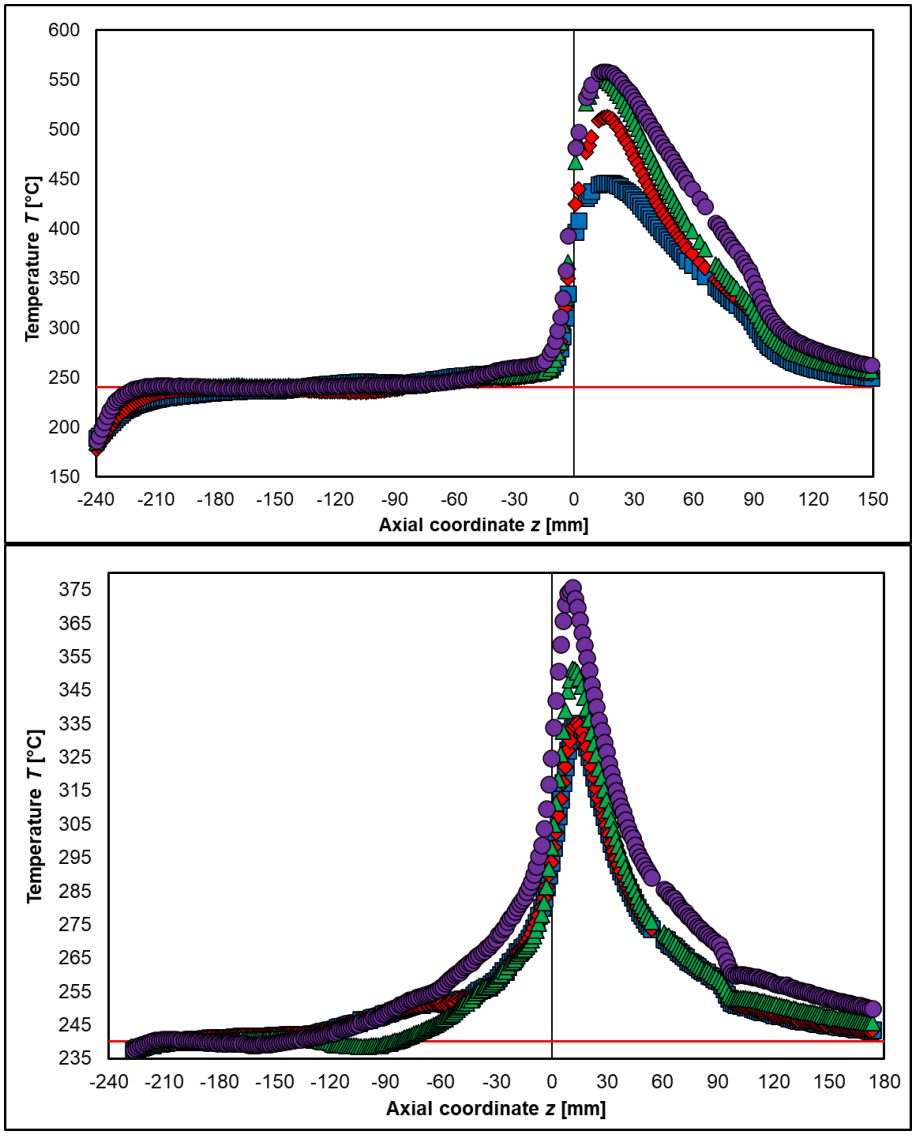

Figure 3.4. Axial temperature profile for different times in center (top) and wall (bottom) of HMR. ■ t = 0 (first steady state), ◆ t = 40 s, ▲ t = 80 s, ● t = 281 s (final steady state). ▬ Cooling medium temperature.

Although increased gas velocity led to intensified convective heat transport and reduced residence time, these did not counteract the increased reaction heat, due to more reactants entering GHSV = 2700 h^{-1}.

Moioli *et al*., [67] identified a similar trend with the increment of feed flow, observing that T_{max} moved further away from the reactor inlet after this fluctuation. This shift was attributed to an increase in convective heat transport, resulting in delayed reactor activation and increased heat transfer from the cooling medium.

Therefore, unlike previous studies by Try *et al*., [118], and Lefebvre *et al*., [73], this experiment did not show a temporal maximum in T_{max}. There was also no evidence of a temporal minimum or decrease, contrary to findings by Tauer *et al*., [105] and Fischer *et al*., [100,102] respectively. In summary, the experiment showed no wrong-way behavior. Moreover, as reported in earlier studies, there was no shift in hot spot location. Lastly, it was found that from a stationary perspective, T_g increased with the GHSV, consistent with the results of Schollenberger, Glockner, and Moioli.

3.3.2.Adaptation of HMR Model to Experiment Results

Several key factors were considered to validate the mathematical model's accuracy during the analysis of experimental outcomes:

I) The simulation was focused on the range from z = 0 mm to z = 90 mm to reduce computational costs, as temperature temporal changes at the reactor's inlet and outlet are already known (Refer to section C.2 for the full HMR experimental diagram).

II) Therefore, a function was developed to describe the T_g profile at the reactor's inlet, varying with time and the radial coordinate. This was also applied to the derivative of T_g at the reactor's exit.

III) At the reactor entrance, recorded Peclet numbers were close to 40, indicating an intermediate amount of dispersion within the reactor [191]. As a result, the Danckwert condition was applied to the inlet composition.

IV) In the experiment, the pressure drop was negligible, thus a pressure drop of 0.001 kPa was considered in the simulation.

3.3.2.1.Inlet temperature and axial gradient of outlet temperature

Figure 3.5 displays the experimental inlet temperature (T_{inlet}) profile for r = 0 (center) and r = 25 mm (wall).

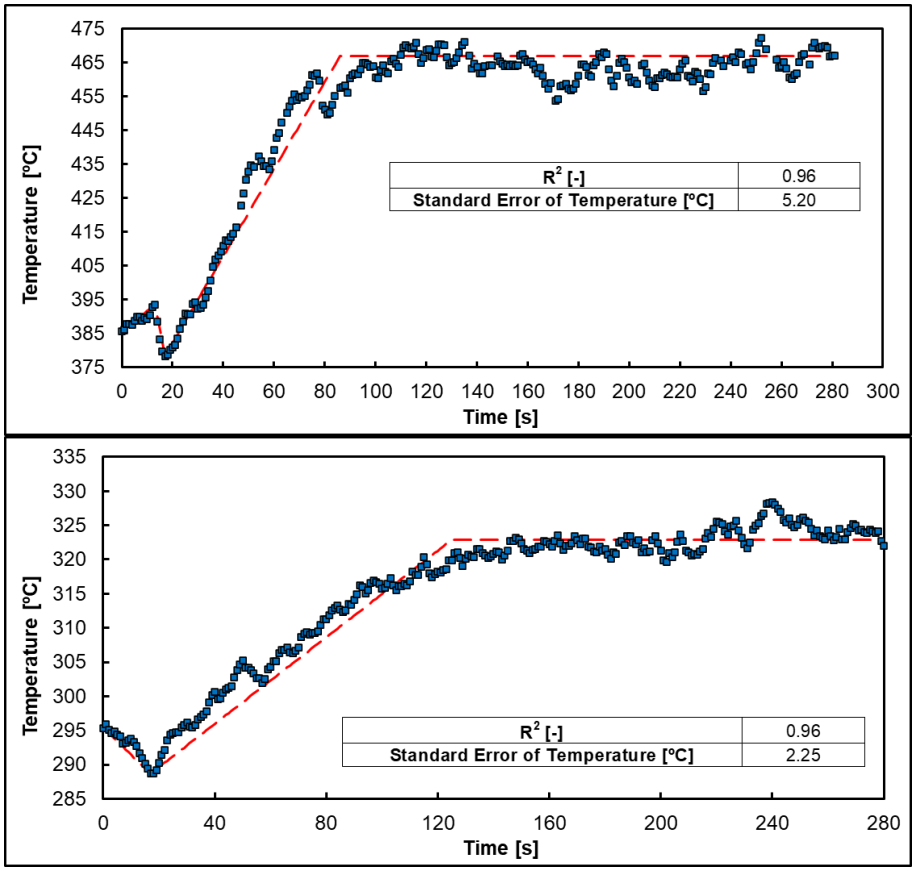

Figure 3.5. Inlet temperature profile for different times in center (top) and wall (bottom). ■ Experiment, - - - Model.

The experimental T_{inlet} data correspond closely with the fitted functions shown by the red curves in Figure 3.5, attaining a coefficient of determination (R^2) of 0.96. It is important to mention that T_{inlet} rises over time because the heat of the reaction increases, driven by the accumulation of reactants at the inlet during fluctuations.

The axial gradient of the gas temperature at the reactor outlet ($\partial T/\partial z_{outlet}$) decreases over time, showing that the gas cools more rapidly as it exits the HMR (Figure 3.6). This accelerated cooling is due to the increased temperature difference between the gas and the cooling medium, resulting from the rise in gas exit temperature following the disturbance in the feed flow. The fitted functions used to represent $\partial T/\partial z_{outlet}$ closely match the experimental data, with R^2 values between 0.97 and 0.98.

3.3.2.2.Functionality of T_{inlet} and $\partial T/\partial z_{outlet}$ in relation to time and the radial coordinate

After examining the trends for T_{inlet} and $\partial T/\partial z_{outlet}$ over time, a relationship was established regarding the radial coordinate. Unlike Schollenberger [189] and Glockner [190]'s investigations, there was no data on the axial temperature profile for radial positions other than the center and wall of the HMR. Therefore, a symmetric parabolic profile for T_{inlet} and $\partial T/\partial z_{outlet}$ was assumed, peaking at $r = 0$. This led to the formulation of the T_{inlet} and $\partial T/\partial z_{outlet}$ as function of both radius and time, expressed in Equation 3.4.

$$T_{inlet}(r,t) = T_{inlet,center}(t) + \left(T_{inlet,wall}(t) - T_{inlet,center}(t)\right)\left(\frac{r}{25\ mm}\right)^2$$

$$\left.\frac{\partial T}{\partial z}\right|_{outlet}(r,t) = \left.\frac{\partial T}{\partial z}\right|_{outlet,center}(t) + \left(\left.\frac{\partial T}{\partial z}\right|_{outlet,wall}(t) - \left.\frac{\partial T}{\partial z}\right|_{outlet,center}(t)\right)\left(\frac{r}{25\ mm}\right)^2 \quad 3.4$$

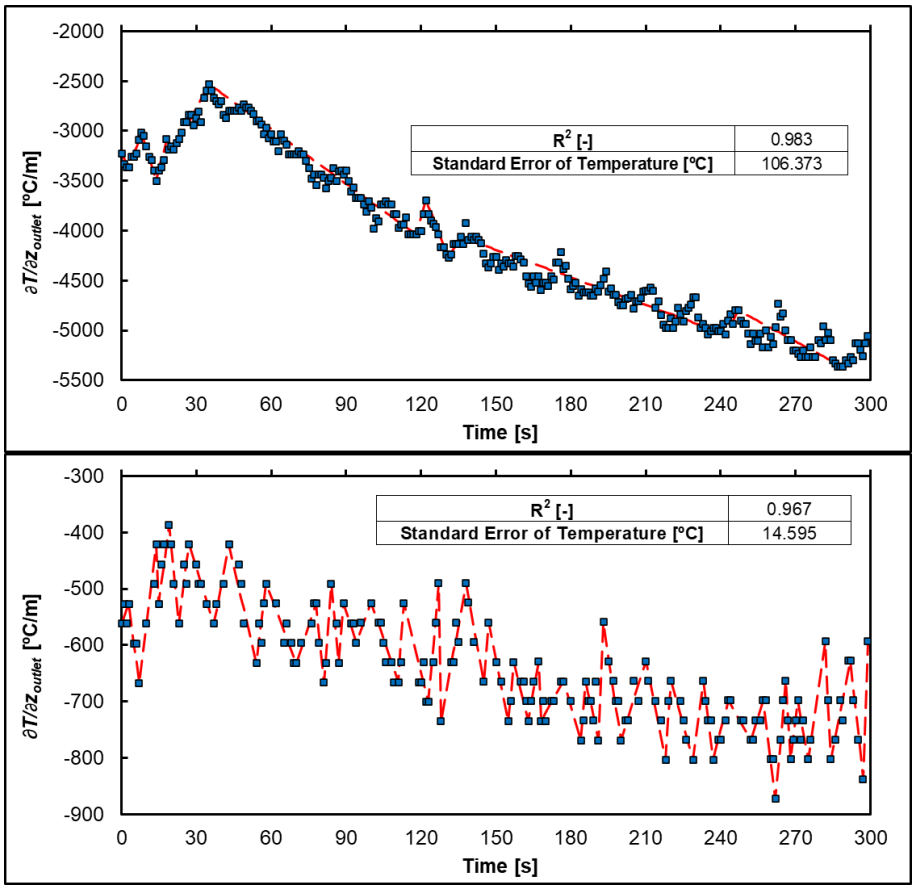

Figure 3.6. Axial gradient in outlet temperature for different times. Center (top) and wall (bottom). ■ Experiment, - - - Model.

3.3.3. Validation of the HMR mathematical model

A theoretical validation of the mathematical model of the HMR was presented in Pérez-Vilela & García research [20]. The model's solutions are unaffected by the number of elements in axial and radial directions, or by the number of subintervals in the mass balance resolution domain within the catalyst.

3.3.3.1.Effect of $\delta_{\lambda_{radial,s}}$ and $U_{coolant}$ on results predicted by the model

To ensure temperatures exceed 240 °C at both the reactor center and wall, $\delta_{\lambda_{radial,s}}$ (Figure C.3) must be at least 10 μm, and $U_{coolant}$ should be 125 W/(m²°C) maximum. These conditions are essential to counteract the cooling influence at the reactor outlet. Figure 3.7 illustrates the influence of $\delta_{\lambda_{radial,s}}$ values on the gas temperature profile in both steady states, with a $U_{coolant}$ of 125 W/(m²°C).

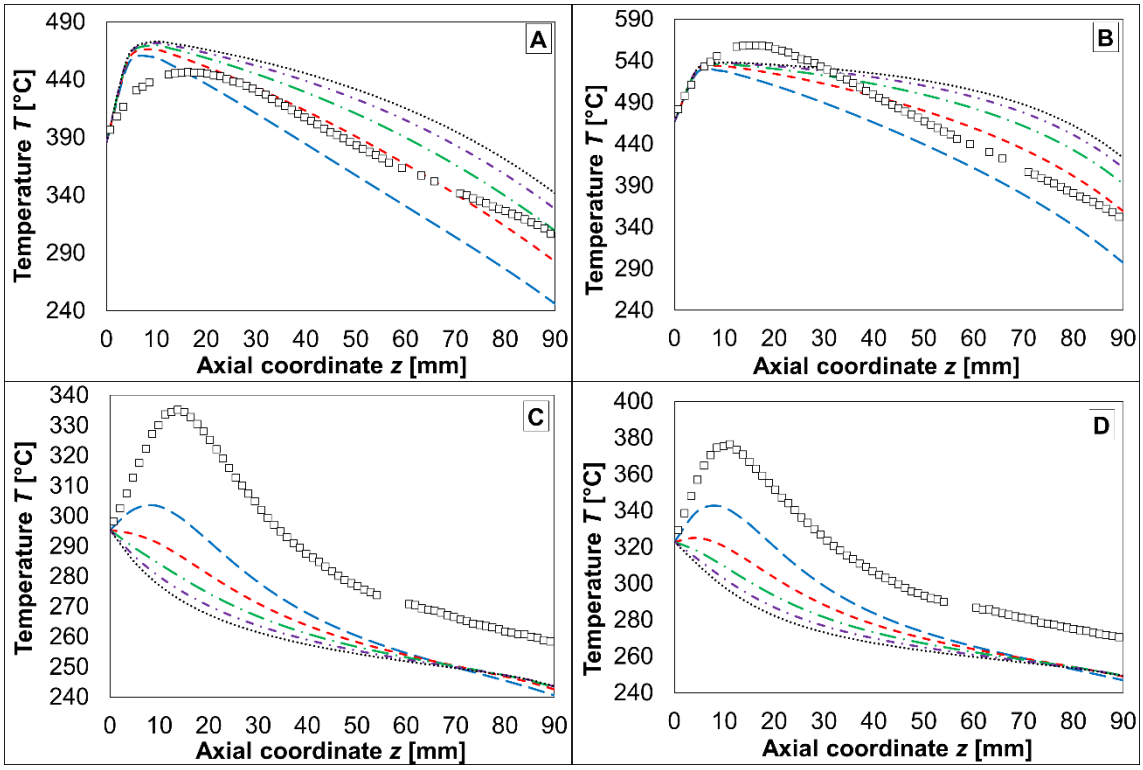

Figure 3.7. Effect of $\delta_{\lambda_{radial,s}}$ on temperature profile, with $U_{coolant}$ = 125 W/(m²°C). Center (A, B) and wall (C, D) of HMR. First (A, C) and second (B, D) steady state. ▬▬ $\delta_{\lambda_{radial,s}}$ = 10 micron, ▬ ▬ $\delta_{\lambda_{radial,s}}$ = 20 micron, ▬▬▬ $\delta_{\lambda_{radial,s}}$ = 30 micron, ▬ ▬ ▬ $\delta_{\lambda_{radial,s}}$ = 40 micron, ··· $\delta_{\lambda_{radial,s}}$ = 50 micron, □ Experiment.

In Figure 3.7.A-B, as $\delta_{\lambda_{radial,s}}$ increases, the center temperature rises. This occurs because $\lambda_{radial,s}$ decreases with higher $\delta_{\lambda_{radial,s}}$ values, which means the solid's thermal resistance increases.

Consequently, heat, from the Sabatier reaction, accumulates. Concerning the wall temperature (Figure 3.7.C-D), its decrease is noticeable. When $\lambda_{radial,s}$ decreases, the heat transferred to the surroundings diminishes, indicating that the cooling effect is confined to areas near the wall, rather than throughout the entire reactor as operationally desired.

Figure 3.8. A-B shows that reducing $U_{coolant}$ leads to an increase in the center temperature in both steady-state conditions. This is because the cooling medium becomes less effective to counteract the heat generated during CO_2 methanation. However, this temperature increase is not as significant as the increase observed when $\delta_{\lambda_{radial,s}}$ is raised.

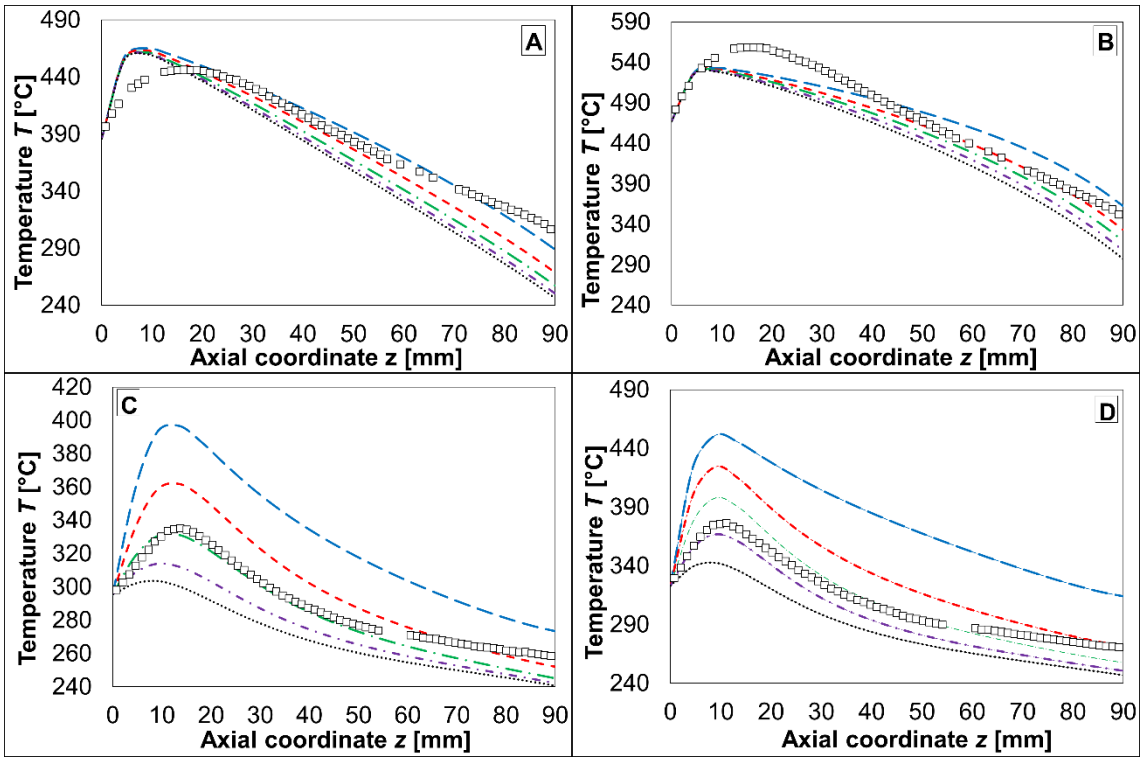

Figure 3.8. Effect of $U_{coolant}$ on temperature profile, with $\delta_{\lambda_{radial,s}}$ = 10 µm. Center (A, B) and wall (C, D) of HMR. First (A,C) and second (B, D) steady state. ▬ ▬ $U_{coolant}$ = 25 W/(m²°C), ▬ ▬ $U_{coolant}$ = 50 W/(m²°C), ▬▪▬ $U_{coolant}$ = 75 W/(m²°C), ▬ ▪ ▬ $U_{coolant}$ = 100 W/(m²°C), ··· $U_{coolant}$ = 125 W/(m²°C), □ Experiment.

On the other hand, decreasing the $U_{coolant}$ significantly affects the wall temperature. This happens because the thermal resistance of the cooling medium increases. Therefore, the temperature gradient between the monolith wall and the medium increases, resulting in substantial radial heating of the HMR due to the heat of reaction, especially in locations near the monolith wall.

Table 3.4 highlights the differences between the model's predicted outcomes and the actual experimental results for various $\delta_{\lambda_{radial,s}}$ values. When $\delta_{\lambda_{radial,s}}$ is set to 20 μm, the results show the lowest errors, along with the greater R^2 value. However, accurately predicting the maximum reactor temperature is crucial to avoid exceeding the catalyst's sintering temperature. A $\delta_{\lambda_{radial,s}}$ of 10 μm provides the least discrepancies between predicted and actual maximum temperatures, except at the HMR center during the second steady state.

Table 3.4. Deviations between model predictions and experimental results. Effect of $\delta_{\lambda_{radial,s}}$, with $U_{coolant}$ = 125 W/(m²°C).

$\delta_{\lambda_{radial,s}}$ **[μm]**	10	20	30	40	50
R^2 **[-]**	0.89	0.93	0.90	0.87	0.84
Standard error [°C]	28.94	24.66	31.64	37.87	42.45
Average relative error [%]	7.48	6.20	7.99	9.54	10.60
Relative error of maximum temperature in HMR center [%]					
First steady state	0.24	2.46	3.80	4.59	5.11
Second steady state	7.35	5.37	4.54	4.11	3.86
Relative error of maximum temperature in HMR wall [%]					
First steady state	10.50	14.29	16.37	17.70	18.63
Second steady state	9.63	15.37	18.35	20.19	21.45

Table 3.5 compares the predicted model outcomes with experimental results after varying $U_{coolant}$, using $\delta_{\lambda_{radial,s}}$ = 10 μm. As shown in Figure 3.8 C-D, the smallest average relative and standard errors, along with the highest R^2 value, were achieved for a $U_{coolant}$ of 75 W/(m²°C).

Table 3.5. Deviations between model predictions and experimental results. Effect of $U_{coolant}$ with $\delta_{\lambda_{radial,s}}$ = 10 µm.

$U_{coolant}$ [W/(m²°C)]	25	50	75	100	125
R^2 [-]	0.68	0.93	0.95	0.93	0.89
Standard error [°C]	42.43	20.86	18.22	23.09	28.94
Average relative error [%]	10.50	4.66	3.83	5.60	7.48
Relative error of maximum temperature in HMR center [%]					
First steady state	2.11	1.15	0.47	0.03	0.24
Second steady state	5.61	6.27	6.64	7.02	7.35
Relative error of maximum temperature in HMR wall [%]					
First steady state	18.28	7.91	1.23	6.96	10.50
Second steady state	19.62	12.14	5.29	2.89	9.63

Regarding the maximum deviation of the center temperature, the smallest deviation was observed during the initial steady state with $U_{coolant}$ at 100 W/(m²°C), although this deviation increased in the subsequent steady state as $U_{coolant}$ increased. A notable benefit is the reduction of maximum temperature deviation at the HMR wall, with the lowest values occurring at 75 and 100 W/(m²°C) during the first and second steady states, respectively.

As shown in Figure 3.8 C-D, the smallest average relative and standard errors, along with the highest R^2 value, were achieved for a $U_{coolant}$ of 75 W/(m²°C). Regarding the maximum deviation of the center temperature, the smallest deviation was observed during the initial steady state with $U_{coolant}$ at 100 W/(m²°C), although this deviation increased in the subsequent steady state as $U_{coolant}$ increased. A notable benefit is the reduction of maximum temperature deviation at the HMR wall, with the lowest values occurring at 75 and 100 W/(m²°C) during the first and second steady states, respectively.

By performing parametric studies using a $U_{coolant}$ value of 75 W/(m²°C) with varying $\delta_{\lambda_{radial,s}}$ values, and a $\delta_{\lambda_{radial,s}}$ of 20 µm with different $U_{coolant}$ values, these studies confirmed that these specific

values again reduce the discrepancy between the model's predictions and the experimental results. Considering the outcomes discussed earlier, a $\delta_{\lambda_{radial,s}}$ of 20 µm and a $U_{coolant}$ of 75 W/(m^2°C) were used to verify the model. Table 3.6 shows the differences between the model's predictions and the experimental results using these parameters. By applying these values, discrepancies between the model's predictions and experimental results are minimized, as evidenced by a reduced average relative error and standard error, as well as a higher R^2 value compared to those in Table 3.4 and Table 3.5.

Table 3.6. Deviations between model predictions and experimental results. $U_{coolant}$ = 75 W/(m^2°C) and $\delta_{\lambda_{radial,s}}$ = 20 µm.

R^2 [-]	0.97
Standard error [°C]	15.40
Average relative error [%]	3.37
Relative error of maximum temperature in HMR center [%]	
First steady state	1.42
Second steady state	2.45
Relative error of maximum temperature in HMR wall [%]	
First steady state	4.11
Second steady state	0.11

Although the deviations in maximum temperatures aren't the smallest, especially regarding the initial steady-state wall temperature, the model accurately forecasts the peak temperature at the reactor's center, which is the highest during the reaction. These values also allow for precise prediction of the highest outlet temperature at the HMR's center. These trends can be observed in Figure 3.9 as described in the following section.

3.3.3.2.Validation of the model: Steady state.

Figure 3.9 compares the model's outcomes with experimental findings, showing a similar axial temperature profile to that of studies by Glockner [190] and Schollenberger [189]. The model

reflects an initial rise in T_{gas}, followed by cooling along the reactor, with the central reactor area being hotter than the monolith wall. The T_{max} values predicted by the model, although not perfectly match the experimental HMR values, they are considered as satisfactory with discrepancies in the range of 0 and 4 %. As can be appreciated in Figure 3.9, the position of z_{Tmax} at r = 0 differs for both steady states, with the model showing it closer to the inlet compared to the experimental data (9 vs 16.40 mm). The model also predicts a slower cooling process at the center of the HMR, aligning with Glockner and Schollenberger's findings. At r = 25 mm, the difference between the model and experimental T_{max} is larger during the first steady state.

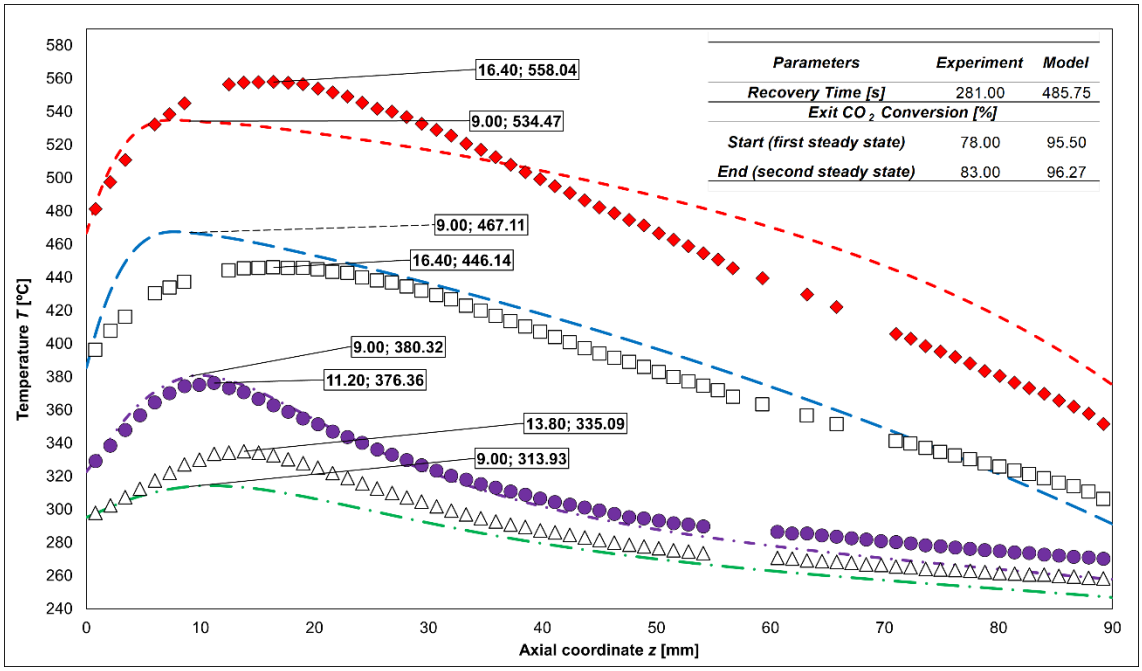

Figure 3.9. Model validation, with $\delta_{\lambda_{radial,s}}$ = 20 µm and $U_{coolant}$ = 75 W/(m²°C). Experiment (points) and model (lines). □ Center (first steady state), ◆ Center (second steady state), △ Wall (first steady state), ● Wall (second steady state). ▬ Center (first steady state), ▬ Center (second steady state), ▬ Wall (first steady state), ▬ Wall (second steady state).

Like Glockner [190], the discrepancies between the model's predicted values and the experimentally measured temperatures for the HMR center and wall could be due to the model's

limitations to capture the true thermal behavior of the HMR. Furthermore, the model does not account for the possible non-uniform distribution of the catalyst within the monolith channels, which can also significantly influence the prediction of temperature profiles.

On the other hand, the X_{CO2} values calculated at the reactor outlet (Figure 3.9) represent the radial average at z = 90 mm for any given time. The X_{CO2} predicted by the model is higher due to Schollenberger's reasoning, which suggests that his mathematical model calculates reaction rates that are higher than those found in experimental observations. This discrepancy arises from extrapolating the reaction rate for temperatures exceeding 300 °C, leading the model to forecast a higher X_{CO2} at the reactor's exit. Additionally, this accounts for the model's prediction of the hot spot being nearer to the reactor inlet, contrary to what is observed experimentally.

3.3.3.3.Validation of the model: Dynamic response to load fluctuation.

Figure 3.10.A-C show a very good prediction of the increase in T_{gas} after a disturbance in the feed flow. The higher reactant concentration at the monolith entrance leads to more energy accumulation, raising T_{gas} due to increased heat release during the reaction until a new steady state is reached.

The conversion of CO_2 near the wall (Figure 3.10.D) is reduced due to the lower temperature, which slows down the reaction process and consumption of reagents. An increase in load resulted in a reduction in CO_2 conversion at the center of the HMR (Figure 3.10.B), consistent with previous research of FXB reactor [73,100,102,105,118].

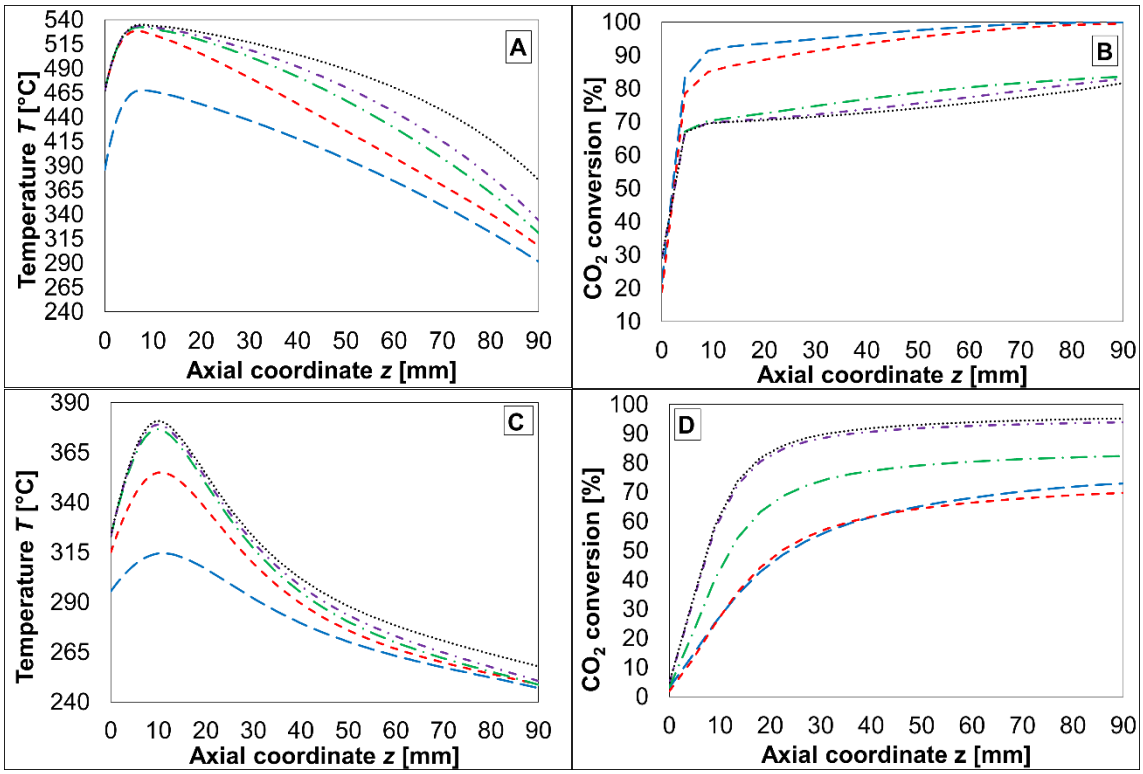

Figure 3.10. Model validation, with $\delta_{\lambda_{radial,s}}$ = 20 µm and $U_{coolant}$ = 75 W/(m²°C). . ▬ ▬ t = 0 s, ▬ ▬ t = 100 s (A, C) and t = 50 s (B, D), ▬ ▪ ▬ t = 200 s (A, C) and t = 100 s (B, D), ▬ ▪ ▪ ▬ t = 281 s, ··· t = 485.75 s.

However, the conversion increased over time at the wall, even reaching a temporal minimum. In the center, a shorter residence time decreased reagent consumption. Nevertheless, at the wall, increased convective heat transfer did not compensate for the rise in reaction rate due to reagent accumulation in the inlet reactor, leading to an increment in temperature and CO_2 conversion as time progressed. This explains the reason for the observed increase in average CO_2 conversion at the outlet. This finding is consistent with the experimental results obtained in this study and aligns with the research conducted by Schollenberger [189] and Glockner [190] on the HMR.

Therefore, the mathematical model accurately reflects the steady-state behavior of the HMR, similar to Schollenberger [189]and Glockner [190]'s research findings. However, like these

authors, there are differences between the model's predictions and experimental observations, suggesting that further improvements to the model are necessary for more precise results.

Nonetheless, the developed model predicts outcomes with a deviation of 1-4% compared to experimental data and accurately represents the behavior of the HMR. More revelant, the proposed model correctly simulates the HMR's dynamic response to feed flow changes, contributing to the dynamic analysis of CO_2 methanation reactors.

As a result, the model is considered fully validated both, theoretically and experimentally, enabling its use in future HMR research (e.g., design, parametric studies), as Schollenberger and Glockner did in their studies on this reactor type following experimental validation.

3.3.4.HMR vs. FXB: Analysis of dynamic behavior for both reactors in the Sabatier reaction

As a explained in section 3.2.4, following experimental validation, the mathematical model was used to evaluate the HMR's response under the same operating conditions as those of three selected dynamic FXB studies [73,100,105]. The evaluation results of HMR were compared based on recovery time to a new steady state, final maximum reactor temperature, new HMR hot spot location, and final CO_2 conversion.

Stainless steel was selected for the HMR due to its common use in FXB reactors. This decision ensures that the monolithic substrate's physical and thermal properties, especially thermal conductivity, do not affect the HMR model's results across the three case studies.

Besides, a 200 CPSI HMR with a substrate thickness of 110 μm between channels is used, like the stainless-steel monolith used by Schollenberger [189] and Glockner [190]. These

specifications are chosen for their capability to create a large gas volume fraction, achieving 0.86 and 0.88 for sinusoidal and square channels, respectively.

Based on the above, a catalyst coating thickness of 200 μm was employed, as in the works of Schlereth [22] *et al*., and Pérez-Vilela & García [20], to maximize the catalyst volume fraction. This resulted in a catalyst volume fraction of 0.3685 in a square channel HMR, achieving the maximum catalyst loading possible for this reactor type. However, as mentioned in section 3.2.4, this catalyst load remains lower than what is achieved with the FXB reactor.

3.3.4.1.HMR vs. FXB: Operation conditions of Tauer *et al.,*

Figure 3.11 shows that as the feed flow increased from 27 to 217 h^{-1}, the temperature at the center of the HMR also rose over time. The peak temperature within the HMR increased from 190 to 193 °C. A U_{sc} value of 56 W/(m^2°C) was adjusted to achieve these results. On the other hand, Tauer *et al.,* [105].'s model forecasted a change from 192 to 193 °C for FXB. Additionally, the position of the highest temperature within the HMR shifted, now extending from 4.4 to 11 cm, which is further from the reactor inlet compared to both the experimental data (4.17 to 5.26 cm) and the forecasts by Tauer *et al.,* [105] (1.46 to 2.31 cm) in the FXB reactor. Furthermore, the recovery time for the new steady state in the HMR was 253 s, which is longer than the 120 s predicted by Tauer *et al.,* but closer to the 300 s observed by this authors experimentally.

Like section 3.3.1.2, the temperature profile trends predicted by Tauer *et al.,* [105] and this study are consistent with the experimental results from Moioli *et al.,* [67]. These authors attribute the behavior of the temperature profile to the increase in reaction heat and changes in thermal properties as the feed flow rises. They emphasize that the hot spot shifts further from the reactor inlet due to increased convective heat transport, potentially delaying thermodynamic and kinetic equilibrium, slowing reactor activation, and increasing heat transfer to the cooling medium.

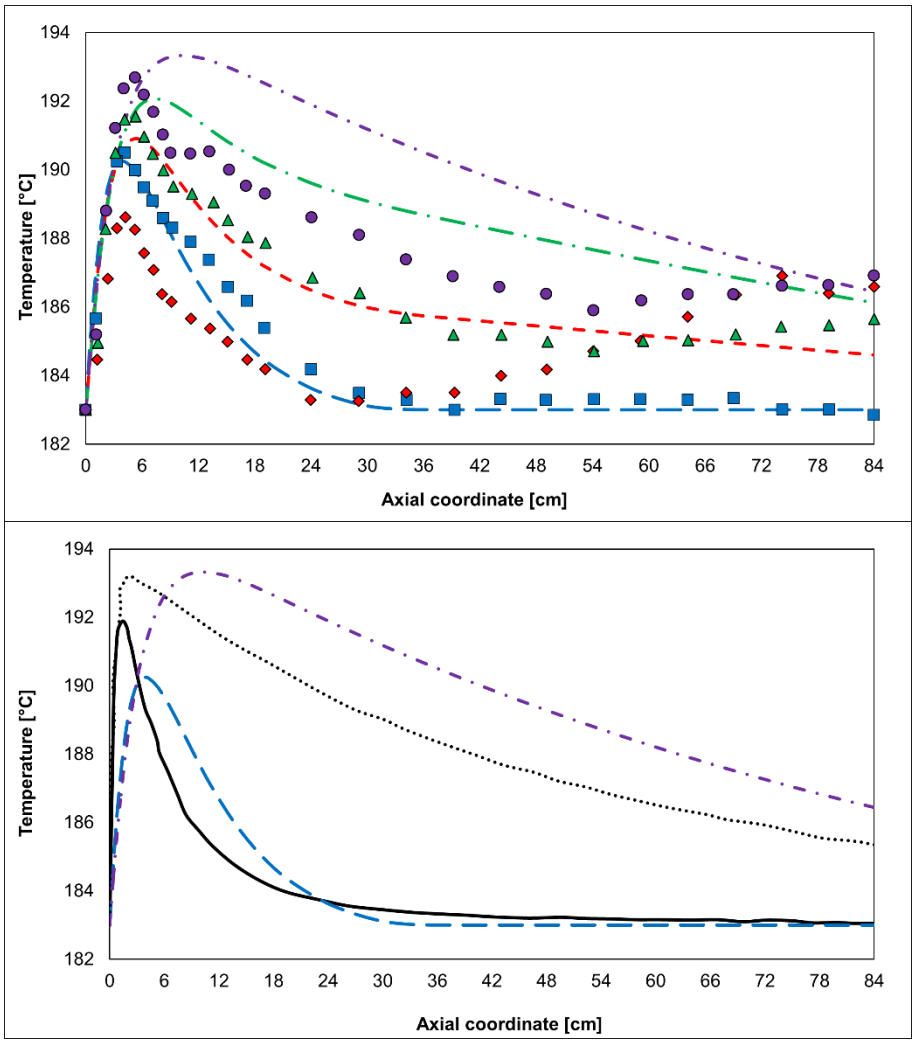

Figure 3.11. Temperature profile for different times for the operation conditions of Tauer *et al.*, [105]. Centerline of HMR. Increment of GHSV, from 27 to 217 h^{-1}. Lines for HMR and points for FXB. ■ and . ▬ ▬ for t = 0 s, ◆ and ▬ ▬ for t = 60 s, ▲and ▬▪▬ for t = 180 s, ● for t = 360 s and ▬ ▪ ▬ for t = 253 s. Tauer's FXB model, ▬ t = 0 s and ··· for t = 360 s.

Figure 3.12 shows the temporal profile of peak reactor temperature at the hot spot. Both Tauer *et al.,*'s research and the current study don't show a temporal minimum of peak temperature, unlike the experiment. Tauer *et al.,* [105] attribute this to delayed equilibrium in H_2O adsorption, which is overlooked in the stationary selected kinetic model (Koschany *et al.,* [146]). The kinetic model assumes instantaneous reactions at specific temperatures; thus, the reactor's mathematical model

only considers transient thermal effects, excluding the influence of kinetic desorption and adsorption capabilities of the catalyst [105].

This explains why reaching the new steady state takes longer than predicted by mathematical models for both reactor types. The delay is due to the water content in the gas, as initially, the reaction rate and the temperature of the hot spot decrease until the excess adsorbed water is released from the gas [105].

On the other hand, CO_2 conversion was nearly 100% in the first steady state. However, a sudden increase in feed flow led to reduced CO_2 consumption due to a shorter residence time. In the second steady state, CO_2 conversion reduced to 83% for the HMR, surpassing Tauer *et al.,*'s forecast of 69% and the 60% achieved experimentally. Tauer *et al.,* noted that discrepancies between predictions and experimental results were due to inaccuracies related to high H_2O/H_2 ratios [105].

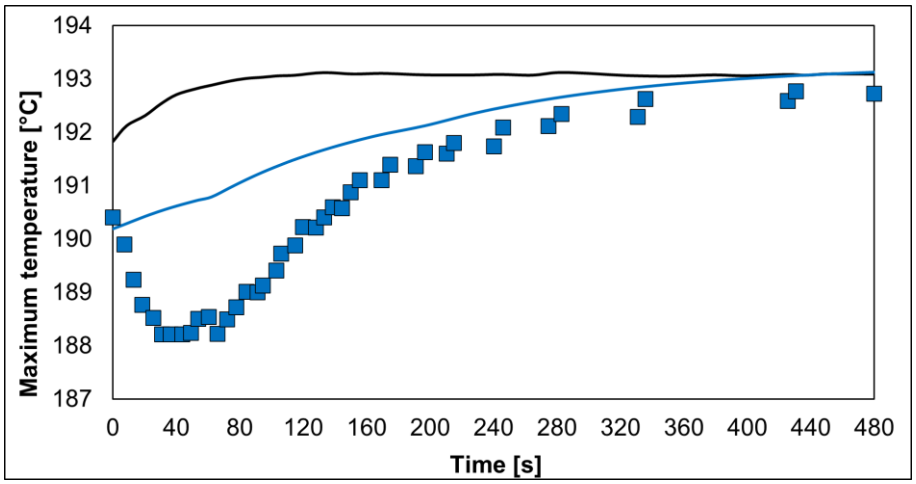

Figure 3.12. Temporal profile of maximum temperature in hotspot location. Operation conditions of Tauer *et al*., [105]. Increment of GHSV, from 27 to 217 h^{-1}. ■ Experiment, - - HMR, ▬ Tauer's FXB model.

Moreover, Figure C.6 shows a different trend from Figure 3.12 when the feed flow is reduced from 217 to 27 h^{-1}, resulting in a reduction in maximum temperature across all case studies. In the experimental case, a temporary temperature peak is observed. Tauer *et al.,* [105] explain that this is due to increased adsorption of water produced near the hot spot. This aspect is not included in the mathematical models of the FXB reactor proposed by these authors or in the HMR model of this study, due to the use of stationary kinetics.

3.3.4.2.HMR vs. FXB: Operation conditions of Fischer *et al.,*

A U_{sc} value of 342 W/(m^2°C) was used, resulting in a peak temperature of 508 K (235 °C) at the centerline of HMR (Figure 3.13).

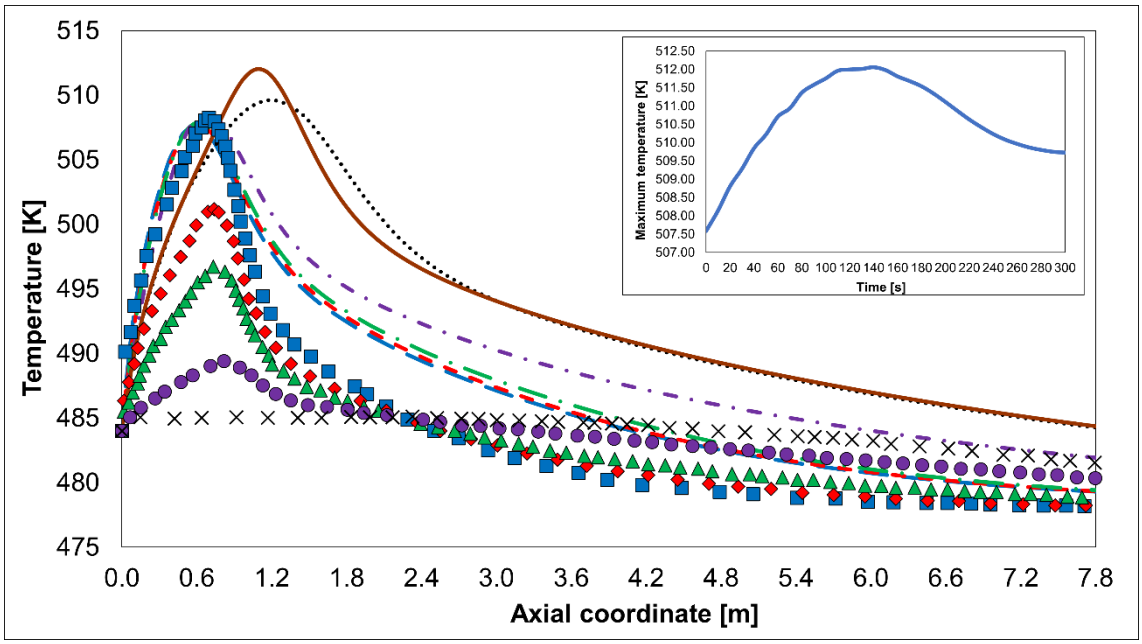

Figure 3.13. Temperature profile for different times for the operation conditions of Fischer *et al*., [102]. Centerline of HMR. Increment of GHSV, from 1572 to 3144 h^{-1}. Lines for HMR and points for FXB. ■ and ▬ ▬ for t = 0 s, ◆ and ▬ ▬ for t = 2 s, ▲and ▬▪▬ for t = 4.5 s, ● and ▬ ▪ ▬ for t = 16 s, **x** for t = 112 s (final steady state) and ··· for t = 285 s (final steady state). ▬ for t = 117 s (transient maximum).

Increasing the GHSV from 1572 to 3144 h^{-1} raised the peak temperature from 508 to 510 K (235 to 237 °C), reaching the second steady state in 285 s. At 117 s, the HMR hot spot experiences a temporary temperature peak, reaching 512 K (239 °C) at 1.27 m. The location of the peak temperature shifted further from the reactor inlet, moving from 0.59 to 1.17 m.

This pattern contrasts with Fischer *et al.,*'s findings, where doubling the GHSV decreased the maximum temperature from 508 to 485 K (235 to 212 °C) in 112 s, with a more pronounced shift in peak temperature location from 0.70 to 2.33 m.

Fischer *et al.,* note that FXB's reaction to a higher feed flow rate results from increased convective heat transport and improved heat transfer from the cooling medium. Despite this, the reaction-generated heat escalates more significantly over time in HMR, attributed to the accumulation of reactants at the inlet. After 117 s, the convective heat transfer and cooling rate become more important than the heat generated by the CO_2 methanation reaction in the HMR. Despite this, the peak temperature during the second steady state is still higher than the peak temperature before the fluctuation in feed flow for HMR.

Figure 3.14 shows that an increase in feed flow leads to a decrease in CO_2 conversion for both reactor types due to reduced residence time. In the HMR, a brief peak in outlet temperature at 11 s results in a maximum reaction rate, partially compensating for the reduced CO_2 conversion. This effect increases the parameter from 11 s until stabilizing at 285 s.

It is important to note that the highest difference between the center and wall temperature of the HMR ranges from 15 to 16 °C, leading to decreased reagent consumption at the wall (Figure 3.14). Consequently, the average CO_2 conversion in the reactor is lower than predicted by Fischer *et al.,*'s one-dimensional pseudohomogeneous model for the FXB.

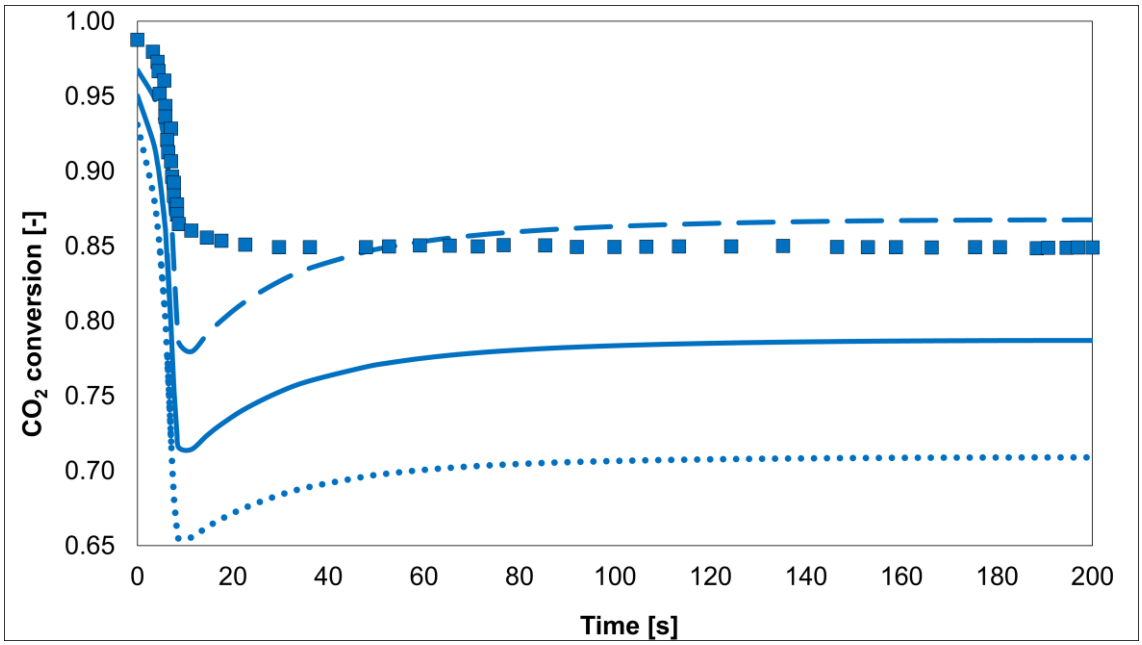

Figure 3.14. Temporal profile of outlet CO_2 conversion for the operation conditions of Fischer *et al.*, [102]. Increment of GHSV, from 1572 to 3144 h^{-1}. ■ FXB, - - Centerline HMR, ▬ Average HMR, ··· Wall HMR.

Furthermore, reducing the feed flow from 3144 to 1572 h^{-1} lowers the maximum temperature at the center of the HMR from 510 K to 508 K (237 to 235 °C) (Figure C.7) and increases the average CO_2 conversion at the reactor exit from 80% to 95% (Figure C.8). The reduction in inlet flow decreases convective heat transport and slows the cooling process, favoring an increase in temperature. However, the HMR maximum temperature briefly dropped to 505 K (232 °C) at 0.68 m and 53 s. After this point, the convective heat transfer and cooling rate decreased relative to the heat generated by the CO_2 methanation reaction. Nevertheless, the peak temperature during the second steady state was still lower than the maximum temperature noted before the abrupt change in feed flow. Finally, the system reached a new steady state in 340 s, with the hot spot moving from 1.17 to 0. 59 m.

3.3.4.3.HMR vs. FXB: Operation conditions of Lefebvre *et al.,*

Lefebvre *et al.,* [73] initially employed a two-dimensional model for the FXB reactor but switched to a one-dimensional model due to lengthy calculation times. In this study, the radial temperature gradient in the HMR was notably significant, with a 150 °C difference between the center and the wall. This difference is considerably larger than the results obtained for HMR with operation conditions by Tauer *et al.,* [105], who observed a 2 °C difference, and Fischer *et al.,* [102], who found a 15 °C difference.

It is important to note that, like Lefebvre *et al.,*'s study, the mass transfer limitation within the catalytic washcoat was considered relevant in this case. In contrast, this limitation was negligible for the Tauer [105] and Fischer [102] studies. On the other hand, the concentration gradient between the gas and the catalyst surface was found to be negligible for the HMR under the operating conditions of the three FXB studies. This confirms the correct application of the Mears criterion in the work of Lefebvre *et al.,* [73].

On the other hand, Lefebvre *et al*., [73] using Anderson and Mears criteria highlighted that there are no heat transfer limitations inside the catalyst or on its surface. This work confirmed that the HMR operates without heat transfer constraints within the catalytic coating for operational conditions of fixed-bed studies.

With the conditions of Tauer *et al.,* [105] and Fischer *et al.,* [102], no temperature gradient is observed between the gas and the catalyst surface in the HMR. However, the operational conditions of Lefebvre *et al.,* [73] are not the case. The small temperature difference between the gas and the catalytic washcoat surface near the inlet meets the Mears criterion, according to Lefebvre *et al*.,'s study on FXB reactor. Nevertheless, the temperature difference becomes more pronounced near the 0.35-0.38 m length of the HMR, where the main reaction occurs. In the HMR,

the maximum solid-gas temperature gradient was about 25 °C during the first steady state and increased to 150 °C in the second steady state.

Based on the above, the radial and interparticle heat transfer limitations notably impact the recovery time and dynamic trend of the HMR under the conditions studied by Lefebvre *et al*., [73] differing from the predictions made with a pseudohomogeneous 1D model for a FXB reactor. This lead to an imbalance in their comparison. For the third comparative study, the dynamic-heterogeneous model of the HMR was simplified into a one-dimensional case without gas-solid heat transport limitations.

Figure 3.15 shows the temperature profile shift to the right for the two reactor types. The HMR reactor has a hot spot shift (from 0.44 to 0.59 m) like FXB (from 0.46 to 0.60 m). To achieve peak temperatures in the HMR similar to those in the FXB, an U_{sc} value of 811.5 W/(m²°C) was used.

In Lefebvre et al., [73] 's study, the FXB reactor's maximum gas temperature decreased from 510 to 351 °C, whereas the HMR reactor's hotspot temperature rose from 395 to 397 °C. The FXB reactor reached its new steady state in 18 s, while the HMR took 49 s.

Lefebvre et al., [73] note that trends are influenced by the increase in axial convective heat of the gas and the reactor cooling rate due to a sudden rise in feed flow. These factors decrease the gas temperature, counteracting the heat of reaction. However, they do not fully compensate for the increased heat of reaction in the HMR, which is caused by the accumulation of reactants at the reactor inlet after the disturbance, leading to a light rise in gas temperature in the HMR.

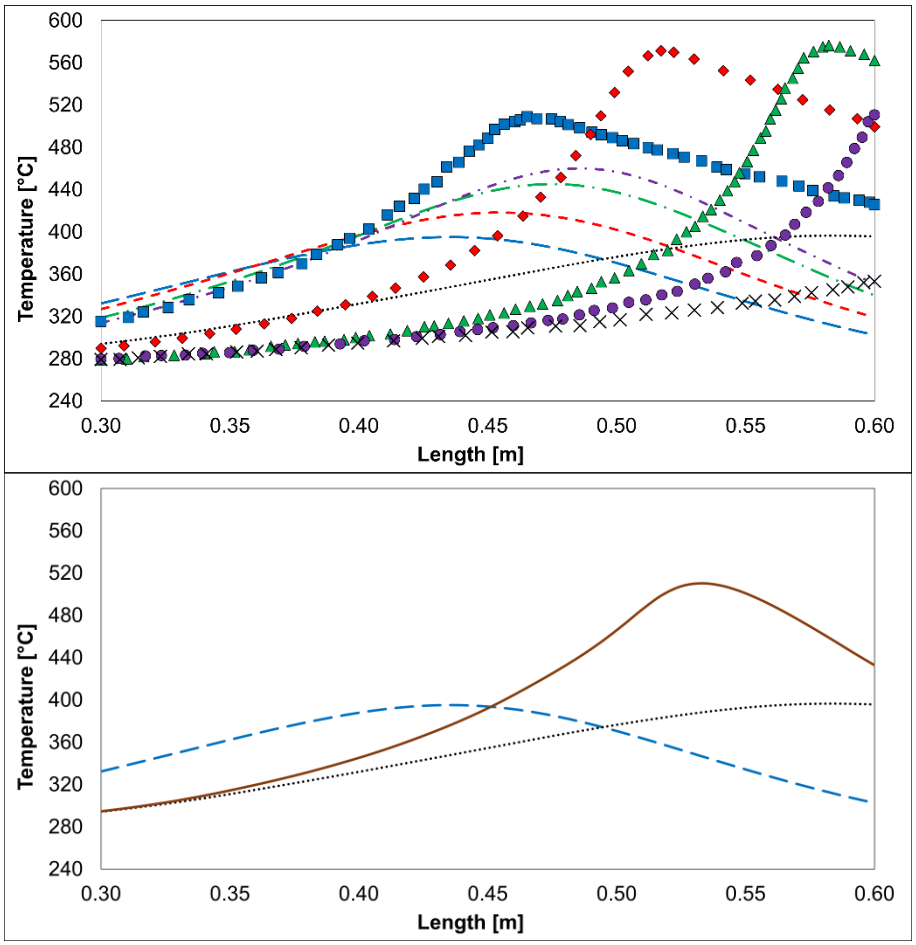

Figure 3.15. Temperature profile for different times for the operation conditions of Lefebvre *et al.*, [73]. Centerline of HMR. Increment of GHSV, from 44762 to 59683 h^{-1}. Lines for HMR and points for FXB. ■ and ▬ ▬ for t = 0 s, ◆ and ▬ ▬ for t = 4 s, ▲ and ▬ ▬ for t = 8 s, ● and ▬ ▬ for t = 10 s, **x** for t = 16 s (final steady state) and ··· for t = 49 s (final steady state). ▬ for t = 21 s (transient maximum).

Figure 3.16 presents maximum temperature time profiles for the FXB reactor from Lefebvre et al., [73] and the HMR reactor from this study. In Lefebvre et al's FXB reactor, a temporary peak occurs as the hot spot temperature rises from 510 to 579 °C within 7 s, then drops to 351 °C. The FXB reactor achieves a new steady state in 18 s. In the case of the HMR, the maximum gas temperature reaches a peak of 510 °C over 21 s. Lastly, the temperature declines from 510 to 397 °C, stabilizing at this new steady state after 49 s.

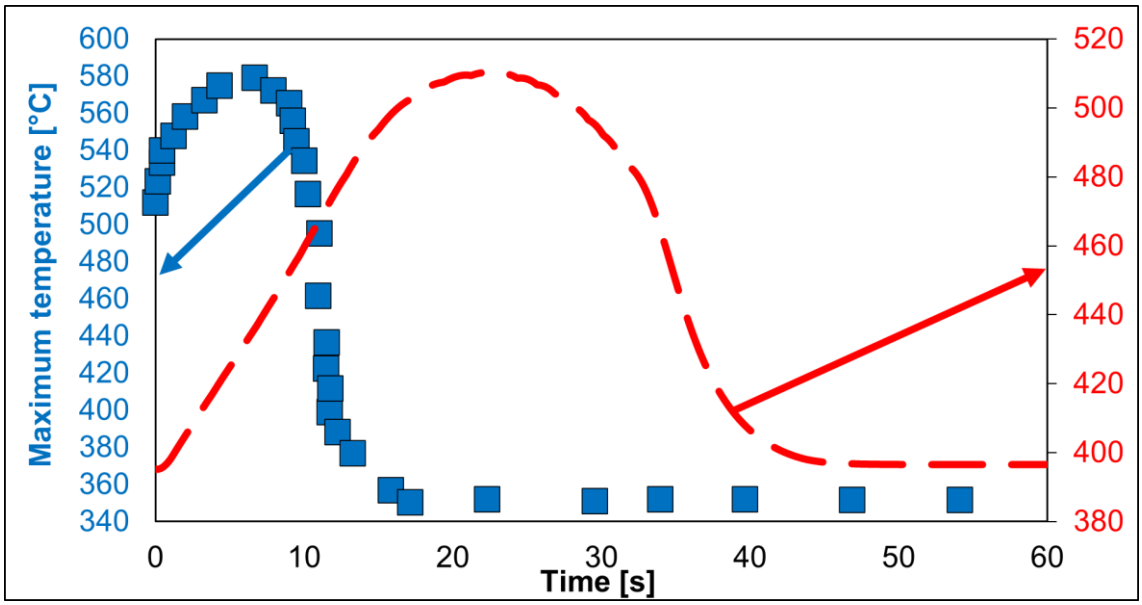

Figure 3.16. Temporal profile of maximum temperature in hotspot location. Operation conditions of Lefebvre *et al*., [73]. Increment of GHSV, from 44762 to 59683 h^{-1}. ■ FXB, - - HMR

The initial rise in the maximum FXB hot spot temperature results from the significant heat of reaction during the first few seconds, which is due to the already observed accumulation of reactants at the equipment inlet. Subsequently, again, axial convective heat transport and the cooling rate surpass the heat of reaction, leading to a decrease in the hot spot temperature to a new steady state. In the HMR case, the maximum gas temperature rises due to increased heat of reaction. A temporal maximum is noted after 21 s, when axial convective heat transport and reactor cooling rate exceed the heat of reaction.

Figure 3.17 illustrates the time evolution of CO_2 conversion. Initially, CO_2 conversion is reduced from 86 to 76 %, due to increased flow that shortens residence time. However, the heat from the reaction surpasses convective axial heat transport, leading to a temperature rise. This temperature increase enhances the reaction rate, thereby boosting CO_2 consumption from 76 to 86 %.

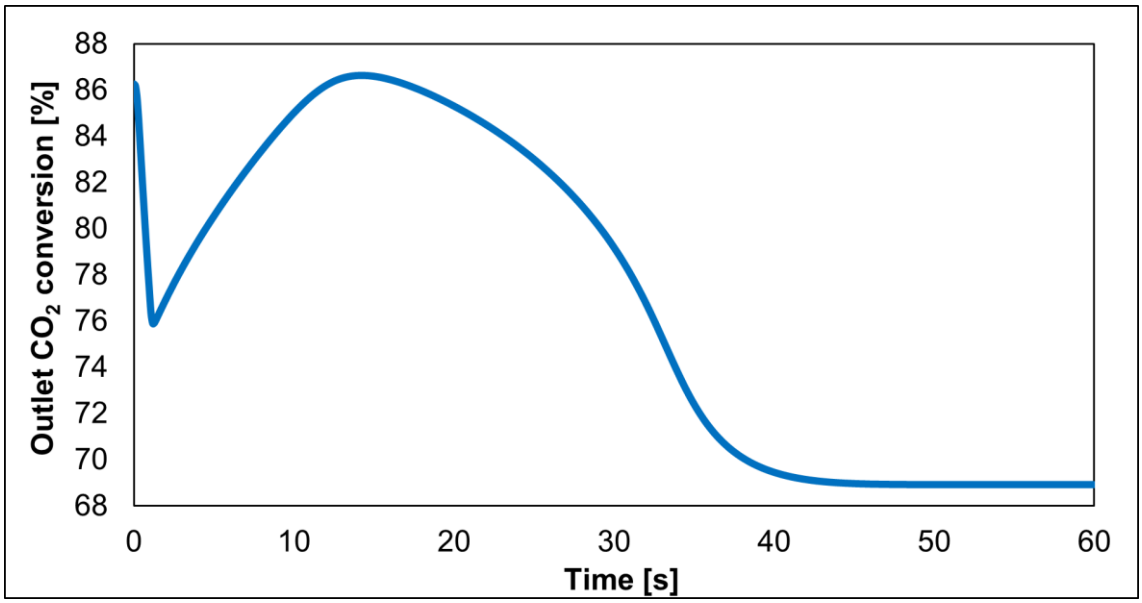

Figure 3.17. Temporal profile of outlet CO_2 conversion of HMR, for the operation conditions of Lefebvre *et al.*, [73]. Increment of GHSV, from 44762 to 59683 h^{-1}.

Lastly, this parameter decreased again for the effect of axial convection heat until a new steady state is achieved with a final conversion to 69 %. Concerning to Lefebvre et al study, the CO_2 conversion decreases from 92 to 47 %.

3.3.4.4.HMR vs. FXB: Effect of GHSV and pressure

For the three cases analyzed, differences are observed in dynamic trends, maximum temperature changes, and hotspot displacement. Tauer et al use lower pressure and GHSV. Lefebvre, on the other hand, employs higher GHSV and pressure. Fischer's conditions fall in between these two approaches.

Under low GHSV conditions, high CO_2 consumption is favored. This explains the increase in the maximum temperature at a sudden increase of the feed flow and the higher CO_2 conversion values in the first case for both reactors.

In contrast, despite the pressure increase in the intermediate case, increased GHSV leads to an increment of axial convective heat in the FXB reactor, being more dominant than the heat of reaction. As a result, the temperature of the FXB reactor decreased under a sudden increase in feed flow. On the other hand, in the HMR reactor, the maximum temperature increases with a sudden rise in inlet flow because its thermal properties cause the heat of reaction to dominate over axial convective heat transport.

In the latter case, high pressure supports the Sabatier reaction, thereby balancing the reduced CO_2 consumption resulting from using a higher GHSV. In this extreme case, GHSV was 40 to 1000 times higher than in previous studies, showing that axial convective heat transport is significantly greater. The extreme differences result in a noticeable drop in maximum temperature, a significant decrease in CO_2 conversion, and a considerable shift of the hot spot in the FXB reactor, all due to fluctuations in the feed flow. This also creates a maximum transient in the peak temperature. In the HMR case, there's an increase in maximum temperature because of its distinct thermal properties compared to the FXB reactor. Convective transport is more dominant, greatly reducing the maximum temperature gradient after the temporal peak, unlike the intermediate case.

3.3.4.5.HMR vs. FXB: Comparison

It was confirmed that axial mass dispersion of the gas and temperature gradient within catalyst was negligible. On the other hand, there are no mass and heat transfer limitations on catalyst surface. In the case of Lefebvre et al, mass transport limitations within the catalyst were acknowledged, supported by an effectiveness factor ranging from 22 to 86%, while in another study, there is no concentration gradient inside the catalyst. In addition, it was also confirmed that heat dispersion effect was negligible, except for Tauer et al.

When solving the FXB reactor case of Tauer et al with a one-dimensional model, few differences with the rigorous model were found, except for the steady state recovery time, reporting 266 s instead of 253 s. Furthermore, the axial thermal conductivity of the pseudohomogeneous medium is higher in the Tauer case, ranging from 0.41 to 2.6 W/(m°C), whereas the monolith has an axial thermal conductivity of 1.7 W/(m°C).

In contrast to the previous case, Fischer's study indicates a larger radial temperature gradient of 15 °C, compared to Tauer's 2 °C. In this case, the axial heat dispersion was neglegible. This results in the one-dimensional model predicting a CO_2 conversion of 82% at the second steady state, higher than the 79% estimated by the two-dimensional model. Additionally, the recovery time for the new steady state increases to 408 s from 285 s, due to the effect of radial thermal resistance.

When the effect of dimensions and phase are disregarded, it is noted that the behavior of FXB and HMR is affected by the different volume fractions of catalyst, with the HMR containing an additional solid, the stainless-steel substrate. On the other hand, the catalyst loading is lower in the HMR. In addition, the heat transfer coefficient between the wall and the cooling medium varies significantly in the fixed bed, while it remains constant in the HMR, supporting the use of a constant U_{sc} value for this case (verify with Equations 3.3 and B.7). These elements account for the differences in results for each reactor across the three study cases.

Lastly, it's important to say that the thermal conductivity of the catalyst (λ_{cat}) and substrate material significantly impacts the results obtained with the HMR in the bidimensional case, where the axial conduction heat and resistance to radial heat transfer are not negligible, particularly influencing the axial and radial thermal conductivities as the catalyst volume fraction increases. These parameters, along with those previously mentioned, result in a longer recovery time and improved dynamic response for the HMR compared to the FXB reactor.

Conclusions

Dynamic modeling of the CO_2 methanation reactor is crucial since the reaction may experience non-steady state conditions due to variations in the H_2 flow, which are caused by the renewable energy sources that produce it. Operationally, it is crucial to maintain a constant stoichiometric H_2/CO_2 ratio to prevent side reactions. Consequently, similar to other studies, this research concentrated on the change of the total gas flow entering the reactor.

The maximum reactor temperature, referred to as the hot spot, can change directly or inversely with time based on operating conditions and total flow changes. Temporary maximum or minimum in the hot spot temperature may appear before a new steady state is achieved. Monitoring this temporary maximum temperature is essential, as it might surpass the allowable maximum temperature, potentially deactivating the catalyst or causing a temperature runaway in the reactor.

Based on the results of this study, it is concluded that in a monolithic honeycomb reactor, both the maximum temperature and CO_2 conversion increase when there is a sudden rise in the total flow rate. Additionally, for a step fluctuation in the reactor feed, no temporary minimum occurs before reaching a new steady state under these conditions.

On the other hand, the correct handling of boundary conditions is crucial for ensuring the mathematical model of the monolithic reactor aligns accurately with experimental data. Additionally, achieving accurate values for the radial thermal conductivity of the monolith and the heat transfer coefficient between its wall and the cooling medium is important. This ensures that the mathematical model fits correctly with the experimental data from the dynamic test. However, to reduce the discrepancy between the model and experimental data, employing a kinetic expression that spans a broad temperature range and considers the uneven distribution of the catalyst within the monolith channels is recommended. Also, axial temperature profiles should be

obtained at different radial locations, not only at the center and the wall. It's also important to consider errors in fiber optic temperature measurements and other heat transfer phenomena that affect the thermal behavior of the monolithic reactor. For these reasons, it is also essential that the mathematical model of the reactor accurately represents its real thermal behavior.

After experimentally validating the mathematical model, comparative tests were conducted with studies on the fixed-bed reactor. The tests maintained the same operating conditions and dimensions, differing only in catalyst loading and the internal dimensions of the honeycomb monolith. In both reactor types, CO_2 conversion diminishes as the feed flow increases. The monolithic reactor experiences a rise in maximum temperature with higher flow rates, whereas the fixed-bed reactor generally shows a decrease. When feed flow is abruptly increased, the hot spot shifts in both reactor types, moving the maximum temperature further from the reactor inlet. Additionally, temporary maximum occurs in the monolithic reactor when there is high pressure, large flow and lower catalyst load.

When operating a monolithic reactor under fluctuating conditions akin to a fixed-bed reactor, there were smaller changes in maximum temperature. A lesser reduction in CO_2 conversion was noted, even with lower catalyst load. Lastly, the monolithic reactor has a longer steady state recovery time under the fluctuation of feed flow.

This work demonstrated that the mathematical model formulated is adequate to predict the monolithic honeycomb reactor's dynamic behavior under fluctuating feed flow conditions. This model showed that this type of reactor is a promising technology for dynamic operation of CO_2 methanation, outperforming the traditional fixed-bed reactor. However, optimizing its design variables is crucial to enhance CO_2 conversion while using less catalyst.

General Conclusions

The honeycomb monolith is an promising technology to replace fixed-bed reactors in CO_2 methanation, aiming to reduce emissions of this greenhouse gas more economically and simply. Adaptation to fluctuating H_2 load—due to the intermittent nature of renewable energy sources to generate it—is crucial for the reactor's operation. This study evaluated the monolithic reactor's dynamic response to these fluctuations while maintaining a constant stoichiometric H_2/CO_2 ratio. First, a review of reactor modeling studies determined that a full-scale, dynamic, two-dimensional axialsymmetric heterogeneous model is appropiate for modeling the honeycomb monolith in this industrial application. Additionally, the effectiveness factor was calculated based on its formal definition, reflecting its dependence on temperature and catalyst structure, rather than using a constant value. The mathematical model of the reactor was theoretically validated using chemical equilibrium and kinetic regime methodologies. Additionally, it was confirmed that the model results were independent of the solution domain's element size.

Parametric studies were conducted under typical CO_2 methanation conditions with varying H_2 flow, while keeping the H_2/CO_2 ratio constant. It was found that despite Ru's high catalytic activity, the reactor had the same recovery time as when Ni was used, indicating good response under high reaction rate conditions. The reactor performed best with ramp changes, but also handled step changes well, showing it can manage different inlet flow disturbances. However, as the reactor diameter increases, the dynamic response becomes more complex due to increased radial heat transfer resistance.

After performing model evaluations in different operational scenarios, the model was experimentally validated, reinforcing the validity of its predicted results. During the experimental dynamic evaluation of the monolithic reactor, no temporary maximum or minimum of the hot spot temperature was observed with a sudden increase in the feed flow. In addition, it was noted that in this type of reactor, both equipment temperature and CO_2 conversion increased with increasing gas inflow.

Finally, this work compared theoretically the dynamic response of a monolithic honeycomb reactor to a fixed-bed reactor under differents feed flow conditions, keeping operating conditions and dimensions consistent, except for catalyst loading and internal dimensions. The monolithic reactor demonstrated less fluctuation in peak temperature and CO_2 conversion, though it took longer to reach a new steady state.

Thus, the monolithic reactor is shown as a promising technological alternative to the fixed bed reactor for CO_2 methanation. It is recommended to optimize its operational variables to enhance CO_2 conversion with minimal catalyst loads. The thesis results encourage further studies on this reactor type and provide a foundation for increasing dynamic investigations in CO_2 methanation, crucial for improving the Power to Gas process.

References

[1] Masson-Delmotte V, Zhai P, Pirani A, Connors SL, Péan C, Berger S, et al. IPCC, 2021: Summary for Policymakers. In: Climate Change 2021: The Physical Science Basis. Contribution of Working Group I to the Sixth Assessment Report of the Intergovernmental Panel on Climate Change. 2021.

[2] Mebrahtu C, Krebs F, Abate S, Perathoner S, Centi G, Palkovits R. CO_2 Methanation: Principles and Challenges. Stud Surf Sci Catal, vol. 178, Elsevier; 2019, p. 85–103. https://doi.org/10.1016/B978-0-444-64127-4.00005-7.

[3] Lee WJ, Li C, Prajitno H, Yoo J, Patel J, Yang Y, et al. Recent trend in thermal catalytic low temperature CO_2 methanation: A critical review. Catal Today 2021;368:2–19. https://doi.org/10.1016/j.cattod.2020.02.017.

[4] Schildhauer TJ. METHANATION FOR SYNTHETIC NATURAL GAS PRODUCTION - CHEMICAL REACTION ENGINEERING ASPECTS. Synthetic Natural Gas from Coal, Dry Biomass, and Power-to-Gas Applications, Hoboken, NJ, USA: John Wiley & Sons, Inc.; 2016, p. 77–159. https://doi.org/10.1002/9781119191339.ch4.

[5] Saeidi S, Najari S, Hessel V, Wilson K, Keil FJ, Concepción P, et al. Recent advances in CO_2 hydrogenation to value-added products — Current challenges and future directions. Prog Energy Combust Sci 2021;85. https://doi.org/10.1016/j.pecs.2021.100905.

[6] Ren J, Lou H, Xu N, Zeng F, Pei G, Wang Z. Methanation of CO/CO2 for power to methane process: Fundamentals, status, and perspectives. Journal of Energy Chemistry 2023;80:182–206. https://doi.org/10.1016/j.jechem.2023.01.034.

[7] Akpasi SO, Isa YM. Review of Carbon Capture and Methane Production from Carbon Dioxide. Atmosphere (Basel) 2022;13:1958. https://doi.org/10.3390/atmos13121958.

[8] Palys MJ, Daoutidis P. Power-to-X: A review and perspective. Comput Chem Eng 2022;165:107948. https://doi.org/10.1016/j.compchemeng.2022.107948.

[9] Qi M, Liu Y, He T, Yin L, Shu C-M, Moon I. System perspective on cleaner technologies for renewable methane production and utilisation towards carbon neutrality: Principles, techno-economics, and carbon footprints. Fuel 2022;327:125130. https://doi.org/10.1016/j.fuel.2022.125130.

[10] Jangam A, Das S, Dewangan N, Hongmanorom P, Hui WM, Kawi S. Conversion of CO_2 to C_1 chemicals: Catalyst design, kinetics and mechanism aspects of the reactions. Catal Today 2020;358:3–29. https://doi.org/10.1016/j.cattod.2019.08.049.

[11] Chen S, Abdel-Mageed AM. Methanation reactions for chemical storage and purification of hydrogen: Overview and structure-reactivity correlations in supported metals. Int J Hydrogen Energy 2023. https://doi.org/10.1016/j.ijhydene.2022.12.196.

[12] Fan WK, Tahir M. Recent trends in developments of active metals and heterogenous materials for catalytic CO2 hydrogenation to renewable methane: A review. J Environ Chem Eng 2021;9:105460. https://doi.org/10.1016/j.jece.2021.105460.

[13] Abdel-Mageed AM, Wohlrab S. Review of CO2 Reduction on Supported Metals (Alloys) and Single-Atom Catalysts (SACs) for the Use of Green Hydrogen in Power-to-Gas Concepts. Catalysts 2021;12:16. https://doi.org/10.3390/catal12010016.

[14] Ashok J, Falbo L, Das S, Dewangan N, Visconti CG, Kawi S. Catalytic CO_2 Conversion to Added-Value Energy Rich C_1 Products. An Economy Based on Carbon Dioxide and

Water, Cham: Springer International Publishing; 2019, p. 155–210. https://doi.org/10.1007/978-3-030-15868-2_5.

[15] Lehner M, Tichler R, Steinmüller H, Koppe M. Power-to-Gas: Technology and Business Models. 1st ed. Cham: Springer International Publishing; 2014. https://doi.org/10.1007/978-3-319-03995-4.

[16] Ghaib K, Ben-Fares F-Z. Power-to-Methane: A state-of-the-art review. Renewable and Sustainable Energy Reviews 2018;81:433–46. https://doi.org/10.1016/j.rser.2017.08.004.

[17] Held M, Schollenberger D, Sauerschell S, Bajohr S, Kolb T. Power-to-Gas: CO_2 Methanation Concepts for SNG Production at the Engler-Bunte-Institut. Chemie Ingenieur Technik 2020;92:595–602. https://doi.org/10.1002/cite.201900181.

[18] Vita A, Italiano C, Pino L, Frontera P, Ferraro M, Antonucci V. Activity and stability of powder and monolith-coated Ni/GDC catalysts for CO_2 methanation. Appl Catal B 2018;226:384–95. https://doi.org/10.1016/j.apcatb.2017.12.078.

[19] Rönsch S, Schneider J, Matthischke S, Schlüter M, Götz M, Lefebvre J, et al. Review on methanation – From fundamentals to current projects. Fuel 2016;166:276–96. https://doi.org/10.1016/j.fuel.2015.10.111.

[20] Pérez-Vilela DE, Garcia X. Modeling the dynamic operation of a monolithic CO2 methanation reactor. Evaluation of the response to H2 load fluctuation. Int J Hydrogen Energy 2024;77:769–83. https://doi.org/10.1016/j.ijhydene.2024.06.148.

[21] Liu X, Zeng Y, Chen J, Zhong Z, Xing W. Research progress on the monolithic catalyst for hydrogenation of CO2 to methane. Chin J Chem Eng 2025. https://doi.org/10.1016/j.cjche.2025.02.002.

[22] Schlereth D, Donaubauer PJ, Hinrichsen O. Metallic Honeycombs as Catalyst Supports for Methanation of Carbon Dioxide. Chem Eng Technol 2015;38:1845–52. https://doi.org/10.1002/ceat.201400717.

[23] Schollenberger D, Bajohr S, Gruber M, Reimert R, Kolb T. Scale-Up of Innovative Honeycomb Reactors for Power-to-Gas Applications – The Project Store&Go. Chem Ing Tech 2018;90:696–702. https://doi.org/10.1002/cite.201700139.

[24] Huynh HL, Tucho WM, Shen Q, Yu Z. Bed packing configuration and hot-spot utilization for low-temperature CO2 methanation on monolithic reactor. Chemical Engineering Journal 2021;428. https://doi.org/10.1016/j.cej.2021.131106.

[25] Parra-Marfil A, Ocampo-Pérez R, Aguilar-Madera CG, Carrasco-Marín F, Pérez-Cadenas AF, Bueno-López A, et al. Modeling and experimental analysis of CO2 methanation reaction using Ni/CeO2 monolithic catalyst. Environmental Science and Pollution Research 2024;31:32766–83. https://doi.org/10.1007/s11356-024-33327-5.

[26] Zhang W, Lin Y, Zhang Y, Li T, Li J, Chen Z, et al. Regulation of temperature distribution in fixed bed reactor for CO2 methanation through “CHESS” monolith structure catalyst. Appl Therm Eng 2024;236. https://doi.org/10.1016/j.applthermaleng.2023.121826.

[27] Gao J, Wang Y, Ping Y, Hu D, Xu G, Gu F, et al. A thermodynamic analysis of methanation reactions of carbon oxides for the production of synthetic natural gas. RSC Adv 2012;2:2358–68. https://doi.org/10.1039/c2ra00632d.

[28] Seemann M, Thunman H. Methane synthesis. Substitute Natural Gas from Waste, Academic Press; 2019, p. 221–43. https://doi.org/10.1016/B978-0-12-815554-7.00009-X.

[29] Simakov DSA. Thermocatalytic Conversion of CO_2. Renewable Synthetic Fuels and Chemicals from Carbon Dioxide, Cham: Springer; 2017, p. 1–25. https://doi.org/10.1007/978-3-319-61112-9_1.

[30] Kreitz B, Brauns J, Wehinger GD, Turek T. Modeling the Dynamic Power-to-Gas Process: Coupling Electrolysis with CO2 Methanation. Chem Ing Tech 2020;92:1992–7. https://doi.org/10.1002/cite.202000019.

[31] Fukuhara C, Hayakawa K, Suzuki Y, Kawasaki W, Watanabe R. A novel nickel-based structured catalyst for CO_2 methanation: A honeycomb-type Ni/CeO_2 catalyst to transform greenhouse gas into useful resources. Appl Catal A Gen 2017;532:12–8. https://doi.org/10.1016/j.apcata.2016.11.036.

[32] Ratchahat S, Sudoh M, Suzuki Y, Kawasaki W, Watanabe R, Fukuhara C. Development of a powerful CO_2 methanation process using a structured Ni/CeO_2 catalyst. Journal of CO2 Utilization 2018;24:210–9. https://doi.org/10.1016/j.jcou.2018.01.004.

[33] Baena-Moreno FM, González-Castaño M, Navarro de Miguel JC, Miah KUM, Ossenbrink R, Odriozola JA, et al. Stepping toward Efficient Microreactors for CO_2 Methanation: 3D-Printed Gyroid Geometry. ACS Sustain Chem Eng 2021;9:8198–206. https://doi.org/10.1021/acssuschemeng.1c01980.

[34] Biegger P, Kirchbacher F, Medved A, Miltner M, Lehner M, Harasek M. Development of Honeycomb Methanation Catalyst and Its Application in Power to Gas Systems. Energies (Basel) 2018;11. https://doi.org/10.3390/en11071679.

[35] Schlereth D. Kinetic and Reactor Modeling for the Methanation of Carbon Dioxide. Technische Universität München, 2015.

[36] Hayes RE, Cornejo I. Multi-scale modelling of monolith reactors: A 30-year perspective from 1990 to 2020. Can J Chem Eng 2021;99:2589–606. https://doi.org/10.1002/cjce.24144.

[37] Zergani N, Sari A. Modeling and simulation analysis of methanol conversion to olefins (MTO): A critical comparison of a honeycomb monolith and a fixed-bed of cylindrical extruded HZSM-5 catalyst. Chemical Engineering and Processing - Process Intensification 2021;167:108537. https://doi.org/10.1016/j.cep.2021.108537.

[38] Sudiro M, Bertucco A, Groppi G, Tronconi E. Simulation of a structured catalytic reactor for exothermic methanation reactions producing synthetic natural gas. Computer Aided Chemical Engineering 2010;28:691–6. https://doi.org/10.1016/S1570-7946(10)28116-6.

[39] Tronconi E, Groppi G, Visconti CG. Structured catalysts for non-adiabatic applications. Curr Opin Chem Eng 2014;5:55–67. https://doi.org/10.1016/j.coche.2014.04.003.

[40] Montebelli A, Visconti CG, Groppi G, Tronconi E, Ferreira C, Kohler S. Enabling small-scale methanol synthesis reactors through the adoption of highly conductive structured catalysts. Catal Today 2013;215:176–85. https://doi.org/10.1016/j.cattod.2013.02.020.

[41] Jeifetz LG, Giunta PD, Mariño FJ, Amadeo NE, Laborde MÁ. Simulation of CO Preferential Oxidation (COPrOx) Monolithic Reactors. International Journal of Chemical Reactor Engineering 2014;12:1–12. https://doi.org/10.1515/ijcre-2013-0071.

[42] Batista R, Carrera A, Beretta A, Groppi G. Thermal Deactivation of Rh/α-Al2O3 in the Catalytic Partial Oxidation of Iso-Octane: Effect of Flow Rate. Catalysts 2019;9:532. https://doi.org/10.3390/catal9060532.

[43] Chandraker V, Paramasivan G, Chandy AJ. Computational investigations of enrichment effects for CO2 methanation in Sabatier microchannel reactors. Chemical Engineering Research and Design 2022;182:51–65. https://doi.org/10.1016/j.cherd.2022.03.035.

[44] Fuentes I, Gracia F. Fluid dynamic analytical model of CO2 methanation in a microreactor with potential application in Power-to-Gas technology. Chem Eng Sci 2022;251. https://doi.org/10.1016/j.ces.2022.117465.

[45] Danilov VA, Wichert M, Kolb G. 2D model of the transfer processes for CO2 methanation in a microchannel reactor. Chemical Engineering Journal 2022;450. https://doi.org/10.1016/j.cej.2022.137863.

[46] Blauth S, Leithäuser C, Pinnau R. Optimal control of the Sabatier process in microchannel reactors. J Eng Math 2021;128. https://doi.org/10.1007/s10665-021-10134-2.

[47] Fuentes I, Mmbaga JP, Hayes RE, Gracia F. Potential of microreactors for heat transfer efficient CO2 methanation. Chem Eng Sci 2023;280. https://doi.org/10.1016/j.ces.2023.119047.

[48] Najibi SZ, Fazeli A, Rahimi Chahardeh A. CFD modeling of a feed-distributed microchannel reactor for CO2 methanation using a green or purged hydrogen. Int J Hydrogen Energy 2024;77:149–65. https://doi.org/10.1016/j.ijhydene.2024.05.439.

[49] Engelbrecht N, Chiuta S, Everson RC, Neomagus HWJP, Bessarabov DG. Experimentation and CFD modelling of a microchannel reactor for carbon dioxide methanation. Chemical Engineering Journal 2017;313:847–57. https://doi.org/10.1016/j.cej.2016.10.131.

[50] Fuentes I, Mmbaga JP, Blanco A, Hayes RE, Gracia F. Kinetic model of CO2 methanation in a microreactor under Power-to-Gas conditions. Journal of CO2 Utilization 2023;75. https://doi.org/10.1016/j.jcou.2023.102552.

[51] Iwakiri IGI, Faria AC, Miguel C V., Madeira LM. Split feed strategy for low-permselective membrane reactors: A simulation study for enhancing CO2 methanation. Chemical Engineering and Processing - Process Intensification 2021;163. https://doi.org/10.1016/j.cep.2021.108360.

[52] Currie R, Fowler MW, Simakov DSA. Catalytic membrane reactor for CO2 hydrogenation using renewable streams: Model-based feasibility analysis. Chemical Engineering Journal 2019;372:1240–52. https://doi.org/10.1016/j.cej.2019.04.214.

[53] Schlereth D, Hinrichsen O. A fixed-bed reactor modeling study on the methanation of CO2. Chemical Engineering Research and Design 2014;92:702–12. https://doi.org/10.1016/j.cherd.2013.11.014.

[54] Harkou E, Hafeez S, Adamou P, Zhang Z, Tsiotsias AI, Charisiou ND, et al. Different reactor configurations for enhancement of CO2 methanation. Environ Res 2023;236. https://doi.org/10.1016/j.envres.2023.116760.

[55] Liu Z, Bian Z, Wang Z, Jiang B. A CFD study on the performance of CO2methanation in a water-permeable membrane reactor system. React Chem Eng 2022;7:450–9. https://doi.org/10.1039/d1re00401h.

[56] Catarina Faria A, Miguel C V., Rodrigues AE, Madeira LM. Modeling and Simulation of a Steam-Selective Membrane Reactor for Enhanced CO2Methanation. Ind Eng Chem Res 2020;59:16170–84. https://doi.org/10.1021/acs.iecr.0c02860.

[57] FarisAbadi A, Kazemeini M, Ekramipooya A. Investigating a HEX membrane reactor for CO2 methanation using a Ni/Al2O3 catalyst: A CFD study. Int J Hydrogen Energy 2023;48:25075–91. https://doi.org/10.1016/j.ijhydene.2022.06.290.

[58] Ono Y, Sasayama T, Kosaka F, Morimoto M, Matsuoka K, Kuramoto K. Numerical prediction of spatiotemporal CO2 capture and methanation reaction behavior in a fixed-bed reactor packed with a dual-function material. Int J Hydrogen Energy 2024;90:1128–39. https://doi.org/10.1016/j.ijhydene.2024.10.106.

[59] Bermejo-López A, Pereda-Ayo B, González-Marcos JA, González-Velasco JR. Modeling the CO2capture and in situ conversion to CH4on dual function Ru-Na2CO3/Al2O3catalyst. Journal of CO2 Utilization 2020;42. https://doi.org/10.1016/j.jcou.2020.101351.

[60] Mancusi E, Piso G, Shah HH, Pepe F, Tregambi C, Bareschino P. Modelling of a continuous sorption-enhanced methanation process in an adiabatic packed-bed reactor system. Chem Eng Sci 2025;301. https://doi.org/10.1016/j.ces.2024.120800.

[61] Bareschino P, Piso G, Pepe F, Tregambi C, Mancusi E. Numerical modelling of a sorption-enhanced methanation system. Chem Eng Sci 2023;277. https://doi.org/10.1016/j.ces.2023.118876.

[62] Bermejo-López A, Pereda-Ayo B, González-Marcos JA, González-Velasco JR. Simulation-based optimization of cycle timing for CO2 capture and hydrogenation with dual function catalyst. Catal Today 2022;394–396:314–24. https://doi.org/10.1016/j.cattod.2021.08.023.

[63] Iliuta I, Iliuta MC. Integration of sorption-enhanced steam glycerol reforming with methanation of in-situ removed carbon dioxide - An alternative for glycerol valorization. Int J Hydrogen Energy 2020;45:18574–86. https://doi.org/10.1016/j.ijhydene.2019.04.109.

[64] Gruber M, Wieland C, Habisreuther P, Trimis D, Schollenberger D, Bajohr S, et al. Modeling and Design of a Catalytic Wall Reactor for the Methanation of Carbon Dioxide. Chem Ing Tech 2018;90:615–24. https://doi.org/10.1002/cite.201700160.

[65] Vidal Vázquez F, Kihlman J, Mylvaganam A, Simell P, Koskinen-Soivi ML, Alopaeus V. Modeling of nickel-based hydrotalcite catalyst coated on heat exchanger reactors for CO2 methanation. Chemical Engineering Journal 2018;349:694–707. https://doi.org/10.1016/j.cej.2018.05.119.

[66] Ortiz-Laverde S, Rengifo C, Cobo M, Figueredo M. CFD-aided conceptual design of an intensified reactor for the production of synthetic natural gas within the power-to-methane context. Chemical Engineering and Processing - Process Intensification 2022;171. https://doi.org/10.1016/j.cep.2021.108755.

[67] Moioli E, Senn P, Oestrup S, Hütter C. Results from the operation of an efficient and flexible large-scale biogas methanation system 2023. https://doi.org/10.26434/chemrxiv-2023-0b2kz.

[68] Ich Ngo S, Lim Y Il, Lee D, Won Seo M, Kim S. Experiment and numerical analysis of catalytic CO2 methanation in bubbling fluidized bed reactor. Energy Convers Manag 2021;233. https://doi.org/10.1016/j.enconman.2021.113863.

[69] Jia C, Dai Y, Yang Y, Chew JW. A fluidized-bed model for NiMgW-catalyzed CO2 methanation. Particuology 2020;49:55–64. https://doi.org/10.1016/j.partic.2019.05.004.

[70] Ngo SI, Lim Y Il, Lee D, Seo MW. Flow behavior and heat transfer in bubbling fluidized-bed with immersed heat exchange tubes for CO2 methanation. Powder Technol 2021;380:462–74. https://doi.org/10.1016/j.powtec.2020.11.027.

[71] Ngo SI, Lim Y Il, Lee D, Go KS, Seo MW. Flow behaviors, reaction kinetics, and optimal design of fixed- and fluidized-beds for CO2 methanation. Fuel 2020;275. https://doi.org/10.1016/j.fuel.2020.117886.

[72] Prabhakaran P, Graf F, Koeppel W, Kolb T. Modelling and validation of energy systems with dynamically operated Power to Gas plants for gas-based sector coupling in de-central energy hubs. Energy Convers Manag 2023;276. https://doi.org/10.1016/j.enconman.2022.116534.

[73] Lefebvre J, Bajohr S, Kolb T. Modeling of the transient behavior of a slurry bubble column reactor for CO2 methanation, and comparison with a tube bundle reactor. Renew Energy 2020;151:118–36. https://doi.org/10.1016/j.renene.2019.11.008.

[74] Kiewidt L, Thöming J. Pareto-optimal design and assessment of monolithic sponges as catalyst carriers for exothermic reactions. Chemical Engineering Journal 2019;359:496–504. https://doi.org/10.1016/j.cej.2018.11.109.

[75] Kiewidt L, Thöming J. Multiscale modeling of monolithic sponges as catalyst carrier for the methanation of carbon dioxide. Chemical Engineering Science: X 2019;2. https://doi.org/10.1016/j.cesx.2019.100016.

[76] Raghu AK, Kaisare NS. Thermally integrated microreactor for Sabatier reaction: Study of air-cooled and inert-diluted counter-current operation strategies. Catal Today 2022;383:146–55. https://doi.org/10.1016/j.cattod.2020.08.025.

[77] Raghu AK, Kaisare NS. Analysis of the autothermal operability of the Sabatier reaction in a heat-recirculating microreactor using CFD. React Chem Eng 2019;4:1823–33. https://doi.org/10.1039/c9re00183b.

[78] Raghu AK, Kaisare NS. A compact heat recirculating spiral geometry for thermal integration for Sabatier reaction in microreactor. AIChE Journal 2022;68. https://doi.org/10.1002/aic.17726.

[79] Sánchez A, Milt VG, Miró EE, Güttel R. Impact of heat transport properties and configuration of ceramic fibrous catalyst structures for CO2 methanation: A simulation study. J Environ Chem Eng 2022;10. https://doi.org/10.1016/j.jece.2022.107148.

[80] Sánchez A, Milt VG, Miró EE, Güttel R. Ceramic Fiber-Based Structures as Catalyst Supports: A Study on Mass and Heat Transport Behavior Applied to CO2Methanation. Ind Eng Chem Res 2020;59:16539–52. https://doi.org/10.1021/acs.iecr.0c01997.

[81] Kosaka F, Yamaguchi T, Ando Y, Mochizuki T, Takagi H, Matsuoka K, et al. Effect of Ni content on CO2 methanation performance with tubular-structured Ni-YSZ catalysts and optimization of catalytic activity for temperature management in the reactor. Int J Hydrogen Energy 2020;45:12911–20. https://doi.org/10.1016/j.ijhydene.2020.02.221.

[82] Kosaka F, Yamaguchi T, Ando Y, Mochizuki T, Takagi H, Matsuoka K, et al. Thermal management of CO2 methanation with axial staging of active metal concentration in Ni-YSZ tubular catalysts. Int J Hydrogen Energy 2021;46:4116–25. https://doi.org/10.1016/j.ijhydene.2020.10.247.

[83] Surendran V, Bracconi M, Hernandez Lalinde JA, Maestri M, Kopyscinski J. Assessment of a catalytic plate reactor with in-situ sampling capabilities by means of CFD modeling and experiments. Chemical Engineering Journal 2022;446. https://doi.org/10.1016/j.cej.2022.136999.

[84] Omojola T, Davidson L. 2D CFD simulations of flow and reaction during carbon dioxide methanation: A spatially resolved channel plate reactor study. Chem Eng Sci 2023;282. https://doi.org/10.1016/j.ces.2023.119235.

[85] Pérez S, Del Molino E, Barrio VL. Modeling and Testing of a Milli-Structured Reactor for Carbon Dioxide Methanation. International Journal of Chemical Reactor Engineering 2019;17. https://doi.org/10.1515/ijcre-2018-0238.

[86] Ghaib K. 3D CFD Simulation of Reaction Cells, Cooling Cells, and Manifolds of a Flatbed Reactor for CO2 Methanation. Chem Eng Technol 2020;43:1994–2006. https://doi.org/10.1002/ceat.202000254.

[87] Engl T, Langer M, Freund H, Rubin M, Dittmeyer R. Tap Reactor for Temporally and Spatially Resolved Analysis of the CO2 Methanation Reaction. Chem Ing Tech 2023;95:658–67. https://doi.org/10.1002/cite.202200204.

[88] Kiewidt L, Thöming J. Predicting optimal temperature profiles in single-stage fixed-bed reactors for CO2-methanation. Chem Eng Sci 2015;132:59–71. https://doi.org/10.1016/j.ces.2015.03.068.

[89] Shirsath AB, Schulte ML, Kreitz B, Tischer S, Grunwaldt JD, Deutschmann O. Spatially-resolved investigation of CO2 methanation over Ni/γ-Al2O3 and Ni3.2Fe/γ-Al2O3 catalysts in a packed-bed reactor. Chemical Engineering Journal 2023;469. https://doi.org/10.1016/j.cej.2023.143847.

[90] Zimmermann RT, Bremer J, Sundmacher K. Load-flexible fixed-bed reactors by multi-period design optimization. Chemical Engineering Journal 2022;428. https://doi.org/10.1016/j.cej.2021.130771.

[91] Zimmermann RT, Bremer J, Sundmacher K. Optimal catalyst particle design for flexible fixed-bed CO2 methanation reactors. Chemical Engineering Journal 2020;387. https://doi.org/10.1016/j.cej.2019.123704.

[92] Theurich S, Rönsch S, Güttel R. Transient Flow Rate Ramps for Methanation of Carbon Dioxide in an Adiabatic Fixed-Bed Recycle Reactor. Energy Technology 2020;8. https://doi.org/10.1002/ente.201901116.

[93] Kreitz B, Wehinger GD, Turek T. Dynamic simulation of the CO2 methanation in a micro-structured fixed-bed reactor. Chem Eng Sci 2019:541–52. https://doi.org/10.1016/j.ces.2018.09.053.

[94] Matthischke S, Roensch S, Güttel R. Start-up Time and Load Range for the Methanation of Carbon Dioxide in a Fixed-Bed Recycle Reactor. Ind Eng Chem Res 2018;57:6391–400. https://doi.org/10.1021/acs.iecr.8b00755.

[95] Hauser A, Feldner A, Treiber P, Grimm F, Karl J. Utilization of Synthetic Steel Gases in an Additively Manufactured Reactor for Catalytic Methanation. Sustainability (Switzerland) 2023;15. https://doi.org/10.3390/su15097652.

[96] Herrmann F, Grünewald M, Riese J. Model-based design of a segmented reactor for the flexible operation of the methanation of CO2. Int J Hydrogen Energy 2023;48:9377–89. https://doi.org/10.1016/j.ijhydene.2022.12.122.

[97] Fischer KL, Freund H. Intensification of load flexible fixed bed reactors by optimal design of staged reactor setups. Chemical Engineering and Processing - Process Intensification 2021;159. https://doi.org/10.1016/j.cep.2020.108183.

[98] Scharl V, Fischer F, Herrmann S, Fendt S, Spliethoff H. Applying Reaction Kinetics to Pseudohomogeneous Methanation Modeling in Fixed-Bed Reactors. Chem Eng Technol 2020;43:1224–33. https://doi.org/10.1002/ceat.201900535.

[99] Gruber M, Wiedmann D, Haas M, Harth S, Loukou A, Trimis D. Insights into the catalytic CO2 methanation of a boiling water cooled fixed-bed reactor: Simulation-based analysis. Chemical Engineering Journal 2021;406. https://doi.org/10.1016/j.cej.2020.126788.

[100] Fischer KL, Freund H. On the optimal design of load flexible fixed bed reactors: Integration of dynamics into the design problem. Chemical Engineering Journal 2020;393. https://doi.org/10.1016/j.cej.2020.124722.

[101] Bremer J, Sundmacher K. Operation range extension via hot-spot control for catalytic CO2 methanation reactors. React Chem Eng 2019;4:1019–37. https://doi.org/10.1039/c9re00147f.

[102] Fischer KL, Langer MR, Freund H. Dynamic Carbon Dioxide Methanation in a Wall-Cooled Fixed Bed Reactor: Comparative Evaluation of Reactor Models. Ind Eng Chem Res 2019;58:19406–20. https://doi.org/10.1021/acs.iecr.9b02863.

[103] Martinez Molina M, Kern C, Jess A. Catalytic Hydrogenation of Carbon Dioxide to Methane in Wall-Cooled Fixed-Bed Reactors‡. Chem Eng Technol 2016;39:2404–15. https://doi.org/10.1002/ceat.201500614.

[104] Bremer J, Rätze KHG, Sundmacher K. CO2 methanation: Optimal start-up control of a fixed-bed reactor for power-to-gas applications. AIChE Journal 2017;63:23–31. https://doi.org/10.1002/aic.15496.

[105] Tauer G, Kern C, Jess A. Transient Effects during Dynamic Operation of a Wall-Cooled Fixed-Bed Reactor for CO2 Methanation. Chem Eng Technol 2019;42:2401–9. https://doi.org/10.1002/ceat.201900367.

[106] Alarcón A, Busqué R, Andreu T, Guilera J. Design of a Multi-Tubular Catalytic Reactor Assisted by CFD Based on Free-Convection Heat-Management for Decentralised Synthetic Methane Production. Catalysts 2022;12. https://doi.org/10.3390/catal12091053.

[107] Alarcón A, Guilera J, Andreu T. An insight into the heat-management for the CO2 methanation based on free convection. Fuel Processing Technology 2021;213. https://doi.org/10.1016/j.fuproc.2020.106666.

[108] Alarcón A, Guilera J, Andreu T. CO2 conversion to synthetic natural gas: Reactor design over Ni–Ce/Al2O3 catalyst. Chemical Engineering Research and Design 2018;140:155–65. https://doi.org/10.1016/j.cherd.2018.10.017.

[109] Torcida MF, Curto D, Martín M. Design and optimization of CO2 hydrogenation multibed reactors. Chemical Engineering Research and Design 2022;181:89–100. https://doi.org/10.1016/j.cherd.2022.03.007.

[110] Gómez-Bravo E, González-Marcos JA, González-Velasco JR, Pereda-Ayo B. Critical role of transport phenomena in the performance of a catalytic fixed bed reactor for the CO2 hydrogenation to CH4 evaluated by modeling and simulation. Chem Eng Sci 2024;297. https://doi.org/10.1016/j.ces.2024.120312.

[111] Costamagna P, Pugliese F, Cavattoni T, Busca G, Garbarino G. Modeling of laboratory steam methane reforming and CO2 methanation reactors. Energies (Basel) 2020;13. https://doi.org/10.3390/en13102624.

[112] Garbarino G, Pugliese F, Cavattoni T, Busca G, Costamagna P. A study on CO2 methanation and steam methane reforming over commercial Ni/calcium aluminate catalysts. Energies (Basel) 2020;13. https://doi.org/10.3390/en13112792.

[113] Di Nardo A, Calchetti G, Bassano C, Deiana P. CO2 methanation in a shell and tube reactor CFD simulations: high temperatures mitigation analysis. Chem Eng Sci 2021;246. https://doi.org/10.1016/j.ces.2021.116871.

[114] Fache A, Marias F, Chaudret B. Catalytic reactors for highly exothermic reactions: Steady-state stability enhancement by magnetic induction. Chemical Engineering Journal 2020;390. https://doi.org/10.1016/j.cej.2020.124531.

[115] Fache A, Marias F, Guerré V, Palmade S. Optimization of fixed-bed methanation reactors: Safe and efficient operation under transient and steady-state conditions. Chem Eng Sci 2018;192:1124–37. https://doi.org/10.1016/j.ces.2018.08.044.

[116] Fache A, Marias F, Guerré V, Palmade S. Intermittent Operation of Fixed-Bed Methanation Reactors: A Simple Relation Between Start-Up Time and Idle State Duration. Waste Biomass Valorization 2020;11:447–63. https://doi.org/10.1007/s12649-018-0507-3.

[117] Fache A, Marias F. Dynamic operation of fixed-bed methanation reactors: Yield control by catalyst dilution profile and magnetic induction. Renew Energy 2020;151:865–86. https://doi.org/10.1016/j.renene.2019.11.081.

[118] Try R, Bengaouer A, Baurens P, Jallut C. Dynamic modeling and simulations of the behavior of a fixed-bed reactor-exchanger used for CO2 methanation. AIChE Journal 2018;64:468–80. https://doi.org/10.1002/aic.15874.

[119] Ducamp J, Bengaouer A, Baurens P. Modelling and experimental validation of a CO2 methanation annular cooled fixed-bed reactor exchanger. Canadian Journal of Chemical Engineering, vol. 95, Wiley-Liss Inc.; 2017, p. 241–52. https://doi.org/10.1002/cjce.22706.

[120] Moioli E. Enhancement of Power-to-Gas via Multicatalyst Reactors Tailoring Reaction Rate and Heat Exchange. Chimia (Aarau), vol. 76, Swiss Chemical Society; 2022, p. 288–93. https://doi.org/10.2533/chimia.2022.288.

[121] Moioli E, Züttel A. A model-based comparison of Ru and Ni catalysts for the Sabatier reaction. Sustain Energy Fuels 2020;4:1396–408. https://doi.org/10.1039/c9se00787c.

[122] Moioli E, Gallandat N, Züttel A. Parametric sensitivity in the Sabatier reaction over Ru/Al2O3-theoretical determination of the minimal requirements for reactor activation. React Chem Eng 2019;4:100–11. https://doi.org/10.1039/c8re00133b.

[123] Hou B, Huang Y, Wang X, Yang X, Duan H, Zhang T. Optimization and simulation of the Sabatier reaction process in a packed bed. AIChE Journal 2016;62:2879–92. https://doi.org/10.1002/aic.15245.

[124] Lin Y, Zhang W, Machida H, Norinaga K. CFD simulation of the Sabatier process in a shell-and-tube reactor under local thermal non-equilibrium conditions: Parameter sensitivity and reaction mechanism analysis. Int J Hydrogen Energy 2022;47:15254–69. https://doi.org/10.1016/j.ijhydene.2022.03.029.

[125] Shen W, Zhang Y, Zhao L, Ye Y, Tursun Y. Micro-scale simulation and intensification of complex Sabatier reaction system in cylindrical catalyst bed. Fuel 2021;287. https://doi.org/10.1016/j.fuel.2020.119399.

[126] Fukumoto K, Zhang W, Mizoguchi R, Lin Y, Choi C, Machida H, et al. CFD simulation of CO2 methanation through the Sabatier reaction in a shell-and-tube reactor incorporating

phase change on the shell side. Fuel 2023;349. https://doi.org/10.1016/j.fuel.2023.128126.

[127] Zhang W, Lin Y, Norinaga K. Insights into structure-performance relationship in radial flow fixed bed reactor for CO2 methanation. Int J Hydrogen Energy 2023;48:24594–606. https://doi.org/10.1016/j.ijhydene.2023.03.343.

[128] Li Y, An J, Wang S, Geng Z, Dong H. Computational fluid dynamics (CFD) simulation of CO2 methanation in a shell-and-tube reactor with boiling water cooling. Advanced Powder Technology 2024;35. https://doi.org/10.1016/j.apt.2024.104671.

[129] Lin Y, Yang C, Choi C, Zhang W, Fukumoto K, Machida H, et al. Inhibition of temperature runaway phenomenon in the Sabatier process using bed dilution structure: LBM-DEM simulation. AIChE Journal 2021;67. https://doi.org/10.1002/aic.17304.

[130] Zhang W, Machida H, Takano H, Izumiya K, Norinaga K. Computational fluid dynamics simulation of CO2 methanation in a shell-and-tube reactor with multi-region conjugate heat transfer. Chem Eng Sci 2020;211. https://doi.org/10.1016/j.ces.2019.115276.

[131] Yamamoto K, Sakaguchi K. 1D modeling of methanation reactor with circulation (MeRCi) for assessment of reaction characteristics. International Journal of Thermofluids 2023;20. https://doi.org/10.1016/j.ijft.2023.100513.

[132] Ngo SI, Lim Y Il. Solution and parameter identification of a fixed-bed reactor model for catalytic co2 methanation using physics-informed neural networks. Catalysts 2021;11. https://doi.org/10.3390/catal11111304.

[133] Ahn J, Kim H, Ro Y, Kim J, Chung W, Chang S. Development of pilot-scale CO2 methanation using pellet-type catalysts for CO2 recycling in sewage treatment plants and its validation through computational fluid dynamics (CFD) modeling. Catalysts 2021;11. https://doi.org/10.3390/catal11081005.

[134] Chein RY, Chen WY, Yu CT. Numerical simulation of carbon dioxide methanation reaction for synthetic natural gas production in fixed-bed reactors. J Nat Gas Sci Eng 2016;29:243–51. https://doi.org/10.1016/j.jngse.2016.01.019.

[135] Sun D, Khan FM, Simakov DSA. Heat removal and catalyst deactivation in a Sabatier reactor for chemical fixation of CO2: Simulation-based analysis. Chemical Engineering Journal 2017;329:165–77. https://doi.org/10.1016/j.cej.2017.06.160.

[136] Sun D, Simakov DSA. Thermal management of a Sabatier reactor for CO2 conversion into CH4: Simulation-based analysis. Journal of CO2 Utilization 2017;21:368–82. https://doi.org/10.1016/j.jcou.2017.07.015.

[137] Currie R, Mottaghi-Tabar S, Zhuang Y, Simakov DSA. Design of an Air-Cooled Sabatier Reactor for Thermocatalytic Hydrogenation of CO2: Experimental Proof-of-Concept and Model-Based Feasibility Analysis. Ind Eng Chem Res 2019;58:12964–80. https://doi.org/10.1021/acs.iecr.9b01426.

[138] Bolt A, Dincer I, Agelin-Chaab M. Transport phenomena modeling of novel renewable natural gas reactors in various configurations. Chem Eng Sci 2022;264. https://doi.org/10.1016/j.ces.2022.118207.

[139] Bolt A, Dincer I, Agelin-Chaab M. Design and assessment of a new helical fixed bed type CO2 methanation reactor. Fuel 2023;337. https://doi.org/10.1016/j.fuel.2022.127176.

[140] Soto V, Ulloa C, Garcia X. A CFD design approach for industrial size tubular reactors for sng production from biogas (CO2 methanation). Energies (Basel) 2021;14. https://doi.org/10.3390/en14196175.

[141] Soto V, Ulloa C, Garcia X. A 3D Transient CFD Simulation of a Multi-Tubular Reactor for Power to Gas Applications. Energies (Basel) 2022;15. https://doi.org/10.3390/en15093383.

[142] Sun D. Simulation-Based Analysis of a Sabatier Reactor for Conversion of CO_2 into Renewable Natural Gas. University of Waterloo, 2016.

[143] Currie R. Design and Simulation of Novel Sabatier Reactors for the Thermocatalytic Conversion of CO_2 into Renewable Natural Gas. University of Waterloo, 2019.

[144] Xu J, Froment GF. Methane steam reforming, methanation and water-gas shift: I. Intrinsic kinetics. AIChE Journal 1989;35:88–96. https://doi.org/10.1002/aic.690350109.

[145] Rönsch S, Köchermann J, Schneider J, Matthischke S. Global Reaction Kinetics of CO and CO_2 Methanation for Dynamic Process Modeling. Chem Eng Technol 2016;39:208–18. https://doi.org/10.1002/ceat.201500327.

[146] Koschany F, Schlereth D, Hinrichsen O. On the kinetics of the methanation of carbon dioxide on coprecipitated $NiAl(O)_x$. Appl Catal B 2016;181:504–16. https://doi.org/10.1016/j.apcatb.2015.07.026.

[147] Lunde PJ, Kester FL. Rates of methane formation from carbon dioxide and hydrogen over a ruthenium catalyst. J Catal 1973;30:423–9. https://doi.org/10.1016/0021-9517(73)90159-0.

[148] Falbo L, Martinelli M, Visconti CG, Lietti L, Bassano C, Deiana P. Kinetics of CO_2 methanation on a Ru-based catalyst at process conditions relevant for Power-to-Gas applications. Appl Catal B 2018;225:354–63. https://doi.org/10.1016/j.apcatb.2017.11.066.

[149] Janke C, Duyar MS, Hoskins M, Farrauto R. Catalytic and adsorption studies for the hydrogenation of CO_2 to methane. Appl Catal B 2014;152–153:184–91. https://doi.org/10.1016/j.apcatb.2014.01.016.

[150] Vita A, Italiano C, Pino L, Laganà M, Ferraro M, Antonucci V. High-temperature CO_2 methanation over structured Ni/GDC catalysts: Performance and scale-up for Power-to-Gas application. Fuel Processing Technology 2020;202. https://doi.org/10.1016/j.fuproc.2020.106365.

[151] Ahn JY, Chang SW, Lee SM, Kim SS, Chung WJ, Lee JC, et al. Developing Ni-based honeycomb-type catalysts using different binary oxide-supported species for synergistically enhanced CO_2 methanation activity. Fuel 2019;250:277–84. https://doi.org/10.1016/j.fuel.2019.03.123.

[152] Bustinza A, Frías M, Liu Y, García-Bordejé E. Mono- and bimetallic metal catalysts based on Ni and Ru supported on alumina-coated monoliths for CO_2 methanation. Catal Sci Technol 2020;10:4061–71. https://doi.org/10.1039/D0CY00639D.

[153] Middelkoop V, Vamvakeros A, de Wit D, Jacques SDM, Danaci S, Jacquot C, et al. 3D printed Ni/Al_2O_3 based catalysts for CO_2 methanation - a comparative and operando XRD-CT study. Journal of CO2 Utilization 2019;33:478–87. https://doi.org/10.1016/j.jcou.2019.07.013.

[154] Ricca A, Truda L, Palma V. Study of the role of chemical support and structured carrier on the CO_2 methanation reaction. Chemical Engineering Journal 2019;377. https://doi.org/10.1016/j.cej.2018.11.159.

[155] Huynh HL, Tucho WM, Yu Z. Structured NiFe catalysts derived from in-situ grown layered double hydroxides on ceramic monolith for CO_2 methanation. Green Energy & Environment 2020;5:423–32. https://doi.org/10.1016/j.gee.2020.09.004.

[156] Huynh HL, Tucho WM, Shen Q, Yu Z. Bed packing configuration and hot-spot utilization for low-temperature CO_2 methanation on monolithic reactor. Chemical Engineering Journal 2022;428. https://doi.org/10.1016/j.cej.2021.131106.

[157] Navarro JC, Centeno MA, Laguna OH, Odriozola JA. Ru–Ni/$MgAl_2O_4$ structured catalyst for CO_2 methanation. Renew Energy 2020;161:120–32. https://doi.org/10.1016/j.renene.2020.07.055.

[158] García-Moncada N, Navarro JC, Odriozola JA, Lefferts L, Faria JA. Enhanced catalytic activity and stability of nanoshaped Ni/CeO_2 for CO_2 methanation in micro-monoliths. Catal Today 2021. https://doi.org/10.1016/j.cattod.2021.02.014.

[159] Ridder H, Sinn C, Pesch GR, Ilsemann J, Dreher W, Thöming J. A large fixed bed reactor for MRI *operando* experiments at elevated temperature and pressure. Review of Scientific Instruments 2021;92:043711. https://doi.org/10.1063/5.0044795.

[160] Chaparro-Garnica CY, Bailón-García E, Davó-Quiñonero A, Da Costa P, Lozano-Castelló D, Bueno-López A. High Performance Tunable Catalysts Prepared by Using 3D Printing. Materials 2021;14:5017. https://doi.org/10.3390/ma14175017.

[161] Schlereth D, Donaubauer PJ, Hinrichsen O. Metallic Honeycombs as Catalyst Supports for Methanation of Carbon Dioxide. Chem Eng Technol 2015;38:1845–52. https://doi.org/10.1002/ceat.201400717.

[162] Schollenberger D, Bajohr S, Gruber M, Reimert R, Kolb T. Scale-Up of Innovative Honeycomb Reactors for Power-to-Gas Applications – The Project Store&Go. Chemie Ingenieur Technik 2018;90:696–702. https://doi.org/10.1002/cite.201700139.

[163] Méndez JAM, González-Castaño M, Baena-Moreno FM, Arellano-García H. CO_2 methanation: on the modeling of reacting laminar flows in structured Ni/$MgAl_2O_4$ catalysts. J Phys Conf Ser 2022;2367:012015. https://doi.org/10.1088/1742-6596/2367/1/012015.

[164] Lefebvre J, Bajohr S, Kolb T. Modeling of the transient behavior of a slurry bubble column reactor for CO_2 methanation, and comparison with a tube bundle reactor. Renew Energy 2020;151:118–36. https://doi.org/10.1016/j.renene.2019.11.008.

[165] Try R, Bengaouer A, Baurens P, Jallut C. Dynamic modeling and simulations of the behavior of a fixed-bed reactor-exchanger used for CO_2 methanation. AIChE Journal 2018;64:468–80. https://doi.org/10.1002/aic.15874.

[166] Fischer KL, Langer MR, Freund H. Dynamic Carbon Dioxide Methanation in a Wall-Cooled Fixed Bed Reactor: Comparative Evaluation of Reactor Models. Ind Eng Chem Res 2019;58:19406–20. https://doi.org/10.1021/acs.iecr.9b02863.

[167] Tauer G, Kern C, Jess A. Transient Effects during Dynamic Operation of a Wall-Cooled Fixed-Bed Reactor for CO_2 Methanation. Chem Eng Technol 2019;42:2401–9. https://doi.org/10.1002/ceat.201900367.

[168] Theurich S, Rönsch S, Güttel R. Transient Flow Rate Ramps for Methanation of Carbon Dioxide in an Adiabatic Fixed-Bed Recycle Reactor. Energy Technology 2020;8:1901116. https://doi.org/10.1002/ente.201901116.

[169] Fischer KL, Freund H. On the optimal design of load flexible fixed bed reactors: Integration of dynamics into the design problem. Chemical Engineering Journal 2020;393. https://doi.org/10.1016/j.cej.2020.124722.

[170] Soto V, Ulloa C, Garcia X. A 3D Transient CFD Simulation of a Multi-Tubular Reactor for Power to Gas Applications. Energies (Basel) 2022;15:3383. https://doi.org/10.3390/en15093383.

[171] Fache A, Marias F, Guerré V, Palmade S. Optimization of fixed-bed methanation reactors: Safe and efficient operation under transient and steady-state conditions. Chem Eng Sci 2018;192:1124–37. https://doi.org/10.1016/j.ces.2018.08.044.

[172] Fache A, Marias F, Guerré V, Palmade S. Intermittent Operation of Fixed-Bed Methanation Reactors: A Simple Relation Between Start-Up Time and Idle State Duration. Waste Biomass Valorization 2020;11:447–63. https://doi.org/10.1007/s12649-018-0507-3.

[173] Fache A, Marias F. Dynamic operation of fixed-bed methanation reactors: Yield control by catalyst dilution profile and magnetic induction. Renew Energy 2020;151:865–86. https://doi.org/10.1016/j.renene.2019.11.081.

[174] Prabhakaran P, Graf F, Koeppel W, Kolb T. Modelling and validation of energy systems with dynamically operated Power to Gas plants for gas-based sector coupling in de-central energy hubs. Energy Convers Manag 2023;276:116534. https://doi.org/10.1016/j.enconman.2022.116534.

[175] Kreitz B, Wehinger GD, Turek T. Dynamic simulation of the CO2 methanation in a micro-structured fixed-bed reactor. Chem Eng Sci 2019;195:541–52. https://doi.org/10.1016/j.ces.2018.09.053.

[176] Zimmermann RT, Bremer J, Sundmacher K. Load-flexible fixed-bed reactors by multi-period design optimization. Chemical Engineering Journal 2022;428:130771. https://doi.org/10.1016/j.cej.2021.130771.

[177] Fischer KL, Freund H. Intensification of load flexible fixed bed reactors by optimal design of staged reactor setups. Chemical Engineering and Processing - Process Intensification 2021;159:108183. https://doi.org/10.1016/j.cep.2020.108183.

[178] Arab S, Commenge J-M, Portha J-F, Falk L. Methanol synthesis from CO2 and H2 in multi-tubular fixed-bed reactor and multi-tubular reactor filled with monoliths. Chemical Engineering Research and Design 2014;92:2598–608. https://doi.org/10.1016/j.cherd.2014.03.009.

[179] Kota AS, Dadi RK, Luss D, Balakotaiah V. Analysis of light-off during oxidation of reactant mixtures on Pt/Al2O3 using micro-kinetic models. Chem Eng Sci 2017;166:320–33. https://doi.org/10.1016/j.ces.2017.02.050.

[180] Zhou Z, Harold MP, Luss D. Dynamic Oxygen Storage Capacity of Ceria-Zirconia and $Mn_{0.5}Fe_{2.5}O_4$ Spinel: Experiments and Modeling. Ind Eng Chem Res 2021;60:6465–82. https://doi.org/10.1021/acs.iecr.0c05187.

[181] Iliuta I, Larachi F, Fontaine F-G. Performance of catalytic cycloaddition of CO2 to styrene oxide in three-phase co-current (micro)fixed-bed and monolith reactors. Journal of CO2 Utilization 2022;60:101977. https://doi.org/10.1016/j.jcou.2022.101977.

[182] Groppi G, Belloli A, Tronconi E, Forzatti P. A comparison of lumped and distributed models of monolith catalytic combustors. Chem Eng Sci 1995;50:2705–15. https://doi.org/10.1016/0009-2509(95)00099-Q.

[183] Hayes RE, Awdry S, Kolaczkowski ST. Catalytic combustion of methane in a monolith washcoat: Effect of water inhibition on the effectiveness factor. Can J Chem Eng 1999;77:688–97. https://doi.org/10.1002/cjce.5450770410.

[184] Papadias D, Edsberg L, Björnbom P. Simplified method for effectiveness factor calculations in irregular geometries of washcoats. Chem Eng Sci 2000;55:1447–59. https://doi.org/10.1016/S0009-2509(99)00375-9.

[185] GONZO E. Hydrogen from methanol-steam reforming. Isothermal and adiabatic monolith reactors' simulation. Int J Hydrogen Energy 2008;33:3511–6. https://doi.org/10.1016/j.ijhydene.2007.11.001.

[186] Groppi G, Tronconi E, Cortelli C, Leanza R. Conductive Monolithic Catalysts: Development and Industrial Pilot Tests for the Oxidation of *o* -Xylene to Phthalic Anhydride. Ind Eng Chem Res 2012;51:7590–6. https://doi.org/10.1021/ie2021653.

[187] Strucks P, Failing L, Kaluza S. A Short Review on Ni-Catalyzed Methanation of CO_2: Reaction Mechanism, Catalyst Deactivation, Dynamic Operation. Chemie Ingenieur Technik 2021;93:1526–36. https://doi.org/10.1002/cite.202100049.

[188] Jakobsen HA. Chemical Reactor Modeling. Cham: Springer International Publishing; 2014. https://doi.org/10.1007/978-3-319-05092-8.

[189] Schollenberger D. Anwendung von Wabenreaktoren für die Methanisierung bei Power-to-Gas-Prozessen. Karlsruher Instituts für Technologie, 2022.

[190] Glockner F. Modellierung von technischen Wabenkatalysatoren für die katalytische Methanisierung. Karlsruher Institut für Technologie, 2023.

[191] Froment GF, Bischoff KB, De Wilde J. Chemical Reactor Analysis and Design. 3rd ed. John Wiley & Sons; 2011.

[192] Grigull U, Tratz H. Thermischer einlauf in ausgebildeter laminarer rohrströmung. Int J Heat Mass Transf 1965;8:669–78. https://doi.org/10.1016/0017-9310(65)90016-5.

[193] Groppi G, Tronconi E. Design of novel monolith catalyst supports for gas/solid reactions with heat exchange. Chem Eng Sci 2000;55:2161–71. https://doi.org/10.1016/S0009-2509(99)00440-6.

[194] Visconti CG, Tronconi E, Groppi G, Lietti L, Iovane M, Rossini S, et al. Monolithic catalysts with high thermal conductivity for the Fischer–Tropsch synthesis in tubular reactors. Chemical Engineering Journal 2011;171:1294–307. https://doi.org/10.1016/j.cej.2011.05.014.

[195] Visconti CG, Groppi G, Tronconi E. Accurate prediction of the effective radial conductivity of highly conductive honeycomb monoliths with square channels. Chemical Engineering Journal 2013;223:224–30. https://doi.org/10.1016/j.cej.2013.02.095.

[196] Groppi G, Tronconi E. Honeycomb supports with high thermal conductivity for gas/solid chemical processes. Catal Today 2005;105:297–304. https://doi.org/10.1016/j.cattod.2005.06.041.

[197] Poling BE, Prausnitz JM, O'Connell JP. The properties of gases and liquids. 5th ed. McGraw-Hill Education; 2004.

[198] VDI. VDI Heat Atlas. 2nd ed. Springer Berlin, Heidelberg; 2010.

[199] Green DW, Southard MZ. Perry's Chemical Engineers' Handbook. 9th ed. McGraw-Hill Education; 2019.

[200] Matthischke S, Roensch S, Güttel R. Start-up Time and Load Range for the Methanation of Carbon Dioxide in a Fixed-Bed Recycle Reactor. Ind Eng Chem Res 2018;57:6391–400. https://doi.org/10.1021/acs.iecr.8b00755.

[201] Zimmermann RT, Bremer J, Sundmacher K. Optimal catalyst particle design for flexible fixed-bed CO2 methanation reactors. Chemical Engineering Journal 2020;387:123704. https://doi.org/10.1016/j.cej.2019.123704.

[202] Try R. Étude expérimentale et modélisation dynamique d'un réacteur catalytique modulaire pour l'hydrogénation du CO2 en méthane. Université de Lyon, 2018.

[203] Tauer GS. Verhalten eines wandgekühlten Festbett-reaktors zur CO2-Methanisierung bei instationären Betriebsbedingungen. Universität Bayreuth, 2021.

[204] Fischer KL. Model-based design of load flexible fixed bed reactors. Friedrich-Alexander-Universität Erlangen-Nürnberg, 2021.

[205] Theurich S. Unsteady-State Operation of a Fixed-Bed Recycle Reactor for the Methanation of Carbon Dioxide. Ulm University, 2019.

[206] Lefebvre J. Three-phase CO_2 methanation: methanation reaction kinetics and transient behavior of a slurry bubble column reactor. Karlsruher Institut für Technologie, 2019.

A. Appendix A: Supporting Information of CO_2 Methanation Reactors Modeling. Reviewing the last decade.

A.1.Boundary and initial conditions

Reactors often have unique starting conditions, but dynamic modeling studies frequently assume that the initial composition, temperature, and pressure align with the feed flow of the equipment. This approach also applies to velocity, with most studies choosing the feed flow velocity as the initial value rather than a specific value or a scenario where the fluid is stationary (zero velocity).

In reactor modeling for CO_2 methanation, the Dirichlet condition (82) is commonly used at the reactor entrance. It sets constant values for gas composition, temperature, pressure, and velocity, reflecting the feed flow parameters. However, some studies prefer Robin's condition $\left(\frac{\partial y}{\partial z} = ay + b\right)$ for gas composition and temperature, employing Danckwerts conditions when the system is closed-closed [30,51,52,56,57,60,61,63,67,71,90,93,110,135–137]. If axial dispersion of mass and heat is significant, Danckwerts conditions are advised, as fixed inlet values may lead to inaccurate predictions. For the solid's temperature, the Neumann condition (5) is mainly applied, suggesting an adiabatic state $\left(\frac{\partial T_{solid}}{\partial z} = 0\right)$ at the inlet, particularly relevant to the monolithic substrate of the HM reactor (3/6) and the FXB reactor wall (2/64).

For the reactor outlet boundary condition, the Neumann condition is often used (40), indicating no gradients $\left(\frac{\partial y}{\partial z} = 0\right)$ in gas composition and temperature at the exit. Another approach involves setting the second derivatives of composition and concentration concerning the axial direction (z) to zero $\left(\frac{\partial^2 y}{\partial z^2} = 0\right)$ [30,67,90,93], relevant when the reaction rate remains significant at the outlet, suggesting linear gradients along the axial coordinate [30,93]. For the monolithic substrate and

FXB wall scenarios, outputs are suggested to be adiabatic (5). When considering axial momentum dispersion, most models assume a constant pressure at the reactor outlet (34), differing from studies that consider a zero velocity gradient at the outlet [20,45,49,84,134] .

In studies involving 2D-3D modeling of reactors, a symmetric boundary condition is typically assumed at the reactor's center, except in cases focusing on annular reactors where the catalyst is in the shell area. This symmetrical assumption implies the absence of gradients in composition, temperature, pressure, or velocity along the reactor's central axis $\left(\frac{\partial y}{\partial r} = 0\right)$.

In modeling studies, it's suggested that there should be no gradient in gas composition at the reactor wall, assuming the equipment is neither permeable nor membrane-surrounded. If these conditions aren't met, a Robin condition should be used to model mass transport at that point. Regarding velocity, most studies use the non-slip condition, meaning the gas velocity at the wall is zero. The gas temperature boundary condition depends on the model's thermal situation. In an adiabatic reactor, there is no radial temperature gradient at the wall. If a cooling medium maintains the wall temperature effectively, the gas temperature can be assumed to match it, assuming no heat transfer resistance exists. Alternatively, a Robin condition is advised for detailed energy transfer representation between the gas and wall. For a monolithic substrate and FXB wall, similar temperature considerations apply, necessitating an appropriate boundary condition to accurately reflect the reactor's radial behavior (*r*).

In scenarios involving catalyst particles, composition and temperature profiles typically show symmetry along their central axis. However, when catalysts are applied to channel walls in structures like HM, MC, PHE, foams, fibers, millichannels, plates, taps, parallel channels, U-channels, and spirals, if the walls are impermeable, it is assumed that there are no composition and temperature gradients at the interface catalyst-channel wall. At the catalyst gas-surface

interface, HET studies use Robin's condition for mass and energy transfer or assume fixed gas composition and temperature values matching the bulk gas, assuming minimal resistance to mass and energy transfer.

This analysis suggests that selecting boundary conditions for a reactor's mathematical model depends on the study's goals and operational conditions. For experimental validation, it's crucial to choose appropriate boundary conditions; otherwise, the results may significantly differ from the actual reactor's observed behavior.

A.2.Boundary and initial conditions

This section will highlight the key aspects of assumptions used in modeling CO_2 methanation reactors, organized into four main subsections.

A.2.1.Physical properties

In many reviewed studies (85), the physical properties of gas—viscosity, specific heat, thermal conductivity, and diffusivity—are determined using established literature correlations, with few instances of them being assumed constant. This meticulous determination is essential for industrial applications. The choice to assume constant properties can significantly impact mathematical model outcomes, as these properties are influenced by composition, temperature, and pressure.

The physical properties of the reactor tube (31), catalyst (100), and cooling medium (59) are generally considered constant, especially for the solid-phase tube and catalyst, except for temperature-dependent properties. This constancy also applies to the monolithic substrate of HM (4). However, the cooling medium's properties can vary significantly with temperature changes,

and whether this simplification is applicable depends on the cooling fluid. For example, if water or air are used as the cooling medium, this simplification is not recommended.

Moreover, while catalyst porosity can be considered constant in scenarios without deactivation reactions, this is often not the case for reactors with catalyst particle beds. In FB and SBC reactors, bed porosity usually varies because of particle movement. Other reactors using catalyst particle beds or foams have been studied in modeling research, which considers porosity changes relative to the radial coordinate [53,74,75,98,99,115,117].

Consequently, most modeling publications calculate the gas's physical properties, while further examination is needed to determine if other properties should be considered constant, based on the reactor's conditions and study objectives.

A.2.2.Thermal conditions

Nine modeling studies have investigated CO_2 methanation reactors operating under isothermal conditions [25,54,55,58,59,62,69–71]. Conversely, there are 6 published studies focused on reactors that operate under adiabatic conditions [43,48,60,92,94,121]. Additionally, some studies have investigated how changing the temperature of the cooling medium [26,30,52,93,102,113,115,116,124,126,135,136,140,141,143] (15) and/or the reactor wall impacts the process [23,92,94,96,106,113–119,124,126,127,140,141] .

It is observed that most reactor modeling studies for the Sabatier reaction do not assume isothermal conditions due to the highly exothermic nature of CO_2 methanation. However, isothermal conditions might be feasible with substantial cooling, effective mixing, and superior thermal characteristics. There are few studies on adiabatic conditions, despite the aim to replace adiabatic FXB reactor technology. Existing studies help improve reactor operation and design

under adiabatic conditions. Most studies assume constant reactor wall and cooling medium temperatures, valid if there's a high flow rate of the cooling medium and minimal heat transfer resistance. For assessing cooling medium impact, determining optimal flow rates, or proposing suitable reactor designs, existing literature provides valuable insights for future research.

A.2.3.Effects of axial/radial dispersion and limitations on energy and mass transport.

To begin with, much of the research has focused on axial mass dispersion with 76 publications and heat dispersion of gas with 71 publications. There is also significant examination of radial dispersion of mass and heat in 2D-3D modeling studies.

The influence of axial diffusion of mass and energy on gas composition and temperature in a reactor can be significant or negligible, depending on operating conditions and reactor dimensions. Radial gradients in composition and temperature are typically insignificant with substantial mixing and minimal radial thermal resistance. Correct boundary conditions at the reactor's entrance must be selected based on the level of axial dispersion, using either Dirichlet or Danckwerts closed-closed conditions. For the FXB reactor’s wall and the HM reactor’s monolithic substrate, analyses account for axial and radial heat dispersion, assuming negligible gradients in solids with high thermal conductivity.

Conversely, 63 studies focus on the limitations of mass and heat transfer at the gas-catalyst boundary. These resistances can be ignored if fluid velocity and contact specific surface area are large enough, potentially aligning the composition at the catalyst surface with that in the gas. For intraparticle mass (75) and heat (79) transfer limitations, most modeling studies take them into account. However, these resistances can be overlooked if the catalyst size is sufficiently small.

From the information provided, a significant part of CO_2 methanation reactor modeling research has focused on including the effects of both axial and radial mass and heat dispersion, as well as axial and radial conduction impacts on the monolithic HM reactor substrate and the FXB reactor wall. Additionally, many studies have mainly addressed the limitations of mass and heat transfer within the solid catalyst. These findings are particularly useful in scenarios where these phenomena are crucial, providing more accurate predictions of reactor performance.

A.2.4.Equation of state and fluid dynamics

The ideal gas equation is primarily used for modeling CO_2 methanation reactors because the gas mixture involved (CO_2, H_2, CH_4, H_2O, etc.) behaves as an ideal gas under the usual industrial conditions of temperature, pressure, and composition [57,65,73]. For instance, Lefebvre *et al.*, [73] illustrated that the difference between the density estimated using the ideal gas equation and that obtained with the Peng Robinson equation of state was less than 1%. Moreover, there are investigations that have calculated gas density using tabulated values [135,136] and the Soave-Redlich-Kwong equation of state [96], while in some instances, the density is assumed to remain constant [47,103,105,132].

In examining fluid dynamics within reac}}tors, modeling studies often adopt various assumptions to simplify calculations. Some assume weak compressibility (27), others a plug flow velocity profile (57), while some consider pressure drop insignificant (22) and restrict fluid movement to the axial direction (58). Additionally, some studies disregard axial and radial momentum transport (60). These assumptions are made because the momentum balance introduces minor time constant effects compared to component mass and energy balances, which significantly increase the stiffness of the system's partial differential equations during non-steady-state conditions, thereby elevating computational costs [74,75,101,104]. Most studies in literature, excluding those using computational fluid dynamics tools, focus on the pressure drop as the key factor in the momentum

equation. They use a pseudo-stationary momentum conservation equation when solving transient state mass and energy conservation equations. To simplify reactor modeling for the Sabatier reaction, researchers often assume constant gas density over time. This assumption addresses the problem's stiffness and is based on no mass accumulation [30,93], weak compressibility, or a plug flow velocity profile.

Therefore, the ideal gas equation is considered a suitable alternative for calculating gas density under the operating conditions of CO_2 methanation. It is suggested to compare these results with those from more accurate equations of state. The momentum balance resolution for deriving velocity and pressure profiles is challenging without proper computational tools. Simplifications may be recommended if the study's primary focus is not on gas fluid dynamics and if velocity and density have lower time constants compared to composition and temperature.

A.3.Contributions

This review examines several contributions to comparative studies on anticipated reactor behavior concerning different model dimensions and phases. It analyzes the reactors' dynamic response to various H_2 load fluctuations and other operational parameters. The review also includes a study on how different methodologies for calculating the effectiveness factor impact model predictions. Additionally, it investigates how catalytic activities linked to different reaction rate expressions influence the performance of the CO_2 methanation reactor.

In addition to the previously mentioned points, the primary contributions from most modeling studies of reactors used in the Sabatier reaction focus on evaluating the reactor's behavior under specific operating conditions. These studies conduct parametric analysis to explore the dependence of performance variables like CO_2 conversion, temperature, and pressure on

operational factors such as inlet flow, feed temperature, and cooling temperature. Some have also contributed to advancements in reactor design and optimization of operating conditions.

Beyond these contributions, other significant advancements in modeling work include comparative studies of various reactor types and the creation of innovative operational methodologies.

A.3.1.Comparative studies: Alternative technologies vs FXB reactor

In comparative studies on reactors, the FXB reactor is often used as a benchmark due to its prevalent use in modeling studies and its adiabatic form in CO_2 methanation technology. However, Raghu *et al*.,'s research deviates from this trend, showing that a spiral reactor outperforms a U-shaped reactor [78]. In contrast, the U-shaped reactor performs better for CO_2 methanation than a parallel channel reactor operating in a co-current manner [77].

Schlereth *et al*., [22] found that the HM reactor maintains consistent temperatures even at high levels, unlike the FXB reactor. However, the FXB reactor's temperature variation can lead to higher CO_2 conversion rates if the temperature hot spot is moderate. They suggest combining both reactors: starting with the HM reactor for intermediate conversion and stable temperatures, followed by the FXB reactor to achieve a higher conversion rate than either reactor alone. Conversely, Zhang *et al*., [26] discovered that the HM reactor has less pressure drop and better heat transfer than the FXB reactor, though it converts less CO_2. They noted that smaller channel sizes can improve conversion but warned this could increase pressure drop. If the conversion rate per pressure drop decreases too much, the FXB reactor might become more effective, potentially negating the HM reactor's advantages.

Currie *et al*., [52] emphasized that using a hydrogen-selective membrane in the FXB reactor aids in preventing catalyst deactivation due to coking and ensures a more uniform temperature

distribution. Similarly, Faria *et al*., [56] showed that adding a hydrogen-selective membrane greatly improves the performance of the FXB reactor over a wide range of operations. Conversely, it is essential to mention that Iwakiri *et al*., [51] conducted research using a membrane with low selectivity and suggested that besides enhancing the membrane's material properties, employing a flow-splitting strategy to divide the M reactor into two zones could provide the benefits of a water-selective membrane. Lastly, Harkou *et al*., [54] performed studies similar to previous research, evaluating two membranes with varying selectivities. They discovered that changing the membrane's thickness was not beneficial for one membrane, but reducing the thickness of the other was recommended to optimize its use in the FXB reactor.

In examining the FB reactor, Ngo *et al*., [71] discovered that it provides better thermal regulation than the FXB reactor in different operational settings. They suggest using recirculation currents and arranging reactors in series to attain comparable thermal efficiency in a FXB reactor. Conversely, Lefebvre *et al*., [73] compared the SBC reactor with the FXB reactor under both stationary and transient conditions. They found that the FXB reactor operates at a higher space velocity in a steady-state. However, the SBC reactor outperforms in thermal control and maintains product quality during non-steady conditions with fluctuating feed. Furthermore, Kiewidt *et al.,* [74,75] conducted a comparative analysis of the foam reactor and FXB reactor, finding the foam reactor promising for small to medium-scale operations in transient scenarios. It offers exceptional thermal properties but operates at lower gas loads than the FXB reactor. While the foam reactor has reduced pressure drops compared to traditional reactors, this advantage is offset by the need for a smaller window diameter to achieve optimal performance.

Therefore, comparing different reactor types, using the FXB reactor as a benchmark, is essential for selecting the appropriate technology for CO_2 methanation. This choice depends on factors like budget, process scale, operational conditions, and the reactor's dynamic properties.

A.3.2.Other type of comparative studies

Moreover, various studies have examined the efficiency of FXB and SBC reactors [73], as well as examining the thermal characteristics of the fiber reactor [79,80]. In contrast, research by Kiewidt *et al*., [88] highlighted that optimizing the Semenov number can create an ideal temperature profile for an FXB reactor, balancing kinetic and thermodynamic constraints to achieve high CO_2 conversion rates. Additionally, research has focused on kinetic [50,59,69,83,87,89,111,112] and fluid dynamic [68,70] studies. Lastly, there have been investigations utilizing neural networks [132] and LBM-DEM simulations [129] to assess the performance of the FXB reactor.

Although these studies may not be as numerous as those on evaluation work, parametric studies, reactor design, and optimization, they can lay the groundwork for tackling future challenges in CO_2 methanation reactor modeling and enhance the quality of results in related areas.

A.3.3.New operating methodologies

Over time, new methods have been developed to improve the catalytic efficiency and thermal management of CO_2 methanation reactors.

The FXB reactor utilizes a recirculation method effectively for both adiabatic and polytropic operations. This approach meets the required operational standards for steady-state and transient conditions and is efficient for reactor startup and achieving a new steady-state following a disturbance [92,94]. Similar research on steady-state operations was conducted by Yamamoto *et al*., [131].

Conversely, the placement of the bed inside the reactor is crucial for optimal temperature distribution, with a recommendation to extend the inlet zone of the reaction system [133].

Furthermore, efforts have been focused on improving the FXB reactor's performance by optimizing the arrangement of cylindrical catalysts within the bed and identifying the ideal number of holes they should have [125]. Bolt *et al*., [138] aimed to enhance the FXB reactor's performance through four strategies: using series reactors, creating a dual compartment with equal volumes for gas and coolant flow, and employing rectangular prism and helicoid designs. In contrast, Herrmann *et al*., [96] proposed a 4-chamber reactor design to enhance the performance of FXB reactors. Lastly, Zhang *et al*., [127] investigated different configurations for radial gas flow in the FXB reactor, finding that centrifugal flow provides better thermal regulation and centripetal flow improves selectivity towards CH_4.

In their study of HM reactors, Schollenberger *et al*., [23] explored HM reactors by using two reactors in series, each made from different materials. The first reactor is aluminum, allowing controlled heat management during reactions. The second is stainless steel, preventing rapid cooling and achieving higher conversion rates than when each material is used independently in HM reactors. Conversely, Huynh *et al*., [24] developed a sequence of three HM reactors, with the first two having lower catalytic activity than the third. This setup improves temperature control, reduces hot spots, and boosts CO_2 conversion. Furthermore, Zhang *et al*., [26] proposed modifying the HM reactor by obstructing some channels to create a chess pattern. This change enhances heat transfer efficiency and reduces hot spot formation, though it lowers CO_2 conversion. By blocking only half of the channels, the pressure drop decreases, while maintaining the conversion rate of the original HM reactor. This makes it potentially more effective than the FXB reactor evaluated in the study.

According to the analysis mentioned above, these proposals contribute to improving reactor performance, but securing adequate funding is essential to conducting tests and confirming their

future applicability. Additionally, it is suggested that these studies extend to encompass other reactors beyond FXB and HM.

B. Appendix B: Supporting Information of Modeling the dynamic operation of a monolithic CO_2 methanation reactor. Evaluation of the response to H_2 load fluctuation.

B.1.Mass/heat transfer coefficients, friction factor, axial dispersion, and axial/radial thermal conductivity of the solid

Table B.1 exhibits the correlations chosen for this study to compute the heat and mass transfer coefficients between phases, the friction factor, and the axial/radial thermal conductivities of the solid for the monolithic honeycomb reactor.

Table B.1. Correlations to calculate mass/heat transfer coefficients, friction factor, axial dispersion, and axial/radial thermal conductivity of the solid.

Gas-solid heat transfer coefficient $Nu_{gs} = \frac{h_{gs} d_h}{\lambda_g} = 3.095 + 8.9336 \cdot \left(\frac{1000}{Gr_{z,T}}\right)^{-0.5386} exp\left(\frac{-6.7275}{Gr_{z,T}}\right);$ $Gr_{z,T} = \frac{Re_g \cdot Pr_g \cdot d_h}{z};\ Re_G = \frac{\rho_g u_{z,g} d_h}{\varepsilon_g \mu_g};\ Pr_g = \frac{C_{p,g}\mu_g}{\lambda_g}$	B.1
Gas-solid mass transfer coefficient $Sh_{i,gs} = \frac{k_{i,gs} d_h}{D_{i,g}} = 3.095 + 8.9336 \cdot \left(\frac{1000}{Gr_{z,m}}\right)^{-0.5386} exp\left(\frac{-6.7275}{Gr_{z,m}}\right);$ $Gr_{z,m} = \frac{Re_g \cdot Sc_{i,g} \cdot d_h}{z};\ Sc_{i,g} = \frac{\mu_g}{\rho_g D_{i,g}}$	B.2
Friction factor $fRe_g = 14.227 + 17.76323 \cdot \left(1000 z_{f,Re_g}\right)^{-0.4715} exp\left(-59.57 z_{f,Re_g}\right)$ $z_{f,Re_g} = \frac{z}{Re_g \cdot d_h}$	B.3
Axial dispersion of each compound in the gas $D_{i\_axial,g} = D_{i,g} + \frac{\left(\frac{u_{z,g}}{\varepsilon_g} d_h\right)^2}{192 \cdot D_{i,g}}$	B.4
Axial thermal conductivity of the solid $\lambda_{axial,s} = \varepsilon_{cat}\lambda_{cat} + \varepsilon_{sup}\lambda_{sup}$	B.5

Radial thermal conductivity of the solid

$$\lambda_{radial,s} = \lambda_{sup}\left(\frac{\frac{\lambda^{*2}}{\lambda_{sup}{}^2}\frac{1-(\varepsilon_g+\varepsilon_{cat})}{1+(\varepsilon_g+\varepsilon_{cat})}+\frac{\lambda^*}{\lambda_{sup}}\frac{3(\varepsilon_g+\varepsilon_{cat})^2+2(\varepsilon_g+\varepsilon_{cat})+3}{(1+(\varepsilon_g+\varepsilon_{cat}))^2}+2\frac{1-(\varepsilon_g+\varepsilon_{cat})}{1+(\varepsilon_g+\varepsilon_{cat})}}{\frac{\lambda^{*2}}{\lambda_{sup}{}^2}\left(\frac{1-(\varepsilon_g+\varepsilon_{cat})}{1+(\varepsilon_g+\varepsilon_{cat})}\right)^2+3\frac{\lambda^*}{\lambda_{sup}}\frac{1-(\varepsilon_g+\varepsilon_{cat})}{1+(\varepsilon_g+\varepsilon_{cat})}+2}\right); \quad \text{B.6}$$

$$\lambda^* = \lambda_{cat}\left(\frac{\frac{\lambda_g{}^2}{\lambda_{cat}{}^2}\frac{1-\varepsilon_g}{1+\varepsilon_g}+\frac{\lambda_g}{\lambda_{cat}}\frac{3\varepsilon_g{}^2+2\varepsilon_g+3}{(1+\varepsilon_g)^2}+2\frac{1-\varepsilon_g}{1+\varepsilon_g}}{\frac{\lambda_g{}^2}{\lambda_{cat}{}^2}\left(\frac{1-\varepsilon_g}{1+\varepsilon_g}\right)^2+\frac{\lambda_g}{\lambda_{cat}}\frac{1-\varepsilon_g}{1+\varepsilon_g}+2}\right)$$

Solid-Cooling System Heat Transfer Coefficient

$$U_{sc}\left[\frac{W}{m^2\cdot K}\right] = 2410.1\lambda_g + 271.64;\ \lambda_g\ in\ \frac{W}{m\cdot K} \quad \text{B.7}$$

The expression for determining the h_{gs} value (Equation B.1) suggested by Groppi *et al*., [182] is an adjusted version, tailored for square channels, of Grigull & Tratz's original formulation for laminar flow in circular channels [192]. The calculation for $k_{i,gs}$ was performed through Equation B.2, which was also a formulation by Groppi *et al*., [182]. Shah & London's expression was utilized for the friction factor *f (*Equation B.3), which is designed for ducts in laminar flow and has been adjusted for square monolith channels [38,40,193,194]. In contrast, the axial dispersion of gas in the channels was derived from the Aris & Taylor equation (Equation B.4). This has been applied in situations involving monoliths with square channels in laminar flow [37,40,178]. According to Visconti *et al.*, [195] Equations B.5 and B.6 are suitable for computing $\lambda_{axial,s}$ and λ_{radial} in the square channel monolithic reactor. Finally, the Usc value was derived from Equation B.7 as proposed by Groppi & Tronconi [196].

B.2.Physical properties of the gas

Upon reviewing the literature and considering the recommendations of Poling *et al*., [197], VDI, 2010 [198], and Green *et al*., [199] , the selected correlations for calculating the physical properties of the gas phase for both individual compounds and their mixture are presented in Table B.2. Following this, the mass concentration of each compound was determined using their formal

definition (Equation B.8). The DIPPR equation was chosen for the calculation of viscosity (Equation B.9) and thermal conductivity (Equation B.13) for each gaseous compound. The Wilke and Wassiljewa mixing rules were applied for calculating the viscosity (Equation B.10) and thermal conductivity (Equation B.14) of the gas. It was established that the axial thermal conductivity of the gas phase matches that of the bulk gas. To calculate the specific heat at constant pressure for each species in an ideal gas state, the Aly-Lee equation (Equation B.11) was employed. The specific heat of the ideal gas mixture was then determined using its formal definition (Equation B.12). The Fuller equation (Equation B.15) was used to calculate the binary diffusivities of the gaseous compounds [37,38,41,161,165,166,175,200,201] . The diffusivity of each compound in the gas was calculated with the Equation B.16. Lastly, Equation B.17 was used to determine the effective diffusivities of each gaseous species within the catalyst. This required obtaining the molecular and Knudsen diffusivity values for each gaseous compound in the solid.

Table B.2. Correlations and definitions of physical properties.

Gas density $\rho_g = \frac{P \cdot MW}{R_{gases} \cdot T_g} \rightarrow \rho_{i,g} = w_{i,g}\rho_g$	B.8
Viscosity of each compound in the gas $\mu_{i,g}[Pa \cdot s] = \frac{A_{\mu i} T_g^{\,B_{\mu i}}}{1 + \frac{C_{\mu i}}{T_g} + \frac{D_{\mu i}}{T_g^{\,2}}};\ T_g\ in\ K$	B.9
Gas viscosity $\mu_g = \sum_{i=1}^{NC} \frac{x_{i,g} \cdot \mu_{i,g}}{\sum_{j=1}^{NC} x_{j,g} \cdot \zeta_{\mu\_i,j}};\ \zeta_{\mu\_i,j} = \frac{\left(1 + \left(\frac{\mu_{i,g}}{\mu_{j,g}}\right)^{1/2} \left(\frac{MW_j}{MW_i}\right)^{1/4}\right)^2}{\sqrt{8}\left(1 + \frac{MW_i}{MW_j}\right)^{1/2}}$	B.10
Specific heat of each compound in the gas $C_{pi,g}\left[\frac{J}{kmol \cdot K}\right] = \left(A_{C_p i} + B_{C_p i}\left(\frac{C_{C_p i}}{T} csch\left(\frac{C_{C_p i}}{T}\right)\right)^2 + D_{C_p i}\left(\frac{E_{C_p i}}{T} sech\left(\frac{E_{C_p i}}{T}\right)\right)^2\right);\ T\ in\ K$	B.11
Specific heath of gas	B.12

$$C_{p,g} = \sum_{i=1}^{NC} w_{i,g} C_{pi,g}$$

Thermal conductivity of each compound in the gas

$$\lambda_{i,g}\left[\frac{W}{m \cdot K}\right] = \frac{A_{\lambda i} T_g^{\,B_{\lambda i}}}{1 + \frac{C_{\lambda i}}{T_g} + \frac{D_{\lambda i}}{T_g^{\,2}}};\ T_g\ in\ K \qquad \text{B.13}$$

Thermal conductivity of the gas

$$\lambda_{axial,g} = \lambda_g = \sum_{i=1}^{NC} \frac{x_{i,g} \cdot \lambda_{i,g}}{\sum_{j=1}^{NC} x_{j,g} \cdot \zeta_{\lambda\_i,j}};\ \zeta_{\lambda\_i,j} = 1.065 \frac{\left(1 + \left(\frac{\mu_{i,g}}{\mu_{j,g}}\right)^{1/2} \left(\frac{MW_j}{MW_i}\right)^{1/4}\right)^2}{\sqrt{8}\left(1 + \frac{MW_i}{MW_j}\right)^{1/2}} \qquad \text{B.14}$$

Binary diffusivity of each compound in the gas

$$D_{i,j\_g}\left[\frac{cm^2}{s}\right] = \frac{0.0143 \cdot T^{1.75}}{P \cdot MW_{i,j}^{\frac{1}{2}} \left(\left(\Sigma_{v_i}\right)^{\frac{1}{3}} + \left(\Sigma_{v_j}\right)^{\frac{1}{3}}\right)^2};\ MW_{i,j} = 2\left(\frac{1}{MW_i} + \frac{1}{MW_j}\right)^{-1}; \qquad \text{B.15}$$

$T_g\ in\ K\ and\ P\ in\ bar$

Diffusivity of each compound in the gas

$$D_{i,g} = \left(1 - x_{i,g}\right)\left(\sum_{j=1.j\neq i}^{NC} \frac{x_{j,g}}{D_{i,j\_g}}\right)^{-1} \qquad \text{B.16}$$

Effective diffusivity of each compound in the catalyst

$$D_{i_{eff},cat} = \frac{\varepsilon_{g,cat}}{\tau_{cat}}\left(\frac{1}{D_{i,g\_cat}} + \frac{1}{D_{i,K}}\right)^{-1};\ D_{i,g\_cat}\ with\ Eq.42\ for\ x_{i,g}\ and\ D_{i,j\_g}\ in\ catalyst; \qquad \text{B.17}$$

$$D_{i,K} = \frac{d_{pore}}{3}\sqrt{\frac{8RT_s}{\pi MW_i}}\ (Knudsen\ diffusion\ of\ component\ i)$$

B.3.Multiplication factor applied to Falbo's reaction rate expression

To perform the comparative study of the effect of the type of catalyst on the dynamic response of the monolithic reactor to the fluctuation of H_2 loading, a multiplication factor was applied, which transforms the reaction rate from the Falbo kinetic expression (Equation 2.30) to turnover frequency. This factor contains the mass percentage and the dispersion of Ru in the Falbo catalyst.

$$TOF_{Falbo}[s^{-1}] = \frac{MW_{RU}}{w_{Ru\ in\ catalyst} Dispersion_{Ru\ in\ catalyst}} r_{Falbo}\left[\frac{kmol}{kg_{catalyst} \cdot s}\right] = \frac{101.07 \frac{kg_{Ru}}{kmol_{Ru}}}{0.0005 \frac{kg_{Ru}}{kg_{catalyst}} 0.35 \frac{kmol_{Ru\ in\ catalyst\ surface}}{kmol_{Ru}}} r_{Falbo}\left[\frac{kmol}{kg_{catalyst} \cdot s}\right]$$

As a result, a reaction rate expression (Equation B.18) was obtained, which is not dependent on the load and dispersion of the active phase of the catalyst.

$$TOF_{Falbo}[s^{-1}] = 577543 \ \frac{kg_{catalyst}}{kmol_{Ru\ in\ catalyst\ surface}} \ r_{Falbo}\left[\frac{kmol}{kg_{catalyst}\cdot s}\right] \qquad \text{B.18}$$

To obtain a reaction rate expression for Ru as a function of the same Ni loading and dispersion from the Koschany kinetic expression (Equation 2.27), the above expression was multiplied by another multiplication factor, which contains the values of the loading and dispersion of the selected Ni catalyst.

$$r_{Falbo,corrected}\left[\frac{kmol}{kg_{catalyst}\cdot s}\right] = TOF_{Falbo}[s^{-1}]\frac{w_{Ni\ in\ catalyst} Dispersion_{Ni\ in\ catalyst}}{MW_{Ni}} = TOF_{Falbo}[s^{-1}]\frac{0.58\frac{kg_{Ni}}{kg_{catalyst}} 0.06\frac{kmol_{Ni\ in\ catalyst\ surface}}{kmol_{Ni}}}{58.69\frac{kg_{Ni}}{kmol_{Ni}}}$$

$$r_{Falbo,corrected}\left[\frac{kmol}{kg_{catalyst}\cdot s}\right] = 5.93\cdot 10^{-4}\ \frac{kmol_{Ni\ in\ catalyst\ surface}}{kg_{catalyst}} TOF_{Falbo}[s^{-1}]$$

By showing the reaction rate expression obtained for Ru in terms of the original Falbo rate expression for this catalyst, Equation B.19 was obtained, which contains a multiplication factor that makes the reaction rate a function of the same loading and dispersion of the Ni catalyst used in the Koschany kinetic expression.

$$r_{Falbo,corrected}\left[\frac{kmol}{kg_{catalyst}\cdot s}\right] = 342.45\ \frac{kmol_{Ni\ in\ catalyst\ surface}}{kmol_{Ru\ in\ catalyst\ surface}}\ r_{Falbo}\left[\frac{kmol}{kg_{catalyst}\cdot s}\right] \qquad \text{B.19}$$

Thus, the comparison of the effect of both catalysts on the dynamic response of the monolithic reactor to H_2 loading fluctuation was carried out under the same reaction conditions.

B.4.Model validation

B.4.1.Impact of the Number of Selected Intervals for each Spatial Coordinate on the Precision of Results

Initially, the adequacy of the number of intervals suggested for each spatial coordinate was confirmed, ensuring that the accuracy of the model's results met the desired criteria. The operating conditions listed in Table 2.5 were employed for this purpose, along with the Koschany *et al*., kinetic expression. This process was carried out from the start-up to the steady state condition. Subsequently, new results were achieved with an increased number of intervals for each coordinate, and these were compared with the originally calculated results. If the results derived from the base number of intervals do not deviate by more than 5 % from those calculated with a larger number of intervals, then the initial interval size for each spatial coordinate was deemed suitable.

Table B.3 presents the values of the main performance indicators (maximum temperature and CO_2 conversion) during the start-up of the monolithic reactor in correspondence to the change and quantity of evenly spaced intervals of each spatial coordinate.

The difference between the results derived from the base intervals number (5 for both r/R and ξ/δ) and those computed by doubling the intervals of the dimensionless radial coordinate (r/R) and the dimensionless spatial coordinate (ξ/δ) of the catalytic coating is far below 1 %. When it comes to the dimensionless axial coordinate (z/L), it's worth observing that the parameters determined aren't affected by the number of intervals implemented (> 50).

Thus, it can be highlighted that the initially suggested number of intervals for each spatial coordinate was sufficient to acquire the results of this investigation, with the required precision.

Table B.3. Deviation of model results as a function the number of intervals for each spatial coordinate. Base case.

Spacing (N° of intervals)	$T_{reactor,\ max}$ [°C]	$X_{CO2,max}$ [%]
Δ(r/R) **[-]**	***Δ(z/L)*** **= 0.02 [-] and** ***Δ(ξ/δ)*** **= 0.2 [-]**	
0.2 (5)	299.89	97.84
0.1 (10)	299.86	97.84
Percentage deviation [%]	**0.01**	**0.00**
Δ(ξ/δ) **[-]**	***Δ(z/L)*** **= 0.02 [-] and** ***Δ(r/R)*** **= 0.2 [-]**	
0.2 (5)	299.89	97.84
0.1 (10)	299.87	97.83
Percentage deviation [%]	**0.01**	**0.01**
Δ(z/L) **[-]**	***Δ(r/R)*** **= 0.2 [-] and** ***Δ(ξ/δ)*** **= 0.2 [-]**	
0.0200 (50)	299.89	97.84
0.0164 (60)	299.82	97.81
Percentage deviation [%]	**0.02**	**0.03**

B.4.2.Model Validation through the Steady State Chemical Equilibrium Condition

The initial validation examines the state of chemical equilibrium in steady state. As such, upon achieving a steady state, the reaction system met the chemical equilibrium condition. The results were then compared to against those reported by Gao *et al*., [27], concerning the Sabatier reaction's chemical equilibrium state. If the average percentage deviation of the results under this condition, compared to the numerical/experimental data from Gao *et al*., falls below 5 %, then the mathematical model developed in this study will be valid from this theoretical perspective.

The mathematical model proposed in this research is validated by calculating the CO_2 conversion values under the chemical equilibrium condition for various temperature ranges (200 – 375 °C), and these are then compared with the results obtained by Gao *et al*., [27] for 1 atm and a 4/1 H_2/CO_2 ratio.

The values of the operational parameters related to mass and heat transfer limitations had to be modified to fully achieve the condition of chemical equilibrium in steady state. The following modifications were made:

- The thickness of the catalytic coating was reduced from 200 to 2 μm, leading to a 100 % effectiveness factor for the Sabatier reaction. Hence, the resistance to intraparticle mass transfer is insignificant.
- The GHSV value was reduced until axial gradients caused by the transport of mass, heat, and momentum in the gas became unnoticeable.
- Aluminum was used as the monolith's substrate instead of cordierite. This ensured a completely isothermal operation of the CO_2 methanation reactor.
- Finally, it was verified that, under the base case's proposed operating conditions and dimensions, the effects of axial dispersion of mass and heat of the gas were insignificant.

As a result, all study cases achieved the condition of chemical equilibrium in steady state. An equilibrium approach value (φ_{eq}) of one (1.0) was obtained for all cases. Moreover, it was also demonstrated that in all studies conducted in this section, there were no mass and heat transfer resistances between the gas and solid. Additionally, it was evident that the temperature difference between the solid and the cooling medium, the pressure drop, radial gradient of reactor temperature, and the axial dispersion of mass/heat were insignificant in all cases examined. Figure B.1 illustrates the results of the initial validation (chemical equilibrium).

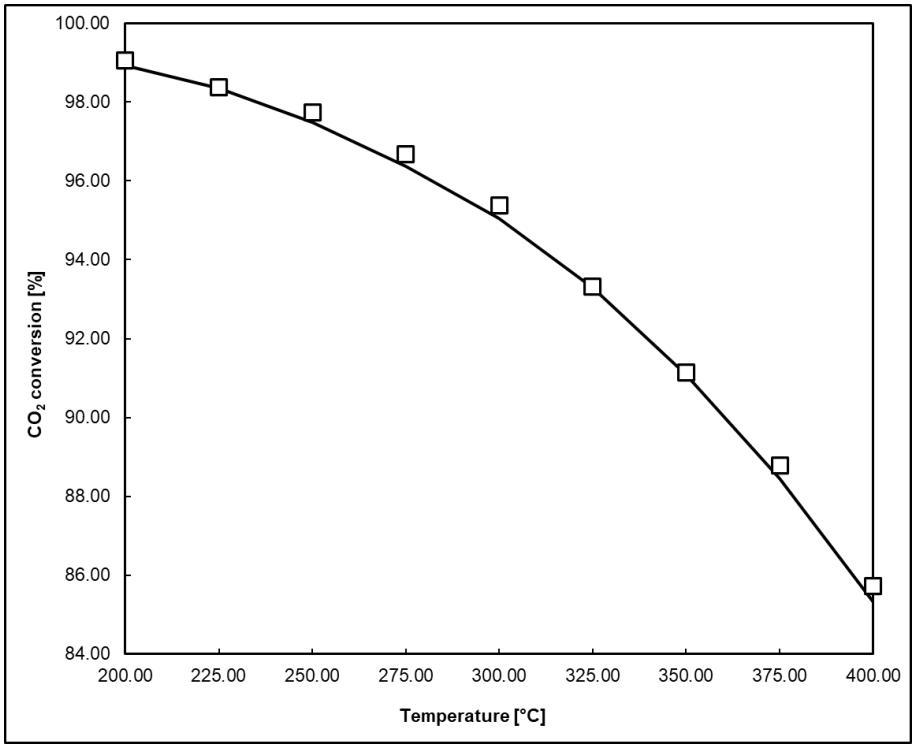

Figure B.1. Comparison of modeled and experimental CO_2 conversion profile as a function of temperature, for the chemical equilibrium condition in the Sabatier reaction. □ X_{CO2}, Gao *et al.,*, ── X_{CO2}, Model.

B.4.3.Model Validation via Steady State Kinetic Regime Condition

As another verification approach, the kinetic regime condition in steady state was employed. The identical operating conditions and kinetic expression from the research by Koschany *et al*., [146] were replicated. As such, upon achieving a steady state, the reaction system met the kinetic regime condition. The results derived from this condition were compared to the findings gathered by Koschany. If the average percentage deviation of the results achieved under this condition, in relation to the numerical or experimental data from Koschany *et al*., falls below 5 %, then the mathematical model developed in this study will also be valid from this theoretical standpoint.

The mathematical model presented in this study was further validated using a strategy that applied the kinetic regime condition in a steady state. The CO_2 conversion values in the kinetic regime were computed for varying temperatures (252, 266, 286, and 314 °C) and compared with the values recorded by Koschany *et al*., [146] under operating conditions of 3, 6, and 9 bars, with an H_2/CO_2/Ar ratio of 4/1/5, and 120 LSTD/(h·gcat). Modifications were made to the operational parameters linked to the process's mass and energy transport resistances to achieve the steady state kinetic regime condition fully. These modifications were as follows:

- The thickness of the catalytic coating was decreased from 200 μm to 2 μm, resulting in a Sabatier reaction effectiveness factor of 100 % (intraparticle mass transfer resistance is considered insignificant).
- Aluminium was utilized as the monolith's substrate instead of cordierite, enabling the CO_2 methanation reactor to function entirely in an isothermal condition.

Through these modifications, the steady state kinetic regime was achieved for all cases examined in this validation. It was also validated that φ_{eq} was zero. Additionally, it was confirmed that there was no resistance to mass/energy transport limitations between the gas and the solid, and that the temperature difference between the solid and the cooling medium, the pressure drop, the reactor's radial temperature gradient, and the axial mass/heat dispersion were all negligible in all the cases during this model validation. Consequently, it can be concluded that this validation strategy was correctly implemented in this study.

Figure B.2 displays a minor difference between the CO_2 conversion calculated by the proposed model, for the kinetic regimen condition, and the ones reported by Koschany *et al.,*, where the average percentage deviation also falls under 1 %.

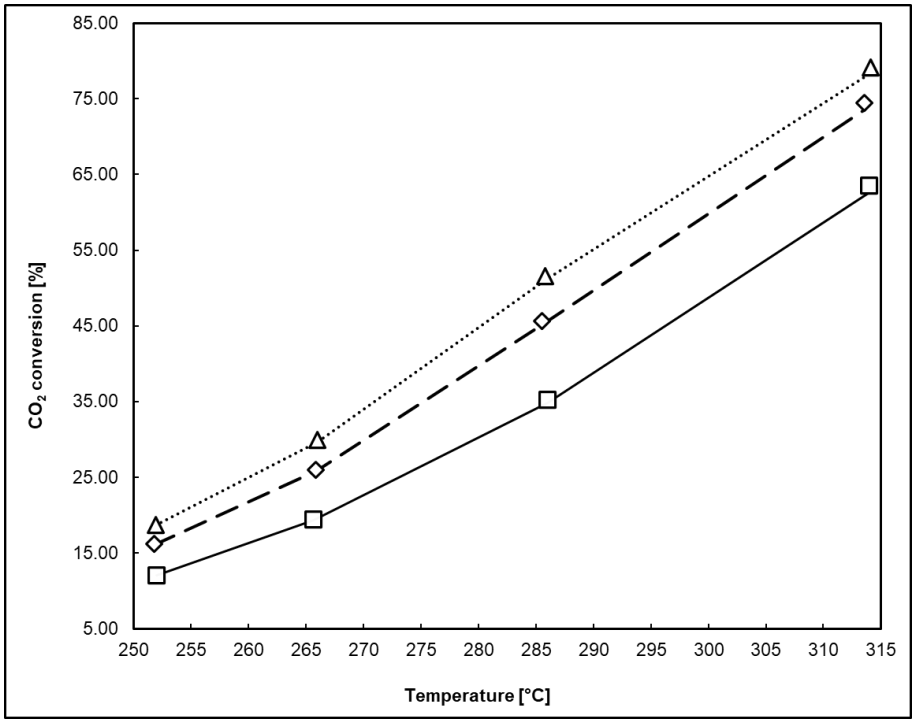

Figure B.2. Comparison of modeled and experimental CO_2 conversion profile as a function of temperature, for the kinetic regime condition in the Sabatier reaction. □ X_{CO2}, Koschany, 3 bar ◊ X_{CO2}, Koschany, 6 bar, Δ X_{CO2}, Koschany, 9 bar, ── X_{CO2}, Model, 3 bar, ─ ─ X_{CO2}, Model, 6 bar, ···· X_{CO2}, Model, 9 bar.

As such, these results, derived using the two validation methodologies, confirm the full theoretical validity of the reactor's mathematical model, thereby strengthening its use for obtaining reliable values and trends for each of the test cases established in this research.

B.5.Effect of H_2 Load Fluctuation on Reaction Rate for each Study Case

For determining the time at which the steady state was attained, both during the initial start-up and after recovering from the fluctuation in the H_2 load, an error function was formulated. This function, defined as $Error_{ss} = |X_{k+1} - X_k|_{max}$ was computed for consecutive time intervals (t_k and t_{k+1}) at each point within the reactor. Whenever $Error_{ss}$ falls below 0.01 for all variables being examined in this research, it implies that the steady state has been achieved at the time t_k.

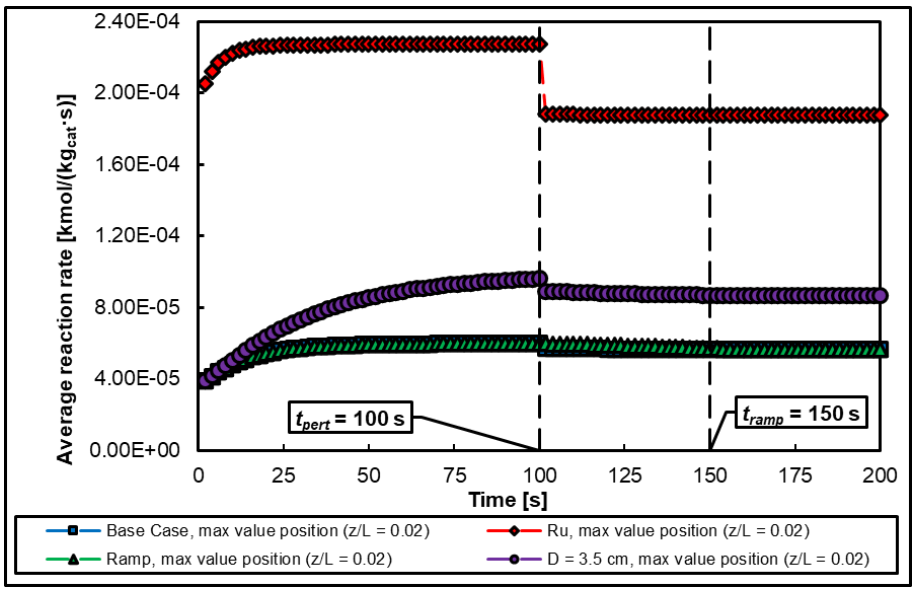

Figure B.3. Average reaction rate profile as a function of time at the reactor centerline.

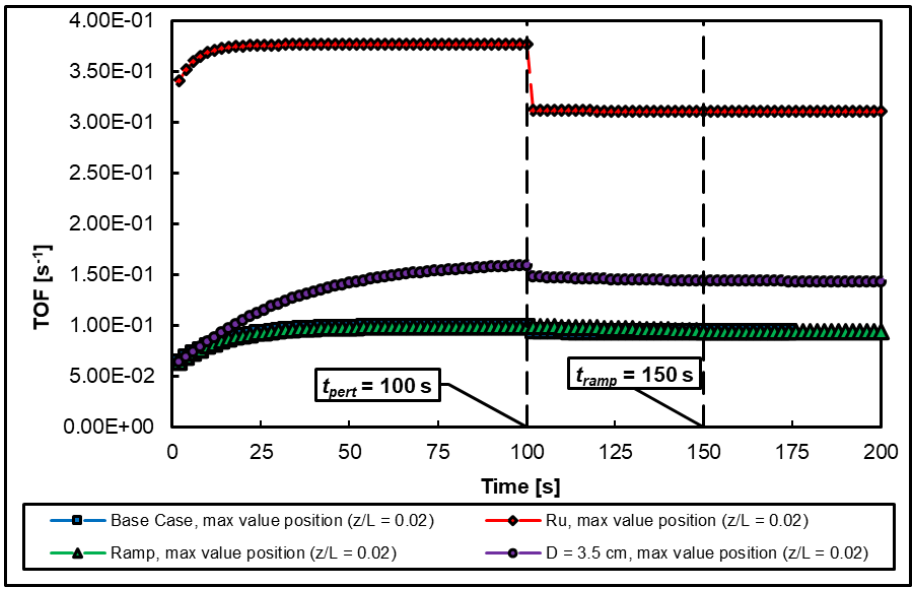

Figure B.4. Turn Over Frequency (TOF) profile as a function of time in the reactor centerline.

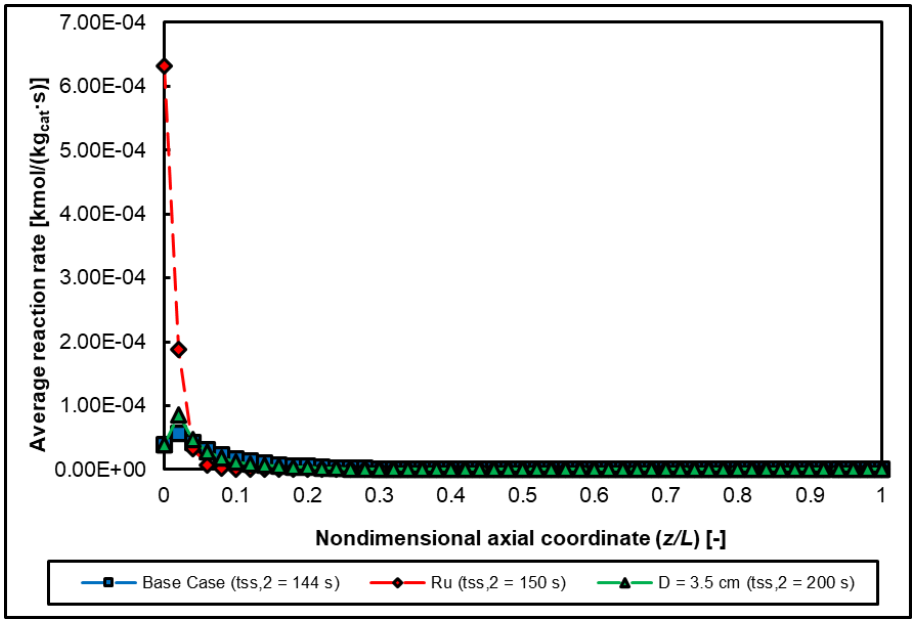

Figure B.5. Average reaction rate profile as a function of z/L at the reactor centerline.

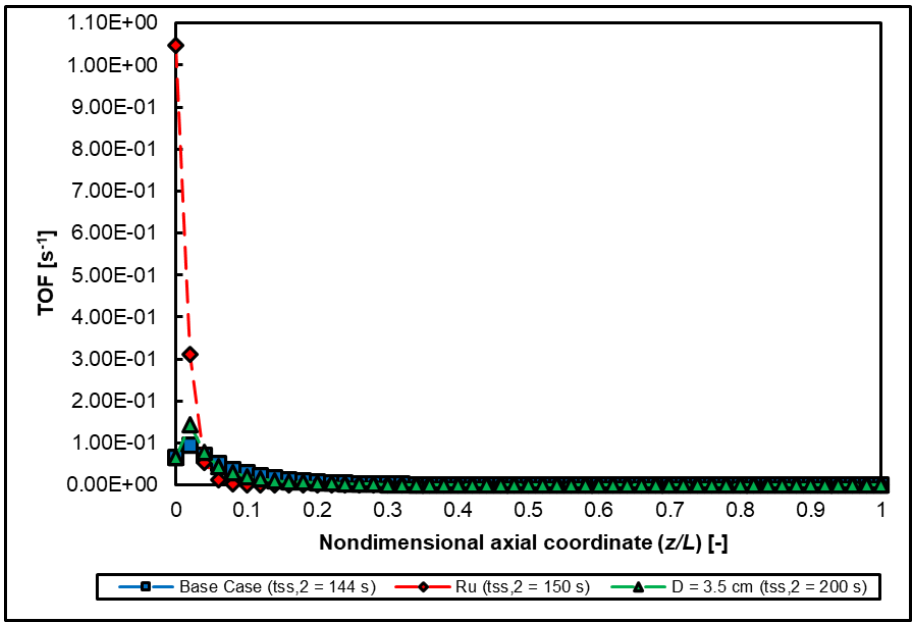

Figure B.6. Average Turn Over Frecuency (TOF) profile as a function of z/L in the reactor centerline.

B.6.Reactor Temperature and CO_2 Conversion Profiles

For determining the time at which the steady state was attained, both during the initial start-up and after recovering from the fluctuation in the H_2 load, an error function was formulated. This function, defined as $Error_{ss} = |X_{k+1} - X_k|_{max}$ was computed for consecutive time intervals (t_k and t_{k+1}) at each point within the reactor. Whenever $Error_{ss}$ falls below 0.01 for all variables being examined in this research, it implies that the steady state has been achieved at the time t_k.

B.6.1.Effect of Catalyst: Ni vs Ru

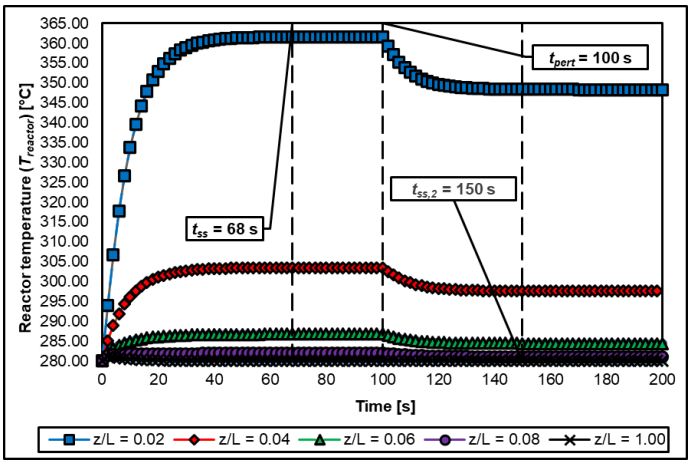

Figure B.7. Temperature profile as a function of time in the reactor centerline. Ru as the active phase of the catalyst.

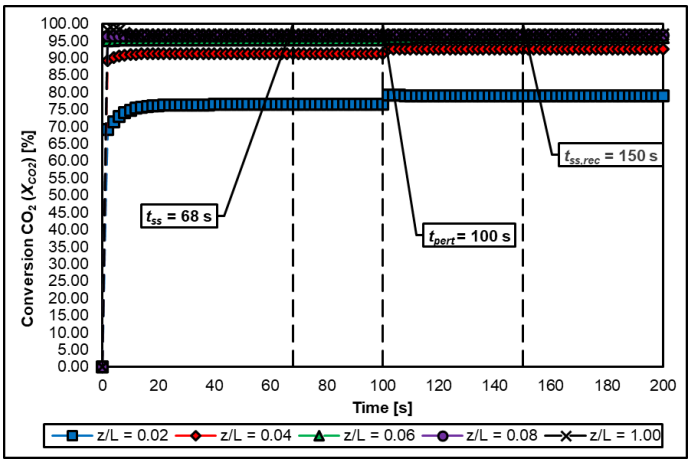

Figure B.8. CO_2 conversion profile as a function of time at the reactor centerline. Ru as the active phase of the catalyst.

C. Appendix C: Supporting Information of Dynamic behavior of a monolithic CO_2 methanation reactor to H_2 load disturbance. Experimental validation and theoterical comparison with fixed bed.

C.1.Inlet conditions, catalyst properties and dimensions of dynamic studies of CO_2 methanation reactors

Table C.1. Inlet conditions of dynamic studies for CO_2 methanation reactors.

Reactor	Temperature [°C]	Pressure [kPa]	Molar flow [kmol/s]	Volumetric flow STP [m^3/s]	GHSV [$m^3_{gasSTD}m^{-3}_{reactor}h^{-1}$]	H_2/ CO_2 molar ratio [-]	Inert molar fraction [%]	Products molar fraction [%]	Cooling medium temperature [°C]	Reference
FXB	270	400	9.30E-07	2.08E-05	15000	4.00	-	-	270	[118,202]
	183	101	9.30E-08	2.08E-06	27	4.12	21.7 (N_2)	-	183	[105,203]
	183	101	7.44E-07	1.67E-05	217	4.12	21.7 (N_2)	-	183	[105,203]
	238	1500	3.85E-05	8.63E-04	11531	4.00	-	-	216	[102,204]
	280	1500	1.24E-04	2.78E-03	10186	4.00	75.0 (N_2)	-	-	[92,205]
	211	1500	1.20E-05	2.68E-04	1572	4.00	-	-	205	[100,204]
	211	1500	2.39E-05	5.36E-04	3144	4.00	-	-	205	[100,204]
	240	2000	1.05E-04	2.34E-03	44762	4.00	-	16.67 (CH_4)	240	[73,206]
	251	2000	1.39E-04	3.13E-03	59683	4.00	-	16.67 (CH_4)	251	[73,206]
SBC	320	2000	8.37E-03	1.88E-01	2939	4.00	-	16.67 (CH_4)	278	[73,206]
	320	2000	1.12E-02	2.50E-01	3918	4.00	-	16.67 (CH_4)	269	[73,206]
PHE	200	800	2.73E-04	6.11E-03	N/A	4.15	-	16.26 (CH_4)	230	[67]
HMR	280	101	3.59E-06	8.05E-05	286	4.00	-	-	280	[20]

Table C.2. Catalyst properties for dynamic studies of CO_2 methanation reactors.

Reactor	Kinetic expression	Catalyst load [$kg_{catalyst}$ / $m^3_{reactor}$]	Catalyst size [mm]	Catalyst shape	Density particle [$kg_{catalyst}$ / $m^3_{particle}$]	Catalyst Porosity [-]	Mean pore diameter[nm]	Catalyst volumetric fraction in reactor [-]	Reference
FXB	Ducamp *et al*., 2016	764	0.340	Sphere	1274	0.59	8.2	0.600	[118,202]
	Koschany *et al*., 2016	720	2.100	Sphere	1390	0.62	6.6	0.518	[105,203]
	Koschany *et al*., 2016	720	2.100	Sphere	1390	0.62	6.6	0.518	[105,203]
	Koschany *et al*., 2016	1281	2.000	Sphere	2300	0.40	-	0.557	[102,204]
	Koschany *et al*., 2016	1475	3.000	Sphere	2418	0.37	12.4	0.610	[92,205]
	Koschany *et al*., 2016	1281	2.000	Sphere	2300	-	-	0.557	[100,204]
	Koschany *et al*., 2016	1281	2.000	Sphere	2300	-	-	0.557	[100,204]
SBC	Lefebvre *et al*., 2018	630	3.000	Sphere	1050	0.4	10	0.600	[73,206]
	Lefebvre *et al*., 2018	630	3.000	Sphere	1050	0.4	10	0.600	[73,206]
	Lefebvre *et al*., 2018-2019	Dependent of gas holdup	0.075	Sphere	1050	0.4	10	Dependent of gas holdup	[73,206]
	Lefebvre *et al*., 2018-2019	Dependent of gas holdup	0.075	Sphere	1050	0.4	10	Dependent of gas holdup	[73,206]
PHE	Koschany *et al*., 2016 and Xu & Froment *et al*., 1989	N/A	4.5 (3x3 original dimensions)	-	-	-	-	-	[67]
HMR	Koschany *et al*., 2016 and Falbo *et al*., 2018	121	0.200	Flat	900	0.7	50	0.134 (catalyst) and 0.231 (substrate)	[20]

Table C.3. Dimensions of dynamic studies for CO_2 methanation reactors.

Reactor	Length [mm]	Diameter [mm]	Reference
FXB	160	6.31	[118,202]
	880	20.00	[105,203]
	880	20.00	[105,203]
	3430	10.00	[102,204]
	500	50.00	[92,205]
	7810	10.00	[100,204]
	7810	10.00	[100,204]
SBC	600	20.00	[73,206]
	600	20.00	[73,206]
	2530	340.00	[73,206]
	2530	340.00	[73,206]
PHE	1000	-	[67]
HMR	2000	25.40	[20]

C.2.Experimental setup and experimental diagram of reactor

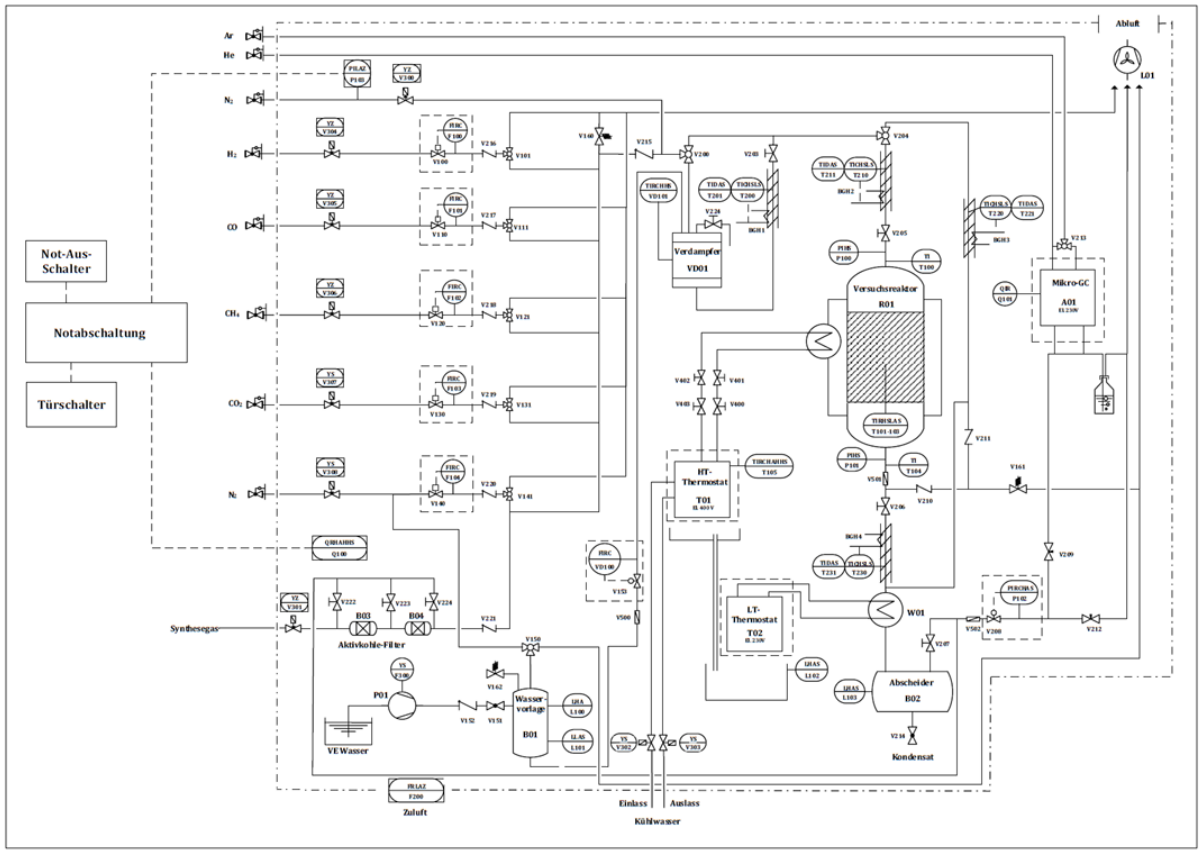

Figure C.1. Experimental setup [189].

Figure C.2. Experimental diagram of HMR.illustrates the experimental diagram of the honeycomb monolith reactor (HMR). The gas and cooling medium flows are designed to operate in countercurrent. Reactants enter the upstream section of the reactor, which is 247.5 to 397 mm long and fitted with a fabric packing. The 90 mm reactor is copper-lined. The mixture of reactants and products then moves to the downstream section 83.7 to 105 mm long, before leaving the experimental area of the HMR.

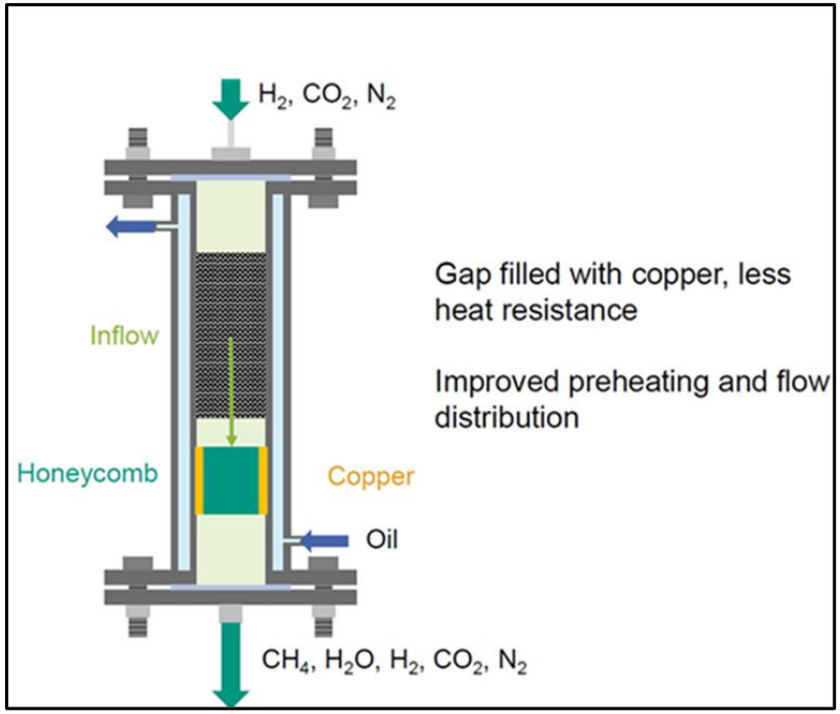

Figure C.2. Experimental diagram of HMR.

C.3. Radial thermal conductivity of honeycomb monolith used in dynamic test

Figure C.3 on the left displays the honeycomb monolith cell with corrugated plates utilized in this research. The channel cell is defined as a rectangle with a height of *b* and a base measuring *d* + $0.5\sqrt{3}b + 2\delta_{\lambda_{radial,s}}$. Here, the parameter *d* represents the thickness of the corrugated (*wellblech*) and smooth (*glatte blechlage*) metal plates, while $\delta_{\lambda_{radial,s}}$ signifies the spacing within the junction area between these plates. It is crucial to acknowledge that the monolith was created by winding a corrugated plate with a smooth one at a specific winding angle *γ*, which can affect the final design of the structure (Figure C.3 on the right) [189]. The sinusoidal channel of the corrugated plate is modeled as a triangular shape between two rectangular plates, each measuring *b x d/2*, representing smooth plates. This geometric setup leads to the formulation for calculating the combined thermal resistances ($R_{r,eff}$) of the solid. From this, the effective radial thermal conductivity of the solid ($\lambda_{radial,eff}$) is derived [189]. It is crucial to emphasize that the peak value of the radial thermal conductivity of the solid ($\lambda_{radial,s}$) occurs at a specific *γ* value, as indicated in Equation 3.2. Additionally, the maximum $\lambda_{radial,s}$ and its corresponding *γ* position are affected by the $\delta_{\lambda_{radial,s}}$ value [189].

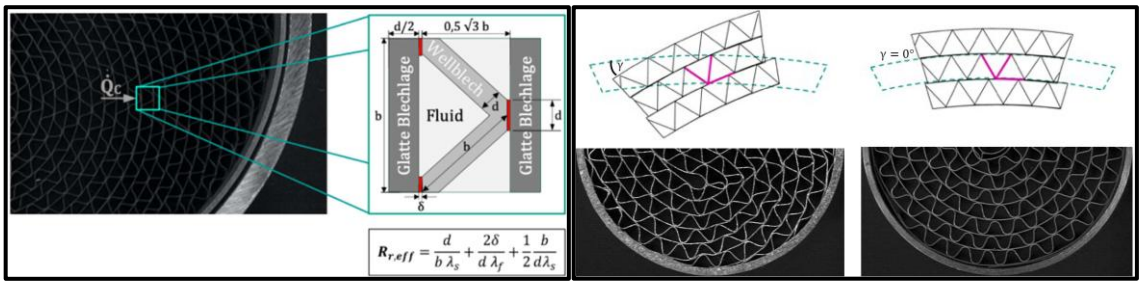

Figure C.3. Geometric representation of the corrugated plate monolith cell (left). Effect of the winding angle on the final design of the monolith (right) [189].

C.4. Profile temperatures of Schollenberger and Glockner

C.4.1.Schollenberger results

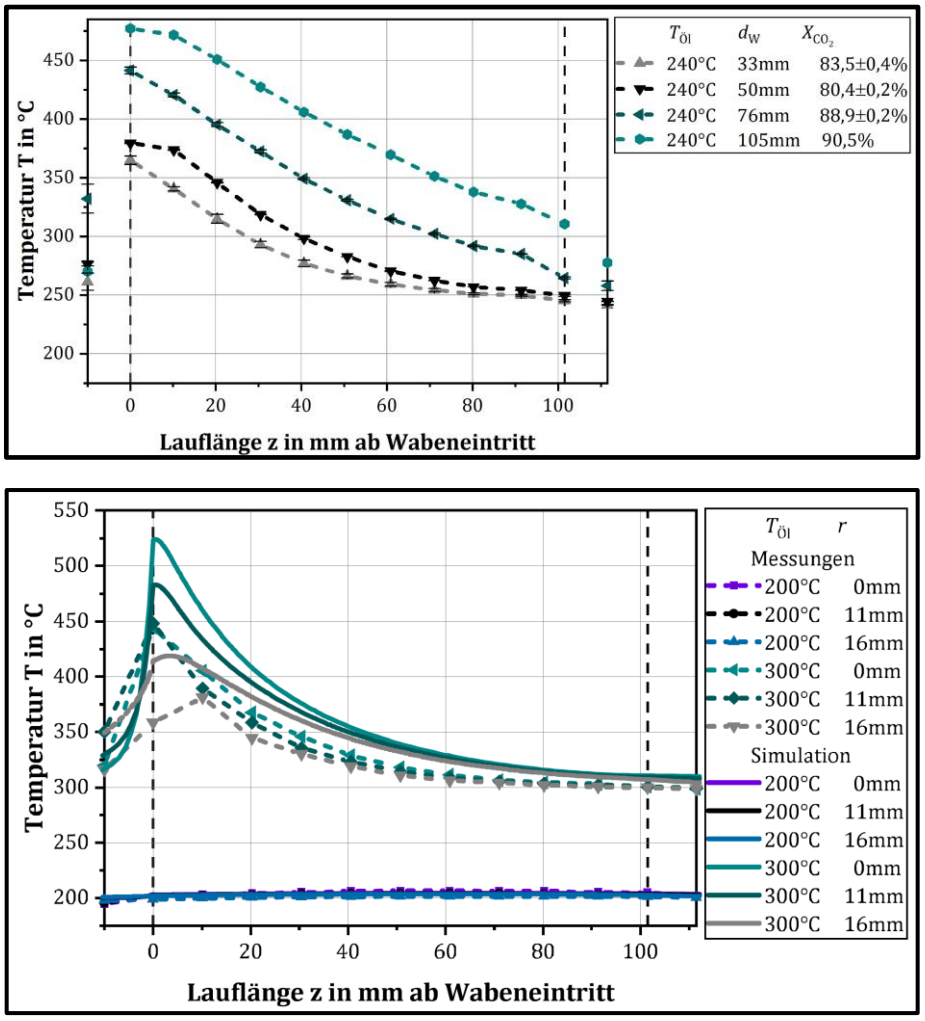

Figure C.4. Axial temperature profile. Effect of diameter d_W (as shown above). Comparison between predicted values from the model and experimental results for different radial positions and cooling medium temperatures ($T_{ôl}$), as shown below (d_W = 33 mm). Length of 101.5 mm, GHSV = 1800 h^{-1}, pressure of 8 bar, H_2/CO_2 molar ratio equal to 4/1 and 5 % molar of N_2 and catalyst load equal to 110 kg/m^3 [189].

C.4.2.Glockner results

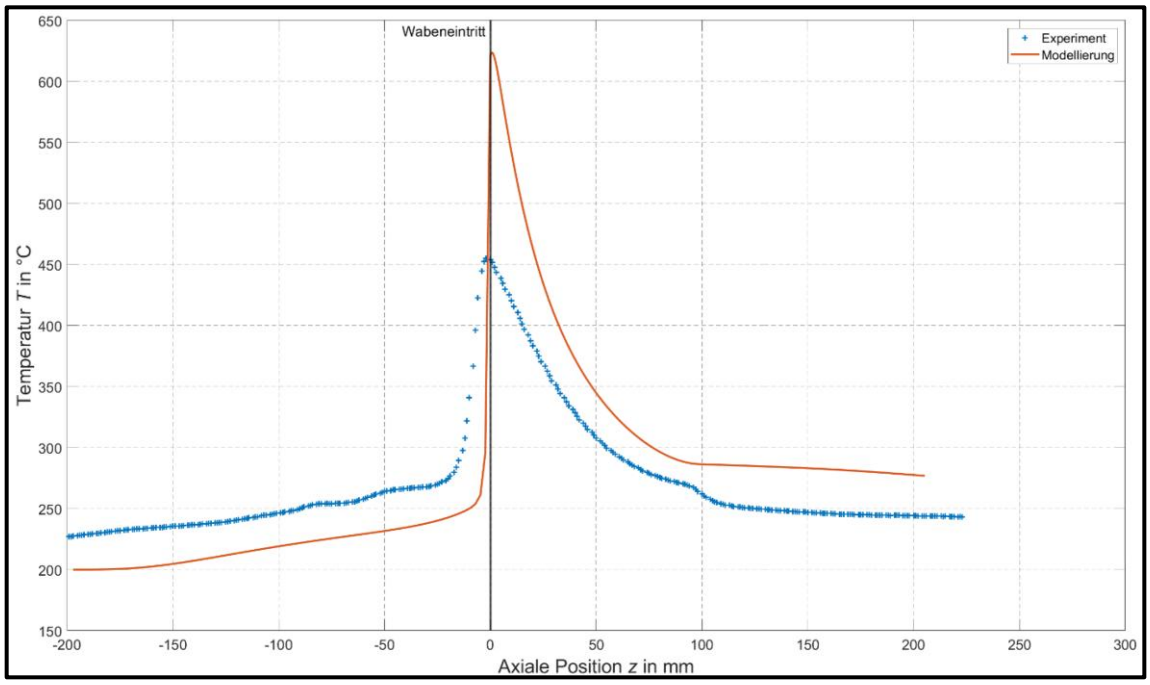

Figure C.5. Axial temperature profile. Comparison between predicted values from the model and experimental results in the centerline of reactor (d_W = 50 mm), Length of 100 mm, GHSV = 1800 h^{-1}, pressure of 8 bar, H_2/CO_2 molar ratio equal to 4/1 and 5 % molar of N_2 and catalyst load equal to 110 kg/m^3 [190].

C.5.Additional results

C.5.1.HMR vs. FXB: Operation conditions of Tauer *et al*.,

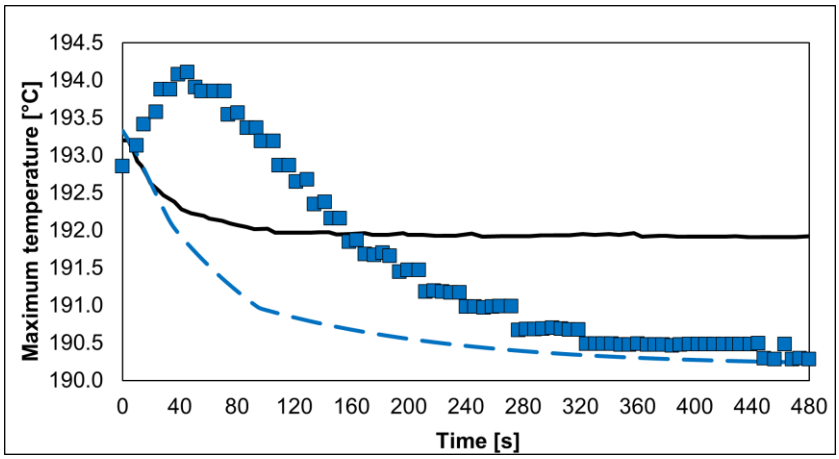

Figure C.6. Temporal profile of maximum temperature in hotspot location. Operation conditions of Tauer *et al*., [105]. Reduction of GHSV, from 217 to 27 h^{-1}. ■ Experiment, - - HMR, ■ Tauer's FXB model.

C.5.2.HMR vs. FXB: Operation conditions of Fischer *et al*.

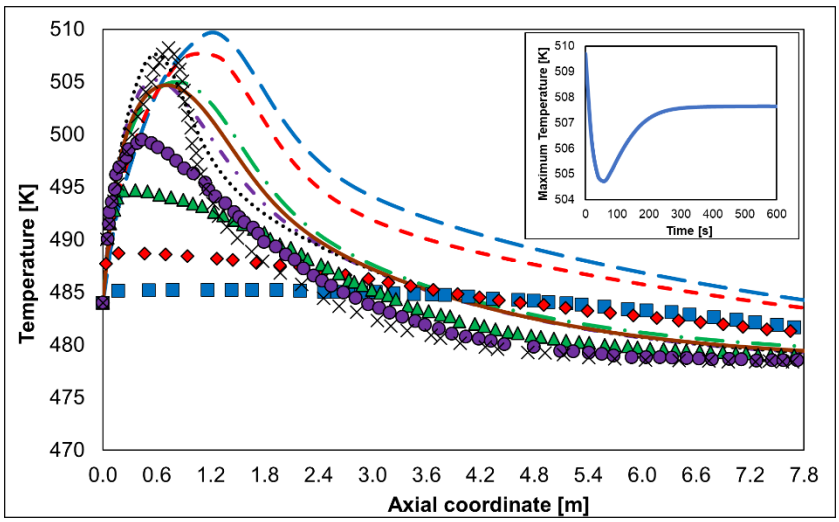

Figure C.7. Temperature profile for different times for the operation conditions of Fischer *et al*., [102]. Centerline of HMR. Reduction of GHSV, from 3144 to 1572 h^{-1}. Lines for HMR and points for FXB. ■ and - - for t = 0 s, ◆ and ▬ for t = 9 s, ▲and ▬ for t = 38 s, ● and ▬ for t = 84 s, **x** for t = 600 s (final steady state) and ▬ for t = 340 s (final steady state). ▬ for t = 53 s (transient maximum).

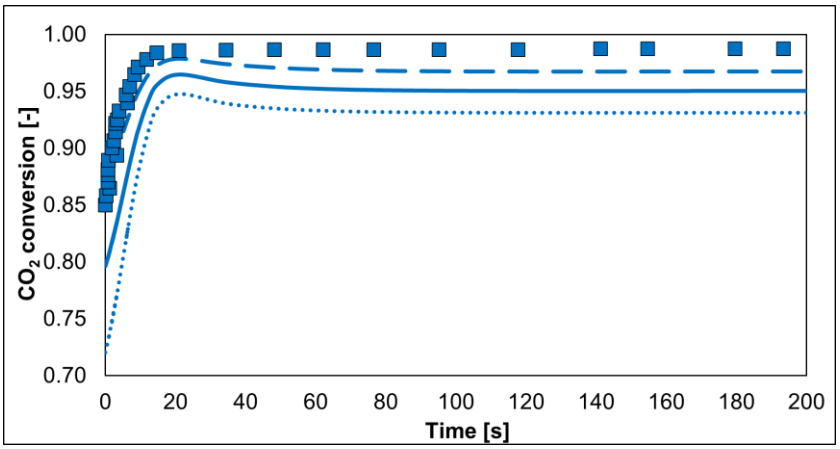

Figure C.8. Temporal profile of outlet CO_2 conversion for the operation conditions of Fischer *et al.*, [102]. Reduction of GHSV, from 3144 to 1572 h^{-1}. ■ FXB, - - Centerline HMR, ▬ Average HMR, ···· Wall HMR.